Graphene and Graphene Related Materials for PBI-Membrane-Based High-Temperature Hydrogen Fuel Cells

A Thesis Submitted to The University of Manchester for the Degree of Doctor of Philosophy in the Faculty of Science and Engineering

2022

Jianuo Chen

Department of Chemical Engineering

Blank page

Contents

Word Count: 66,053

Symbols

Symbol	Definition	Units
$\varnothing$	Instrumental Correction Factor	
A	Absorbance	a.u.
a	Exchange Current Density Related Parameters	
A_{active}	Active Area of Fuel Cell	mm^2
A_{Pt-H_2}	Hydrogen Desorption Area	$\frac{A}{V \tilde{n} cm^2}$
b	Kinetic Overvoltage Related Tafel Slope	
D	The Intrinsic Diffusivity	
d_0	Thickness of Membrane	mm
D^{eff}	The Effective Diffusivity Given by the Presence of the Solid Phase	
E	Potential	V
E_0	Open Circuit Voltage	V
$E_{kinetic}$	Kinetic Energy of Electron	eV
E_L	Laser Energy	eV
E_{photon}	X-ray Photons Energy	eV
F	Axial Force	N
F	Faraday's constant	
G	Gibbs Free Energy	J
H	Enthalpy	J
hf	The Enthalpies of Formation	J
I	Intensity of the transmitted light	a.u.
I_0	Intensity of the Entering Radiation or Beam	a.u.
j	Current Density	mA cm^{-2}
$j_{H_2\,Cross}$	Limiting Current Density of Hydrogen Crossover	mA cm^{-2}
j_{lim}	Diffusion Overvoltage Related Limiting Current Density	mA cm^{-2}
L	Length After Stretch	mm
L_D	Mean interdefect distance	nm
L_e	Pt Loading	
L_O	Initial Length	mm
M_{PA}	Molar mass of Phosphoric Acid	g mol^{-1}
M_{PBI}	Molar mass of Polybenzimidazole	g mol^{-1}

n	The Number of Electrons Taking Part in the Hydrogen Reduction Reaction	
$\dot{\eta}H_{2\ Crossover}$	The Hydrogen Crossover Flux	mol s^{-1}
R_{ct}	Kinetic Resistance	mΩ cm^2
R_{el}	Ohmic Resistance + Uncompensated Contact Resistance	mΩ cm^2
R_s	Sheet Resistance	Ω m^{-2}
S	Entropy	J·K^{-1}
sf	The Entropies of Formation	J·K^{-1}
T	Temperature	°C
t	Thickness	μm
v	Scan Rate	V s^{-1}
w_0	Width of Membrane	mm
W_{PA}	Content of Phosphoric Acid	wt%
W_{PBI}	Content of Polybenzimidazole	wt%
x	Given Distance	mm
Z_d	Mass Transfer Resistance	mΩ cm^2
ε	The Porosity	
ε_s	Strain	mm/mm
λ_L	Laser Wavelength	nm
μ	Linear Attenuation Coefficient	
ρ	Density of the Materials	mg cm^{-3}
σ	Electrical Conductivity	S m^{-1}
σ_E	Stress	MPa
τ	Tortuosity Factor	

Abbreviations

Abbreviation	Full Name
AB-PBI	Poly(2,5-benzimidazole)
ABS	Acrylonitrile Butadiene Styrene
ADL	Acid Doping Level
AST	Accelerated Stress Test
CAD	Computer-aided Design
CHP	Combined Heating and Power
CL	Catalyst Layer
CPE	Constant Phase Element
cPSD	Continuous Particle Size Distribution
CT	Computed Tomography
CV	Cyclic Voltammetry
CVD	Chemical Vapor Deposition
DMAc	Dimethylacetamide
DMF	Dimethylformamide
DMSO	Dimethylsulfoxide
DoE	Department of Energy
ECSA	Electrochemical Surface Area
EDS	Energy Dispersive X-ray Spectroscopy
EGO	Electrochemically Exfoliated Graphene Oxide
EIS	Electrochemical Impedance Spectroscopy
FDK	Feldkamp-Davis-Kress
FT-IR	Fourier-Transform Infrared Spectroscopy
FWHM	Full-width Half-maximum
GDE	Gas Diffusion Electrode
GDL	Gas Diffusion Layer
GO	Graphene Oxide
HOR	Hydrogen Oxidation Reaction
HT-PEMFC	High-temperature Proton Exchange Membrane Fuel Cell
IPA	Isopropanol
ITO	Indium Tin Oxide
LSV	Linear Sweep Voltammetry

MEA	Membrane-electrode-assambly
Meta-PBI	Poly[2,2-(m-phenylene)-5,5bibenzimidazole]
MMO	Mixed Metal Oxide
MPL	Microporous Layer
MSA	Methanesulfonic Acid
MW-CNT	Multiwall Carbon Nanotube
NMP	N-methyl-2-pyrrolidone
OCV	Open Circuit Voltage
ORR	Oxygen Reduction Reaction
PA	Phosphoric Acid
Para-PBI	Poly(2,2'-(p-phenylene)5,5'-bibenzimidazole
PBI	Polybenzimidazole
PEM	Proton Exchange Membrane
PETG	Polyethylene Terephthalate Glycol
PFSA	Perfluorosulfonic Acid
PGO	Phosphonated Graphene Oxide
PMMA	Poly(methyl methacrylate)
PNM	Pore Network Model
PSU	Polysulfones
PTFE	Polytetrafluoroethylene
PVDF	Polyvinylidene Difluoride
PVPA	Poly(vinylphosphonic acid)
SEM	Scanning Electron Microscopy
SLG	Single Layer Graphene
SPEEK	Polyetheretherketones
SPIs	Sulfonated Polyimides
SW-CNT	Single-wall Carbon Nanotube
TEM	Transmission Electron Microscopy
TGA	Thermogravimetric Analysis
VSSA	Volume-specific Surface Area
XPS	X-ray Photoelectron Spectroscopy

List of Tables and Figures

Publications

[1]   **J. Chen**, J.J. Bailey, L. Britnell, M. Perez-Page, M. Sahoo, Z. Zhang, A. Strudwick, J. Hack, Z. Guo, Z. Ji, P. Martin, D.J.L. Brett, P.R. Shearing, S.M. Holmes, The performance and durability of high-temperature proton exchange membrane fuel cells enhanced by single-layer graphene, Nano Energy. 93 (2022) 106829. https://doi.org/10.1016/J.NANOEN.2021.106829.

[2]   **J. Chen**, M. Perez-Page, Z. Ji, Z. Zhang, Z. Guo, S. Holmes, One step electrochemical exfoliation of natural graphite flakes into graphene oxide for polybenzimidazole composite membranes giving enhanced performance in high temperature fuel cells, Journal of Power Sources. 491 (2021) 229550.

[3]   **J. Chen**, M. Perez-Page, A. Sing, E.P.L. Roberts, S. Holmes, Synthesis of High-Quality Graphene Oxide Made By a Novel One-Step Electrochemical Exfoliation of Natural Graphite Flakes Based on a 3D-Printed Reactor, ECS Meeting Abstracts. MA2020-02 (2020) 1100. https://doi.org/10.1149/MA2020-0271100MTGABS.

[4]   **J. Chen**, M. Perez-Page, A. Sing, E.P.L. Roberts, S. Holmes, Synthesis and Applications of High Quality Graphene Made By a Novel Electrochemical Exfoliation of Natural Graphite Flakes, ECS Meeting Abstracts. MA2020-01 (2020) 862. https://doi.org/10.1149/MA2020-0110862MTGABS.

[5]   J.J. Bailey, **J. Chen**, J. Hack, M. Perez-Page, S.M. Holmes, D.J.L. Brett, P.R. Shearing, Lab-based X-ray micro-computed tomography coupled with machine-learning segmentation to investigate phosphoric acid leaching in high-temperature polymer electrolyte fuel cells, Journal of Power Sources. 509 (2021) 230347. https://linkinghub.elsevier.com/retrieve/pii/S0378775321008594 (accessed August 19, 2021).

[6]   Z. Guo, M. Perez–Page, **J. Chen**, Z. Ji, S.M. Holmes, Recent advances in phosphoric acid–based membranes for high–temperature proton exchange membrane fuel cells, Journal of Energy Chemistry. (2021). https://doi.org/10.1016/J.JECHEM.2021.06.024.

[7]   Z. Guo, **J. Chen**, J.J. Byun, R. Cai, M. Perez-Page, M. Sahoo, Z. Ji, S.J. Haigh, S.M. Holmes, High-performance polymer electrolyte membranes incorporated with 2D silica nanosheets in high-temperature proton exchange membrane fuel cells, Journal of Energy Chemistry. 64 (2021) 323–334. https://doi.org/10.1016/j.jechem.2021.04.061.

[8]   Z. Guo, **J. Chen**, J.J. Byun, M. Perez–Page, Z. Ji, Z. Zhao, S.M. Holmes, Insights into the performance and degradation of polybenzimidazole/muscovite composite membranes in high–temperature proton exchange membrane fuel cells, Journal of Membrane Science. 641 (2021) 119868. https://doi.org/10.1016/j.memsci.2021.119868.

[9]   Z. Ji, M. Perez-Page, **J. Chen**, R.G. Rodriguez, R. Cai, S.J. Haigh, S.M. Holmes, A structured catalyst support combining electrochemically exfoliated graphene oxide and carbon black for enhanced performance and durability in low-temperature hydrogen fuel cells, Energy. 226 (2021) 120318. https://doi.org/10.1016/j.energy.2021.120318.

[10]   Z. Ji, **J. Chen**, M. Pérez-Page, Z. Guo, Z. Zhao, R. Cai, M.T.P. Rigby, S.J. Haigh, S.M. Holmes, Doped graphene/carbon black hybrid catalyst giving enhanced oxygen reduction reaction activity with high resistance to corrosion in proton exchange membrane fuel cells, Journal of Energy Chemistry. 68 (2022) 143–153. https://doi.org/10.1016/J.JECHEM.2021.09.031.

[11]   Z. Ji, M. Perez-Page, **J. Chen**, S. Holmes, Nitrogen Doped Reduced Electrochemically Exfoliated Graphene Oxide Inserted Carbon Black As Novel Catalyst Support for the Hydrogen Fuel Cell, ECS Meeting Abstracts. MA2020-02 (2020) 2323. https://doi.org/10.1149/MA2020-02362323MTGABS.

[12]   M. Perez-Page, **J. Chen**, A. Parra-Puerto, J. Rubio-Garcia, A.R.J. Kucernak, S. Holmes, Incorporation of Graphene and Graphene-Based Materials into Membranes As an Alternative Electrolyte Configuration for Low and High Temperature Polymeric Electrolyte Membranes Fuel Cells., ECS Meeting Abstracts. MA2020-02 (2020) 2247–2247. https://doi.org/10.1149/ma2020-02352247mtgabs.

Abstract

The high-temperature proton exchange membrane fuel cell (HT-PEMFC) is a promising alternative to low temperature PEMFC, due to its low demand for hydrogen purity, simple water management, and high waste heat utilization. However, HT-PEMFC based on phosphoric acid (PA)-doped polybenzimidazole (PBI) membrane still has problems such as insufficient mechanical strength under high PA doping level, insufficient proton conductivity, and phosphoric acid leaching. This thesis explores the influence of PA distribution and migration on HT-PEMFC, and the application of single layer graphene (SLG) and electrochemical exfoliated (functionalized) graphene oxide (GO) in HT-PEMFC. This work is the first to apply high-quality SLG to HT-PEMFC. The coverage of the SLG on the electrode surface and the impact of SLG on the performance and durability when loaded between membrane and electrodes at anode, cathode or both sides of the HT-PEMFC are tested. After nearly 70 hours of accelerated stress testing, the peak power density at 150 ℃ of the membrane electrode assembly with SLG on both sides, with SLG on anode, with SLG on cathode and no SLG was measured as 480 mW cm^{-2}, 367 mW cm^{-2}, 365 mW cm^{-2} and 249 mW cm^{-2}, respectively. Moreover, through electrochemical characterization, X-ray micro-computed tomography (CT) and Raman spectroscopic mapping, this work proposes the mechanism by which monolayer graphene improves the performance and durability of high-temperature fuel cell by controlling its PA leaching and hydrogen crossover. Also, a reactor based on 3D printing was designed and manufactured to utilize natural graphite flakes as raw materials to synthesize GO with a reasonable oxygen content through one-step electrochemical exfoliation in a rapid and high-volume manner. Based on the established reactor-based one-step electrochemical exfoliation method to prepare GO, phosphonated (P)GO with a reasonable P content was prepared by using appropriate electrolytes. The as-prepared GO and PGO were doped in the PBI membranes to explore their effects on the mechanical properties of PBI, and the

performance and durability of HT-PEMFC. Compared with the pure PBI membrane, 0.5wt%, 1wt% and 2wt% of GO doping increased the peak power density of HT-PEMFC at 150℃ by 13.8%, 24.4% and 29.2%, respectively. The performance study of PGO adopts different PBI membrane material and preparation process from the GO study. The doping of 1.5wt% PGO in the PBI membrane increases the peak power density by 35.4%. The thesis is presented as a collection of four published or processing papers.

Declaration

I, the author Jianuo Chen, declare that no portion of the work referred to in this thesis has been submitted in support of an application for another degree or qualification in this, or any other, university or other institute of learning.

Copyright

i.   The author of this thesis (including any appendices and/or schedules to this thesis) owns certain copyright or related rights in it (the "Copyright") and s/he has given The University of Manchester certain rights to use such Copyright, including for administrative purposes.

ii.   Copies of this thesis, either in full or in extracts and whether in hard or electronic copy, may be made only in accordance with the Copyright, Designs and Patents Act 1988 (as amended) and regulations issued under it or, where appropriate, in accordance with licensing agreements which the University has from time to time. This page must form part of any such copies made.

iii. The ownership of certain Copyright, patents, designs, trademarks and other intellectual property (the "Intellectual Property") and any reproductions of copyright works in the thesis, for example graphs and tables ("Reproductions"), which may be described in this thesis, may not be owned by the author and may be owned by third parties. Such Intellectual Property and Reproductions cannot and must not be made available for use without the prior written permission of the owner(s) of the relevant Intellectual Property and/or Reproductions.

iv.   Further information on the conditions under which disclosure, publication and commercialisation of this thesis, the Copyright and any Intellectual Property and/or Reproductions described in it may take place is available in the University IP Policy (see http://documents.manchester.ac.uk/DocuInfo.aspx?DocID=24420), in any relevant Thesis restriction declarations deposited in the University Library, The University Library's regulations (see http://www.library.manchester.ac.uk/about/regulations/) and in The University's policy on Presentation of Theses

1. Introduction

With the drive to phase out fossil fuels caused by the increasingly serious environmental pollution, the development and utilization of renewable or sustainable energy becomes more and more important [1]. Among the numerous renewable energy sources, hydrogen stands out for its versatility, efficiency, and cleanliness [2]. Among the applications of hydrogen, the importance of hydrogen fuel cells cannot be underestimated for the efficient recovery of electrical energy from the stored hydrogen. High-temperature proton exchange fuel cells (HT-PEFC) based on phosphoric acid (PA)-doped polybenzimidazole (PBI) membranes have become a promising technology due to their reasonable proton conductivity, high tolerance to hydrogen impurity, thermal stability, and high utilization of waste heat [3][4]. Unlike low-temperature fuel cells based on perfluorosulfonic acid (PFSA) polymers, HT-PEMFCs do not rely on water as a conductor for proton transfer, but instead on the hydrogen bond matrix established by PA and PBI. Therefore, opting for HT-PEMFC reduces or even eliminates the need for humidification. As a result, the proton conductivity of the PA-doped PBI membrane is closely related to the PA doping level in the PBI membrane. However, each PBI repeat unit can only be combined with two PA molecules, most PA is distributed in the PBI matrix in a free state. This often leads to leaching of a portion of PA from the membrane to the electrodes during cell operation [5][6]. Firstly, excessive leaching of PA affects the proton conductivity of the membrane as the electrolyte reservoir is reduced [5][7][8]. Secondly, Although a small amount of PA leaching into the catalyst layer helps to establish more gas, catalyst and phosphoric acid three-phase points, excessive phosphoric acid leaching will block the gas transfer in the gas diffusion layer and coat the catalyst layer to reduce the activation sites of the catalyst, resulting in an increase in mass transfer and charge transfer resistances, respectively [7].

Graphene, as the first two-dimensional material isolated, has attracted worldwide attention for its excellent properties [9]. With its unique two-dimensional hexagonal structure, it has been shown to have a screening effect on atoms. Even the smallest atom, the hydrogen atom, can take billions of years to pass through the electron cloud gap of graphene at room temperature without the aid of atomic acceleration [10]. However, graphene has extremely low resistance to proton conduction [11]. Therefore, graphene is a promising barrier to prevent PA from leaching without significantly affecting the proton conductivity [11].

Graphene oxide (GO) is a 2D material containing graphene as a skeleton, functionalized with oxygen containing groups such as hydroxyl, carboxyl and carbonyl groups [12]. The abundant oxygen-containing functional groups on GO not only facilitate the dispersion of GO in water or organic solvents, but also facilitate its further functionalization such as sulfonation and phosphonation [13][14][15]. The doping of GO or functionalized GO in the HT-PEMFC membrane material can build an additional proton transfer channel by virtue of the hydrogen bond network established by its functional group with phosphoric acid or polymer, thus promoting proton hopping to improve proton conductivity [16][17][18][19][20][21]. In addition, GO or functionalized GO can act as a trap for phosphoric acid to prevent excessive leaching. Therefore, GO, which enables low-cost application of graphene-related materials, becomes an attractive material for improving the performance and durability of PA doped HT-PEMFC [21][22]. However, the traditional GO preparation method based on chemical exfoliation requires a long time reaction under strong acid and strong oxidant, which may cause environmental and safety issues [23][24]. Therefore, exploring a clean, safe, efficient, and high-quality GO preparation method is important [24][25].

1.1 Aims and Objectives

Aimed at solving the adverse effects of phosphoric acid leaching and insufficient proton conductivity of PBI membrane in HT-PEMFC on performance and durability, this thesis focuses on exploring the application of single-layer graphene (SLG) and (functionalized) GO in HT-PEMFC and a new method of (functionalized) GO preparation. The specific objectives are as follows:

- The application of Lab-based X-ray micro-computed tomography (CT) coupled with machine-learning segmentation to investigate phosphoric acid leaching in high-temperature polymer electrolyte fuel cells.

- Explore the effect of SLG load at different positions of HT-PEMFC on its performance, durability, and phosphoric acid leaching.

- Design a reactor for electrochemical exfoliation using natural graphite flakes as raw material and characterizes its products under different conditions

- Synthesis of functionalized GO by electrochemical exfoliation through using appropriate electrolyte and designed reactor.

- Apply electrochemical exfoliated (functionalized) GO in HT-PEMFC to explore its effect on the performance and durability of HT-PEMFC.

1.2 Thesis Outline

The thesis is written and edited in the form of journal research papers. It is divided into 7 chapters including introduction, methodology, published research papers or manuscripts submitted to journals, and finally, conclusions.

Chapter 1 provides an overview of HT-PEMFC, including working principles, materials, and development prospects. Then followed by the literature review on graphene and graphene oxide and their applications in HT-PEMFC.

Chapter 2 summarizes the basic theory of the characterization methods of graphene (oxide) and the performance test methods of HT-PEMFC utilized in this thesis. The preparation of GO, the design of the reactor and the specific parameters of the characterization will be detailed in Chapter 3-6.

Chapter 3 proposes the method of PA leaching investigation in HT-PEMFC through Lab-based X-ray micro-computed tomography combined with machine-learning segmentation. The distribution of the different components of the PBI membrane-based MEA at different stages of the life test or accelerated stress test (AST) is detected and quantified to explore the components migration during the operation of the HT-PEMFC. (J.J. Bailey, J. Chen, J. Hack, M. Perez-Page, S.M. Holmes, D.J.L. Brett, P.R. Shearing, Lab-based X-ray micro-computed tomography coupled with machine-learning segmentation to investigate phosphoric acid leaching in high-temperature polymer electrolyte fuel cells, Journal of Power Sources. 509 (2021) 230347. https://doi.org/10.1016/J.JPOWSOUR.2021.230347.)

Chapter 4 reports a method of loading SLG between electrodes and the membrane to control the leaching of phosphoric acid which affect the three-phase boundary. Combining the method proposed in Chapter 3 and the characterization of Raman spectroscopic mapping and cyclic voltammetry (CV), the influence of SLG on the performance and durability of HT-PEMFC is explored and its mechanism is explained. (J. Chen, M. Perez-Page, Z. Ji, Z. Zhang, Z. Guo, S. Holmes, one step electrochemical exfoliation of natural graphite flakes into graphene oxide for polybenzimidazole composite membranes giving enhanced performance in high temperature

fuel cells, Journal of Power Sources. 491 (2021) 229550. https://doi.org/10.1016/j.jpowsour.2021.229550.)

Chapter 5 presents a fast, safe, and high-yield method of producing electrochemically exfoliated GO by designing and using a reactor based on 3D printing to use natural graphite flakes as raw materials without using strong acids and strong oxidants. The as-prepared graphene oxide was analyzed by Raman spectroscopy, Scanning Electron Microscopy (SEM), Transmission Electron Microscopy (TEM), Fourier-Transform Infrared Spectroscopy (FT-IR), X-ray photoelectron spectroscopy (XPS) and Thermogravimetric analysis (TGA). The electrochemical exfoliated GO was doped in the PBI membrane to improve the performance and durability of HT-PEMFC. Compared with the SLG used in the previous chapter, the graphene oxide obtained by electrochemical exfoliation has obvious cost advantages. (J. Chen, J.J. Bailey, L. Britnell, M. Perez-Page, M. Sahoo, Z. Zhang, A. Strudwick, J. Hack, Z. Guo, Z. Ji, P. Martin, D.J.L. Brett, P.R. Shearing, S.M. Holmes, The performance and durability of high-temperature proton exchange membrane fuel cells enhanced by single-layer graphene, Nano Energy. 93 (2022) 106829. https://doi.org/10.1016/J.NANOEN.2021.106829.)

Chapter 6 based on the method established in Chapter 5, phosphonated (P)GO was further synthesized with different electrolytes. The effect of its doping in the PBI membrane on the performance and durability of HT-PEMFC was explored. (J. Chen, Z. Guo, M. Perez-Page, S. Holmes, Synthesis of Phosphonated Graphene Oxide by Electrochemical Exfoliation to Enhance the Performance and Durability of High-temperature Proton Exchange Membrane Fuel cells, (prepared))

Chapter 7 summarizes the conclusions drawn throughout the thesis and proposes expected future work related to the thesis.

1.3 High-temperature Proton Exchange Membrane Fuel Cells

1.3.1 Overview of HT-PEMFC

Unlike a heat engine such as internal combustion engines and turbines, the fuel cell converts the Gibbs free energy of the reaction between hydrogen and oxygen into electricity. This working mechanism of fuel cell determines that its efficiency is not limited by the Carnot cycle, so the working efficiency of hydrogen fuel cells is higher than heat engines [2]. Fuel cells have a big family. The properties of different fuel cells are shown in **Table 1. 1**. Compared with other fuel cells, PEMFC can produce higher power density, so it is more suitable for high-power equipment, such as automotive, aerospace, building electricity [26]. PA is often used in combination with proton exchange membranes for HT-PEMFC, so phosphoric acid fuel cells can also be considered as a HT-PEMFC.

Table 1. 1. Properties of different fuel cells

Categories	Mobile proton	Operating temperature	Application and notes
Alkaline fuel cell	OH^-	50-200°C	Space vehicles
Proton exchange membrane fuel cell	H^+	30-200°C	Vehicles, mobile applications and lower CHP (combined heating and power) systems
Direct methanol fuel cell	H^+	20-90°C	Portable electronic systems
Phosphoric acid fuel cell	H^+	~220°C	Large numbers of 200-kW CHP systems in use
Molten carbonate fuel cell	CO_3^{2-}	~640°C	Medium- to large-scale CHP systems
Solid oxide fuel cell	O^{2-}	500-1000°C	All size of CHP systems

The working principle and chemical reactions of the fuel cell are shown in **Figure 1. 1**. The typical hydrogen fuel cell consists of a cathode, an anode and a proton exchange membrane sandwiched between two electrodes. When a fuel cell is in operation, hydrogen is oxidized at the anode to form hydrogen ions and electrons, while oxygen is reduced at the cathode to form oxygen ions. Oxygen ions produced on the cathode react with electrons from the outer circuit and hydrogen ions from the proton exchange membrane (PEM) to produce water. This can be regarded as the basic principle of hydrogen fuel cells. As mentioned above, fuel cells covert Gibbs free energy into electricity power. The Gibbs free energy of the reaction between hydrogen and oxygen can be calculated by **HhhhhEquation 1- 1** to **Equation 1- 3**.

$$\Delta G = \Delta H - T\Delta S$$

<div align="right">*HhhhhEquation 1- 1*</div>

G: Gibbs free energy; H: enthalpy; T: temperature; S: entropy

$$\Delta H = \left(h_f\right)_{H_2O} - \left(h_f\right)_{H_2} - \frac{1}{2}\left(h_f\right)_{O_2}$$

<div align="right">*Equation 1- 2*</div>

h_f: the enthalpies of formation

$$\Delta S = \left(s_f\right)_{H_2O} - \left(s_f\right)_{H_2} - \frac{1}{2}\left(s_f\right)_{O_2}$$

<div align="right">*Equation 1- 3*</div>

s_f: the entropies of formation
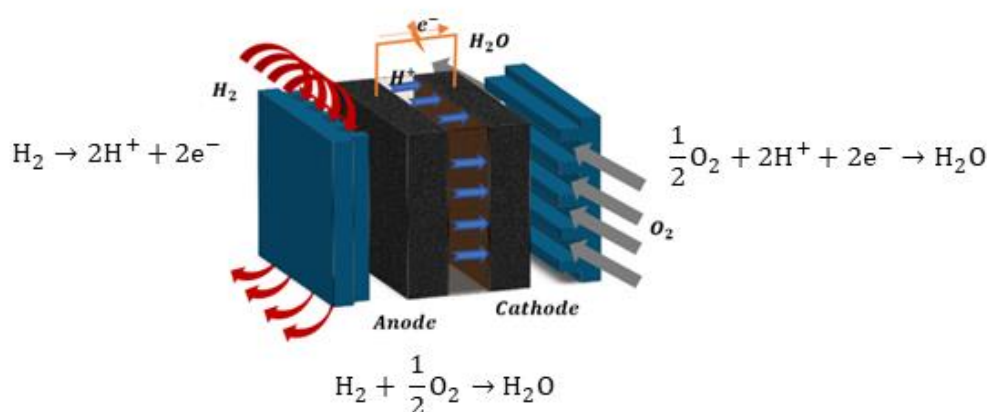
Figure 1. 1. The working principle of a hydrogen fuel cell

The proton exchange membrane which transports hydrogen protons from the anode to the cathode and prevents electrons, hydrogen and oxygen from passing through can be seen as the heart of PEM fuel cells. A large number of polymers have been studied for proton exchange membranes, most of which are developed based on PFSA polymers [27]. Nafion is the representative of the PFSA family. It is also the most developed and widely commercialized polymer for PEM fuel cells [27]. The chemical structure of Nafion is shown in **Figure 1. 2**. At the end of the side chain of the Nafion polymer is a highly hydrophilic SO_3^-. Since the connection between H^+ and SO_3^- is not strong, after hydration, H^+ can detach from SO_3^- and combine with surrounding water to form a dilute acid solution. This provides an excellent channel for the transport of hydrogen ions in the membrane. However, this also leads to a close relationship between the performance of Nafion and the degree of hydration. It also causes the Nafion -membrane-based hydrogen fuel cells to show a terrible performance when the temperature is higher than 80℃ due to dehydration. Therefore, the development of polymer suitable for the high-temperature environment as fuel cell membrane has become a priority. The benefits of the high-temperature environment for PEM fuel cells can be summarized as follows:

- Reduced need for purity of hydrogen, especially increased the tolerance for impurities such as carbon monoxide. HT-PEMFCs mostly use platinum-based catalysts. Carbon monoxide has strong adsorption on the platinum surface and thus easily blocks the hydrogen active sites on the catalyst surface. However, the industrial production of hydrogen is often accompanied by carbon monoxide impurities. The higher operating temperature can greatly reduce the adsorption of carbon monoxide by the catalyst and thus increase the tolerance of carbon monoxide concentration in hydrogen.

- Since high-temperature fuel cells do not need water as a proton carrier, water management is almost unnecessary, although appropriate relative humidity is conducive to improving the performance of high-temperature fuel cells [28].

- Rapid cooling with available waste heat. A large ambient temperature difference can effectively reduce the heat exchanger area or the coolant flow rate of liquid cooling. In addition, the heat generated by the chemical reaction in the HT-PEMFC can be directly supplied for heating.
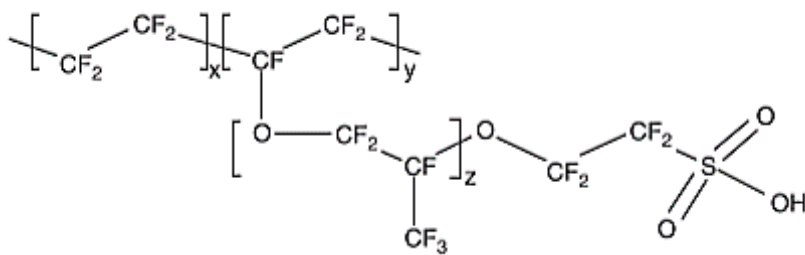
Figure 1. 2. Chemical structure of typical Nafion polymer

Take the single cell of PEMFC as an example, its structure usually consists of cell fixture and membrane-electrode-assembly (MEA). The cell fixture mainly provides mechanical support, sealing, gas transmission and electrical conduction. MEA is the core of PEMFC because it is the main site of electrochemical reactions and energy conversion. The components and

structure of MEA are shown in **Figure 1. 3**. The MEA consists of a cathode electrode, an anode electrode, and a proton exchange membrane in the middle in a sandwich structure. The components of the electrode are the gas diffusion layer (GDL), microporous layer (MPL), and catalyst layer (CL) from outside to inside.
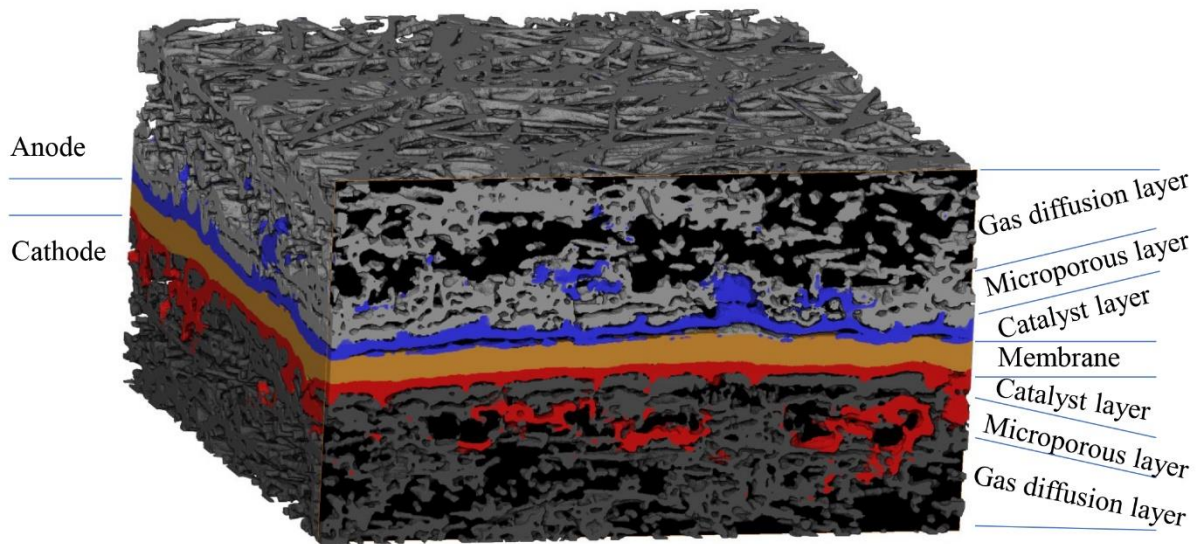
Figure 1. 3. The components and structure of MEA

The manufacture of (HT-)PEMFC requires consideration of gas transport and sealing. It is also necessary to ensure that the outer layer material has high electrical conductivity and that the inner layer material has good insulation to prevent short circuits. Further functions of these two-part are shown in **Table 1. 2**[29][30]. Therefore, the choice of plate material and gasket material is critical. Metal-based materials and graphite-based materials are two main polar plate materials. Metal-based materials have higher electronic conductivity and thermal conductivity. In addition, the high mechanical strength enables the fuel cell to have a small thickness and a more precise processing technology. However, the higher activity of metals makes their use in fuel cells limited by corrosion issues. Therefore, graphite composite electrodes with high corrosion resistance have emerged as required.

Parts	Polar plates	Gasket
Functions	• Electron conduction • Overall heating and cooling of the fuel cell • Uniform distribution of gas over the cathode or anode • Delivers moisture and directs the outflow of water • Mechanical support	• Prevent gas leakage • Provides buffer for volume changes due to temperature changes • Provide external mechanical support for the electrodes

The GDL is the component between the polar plate and catalyst. The functions of GDL are infiltrating the gas into the CL from the polar plate, conducting electrons from the CL to the plates, heat transfer between the CL and the polar plates, and acting as a carrier for the CL to prevent the CL from penetrating into the channels of the polar plates [31]. Carbon paper (non-woven) and carbon cloth (woven) are typical GDL materials [32]. The comparison of carbon paper and carbon cloth is shown in **Table 1. 3**[33]. The MPL can be seen as part of the gas diffusion layer. However, the MPL is extremely important, the MPL can provide good heat transfer to vapourise water at the same time, it also facilitates the diffusion of water to the catalyst. This facilitates the dynamic balance of water in the fuel cell and efficient transportation. The MPL has good electrical contact with the catalyst layer, which reduces ohmic losses and increases the stability of the fuel cell [34]. In addition, electrodes without microporous layer have more significantly catalyst and carbon corrosion issue [32]. Firstly, the good dredging of cathode-generated water by MPL can effectively reduce the corrosion of the carbon-based support of the catalyst [35]. Secondly, the support of CL by MPL also effectively alleviates the migration of CL into GDL and reduces the local thinning of CL. Finally, the intimate contact between MPL and CL can make the degradation of the catalyst more uniform at the microscopic level [36].

Carbon cloth	Carbon paper
- Higher porosity - More efficient water removal - Lower tortuosity - Rough surface - Dual pore size distribution	- Improved distribution of reactants - Lower density - Lower thickness - Mitigating membrane dehydration

CL plays an extremely important role in PEMFC since the activity of the catalyst directly affects the rate of hydrogen oxidation reaction (HOR) at the anode and oxygen reduction reaction (ORR) at the cathode [37]. Although a large number of studies have been carried out to synthesis inexpensive catalysts without precious metal or with low precious metal content, the catalysts currently used are mainly platinum and platinum alloys based. Thus, the catalyst accounts for almost 50% of the fuel cell cost [38]. A typical structure of CL for HT-PEMFC is shown in **Figure 1. 4**. Carbon (graphitized or non-graphitized) is the typical support material since carbon has a high surface area and high conductivity. There are some drawbacks for this Pt/C catalyst such as carbon corrosion, catalyst particle growth and catalyst dissolution. Carbon can react with water to produce carbon dioxide (**Equation 1- 4**).

$$C + 2H_2O \rightarrow CO_2 + 4H^+ + 4e^-$$
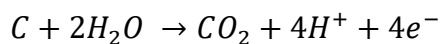
Equation 1- 4

This carbon corrosion mostly occurs during the start-stop phase of the fuel cell. When the fuel cell is not operating, both the anode and cathode are exposed to air, and both are at an equilibrium potential of oxygen relative to the electrolyte potential. However, once the hydrogen reaches the anode catalyst, the potential difference between the cathode electrodes becomes greater than the equilibrium potential of oxygen. This high cathode interfacial potential difference can lead to oxygen evolution and carbon corrosion. Oxidation of carbon leads to a reduction in surface area, which affects the level of adhesion of the catalyst and leads

to a decrease in catalyst activity. There are two ways to mitigate carbon corrosion. One is to develop new support materials such as SnO_2, TiO_2, tungsten monocarbide and Calix[4]arene molecules [39][40][41]. Another method is to optimize the operating conditions, such as reducing the operating time of operations that are unfavourable for performance [42], controlling the potential [43].
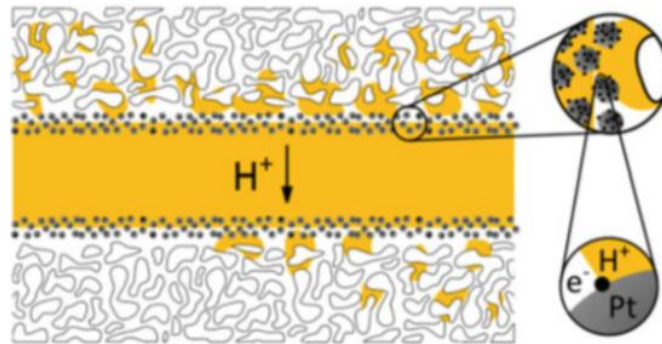
Figure 1. 4. The typical structure of catalyst layer for high-temperature fuel cells [28]

The binder which affects the mechanical properties of the catalyst layer, gas permeation and catalyst utilization plays an essential role. The type of binder is shown in **Table 1. 4** while the performance of these binders is shown in **Figure 1. 5** [4]. According to the performance of HT-PEMFC based on different catalyst binders, Polytetrafluoroethylene (PTFE) has become one of the best choices.

Table 1. 4. The type of binder for the catalyst layer [4]

Binder	Binder content	solvent	Post-treatment
PTFE	~30 wt%	Isopropanol (IPA) /H_2O	Sintered at 350℃
Nafion	~23 wt%	IPA/H_2O	Oven drying 110℃
PBI	~16.7 wt%	Dimethylacetamide (DMAc)	Oven drying 170℃
Polyvinylidene difluoride (PVDF)	~15 wt%	DMAc	Oven drying 170℃
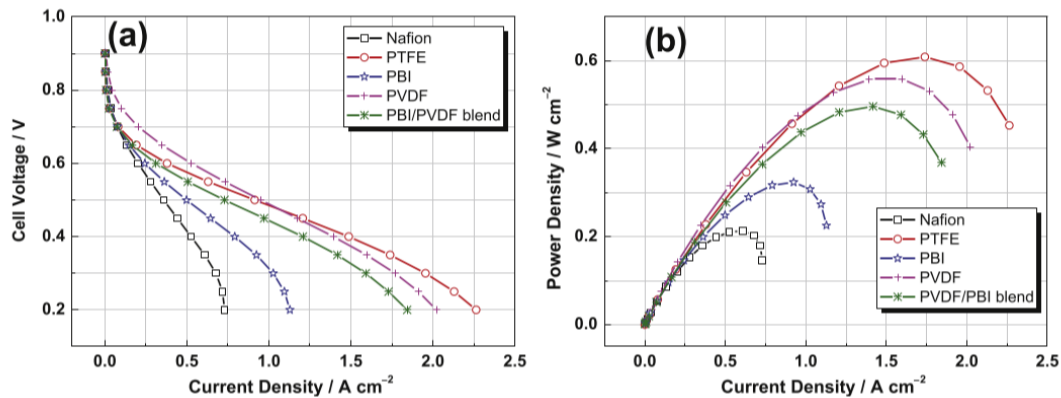
Figure 1. 5. Polarization curves (a) and power density curves (b) of PA-doped ABPBI fuel cell using GDEs prepared with different polymer binders [4]

1.3.2 Polymers for HT-PEMFC
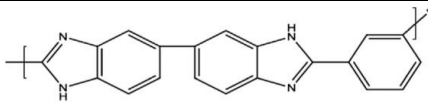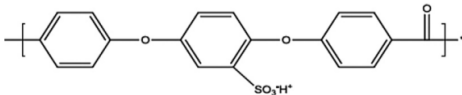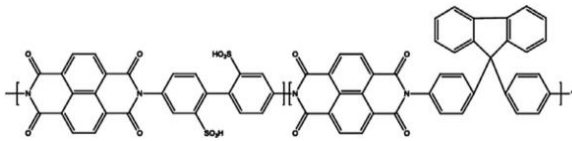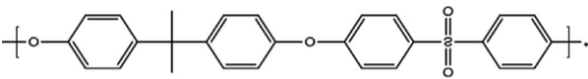
Although an operation temperature of between 120℃ to 200 ℃ is not high in the engineering field, a lot of effort needs to be carried out for this improvement. Optimization and modification based on PFSA polymers can be seen as a solution to enable proton exchange membranes to function at high temperatures. Antonucci et al have developed a Nafion $-$ SiO$_2$ composite membrane, which improves Nafion's water retention at high temperatures [44]. It takes the fuel cell working temperature up to 120 ℃. Stassi et al compared the performance of a short-side chain PFSA membrane called Aquivion^{TM} E79-03S with traditional Nafion membrane with the longer side chain [45]. They found that the short side chain Aquivion^{TM} membranes have better humidification, higher catalyst activity and better durability at high temperatures. This is due to its greater crystallinity [45]. A significant amount of research has been done to modify Nafion^{TM} membranes for higher temperature [46][47][48]. However, the amount of research on new high-temperature fuel cell membrane materials is limited. Some of the new polymers available for HT-PEMFC and their performance are shown in **Table 1. 5**. The chemical structures of these polymers are shown in **Table 1. 6**.

Table 1. 5. Polymers available for high-temperature fuel cells and their performance

Membrane details (name, acid doping)	Pt loading (anode/ cathode)	Temperature (℃)	Relevant Humidity (%)	Conductivity $(S\ cm^{-1})$	Citation
Poly[2,2′-m-(phenylene)-5,5′-bibenzimidazole (PBI)	(0.2mg Pt cm^{-2}/0.4mg Pt cm^{-2})	150	-	0.1774	[49]
Sulfonated polyetheretherketones - WC (SPEEK-WC)	-	95	85	0.0002	[50]
Sulfonated polyetheretherketones / (Imi-alt-chlorotrifluoroethylene)	-	120	25-95	0.001-0.015	[51]
Fluoren-containing Sulfonated polyimides (SPIs)	-	120	100	1.67	[52]
poly(arylene ether sulfone)-b-polybenzimidazole copolymer	-	200	0	0.045	[53]
Polysulfones (PSU) gifted with Poly(vinylphosphonic acid) (PVPA)	-	120	0	0.005	[54]
Polysulfones (PSU) gifted with Poly(vinylphosphonic acid) (PVPA)	-	120	100	0.098	[54]

Table 1. 6. The chemical structures of polymers for high-temperature fuel cells
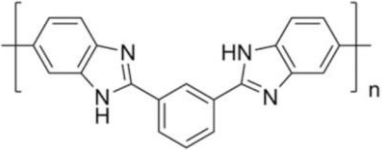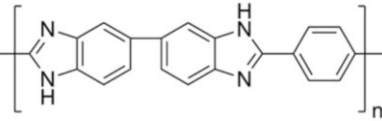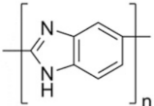
Name	Chemical structure	Citation
PBI		[49]
SPEEK		[50]
SPI		[52]
SPSU		[54]

1.3.3 PBI Membrane for HT-PEMFC

Among HT-PEMFC membrane materials, PBI attracts attention due to its good mechanical properties, high proton conductivity, no need for humidification and better durability [55][56]. There are mainly three commonly used chemical structures of PBI which are shown in **Table 1. 7**. There are two kinds of solvents that can be used to dissolve the PBI polymer. Polyphosphoric acid (PA) is the solvent for the sol-gel transition method to prepare PBI membranes [57]. The membranes prepared by PA as the solvent are directly PA-doped membranes. For poly(2,5-benzimidazole) (AB-PBI) powder, methanesulfonic acid (MSA) can be utilized as the solvent as well. Traditional solvents for PBI powder are organic solvents such as N, N-dimethylformamide (DMF), N, N-dimethylacetamide (DMAc), N-methyl-2-pyrrolidone (NMP), and dimethylsulfoxide (DMSO). The membrane can be prepared by evaporating these organic solvents (casting method) [58]. DMAc is the first choice for

poly[2,2-(m-phenylene)-5,5bibenzimidazole] (meta(m)-PBI) because of the optimum viscosity of the solution synthesized by both [59]. In order to increase the solubility of m-PBI in DMAc, it is usually refluxed at high temperatures and kept agitated. Para-PBI (p-PBI, Poly(2,2'-(p-phenylene)5,5'-bibenzimidazole)) is the least soluble in the PBI family. This is due to the unique chain structure of p-PBI, which makes the polymers closely linked and thus has less free space [60]. LiCl is commonly used as a stabilizer to enhance the dissolution of all kinds of PBI, and this stabilizer also extends the shelf life of the solution, which benefits from the weakening of the inter-molecular van der Waals forces [61][62].

Table 1. 7. Chemical structure of different PBI polymer

Name	Chemical structure
m-PBI	
p-PBI	
AB-PBI	

PBI transmits hydrogen protons in a different way from Nafion^{TM} membranes. Hydrogen ions can jump on the hydrogen bond network within PBI (Grotthuss mechanism). In this case, PBI should be doped with acid to establish a complete network of a hydrogen bonds. PA is one of the best choices due to its specific chemical and thermal properties. PBI itself does not have good proton conductivity, and its performance depends on the doping level of PA. In a way, PBI-membrane-based fuel cell is a kind of Phosphoric Acid fuel cell. The mechanism for

proton conduction of Nafion^{TM}-membrane-based low-temperature fuel cell and PBI-membrane-based HT-PEMFC are shown in **Figure 1. 6**.
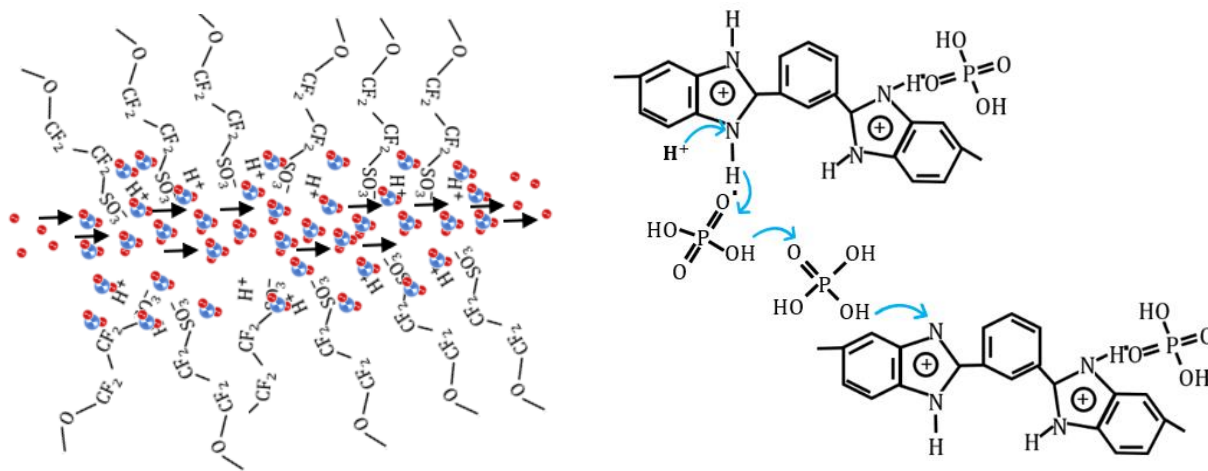
Figure 1. 6. The mechanism for proton conduction of Nafion^{TM}-membrane-based low-temperature fuel cell (left) and PBI-membrane-based high-temperature fuel cells (right)

Because of this mechanism, there are some drawbacks to PA doped PBI membrane. Firstly, the PA can bleed out, especially when the temperature is lower than 100℃ because the PA can be dissolved in the water produced at the Cathode and decreasing doping (PA) level will cause lower proton conductivity. This redistribution of PA within the MEA results in two main problems, the reduction of the proton conductivity of the membrane and blocking of the pathway for the gases to and from catalytically active sites, resulting in an increase in both mass transfer and charge transfer resistances. The research of Yu et al indicates that the speed of PA leaching depends on temperature [63]. Cathode PA loss is the main factor in the MEA total PA loss rate. PA loss rates increased significantly when the temperature is below 100℃ or between 180 to190℃. The dynamic durability test (load, heat and power off-start cycle test) was carried out, and the consistency of PA loss rate with these key working conditions was observed. The combination of these high temperature and high load conditions (the cathode

produces a large amount of water) led to the introduction of a steaming mechanism for removing PA from the MEA [64]. In addition, phosphoric acid can cause damage to fuel cell materials. Üregen et al. took phosphoric acid leaching as the main problem in their research and this is also shown in Li et al. [21]. Oxidative degradation of PBI is another weakness of the PBI membrane. The degradation of the acid-doped-PBI membrane is initiated by the attack of hydroxyl radicals on the carbon atoms connecting the imidazole ring and the benzene ring, which finally leads to the opening of the imidazole ring. Chain breaking produces small molecules and end groups that are further oxidized by terminal oxidation [55]. Finally, hydrogen crossover is also a potential factor affecting the performance of high-temperature fuel cells. Chippar and Ju established a gas crossover model for a PBI-membrane -based fuel cell at a high temperature which theoretically proved that hydrogen crossover does have an effect on the performance of fuel cells, but they also show that the hydrogen crossover is not obvious between 150℃ and 180℃. The worst case is that a gas crossover will result in a power density loss of 0.2A cm^{-2} at 180°C [65]. In another experimental study, it was pointed out that local thinning of the membrane or pinhole formation in the membrane is a significant cause of a sharp increase in hydrogen exchange current. However, they believe that even after the lifetime test, the effect of hydrogen crossover on the fuel cell is still negligible [66].

Recently, a large number of optimization schemes have been proposed for modifying PBI membranes. The main methods can be summarized into the following categories.

- Add ionic liquid with higher conductivity to avoid degradation, such as ($Cs_X H_{3-X} PMo_{12} O_{40}$ (CsPOMo), $Cs_X H_{3-X} PW_{12} O_{40}$ (CsPOW), $Cs_X H_{4-X} SiMo_{12} O_{40}$ (CsSiOMo) and $Cs_X H_{4-X} SiW_{12} O_{40}$ (CsSiOW)), $Sn_{0.95} Al_{0.05} P_2 O_7$ (SAPO), $Sb_{0.2} Sn_{0.8} P_2 O_7$ [67][68][69].

- Add substances or groups with hygroscopic effects to enhance the retention of phosphoric acid to ensure the conductivity of the polymer. Such as silica and titanium dioxide

- Add carbon-based materials to improve the chemical and thermodynamic properties of polymers and improve proton conductivity. Such as carbon nanotube, graphene, graphene oxide [70][71][72].

1.4 Graphene for PEMFC

Graphene is a two-dimensional carbon nanomaterial composed of carbon atoms in hexagonal spheroidal lattices composed of sp^2/ hybrid orbitals [9]. The structure of graphene is shown in **Figure 1. 7** a. This natural two-dimensional hexagonal structure of single-layer graphene acts as a sieve to block all atoms and molecules from passing through [73]. Hydrogen molecules as the smallest gas molecules require billions of years to pass through (at atmospheric pressure) the electron cloud formed by graphene which is shown in **Figure 1. 7** b [74]. However, The selective permeability of graphene to hydrogen protons is quite different from the selective permeability to hydrogen. The interaction mechanism between hydrogen/ graphene and hydrogen protons/graphene is shown in **Figure 1. 7** c. Through their different transfer mechanisms, the energy barrier of proton permeation is much smaller than the permeation energy barrier of hydrogen molecules, so protons have greater permeability [75]. Conductivity testing was performed by loading different 2D materials on a Nafion membrane with higher proton conductivity, the results of which are shown in **Figure 1. 7** d. This further demonstrates that single-layer graphene has good proton conductivity [10]. It has been proven that this proton conductivity is related to temperature, and the relationship between temperature and proton conductivity is shown in **Figure 1. 7** e. It is easy to see that in a high-temperature environment, the proton conductivity of single-layer graphene (SLG) increases with the increase of temperature, which lays a foundation for the application of single-layer graphene in high-

temperature fuel cells. In order to apply SLG to a fuel cell, in addition to considering the action of the SLG and the membrane, the effect between the SLG and the catalyst, particularly platinum metal, should be also considered. The affinity between platinum metal and hydrogen may be a factor affecting the conductivity of SLG to protons. However, measurements of graphene and double-layered hBN films activated by Pt show that the transport of protons is hardly affected by the series resistance, which indicates that the conductivity of hydrogen is not hindered by the affinity of the catalyst [10]. Proton conductivity of 2D crystals decorated with catalytic nanoparticles is shown in **Figure 1. 7** f.
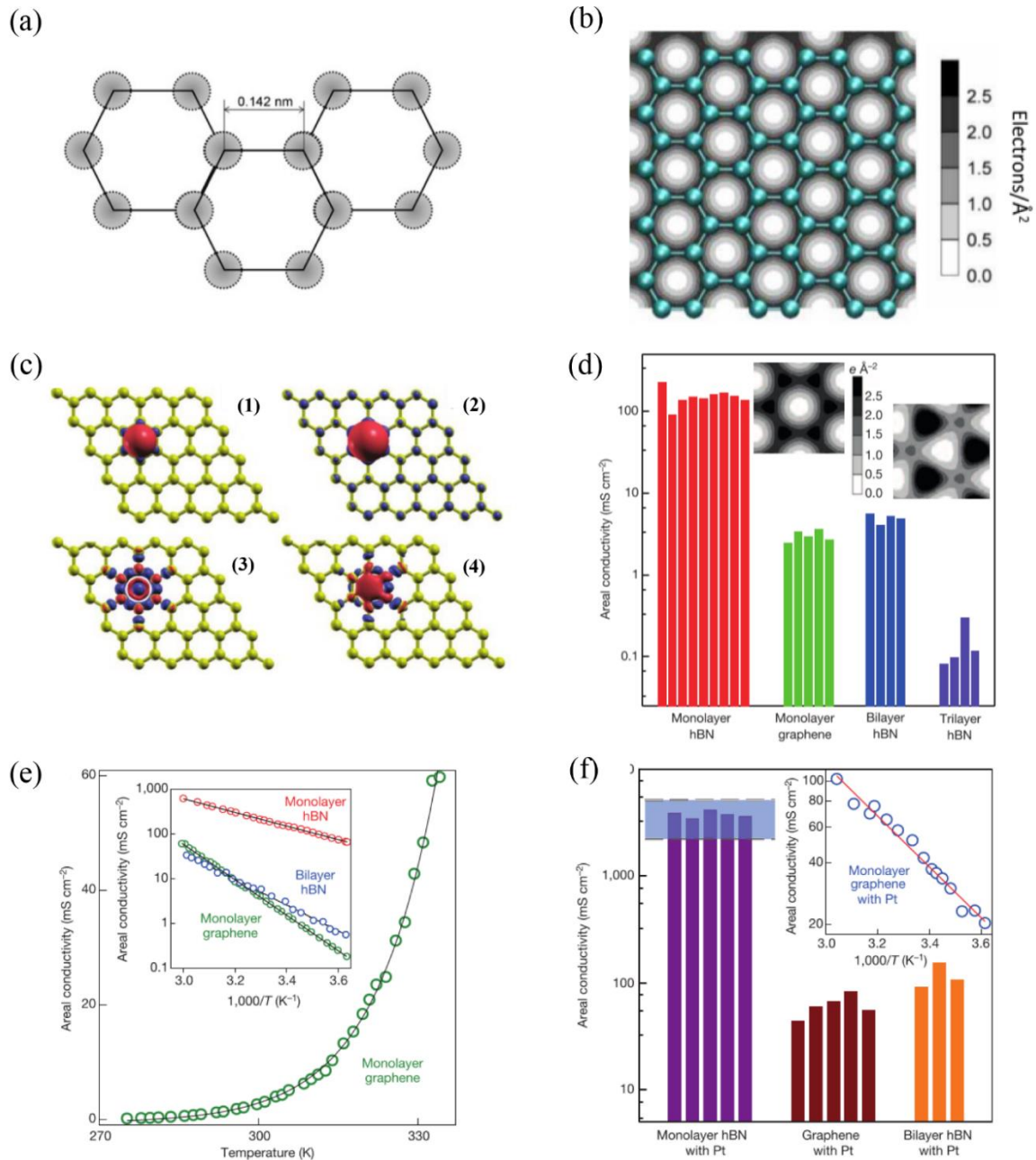
Figure 1. 7. Structure and performance of graphene, (a) Chemical structure of graphene, (b) Electron cloud of graphene, (c) Interaction between hydrogen and graphene, (d) Conductivity of Nafion / 2D materials composite membrane, (e) The relationship between temperature and proton conductivity of 2D materials, (f) Proton conductivity of 2D crystals decorated with catalytic nanoparticles [10].

In addition to the proton conductivity of SLG, which is important in fuel cells, its thermal conductivity and electronic conductivity are also worth studying. The thermal conductivity of SLG is 4840W/mK to 5300W/mK at room temperature which is much higher than single-wall carbon nanotube (SW-CNT) and multiwall carbon nanotube (MW-CNT) (shown in **Table 1. 8**) [76]. It can be seen that single-layer graphene is an excellent conductor of heat, which further

50

demonstrates that single-layer graphene is suitable for high-temperature fuel cells. However, graphene is a zero bandgap semiconductor or zero overlap metal [77]. Graphene can reach a million times the current density of copper [77]. In this case, Single-layer graphene cannot be used as a proton exchange membrane alone or it will cause a short circuit between the cathode and the anode.

Table 1. 8. Thermal conductivity of carbon-based materials at room temperature.

Sample	K(W/mK)	Method	Ref
SLG	4840-5300	optical	[76]
MW-CNT	3000	electrical	[78]
SW-CNT	3500	electrical	[79]
SW-CNT	1750-5800	thermocouples	[80]

There are several methods for graphene single layer preparation, such as the chemical vapour deposition (CVD) method, mechanical exfoliation and chemical exfoliation [81][70][82]. The comparison of cost and quality of some methods is shown in **Figure 1. 8** and further properties of single-layer graphene obtained from different methods are shown in **Table 1. 9**. As can be seen from **Figure 1. 8** and **Table 1. 9**, the CVD method has lower cost and better product performance. Therefore, CVD is one of the most suitable methods for the commercialization of single-layer graphene.
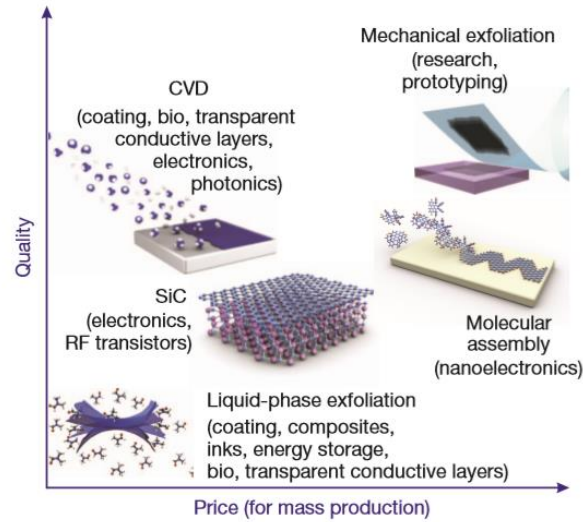
Figure 1. 8. The comparison of price and quality of methods for single layer graphene preparation [83]

Table 1. 9. Properties of single-layer graphene with different preparation methods

Method	Sample size (μm)	Crystallite size (μm)	Charge carrier mobility $(cm^2\ V^{-1}s^{-1})$
CVD	~1000	1000	
Mechanical exfoliation	>1	>1000	$>\ 2\times10^5\ and\ >10^6$ (at low temperature)
Chemical exfoliation	Infinite as a layer of overlapping flakes	≤0.1	100 (for a layer of overlapping flakes)
Chemical exfoliation via graphene oxide	Infinite as a layer of overlapping flakes	~100	1 (for a layer of overlapping flakes)
SiC epitaxial growth	100	50	10000

CVD is a method for producing large-scale SLG crystallites [84]. This method is to grow the graphene on the surface of a metal plate by passing a hydrocarbon gas (methane) over a high-temperature metal plate [85][86]. Nickel and copper and their alloys are the most commonly used metal plate materials. The advantage of this method is that it can obtain graphene with a large area as well as less disorder and defect. However, difficulty in controlling graphene thickness and using expensive substrates for growth are stumbling blocks that limit the commercialization of CVD graphene [87].

1.5 Graphene Oxide for PEMFC

1.5.1 Properties, Preparation and Application of Graphene Oxide

As mentioned above, graphene exhibits many excellent properties, but its cost limits its wide range of applications. Graphene oxide (GO) is a material similar to graphene for low-cost applications [88]. It is a 2D material containing graphene as a skeleton and containing oxidized functional groups [89]. The structure of the typical GO is shown in **Figure 1. 9**. Although graphene oxide is a derivative of graphene, its properties are quite different from those of graphene. Due to the introduction of oxidative functional groups, the integrity of sp^2 hybridization is disrupted, and part of the sp^2 hybridization is converted to sp^3 hybridization [90]. The introduction of these oxidizing functional groups and the formation of these sp^3 hybrids destroy the electronic structure of graphene, resulting in a significant decrease in conductivity (GO can be considered as an insulator). Partial oxidation of functional groups or sp^3 hybridization can be considered as defects. However, due to these defects, the hydrophilicity of GO is increased so that it can be dispersible in water. Functionalization of these groups also make GO useful for certain applications. The main applications of GO are chemical sensors, energy harvesting and storage, GO membrane for molecular separation, GO-based composite materials, toxicity studies and biomedical applications of GO and catalysis

[9][91][92][93]. Since GO exhibits the characteristics of the P-type semiconductor after thermal treatment, it is sensitive to strong oxidizer such as NO_2 thus is suitable for acting as a relevant sensor [94]. As a typical transparent electrode material for the most promising energy harvesting equipment solar cells, indium tin oxide (ITO) has the disadvantages of high cost, poor mechanical properties, high-temperature resistance and acid resistance[95]. GO is expected to replace ITO due to its low cost, high electron mobility, and broad absorption spectrum. In addition, GO can act as electron acceptor, transparent layer, and hole conductor for various components of dye-sensitized solar cells [96]. Graphene-related materials have a wide range of applications in lithium-ion batteries, especially electrode materials, due to their high thermal conductivity, chemical stability, and high specific area [97][98][99]. The edges and defects of GO can provide additional lithium-ion storage sites, which can effectively increase the battery capacity [100][101]. Since the unique chemical structure of GO can hinder the permeation of almost all atoms, the permeation of atoms or molecules can be effectively selected by drilling holes of different sizes in the GO plane. Therefore, GO has become an excellent choice for selectively permeable membranes [102]. As a carbon-rich material, GO's abundant oxygen-containing functional groups make it have good dispersibility in neutral liquids, so that it can interact with bio activators and biomolecules to a certain extent. In addition, GO has good cell membrane permeability and low toxicity, which lays the foundation for the application of GO in biomedicine [103][104].
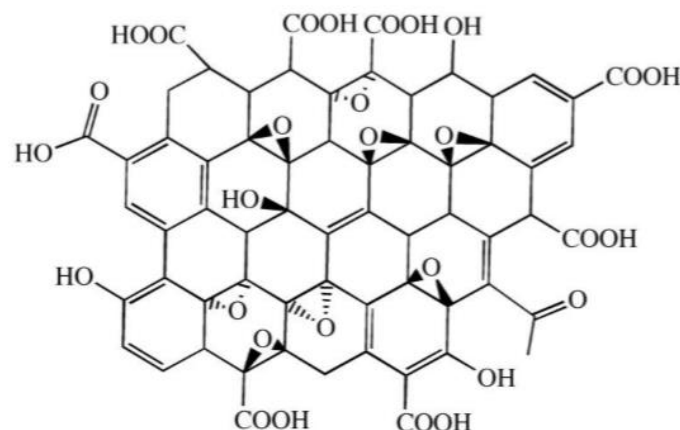
Figure 1. 9. Chemical structure of GO

Traditional GO preparation methods mainly include Brodie's method, Staudenmaier's method and the Hummers' method [105][23]. These methods are based on chemical oxidation of graphite flakes using strong oxidants in strong acid solutions. The first two methods require long-term oxidation cycles, while the Hummers' method is the most effective and commercially viable method of the three. However, Hummers' method still requires the use of strong oxidants, which can cause environmental pollution and lead to defects in the GO that cannot be repaired [106][107]. Therefore, electrochemical exfoliation has attracted more and more attention with its environmental benefits and low price. A schematic diagram of electrochemical exfoliation is shown in **Figure 1. 10** (using sulphuric acid as an electrolyte). The general mechanism of this process can be summarized as follows: the bias voltage between the positive and negative electrodes causes the anions and cations in the electrolyte to move to the anode and cathode, respectively, and the hydroxide attacks the edge of the graphite to expand it. Other anions and oxygen are intercalated between the layers of graphite, causing their further expansion to eventually separate the layers. Graphite and related materials are commonly used as the anode (the source of the GO), the types of these anode materials are shown in **Table 1. 10**.
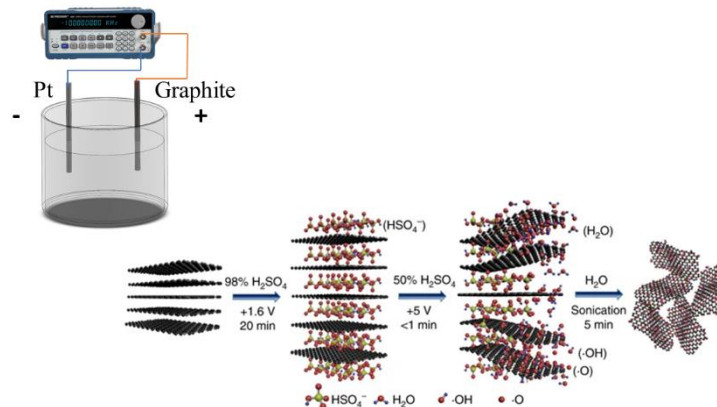
Figure 1. 10. The schematic diagram of electrochemical exfoliation [108].

Table 1. 10. Graphite related materials for electrochemical exfoliation.

Name	Method of Manufacture	Cite
Natural graphite flakes	Natural	[109][110]
Graphite foil	High-purity natural graphite foil is used as raw material for specific acid treatment and heat treatment to form expanded graphite. Expanded graphite is mechanically rolled and made into graphite foil without the aid of adhesives.	[24][111] [112]
Graphite pellet	Pressing graphite flakes under a pressure of 100 bar without binder	[113]
Graphite rod	Connect electrodes to the pressure apparatus, allowing it to be "flash-heated" by passing a high pulse of electric current through it in a few milliseconds at 3500K and 12 GPa.	[114]
Highly oriented pyrolytic graphite (HOPG)	The process for making HOPG is similar to that for making pyrolytic graphite, but with more tensile stress in the basal plane.	[67][110]

As can be seen from **Table 1. 10**, the graphite electrodes used for electrochemical exfoliation,

except for natural graphene flakes, are obtained by using processes such as chemical,

thermodynamic, and mechanical compression. These processes may result in physical or chemical changes that alter their original properties or structure. One of the reasons why graphite flakes are replaced by graphite foil or graphite rods, or the like is because graphite flakes have a small particle size (usually less than -10 mesh (2mm)). Such a small area is not conducive to the large-scale reaction as an electrode. Some solutions are mentioned in the literature. Gurzęda et al. mounted the graphite flakes in a platinum mesh to turn the graphite flakes into an external circuit. There are 120 holes per inch on the platinum mesh for ions to enter [109]. Yu et al. designed a reactor as shown in **Figure 1. 11**. Mixed metal oxide (MMO) coated titanium mesh is used to apply the circuit. The materials used in these metal-based meshes are inert metals that are not electrolyzed and require high electrical conductivity. However, these metals are more conductive than graphite, which makes the oxidation reaction of the anion at the anode more likely to occur on the metal surface than on the graphite surface or inside the graphite. This increases the electrical losses and makes power consumption extremely large during the manufacturing process. In addition, the platinum mesh or the titanium mesh is expensive and easily damaged during the reaction, which increases the cost.
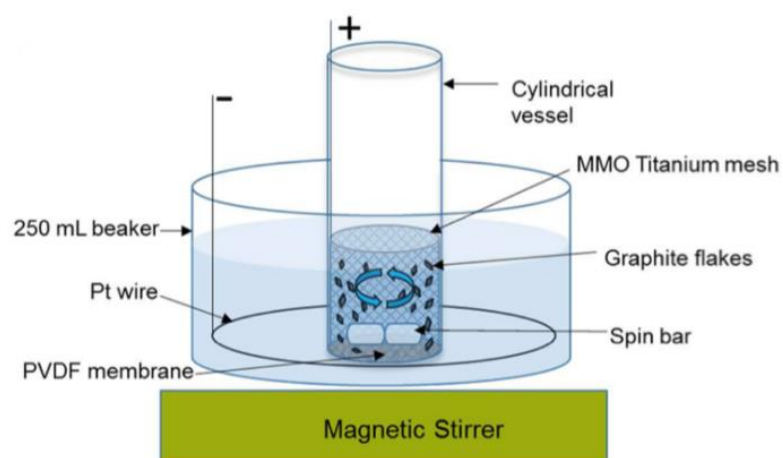
Figure 1. 11. Schematic drawing of the mechanically assisted electrochemical exfoliation setup [15]

In fact, there are many types of graphite, and their classification is shown in **Figure 1. 12**. In the macroscopically crystallized graphite, in addition to graphite flakes, there is vein graphite [115]. Electrochemical exfoliation with vein graphite is extremely rare. Rathnayake et al. prepared oxide graphene by chemical oxidation using needle platy natural vein graphite. They have obtained high-quality products and proved the technical and economic feasibility of using vein graphite as a raw material for the preparation of graphene oxide [116].
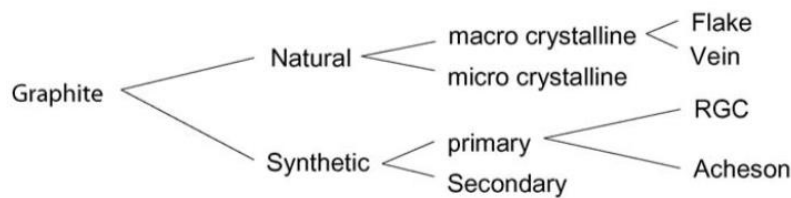
Figure 1. 12. Classification of graphite [115]

In summary, how to effectively use natural graphite for electrochemical exfoliation has not been best solved. Whether the products obtained by electrochemical exfoliation using different graphite materials are different has not been studied. Whether the graphite rods, graphite sheets and the like obtained by manual processing will affect the exfoliation due to acid treatment or high-pressure compression remains to be explored. This project focuses on solving these problems through experimental methods and measurement.

1.5.2 Application of Graphene Oxide in PEMFCs.

GO is widely applied in PEMFC especially in proton exchange membranes and catalysts. The application of GO in proton exchange membranes can be roughly classified into two categories which are free-standing GO based PEMs and GO based nano-hybrid PEM's. The GO paper formed after the GO dispersion is filtered can be directly used as the proton exchange

membrane of Direct Methanol Fuel Cells [117]. Although the oxygen-containing functional groups on GO and the hydrogen bonds inside GO paper provide abundant proton transport channels, GO paper as an independent PEM performs poorly in DMFC. Ravikumar and Scott applied mechanically stable, freestanding sulphonated GO paper as the low-temperature PEMFC membrane and obtained reasonable performance [118]. Gao et al proposed the use of Nafion-ozonated GO-Nafion sandwich membranes to improve the durability of low-temperature PEMFC [119]. Although free-standing GO paper as a proton exchange membrane exhibits reasonable performance in DMFC and low-temperature PEMFC, its power density in fuel cells is still insufficient compared to traditional polymers. Therefore, composite membranes based on GO and polymers have attracted more attention. The most direct benefit brought by the doping of GO in the low-temperature PFMFC based on Nafion membrane is to increase the hydrophilicity of the composite membrane to promote its hydration and increase the proton conductivity [120]. The doping of GO in HT-PEMFC based on PA doping facilitates hopping of protons on external surfaces and establishment of three-dimensional proton transfer channels to improve conductivity and has a trapping effect on PA to prevent its leaching [21]. Recently, functionalized GO, especially acid-functionalized GO, has attracted much attention in HT-PEMFC field because of its better compatibility with polymers, better promotion of proton conduction, better mechanical properties, and stability [16,19,19,121,122]. In addition, GO is also regarded as an excellent choice as a catalyst support material due to its large specific surface area, abundant active sites, and high conductivity after reduction [123].

1.6 Strategies

The strategies of the thesis framework is shown in **Figure 1. 13**. Chapter 3 presented a method for evaluating the migration of phosphoric acid (PA) and catalyst within the membrane-electrode-assembly (MEA) of high-temperature proton exchange membrane fuel cells (HT-PEMFC) using a Lab-based X-ray Micro-computed tomography (CT) method. After

processing the XTM data, a preliminary understanding of the time-dependent migration of PA and catalyst was obtained in HT-PEMFC under accelerated stress test condition. This approach lays the foundation for the effect of new materials on the migration of PA and catalysts within HT-PEMFCs. Chapter 4 will explore the effect of single-layer graphene on the performance and durability of HT-PEMFC and propose the mechanism based on the method established in Chapter 3. Chapter 4 demonstrates the effectiveness of single-layer graphene (SLG) in enhancing the performance and durability of high-temperature proton exchange membrane fuel cells. However, SLG prepared by the chemical vapour deposition (CVD) method has disadvantages such as high cost and enviromental impact. In addition, it is difficult to control the coverage of SLG on the electrodes surface using wet chemical transfer method. Chapter 5 aims to exploit graphene-related materials in HT-PEMFCs more cheaply, conveniently and efficiently to improve their performance and durability. The work in chapter 5 realized the rapid, efficient and high-yield preparation of graphene oxide (GO) with a certain degree of oxidation using natural graphite flakes as raw materials and electrochemical exfoliation through the design of reactor. With aboundent oxygen-contating functional groups, GO can facilitate the hopping of protons and acts as a trap to stop the phosphoric acid excively leaching. Compared with the original hydroxyl, carboxyl and carbonyl groups of GO, GO functionalized with acid functional groups, especially phosphonated functional groups, could more effectively improve the proton conductivity of the membrane in high-temperature proton exchange membrane fuel cells. Chapter 6 will further explore the use of electrochemical exfoliation to prepare phosphonated graphene oxide based on the reactor designed in Chatper 5 and test its doping in polybenzimidazole membranes on the performance and durability of high-temperature proton exchange membrane fuel cells.
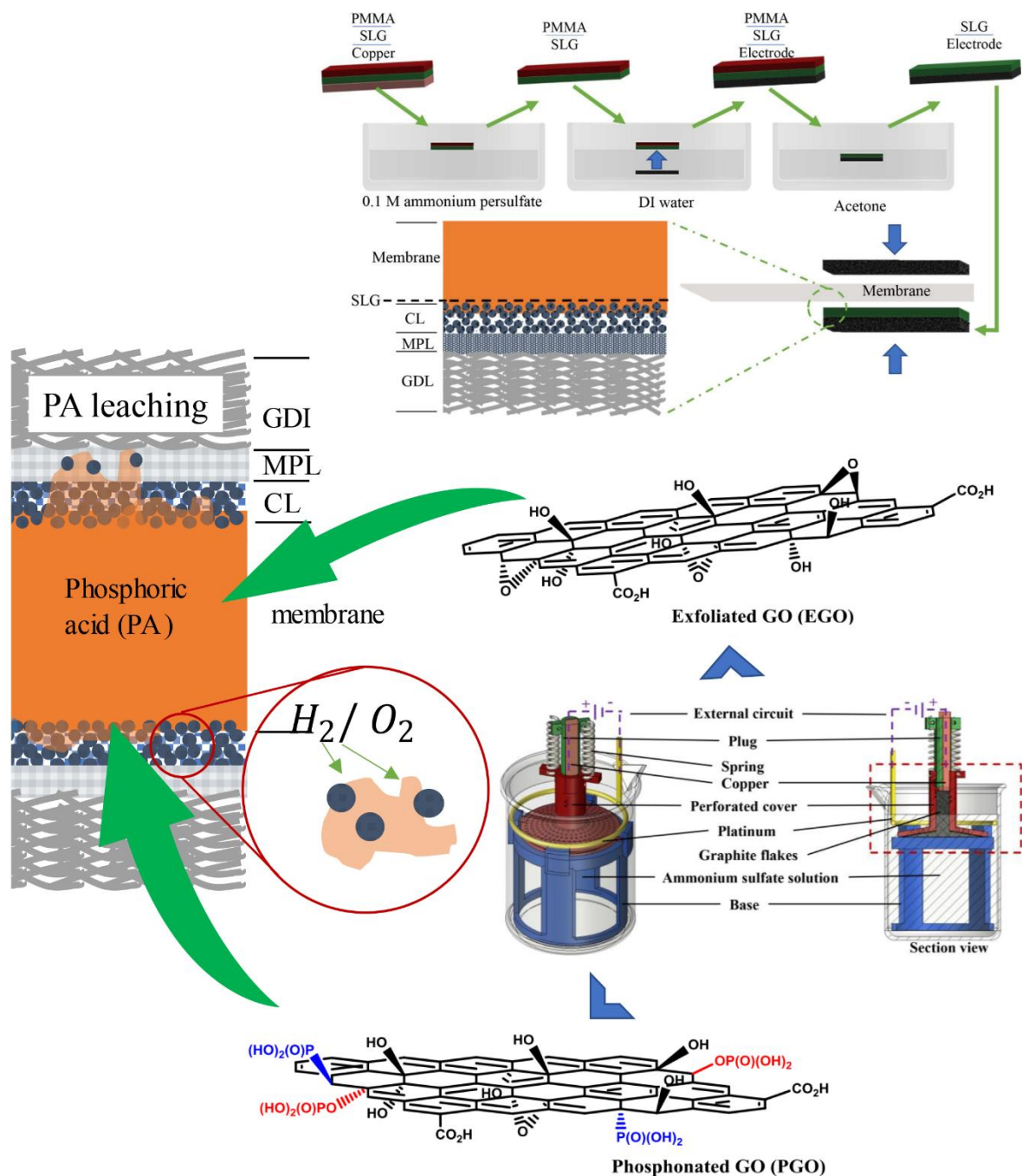
Figure 1. 13. The strategies of the thesis framework

To sum up, this thesis will focus on exploring the effect of PA leaching on the performance and durability of HT-PEMFC and then study the effect of graphene and graphene oxide in HT-PEMFC. SLG synthesized by CVD methode will be transferred in the MEA between membrane and electrode and reactor based electrochemical exfoliated (functionalized)

graphene oxide will be doped in PBI membrane to improve the proton conductivity or slowing

the PA leaching and then improve the performance and durability of HT-PEMFC.

1.7 References

[1] I. Dincer, Renewable energy and sustainable development: a crucial review, Renewable and Sustainable Energy Reviews. 4 (2000) 157–175. https://doi.org/10.1016/S1364-0321(99)00011-8.

[2] D.A.J. Rand, R.M. Dell, Hydrogen from Fossil Fuels and Biomass, Hydrogen Energy: Challenges and Prospective. (2007) 34–66. http://ebook.rsc.org/?DOI=10.1039/9781847558022 (accessed March 7, 2022).

[3] Y.-L. Ma, J.S. Wainright, M.H. Litt, R.F. Savinell, Conductivity of PBI Membranes for High-Temperature Polymer Electrolyte Fuel Cells, Journal of The Electrochemical Society. 151 (2004) A8. https://doi.org/10.1149/1.1630037/XML.

[4] H. Su, S. Pasupathi, B. Bladergroen, V. Linkov, B.G. Pollet, Optimization of gas diffusion electrode for polybenzimidazole-based high temperature proton exchange membrane fuel cell: Evaluation of polymer binders in catalyst layer, International Journal of Hydrogen Energy. 38 (2013) 11370–11378. https://doi.org/10.1016/J.IJHYDENE.2013.06.107.

[5] S. Galbiati, A. Baricci, A. Casalegno, R. Marchesi, Degradation in phosphoric acid doped polymer fuel cells : A 6000 h parametric investigation, International Journal of Hydrogen

Energy. 38 (2013) 6469–6480. https://doi.org/10.1016/j.ijhydene.2013.03.012.

[6]   S. Maity, S. Singha, T. Jana, Low acid leaching PEM for fuel cell based on polybenzimidazole nanocomposites with protic ionic liquid modified silica, Polymer. 66 (2015) 76–85. https://doi.org/10.1016/J.POLYMER.2015.03.040.

[7]   S.H. Eberhardt, F. Marone, M. Stampanoni, F.N. Büchi, T.J. Schmidt, Quantifying phosphoric acid in high-temperature polymer electrolyte fuel cell components by X-ray tomographic microscopy, Journal of Synchrotron Radiation. 21 (2014) 1319–1326. https://doi.org/10.1107/S1600577514016348.

[8]   Q. He, X. Yang, W. Chen, S. Mukerjee, B. Koel, S. Chen, Influence of phosphate anion adsorption on the kinetics of oxygen electroreduction on low index Pt(hkl) single crystals, Physical Chemistry Chemical Physics. 12 (2010) 12544–12555. https://doi.org/10.1039/C0CP00433B.

[9]   Z. Zhen, H. Zhu, Structure and Properties of Graphene, Graphene: Fabrication, Characterizations, Properties and Applications. (2018) 1–12. https://doi.org/10.1016/B978-0-12-812651-6.00001-X.

[10]   S. Hu, M. Lozada-Hidalgo, F.C. Wang, A. Mishchenko, F. Schedin, R.R. Nair, E.W. Hill, D.W. Boukhvalov, M.I. Katsnelson, R.A.W. Dryfe, I. V. Grigorieva, H.A. Wu, A.K. Geim, Proton transport through one-atom-thick crystals, Nature. 516 (2014) 227–230. https://doi.org/10.1038/nature14015.

[11]   S.M. Holmes, P. Balakrishnan, V.S. Kalangi, X. Zhang, M. Lozada-Hidalgo, P.M. Ajayan, R.R. Nair, 2D Crystals Significantly Enhance the Performance of a Working Fuel Cell, Advanced Energy Materials. 7 (2017) 1–7. https://doi.org/10.1002/aenm.201601216.

[12] J. Li, X. Zeng, T. Ren, E. van der Heide, The Preparation of Graphene Oxide and Its Derivatives and Their Application in Bio-Tribological Systems, Lubricants 2014, Vol. 2, Pages 137-161. 2 (2014) 137–161. https://doi.org/10.3390/LUBRICANTS2030137.

[13] J.I. Paredes, S. Villar-Rodil, A. Martínez-Alonso, J.M.D. Tascón, Graphene oxide dispersions in organic solvents, Langmuir. 24 (2008) 10560–10564. https://doi.org/10.1021/la801744a.

[14] N.I. Zaaba, K.L. Foo, U. Hashim, S.J. Tan, W.W. Liu, C.H. Voon, Synthesis of Graphene Oxide using Modified Hummers Method: Solvent Influence, Procedia Engineering. 184 (2017) 469–477. https://doi.org/10.1016/J.PROENG.2017.04.118.

[15] Z. Tian, P. Yu, S.E. Lowe, A.G. Pandolfo, T.R. Gengenbach, K.M. Nairn, J. Song, X. Wang, Y.L. Zhong, D. Li, Facile electrochemical approach for the production of graphite oxide with tunable chemistry, Carbon. 112 (2017) 185–191. https://doi.org/10.1016/J.CARBON.2016.10.098.

[16] C. Xu, Y. Cao, R. Kumar, X. Wu, X. Wang, K. Scott, A polybenzimidazole/sulfonated graphite oxide composite membrane for high temperature polymer electrolyte membrane fuel cells, Journal of Materials Chemistry. 21 (2011) 11359–11364. https://doi.org/10.1039/c1jm11159k.

[17] Graphene Oxide / Polybenzimidazole Nanocomposite Membrane for High Temperature Proton Exchange Membrane Fuel Cell Application Shobha Mantripragada North Carolina A & T State University A thesis submitted to the graduate faculty in partial fulfillment of t, (2017).

[18] Y. Cai, Z. Yue, S. Xu, A novel polybenzimidazole composite modified by sulfonated graphene oxide for high temperature proton exchange membrane fuel cells in anhydrous atmosphere, Journal of Applied Polymer Science. 134 (2017) 1–8.

https://doi.org/10.1002/app.44986.

[19] C. Wang, B. Lin, G. Qiao, L. Wang, L. Zhu, F. Chu, T. Feng, N. Yuan, J. Ding, Polybenzimidazole/ionic liquid functionalized graphene oxide nanocomposite membrane for alkaline anion exchange membrane fuel cells, Materials Letters. 173 (2016) 219–222. https://doi.org/10.1016/j.matlet.2016.03.057.

[20] J. Kim, K. Kim, T. Ko, J. Han, J.C. Lee, Polybenzimidazole composite membranes containing imidazole functionalized graphene oxide showing high proton conductivity and improved physicochemical properties, International Journal of Hydrogen Energy. (2020). https://doi.org/10.1016/j.ijhydene.2020.02.193.

[21] N. Üregen, K. Pehlivanoğlu, Y. Özdemir, Y. Devrim, Development of polybenzimidazole/graphene oxide composite membranes for high temperature PEM fuel cells, International Journal of Hydrogen Energy. 42 (2017) 2636–2647. https://doi.org/10.1016/j.ijhydene.2016.07.009.

[22] E. Abouzari-Lotf, M. Zakeri, M.M. Nasef, M. Miyake, P. Mozarmnia, N.A. Bazilah, N.F. Emelin, A. Ahmad, Highly durable polybenzimidazole composite membranes with phosphonated graphene oxide for high temperature polymer electrolyte membrane fuel cells, Journal of Power Sources. 412 (2019) 238–245. https://doi.org/10.1016/j.jpowsour.2018.11.057.

[23] N.I. Zaaba, K.L. Foo, U. Hashim, S.J. Tan, W.W. Liu, C.H. Voon, Synthesis of Graphene Oxide using Modified Hummers Method: Solvent Influence, Procedia Engineering. 184 (2017) 469–477. https://doi.org/10.1016/J.PROENG.2017.04.118.

[24] J. Cao, P. He, M.A. Mohammed, X. Zhao, R.J. Young, B. Derby, I.A. Kinloch, R.A.W. Dryfe, Two-Step Electrochemical Intercalation and Oxidation of Graphite for the Mass Production of Graphene Oxide, Journal of the American Chemical Society. 139 (2017)

17446–17456. https://doi.org/10.1021/jacs.7b08515.

[25] J. Chen, M. Perez-Page, Z. Ji, Z. Zhang, Z. Guo, S. Holmes, One step electrochemical exfoliation of natural graphite flakes into graphene oxide for polybenzimidazole composite membranes giving enhanced performance in high temperature fuel cells, Journal of Power Sources. 491 (2021) 229550. https://doi.org/10.1016/j.jpowsour.2021.229550.

[26] L.J.M.J. Blomen, M.N. Mugerwa, Fuel cell systems, (1993) 614.

[27] P. Trogadas, V. Ramani, Membrane and MEA Development in Polymer Electrolyte Fuel Cells, Polymer Membranes for Fuel Cells. (2009) 253–280. https://doi.org/10.1007/978-0-387-73532-0_11.

[28] H.A. Hjuler, D. Aili, J.O. Jensen, High temperature polymer electrolyte membrane fuel cells: Approaches, status, and perspectives, High Temperature Polymer Electrolyte Membrane Fuel Cells: Approaches, Status, and Perspectives. (2016) 1–545. https://doi.org/10.1007/978-3-319-17082-4.

[29] H. Husby, O.E. Kongstein, A. Oedegaard, F. Seland, Carbon-polymer composite coatings for PEM fuel cell bipolar plates, International Journal of Hydrogen Energy. 39 (2014) 951–957. https://doi.org/10.1016/J.IJHYDENE.2013.10.115.

[30] P.T. Moseley, Fuel Cell Systems Explained: James Larminie, Andrew Dicks (Eds.), Wiley, Chichester, Weinhein, New York, Brisbane, Singapore and Toronto, ISBN 0-471-49026-1, Journal of Power Sources. 93 (2001) 285. https://doi.org/10.1016/S0378-7753(00)00571-1.

[31] Fuel Cell Technologies: State and Perspectives, Fuel Cell Technologies: State and Perspectives. (2005). https://doi.org/10.1007/1-4020-3498-9.

[32] P.H. Maheshwari, R.B. Mathur, T.L. Dhami, The influence of the pore size and its distribution in a carbon paper electrode on the performance of a PEM Fuel cell, Electrochimica Acta. 54 (2008) 655–659. https://doi.org/10.1016/J.ELECTACTA.2008.07.029.

[33] R. Omrani, B. Shabani, Review of gas diffusion layer for proton exchange membrane-based technologies with a focus on unitised regenerative fuel cells, International Journal of Hydrogen Energy. 44 (2019) 3834–3860. https://doi.org/10.1016/J.IJHYDENE.2018.12.120.

[34] J. Zhou, S. Shukla, A. Putz, M. Secanell, Analysis of the role of the microporous layer in improving polymer electrolyte fuel cell performance, Electrochimica Acta. 268 (2018) 366–382. https://doi.org/10.1016/J.ELECTACTA.2018.02.100.

[35] J.D. Fairweather, D. Spernjak, R. Mukundan, J. Spendelow, K. Artyushkova, P. Atanassov, D.S. Hussey, D.L. Jacobson, R. Borup, Interaction of Heat Generation, MPL, and Water Retention in Corroded PEMFCs, ECS Transactions. 41 (2019) 337–348. https://doi.org/10.1149/1.3635567.

[36] D. Spernjak, J. Fairweather, R. Mukundan, T. Rockward, R.L. Borup, Influence of the microporous layer on carbon corrosion in the catalyst layer of a polymer electrolyte membrane fuel cell, Journal of Power Sources. 214 (2012) 386–398. https://doi.org/10.1016/J.JPOWSOUR.2012.04.086.

[37] H. Su, C. Felix, O. Barron, P. Bujlo, B.J. Bladergroen, B.G. Pollet, S. Pasupathi, High-Performance and Durable Membrane Electrode Assemblies for High-Temperature Polymer Electrolyte Membrane Fuel Cells, Electrocatalysis. 5 (2014) 361–371. https://doi.org/10.1007/S12678-014-0202-5/FIGURES/10.

[38] T. Reshetenko, A. Serov, K. Artyushkova, I. Matanovic, S. Stariha, P. Atanassov,

Tolerance of non-platinum group metals cathodes proton exchange membrane fuel cells to air contaminants, Journal of Power Sources. 324 (2016) 556–571. https://doi.org/10.1016/J.JPOWSOUR.2016.05.090.

[39] B. Genorio, D. Strmcnik, R. Subbaraman, D. Tripkovic, G. Karapetrov, V.R. Stamenkovic, S. Pejovnik, N.M. Marković, Selective catalysts for the hydrogen oxidation and oxygen reduction reactions by patterning of platinum with calix[4]arene molecules, Nature Materials 2010 9:12. 9 (2010) 998–1003. https://doi.org/10.1038/nmat2883.

[40] H. Chhina, S. Campbell, O. Kesler, High surface area synthesis, electrochemical activity, and stability of tungsten carbide supported Pt during oxygen reduction in proton exchange membrane fuel cells, Journal of Power Sources. 179 (2008) 50–59. https://doi.org/10.1016/J.JPOWSOUR.2007.12.105.

[41] H. Su, C. Felix, O. Barron, P. Bujlo, B.J. Bladergroen, B.G. Pollet, S. Pasupathi, High-Performance and Durable Membrane Electrode Assemblies for High-Temperature Polymer Electrolyte Membrane Fuel Cells, Electrocatalysis. 5 (2014) 361–371. https://doi.org/10.1007/S12678-014-0202-5/FIGURES/10.

[42] N. Linse, G.G. Scherer, A. Wokaun, L. Gubler, Quantitative analysis of carbon corrosion during fuel cell start-up and shut-down by anode purging, Journal of Power Sources. 219 (2012) 240–248. https://doi.org/10.1016/J.JPOWSOUR.2012.07.037.

[43] C.A. Reiser, L. Bregoli, T.W. Patterson, J.S. Yi, J.D. Yang, M.L. Perry, T.D. Jarvi, A reverse-current decay mechanism for fuel cells, Electrochemical and Solid-State Letters. 8 (2005) A273. https://doi.org/10.1149/1.1896466/XML.

[44] V. Antonucci, A. Di Blasi, V. Baglio, R. Ornelas, F. Matteucci, J. Ledesma-Garcia, L.G. Arriaga, A.S. Aricò, High temperature operation of a composite membrane-based solid

polymer electrolyte water electrolyser, Electrochimica Acta. 53 (2008) 7350–7356. https://doi.org/10.1016/J.ELECTACTA.2008.04.009.

[45] A. Stassi, I. Gatto, E. Passalacqua, V. Antonucci, A.S. Arico, L. Merlo, C. Oldani, E. Pagano, Performance comparison of long and short-side chain perfluorosulfonic membranes for high temperature polymer electrolyte membrane fuel cell operation, Journal of Power Sources. 196 (2011) 8925–8930. https://doi.org/10.1016/J.JPOWSOUR.2010.12.084.

[46] A. Chandan, M. Hattenberger, A. El-Kharouf, S. Du, A. Dhir, V. Self, B.G. Pollet, A. Ingram, W. Bujalski, High temperature (HT) polymer electrolyte membrane fuel cells (PEMFC) – A review, Journal of Power Sources. 231 (2013) 264–278. https://doi.org/10.1016/J.JPOWSOUR.2012.11.126.

[47] A. Ghielmi, P. Vaccarono, C. Troglia, V. Arcella, Proton exchange membranes based on the short-side-chain perfluorinated ionomer, Journal of Power Sources. 145 (2005) 108–115. https://doi.org/10.1016/J.JPOWSOUR.2004.12.068.

[48] H. Su, C. Felix, O. Barron, P. Bujlo, B.J. Bladergroen, B.G. Pollet, S. Pasupathi, High-Performance and Durable Membrane Electrode Assemblies for High-Temperature Polymer Electrolyte Membrane Fuel Cells, Electrocatalysis. 5 (2014) 361–371. https://doi.org/10.1007/S12678-014-0202-5/FIGURES/10.

[49] A. Verma, K. Scott, Development of higherature PEMFC based on heteropolyacids and polybenzimidazole, Journal of Solid State Electrochemistry. 14 (2010) 213–219. https://doi.org/10.1007/S10008-008-0678-0/FIGURES/8.

[50] E. Fontananova, F. Trotta, J.C. Jansen, E. Drioli, Preparation and characterization of new non-fluorinated polymeric and composite membranes for PEMFCs, Journal of Membrane Science. 348 (2010) 326–336.

https://doi.org/10.1016/J.MEMSCI.2009.11.020.

[51] G. Frutsaert, G. David, B. Ameduri, D.J. Jones, J. Rozière, X. Glipa, Synthesis and characterisation of novel fluorinated polymers bearing pendant imidazole groups and blend membranes: New materials for PEMFC operating at low relative humidity, Journal of Membrane Science. 367 (2011) 127–133. https://doi.org/10.1016/J.MEMSCI.2010.10.047.

[52] K. Miyatake, B. Bae, M. Watanabe, Fluorene-containing cardo polymers as ion conductive membranes for fuel cells, Polymer Chemistry. 2 (2011) 1919–1929. https://doi.org/10.1039/C1PY00103E.

[53] H.S. Lee, A. Roy, O. Lane, J.E. McGrath, Synthesis and characterization of poly(arylene ether sulfone)-b-polybenzimidazole copolymers for high temperature low humidity proton exchange membrane fuel cells, Polymer. 49 (2008) 5387–5396. https://doi.org/10.1016/J.POLYMER.2008.09.019.

[54] N.Y. Abu-Thabit, S.A. Ali, S.M.J. Zaidi, K. Mezghani, Novel sulfonated poly(ether ether ketone)/phosphonated polysulfone polymer blends for proton conducting membranes, Journal of Materials Research. 27 (2012) 1958–1968. https://doi.org/10.1557/JMR.2012.145.

[55] J.H. Liao, Q.F. Li, H.C. Rudbeck, J.O. Jensen, A. Chromik, N.J. Bjerrum, J. Kerres, W. Xing, Oxidative Degradation of Polybenzimidazole Membranes as Electrolytes for High Temperature Proton Exchange Membrane Fuel Cells, Fuel Cells. 11 (2011) 745–755. https://doi.org/10.1002/FUCE.201000146.

[56] J.S. Yang, L.N. Cleemann, T. Steenberg, C. Terkelsen, Q.F. Li, J.O. Jensen, H.A. Hjuler, N.J. Bjerrum, R.H. He, High Molecular Weight Polybenzimidazole Membranes for High Temperature PEMFC, Fuel Cells. 14 (2014) 7–15.

https://doi.org/10.1002/FUCE.201300070.

[57] K.A. Perry, K.L. More, E.A. Payzant, R.A. Meisner, B.G. Sumpter, B.C. Benicewicz, A comparative study of phosphoric acid-doped m-PBI membranes, Journal of Polymer Science Part B: Polymer Physics. 52 (2014) 26–35. https://doi.org/10.1002/POLB.23403.

[58] T.S. Chung, A critical review of polybenzimidazoles: Historical development and future R&D, Journal of Macromolecular Science - Reviews in Macromolecular Chemistry and Physics. 37 (1997) 277–301. https://doi.org/10.1080/15321799708018367.

[59] M.A. Haque, A.B. Sulong, K.S. Loh, E.H. Majlan, T. Husaini, R.E. Rosli, Acid doped polybenzimidazoles based membrane electrode assembly for high temperature proton exchange membrane fuel cell: A review, International Journal of Hydrogen Energy. 42 (2017) 9156–9179. https://doi.org/10.1016/J.IJHYDENE.2016.03.086.

[60] S.C. Kumbharkar, M.N. Islam, R.A. Potrekar, U.K. Kharul, Variation in acid moiety of polybenzimidazoles: Investigation of physico-chemical properties towards their applicability as proton exchange and gas separation membrane materials, Polymer. 50 (2009) 1403–1413. https://doi.org/10.1016/J.POLYMER.2009.01.043.

[61] T.R. Hanley, T.E. Helminiak, C.L. Benner, Expansion of aromatic heterocyclic polymers in salt solution, Journal of Applied Polymer Science. 22 (1978) 2965–2978. https://doi.org/10.1002/APP.1978.070221022.

[62] H.L. Lin, Y.C. Chen, C.C. Li, C.P. Cheng, T.L. Yu, Preparation of PBI/PTFE composite membranes from PBI in N,N′-dimethyl acetamide solutions with various concentrations of LiCl, Journal of Power Sources. 181 (2008) 228–236. https://doi.org/10.1016/J.JPOWSOUR.2008.01.035.

[63] S. Yu, L. Xiao, B.C. Benicewicz, Durability Studies of PBI-based High Temperature

PEMFCs ~, (2008) 165–174. https://doi.org/10.1002/fuce.200800024.

[64] S. Yu, L. Xiao, B.C. Benicewicz, Durability Studies of PBI-based High Temperature PEMFCs, Fuel Cells. 8 (2008) 165–174. https://doi.org/10.1002/FUCE.200800024.

[65] P. Chippar, H. Ju, Numerical modeling and investigation of gas crossover effects in high temperature proton exchange membrane (PEM) fuel cells, International Journal of Hydrogen Energy. 38 (2013) 7704–7714. https://doi.org/10.1016/J.IJHYDENE.2012.07.123.

[66] G. Liu, H. Zhang, J. Hu, Y. Zhai, D. Xu, Z. gang Shao, Studies of performance degradation of a high temperature PEMFC based on H_3PO_4-doped PBI, Journal of Power Sources. 162 (2006) 547–552. https://doi.org/10.1016/J.JPOWSOUR.2006.07.008.

[67] Y.C. Jin, M. Nishida, W. Kanematsu, T. Hibino, An H_3PO_4-doped polybenzimidazole/$Sn_{0.95}Al_{0.05}P_2O_7$ composite membrane for high-temperature proton exchange membrane fuel cells, Journal of Power Sources. 196 (2011) 6042–6047. https://doi.org/10.1016/J.JPOWSOUR.2011.03.094.

[68] X. Wu, M. Mamlouk, K. Scott, A PBI-$Sb_{0.2}Sn_{0.8}P_2O_7$-H_3PO_4 Composite Membrane for Intermediate Temperature Fuel Cells, Fuel Cells. 11 (2011) 620–625. https://doi.org/10.1002/FUCE.201100089.

[69] C. Xu, X. Wu, X. Wang, M. Mamlouk, K. Scott, Composite membranes of polybenzimidazole and caesium-salts-of-heteropolyacids for intermediate temperature fuel cells, Journal of Materials Chemistry. 21 (2011) 6014–6019. https://doi.org/10.1039/C1JM10093A.

[70] J.N. Coleman, U. Khan, W.J. Blau, Y.K. Gun'ko, Small but strong: A review of the mechanical properties of carbon nanotube–polymer composites, Carbon. 44 (2006)

1624–1652. https://doi.org/10.1016/J.CARBON.2006.02.038.

[71] H. Erdemi, Ü. Akbey, W.H. Meyer, Conductivity behavior and solid state NMR investigation of imidazolium-based polymeric ionic liquids, Solid State Ionics. 181 (2010) 1586–1595. https://doi.org/10.1016/J.SSI.2010.08.018.

[72] C. Xu, Y. Cao, R. Kumar, X. Wu, X. Wang, K. Scott, A polybenzimidazole/sulfonated graphite oxide composite membrane for high temperature polymer electrolyte membrane fuel cells, Journal of Materials Chemistry. 21 (2011) 11359–11364. https://doi.org/10.1039/C1JM11159K.

[73] S.P. Koenig, L. Wang, J. Pellegrino, J.S. Bunch, Selective molecular sieving through porous graphene, Nature Nanotechnology 2012 7:11. 7 (2012) 728–732. https://doi.org/10.1038/nnano.2012.162.

[74] L. Tsetseris, S.T. Pantelides, Graphene: An impermeable or selectively permeable membrane for atomic species?, Carbon. 67 (2014) 58–63. https://doi.org/10.1016/J.CARBON.2013.09.055.

[75] First principles study of the permeability of graphene to hydrogen atoms, Physical Chemistry Chemical Physics. 15 (2013) 16132–16137. https://doi.org/10.1039/C3CP52318G. [76] A.A. Balandin, S. Ghosh, W. Bao, I. Calizo, D. Teweldebrhan, F. Miao, C.N. Lau, Superior Thermal Conductivity of Single-Layer Graphene, Nano Letters. 8 (2008) 902–907. https://doi.org/10.1021/NL0731872.

[77] A.K. Geim, Graphene: Status and Prospects, Science. 324 (2009) 1530–1534. https://doi.org/10.1126/SCIENCE.1158877.

[78] T. Luo, G. Chen, Nanoscale heat transfer – from computation to experiment, Physical Chemistry Chemical Physics. 15 (2013) 3389–3412.

https://doi.org/10.1039/C2CP43771F.

[79] C. Shen, A.H. Brozena, Y. Wang, Double-walled carbon nanotubes : Challenges and opportunities, Nanoscale. 3 (2011) 503–518. https://doi.org/10.1039/C0NR00620C. [80] J. Hone, M. Whitney, C. Piskoti, A. Zettl, Thermal conductivity of single-walled carbon nanotubes, Physical Review B. 59 (1999) R2514. https://doi.org/10.1103/PhysRevB.59.R2514.

[81] P. Blake, P.D. Brimicombe, R.R. Nair, T.J. Booth, D. Jiang, F. Schedin, L.A. Ponomarenko, S. V. Morozov, H.F. Gleeson, E.W. Hill, A.K. Geim, K.S. Novoselov, Graphene-Based Liquid Crystal Device, Nano Letters. 8 (2008) 1704–1708. https://doi.org/10.1021/NL080649I.

[82] J. Xu, D.K. Dang, V.T. Tran, X. Liu, J.S. Chung, S.H. Hur, W.M. Choi, E.J. Kim, P.A. Kohl, Liquid-phase exfoliation of graphene in organic solvents with addition of naphthalene, Journal of Colloid and Interface Science. 418 (2014) 37–42. https://doi.org/10.1016/J.JCIS.2013.12.009.

[83] K.S. Novoselov, V.I. Fal'Ko, L. Colombo, P.R. Gellert, M.G. Schwab, K. Kim, A roadmap for graphene, Nature 2012 490:7419. 490 (2012) 192–200. https://doi.org/10.1038/nature11458.

[84] J. Liu, P. Li, Y. Chen, Z. Wang, J. He, H. Tian, F. Qi, B. Zheng, J. Zhou, W. Lin, W. Zhang, Large-area synthesis of high-quality and uniform monolayer graphene without unexpected bilayer regions, Journal of Alloys and Compounds. 615 (2014) 415–418. https://doi.org/10.1016/J.JALLCOM.2014.07.003.

[85] A. Reina, X. Jia, J. Ho, D. Nezich, H. Son, V. Bulovic, M.S. Dresselhaus, K. Jing, Large area, few-layer graphene films on arbitrary substrates by chemical vapor deposition, Nano Letters. 9 (2009) 30–35.

https://doi.org/10.1021/NL801827V/SUPPL_FILE/NL801827V_SI_003.PDF.

[86] S. Bae, H. Kim, Y. Lee, X. Xu, J.S. Park, Y. Zheng, J. Balakrishnan, T. Lei, H. Ri Kim, Y. Il Song, Y.J. Kim, K.S. Kim, B. Özyilmaz, J.H. Ahn, B.H. Hong, S. Iijima, Roll-to-roll production of 30-inch graphene films for transparent electrodes, Nature Nanotechnology 2010 5:8. 5 (2010) 574–578. https://doi.org/10.1038/nnano.2010.132.

[87] M.J. Allen, V.C. Tung, R.B. Kaner, Honeycomb Carbon: A Review of Graphene, Chemical Reviews. 110 (2009) 132–145. https://doi.org/10.1021/CR900070D.

[88] F. Perreault, A. Fonseca De Faria, M. Elimelech, Environmental applications of graphene-based nanomaterials, Chemical Society Reviews. 44 (2015) 5861–5896. https://doi.org/10.1039/C5CS00021A.

[89] J. Li, X. Zeng, T. Ren, E.V. der H.- Lubricants, The preparation of graphene oxide and its derivatives and their application in bio-tribological systems, Mdpi.Com. 2 (2014) 137–161. https://doi.org/10.3390/lubricants2030137.

[90] A.M. Dimiev, S. Eigler, Graphene oxide : fundamentals and applications, John Wiley & Sons, Incorporated, Chichester, West Sussex, 2017.

[91] X. Huang, X. Qi, F. Boey, H. Zhang, Graphene-based composites, Chemical Society Reviews. 41 (2012) 666–686. https://doi.org/10.1039/C1CS15078B.

[92] B.F. MacHado, P. Serp, Graphene -based materials for catalysis, Catalysis Science & Technology. 2 (2011) 54–75. https://doi.org/10.1039/C1CY00361E.

[93] B. Min Yoo, H. Jin Shin, H. Wook Yoon, H. Bum Park, H.B. Park, Graphene and graphene oxide and their uses in barrier polymers, Wiley Online Library. 131 (2014). https://doi.org/10.1002/app.39628.

[94] X. Li, H. Wang, J.T. Robinson, H. Sanchez, G. Diankov, H. Dai, Simultaneous nitrogen

doping and reduction of graphene oxide, Journal of the American Chemical Society. 131 (2009) 15939–15944. https://doi.org/10.1021/JA907098F/SUPPL_FILE/JA907098F_SI_001.PDF.

[95] D.J. Kwak, B.H. Moon, D.K. Lee, C.S. Park, Y.M. Sung, Comparison of transparent conductive indium tin oxide, titanium-doped indium oxide, and fluorine-doped tin oxide films for dye-sensitized solar cell application, Journal of Electrical Engineering and Technology. 6 (2011) 684–687. https://doi.org/10.5370/JEET.2011.6.5.684.

[96] A.M. Dimiev, S. Eigler, Graphene Oxide: Fundamentals and Applications. (2016) 1–439. https://doi.org/10.1002/9781119069447.

[97] E.J. Yoo, J. Kim, E. Hosono, H.S. Zhou, T. Kudo, I. Honma, Large reversible Li storage of graphene nanosheet families for use in rechargeable lithium ion batteries, Nano Letters. 8 (2008) 2277–2282. https://doi.org/10.1021/NL800957B/SUPPL_FILE/NL800957B-FILE003.PDF.

[98] J. Zhu, D. Yang, Z. Yin, Q. Yan, H. Zhang, Graphene and Graphene-Based Materials for Energy Storage Applications, Small. 10 (2014) 3480–3498. https://doi.org/10.1002/SMLL.201303202.

[99] N. Mahmood, C. Zhang, H. Yin, Y. Hou, Graphene-based nanocomposites for energy storage and conversion in lithium batteries, supercapacitors and fuel cells, Journal of Materials Chemistry A. 2 (2013) 15–32. https://doi.org/10.1039/C3TA13033A.

[100] D. Pan, S. Wang, B. Zhao, M. Wu, H. Zhang, Y. Wang, Z. Jiao, Li storage properties of disordered graphene nanosheets, Chemistry of Materials. 21 (2009) 3136–3142. https://doi.org/10.1021/CM900395K/SUPPL_FILE/CM900395K_SI_001.PDF.

[101] W. Lee, S. Suzuki, M. Miyayama, Lithium storage properties of graphene sheets derived

from graphite oxides with different oxidation degree, Ceramics International. 39 (2013) S753–S756. https://doi.org/10.1016/J.CERAMINT.2012.12.030.

[102] B.M. Yoo, H.J. Shin, H.W. Yoon, H.B. Park, Graphene and graphene oxide and their uses in barrier polymers, Journal of Applied Polymer Science. 131 (2014). https://doi.org/10.1002/APP.39628.

[103] T. Nezakati, B.G. Cousins, A.M. Seifalian, Toxicology of chemically modified graphene-based materials for medical application, Arch Toxicol. 3 (2014) 1987–2012. https://doi.org/10.1007/s00204-014-1361-0.

[104] S. Goenka, V. Sant, S. Sant, Graphene-based nanomaterials for drug delivery and tissue engineering, Journal of Controlled Release. 173 (2014) 75–88. https://doi.org/10.1016/J.JCONREL.2013.10.017.

[105] L. Staudenmaier, Verfahren zur Darstellung der Graphitsäure, European journal of inorganic chemistry. 31 (1898) 1481–1487. https://doi.org/10.1002/cber.18980310237.

[106] S. Eigler, Controlled Chemistry Approach to the Oxo-Functionalization of Graphene, Chemistry - A European Journal. 22 (2016) 7012–7027. https://doi.org/10.1002/CHEM.201600174.

[107] S. Eigler, A. Hirsch, S. Eigler, A. Hirsch, Chemistry with graphene and graphene oxide—challenges for synthetic chemists, Wiley Online Library. 53 (2014) 7720–7738. https://doi.org/10.1002/anie.201402780.

[108] S. Pei, Q. Wei, K. Huang, H.-M. Cheng, W. Ren, Green synthesis of graphene oxide by seconds timescale water electrolytic oxidation, (n.d.). https://doi.org/10.1038/s41467-017-02479-z.

[109] B. Gurzęda, P. Florczak, M. Kempiński, B. Peplińska, P. Krawczyk, S. Jurga, Synthesis

of graphite oxide by electrochemical oxidation in aqueous perchloric acid, Carbon. 100 (2016) 540–545. https://doi.org/10.1016/J.CARBON.2016.01.044.

[110] C.-Y. Su, A.-Y. Lu, Y. Xu, F.-R. Chen, A.N. Khlobystov, L.-J. Li, High-Quality Thin Graphene Films from Fast Electrochemical Exfoliation, ACS Nano. 5 (2011) 2332–2339. https://doi.org/10.1021/NN200025P.

[111] A. Ambrosi, M. Pumera, Electrochemically Exfoliated Graphene and Graphene Oxide for Energy Storage and Electrochemistry Applications, Chemistry – A European Journal. 22 (2016) 153–159. https://doi.org/10.1002/CHEM.201503110.

[112] K. Parvez, Z.-S. Wu, R. Li, X. Liu, R. Graf, X. Feng, K. Mü, Exfoliation of Graphite into Graphene in Aqueous Solutions of Inorganic Salts, (2014). https://doi.org/10.1021/ja5017156.

[113] Z. Tian, P. Yu, S.E. Lowe, A.G. Pandolfo, T.R. Gengenbach, K.M. Nairn, J. Song, X. Wang, Y.L. Zhong, D. Li, Facile electrochemical approach for the production of graphite oxide with tunable chemistry, Carbon. 112 (2017) 185–191. https://doi.org/10.1016/j.carbon.2016.10.098.

[114] J. Liu, C.K. Poh, D. Zhan, L. Lai, S.H. Lim, L. Wang, X. Liu, N. Gopal Sahoo, C. Li, Z. Shen, J. Lin, Improved synthesis of graphene flakes from the multiple electrochemical exfoliation of graphite rod, Nano Energy. 2 (2013) 377–386. https://doi.org/10.1016/J.NANOEN.2012.11.003.

[115] M. Wissler, Graphite and carbon powders for electrochemical applications, Journal of Power Sources. 156 (2006) 142–150. https://doi.org/10.1016/j.jpowsour.2006.02.064.

[116] R.M.N.. Rathnayake, H.W.M.A.. Wijayasinghe, H.M.T.G.. Pitawala, M. Yoshimura, H.-H. Huang, Synthesis of graphene oxide and reduced graphene oxide by needle platy

natural vein graphite, Applied Surface Science. 393 (2017) 309–315. https://doi.org/10.1016/j.apsusc.2016.10.008.

[117] R. Kumar, M. Mamlouk, K. Scott, A Graphite Oxide Paper Polymer Electrolyte for Direct Methanol Fuel Cells, Int. J. Electrochem. (2011) 1–7. https://doi.org/10.4061/2011/434186.

[118] K. Scott, Freestanding sulfonated graphene oxide paper: a new polymer electrolyte for polymer electrolyte fuel cell (2012) 5584–5586. https://doi.org/10.1039/c2cc31771k.

[119] W. Gao, G. Wu, M.T. Janicke, D.A. Cullen, R. Mukundan, J.K. Baldwin, E.L. Brosha, C. Galande, P.M. Ajayan, K.L. More, A.M. Dattelbaum, P. Zelenay, Ozonated graphene oxide film as a proton-exchange membrane, Angewandte Chemie - International Edition. 53 (2014) 3588–3593. https://doi.org/10.1002/ANIE.201310908.

[120] U.R. Farooqui, A.L. Ahmad, N.A. Hamid, Graphene oxide: A promising membrane material for fuel cells, Renewable and Sustainable Energy Reviews. 82 (2018) 714–733. https://doi.org/10.1016/J.RSER.2017.09.081.

[121] Y. Cai, Z. Yue, S. Xu, A novel polybenzimidazole composite modified by sulfonated graphene oxide for high temperature proton exchange membrane fuel cells in anhydrous atmosphere, Journal of Applied Polymer Science. 134 (2017) 44986. https://doi.org/10.1002/APP.44986.

[122] J. Yang, C. Liu, L. Gao, J. Wang, Y. Xu, R. He, Novel composite membranes of triazole modified graphene oxide and polybenzimidazole for high temperature polymer electrolyte membrane fuel cell applications, RSC Advances. 5 (2015) 101049–101054. https://doi.org/10.1039/c5ra16554g.

[123] Z. Ji, J. Chen, M. Pérez-Page, Z. Guo, Z. Zhao, R. Cai, M. Rigby, S. Haigh, S. Homes,

Doped graphene/carbon black hybrid catalyst giving enhanced oxygen reduction reaction activity with high resistance to corrosion in proton exchange membrane fuel cells, Journal of Energy Chemistry. 68 (2022) 143–153. https://doi.org/10.1016/J.JECHEM.2021.09.031.

2. Methods

This chapter mainly introduces the technical means and their principles used in this thesis to characterize graphene (oxide) and PBI (composite) membranes and the method of HT-PEMFC performance testing. The specific parameters and conditions used for the various methods are described in Chapters 3 to 6.

2.1 Characterization of Graphene and Graphene Oxide

2.1.1 Raman Spectroscopy of Graphene and Graphene Oxide

Raman spectroscopy is a useful technique for observing the crystal structure of graphene and graphene oxide. Depending on the interaction of light and matter, different materials can cause different displacements in the excitation wavelength [1]. This excitation wavelength interacts primarily with the polarizable electron cloud, so some polarized impurities such as water do not substantially affect the spectrum. In addition, Raman spectroscopy is a non-destructive characterization technique, which provides great convenience for the study of the properties of graphene and graphene oxide [2].

The main peaks of graphite related materials are D peak (about 1340 cm^{-1}), G peak (about 1580 cm^{-1}) and 2D peak (about 2700 cm^{-1}) which are defect-related peak, sp^2 carbon peak and few-layer graphene characteristic related peak, respectively [3]. Raman spectroscopy is a versatile tool for studying the properties of graphene since it can provide information including the number of layers, stacking order, defect caused by functional groups or disorder, edge types and qualities, strain, and stress.

The pristine graphite and graphene are only composed of sp^2 hybridized carbon structures; thus, they do not contain defective related D peak. However, graphite and graphene can be identified by the relationship between the G peak and the 2D peak. The typical Raman spectra of graphite and SLG are shown in **Figure 2. 1**[4]. Compared with graphite, the difference in the 2D peaks

of graphene makes the Raman spectrum of graphene unique. The 2D peak of graphite, which is the second-order overtone of D peak, can be fitted to two broad peaks while the 2D peak of graphene can be fitted to one sharp peak. In addition, with the increase in the number of graphene layers, the 2D peak is accompanied by a certain blue shift and broadening. The increase in the G peak intensity compared to the increase in the 2D peak has a certain linear relationship with the increase in the number of graphene layers. The Raman spectra of graphene with different layers and curve fitted enlarged 2D peaks are shown in **Figure 2. 2** a and b, respectively. As the peak related to sp^2 carbon, the intensity of the G peak compared to the 2D peak increases as the number of graphene layers increases. This is largely due to the increase in the graphite content caused by the increase in the number of graphene layers [4]. As for the broadening of the 2D peak, it is related to the distribution of π electrons [5].
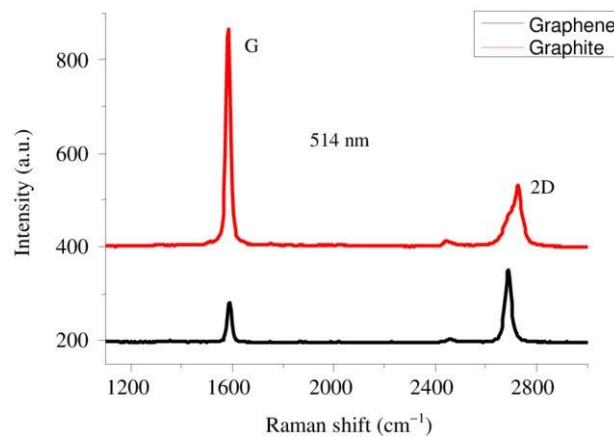
Figure 2. 1. Raman spectra of graphite and SLG at excitation wavelength of 514 nm[4] .
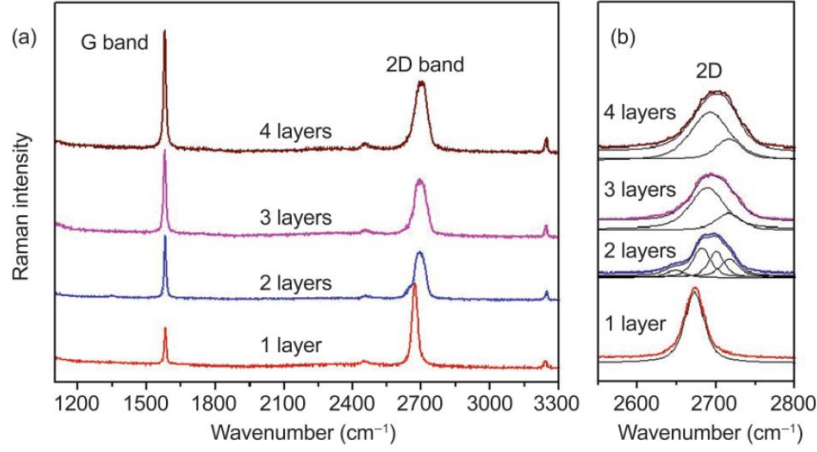
Figure 2. 2. (a)The Raman spectra of graphene with different layers and (b) curve fitted 2D peaks on SiO2/Si substrate at the excitation wavelength of 532nm [6].

GO can be considered as graphene with defects or functionalized graphene. The Raman spectrum of GO can be considered to add defects to the graphene Raman spectrum. As mentioned above, D peak is the defect-activated peak that is donated by structural defects or disorders of the carbon network [7]. For GO, defects can also be caused by the partial carbon conversion from sp^2 hybridization to sp^3 hybridization due to the addition of oxygen-containing functional groups. By comparing the ratio of the intensity of the D peak to the intensity of the G peak (I_D/I_G), the number of defects (or equivalently, mean interdefect distance, L_D) per area can be quantified. In addition to being related to L_D, I_D/I_G also depends on the energy and wavelength of the laser. The relationship between L_D, I_D/I_G, laser energy and laser wavelength are shown in **Figure 2. 3**. The generalized correlation between L_D, laser energy (E_L) and laser wavelength (λ_L) can also be expressed by **Equation 2- 1** and **Equation 2- 2**

$$L_D^2 \ (nm^2) = \frac{(4.3 \pm 1.3) \times 10^3}{E_L^4} \left(\frac{I_D}{I_G}\right)^{-1}$$

Equation 2- 1

$$L_D^2 \ (nm^2) = (1.8 \pm 0.5) \times 10^{-9} \lambda_L^4 \left(\frac{I_D}{I_G}\right)^{-1}$$

Equation 2- 2

The typical Raman spectra of graphite, GO and reduced GO are shown in Figure 2. 4. As mentioned above, a larger I_D/I_G indicates a smaller L_D, that is, more defects, which can be related to the degree of functionalization of GO. However, the I_D/I_G value or defect degree of the GO Raman spectrum does not only depend on the level of functionalization. It may also be affected by the permanent hole [8], and large edges caused by the small size of graphitic domains [9]. Therefore, only relying on Raman spectroscopy to judge the degree of functionalization of GO lacks rigour, and it needs to be further evaluated with other characterizations.
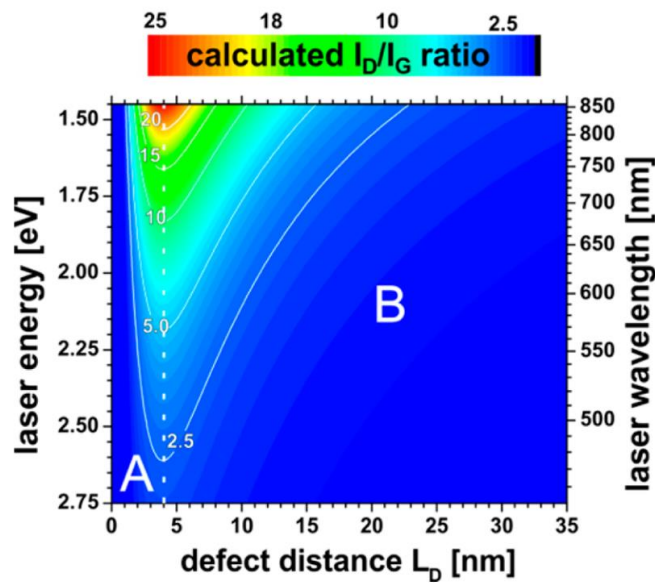
Figure 2. 3. The relationship between LD, ID/IG, laser energy and laser wavelength [7].
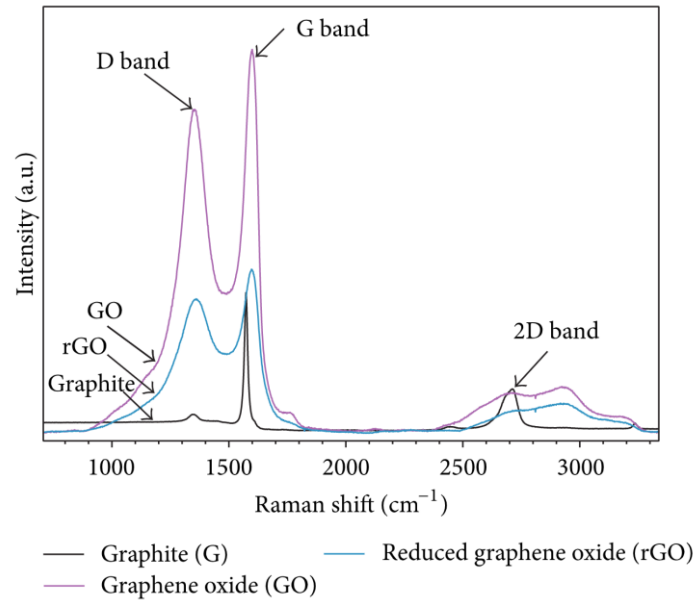
Figure 2. 4. Typical Raman spectra of graphite, graphene oxide and reduced graphene oxide [10].

2.1.2 Fourier Transform Infrared Spectroscopy (FT-IR)

In addition to Raman, infrared is another method to obtain molecular vibration information [11]. The absorbance (A) and transmittance (T) at the given IR wavenumber can be calculated through **Equation 2- 3** and **Equation 2- 4**, respectively.

$$A = log\left(\frac{I_0}{I}\right) = abc$$

Equation 2- 3

$$T = \frac{I}{I_0}$$

Equation 2- 4

I_0: intensity of the entering radiation

I: intensity of the transmitted light

a: absorptivity

b: cell thickness

c: concentration

FT-IR is different from how Raman's photon energy is transferred to molecules, so the information it extracts can express different characteristics. Although FT-IR cannot judge the number of layers of GO or the degree of functionalization through the comparison of its peak intensity, it can qualitatively determine the types of functional groups. Therefore, FT-IR has become an essential tool for the characterization of GO components [12]. Typical FT-IR absorbance spectra of GO with the different number of layers are shown in **Figure 2. 5**. The regions α, β, and γ are the infrared frequencies where the chemical species overlap [13]. In different works, the summary of the wavelength area of different chemical bonds may be slightly different. The infrared wavelength corresponding to different chemical bonds can also refer to in **Table 2. 1**.
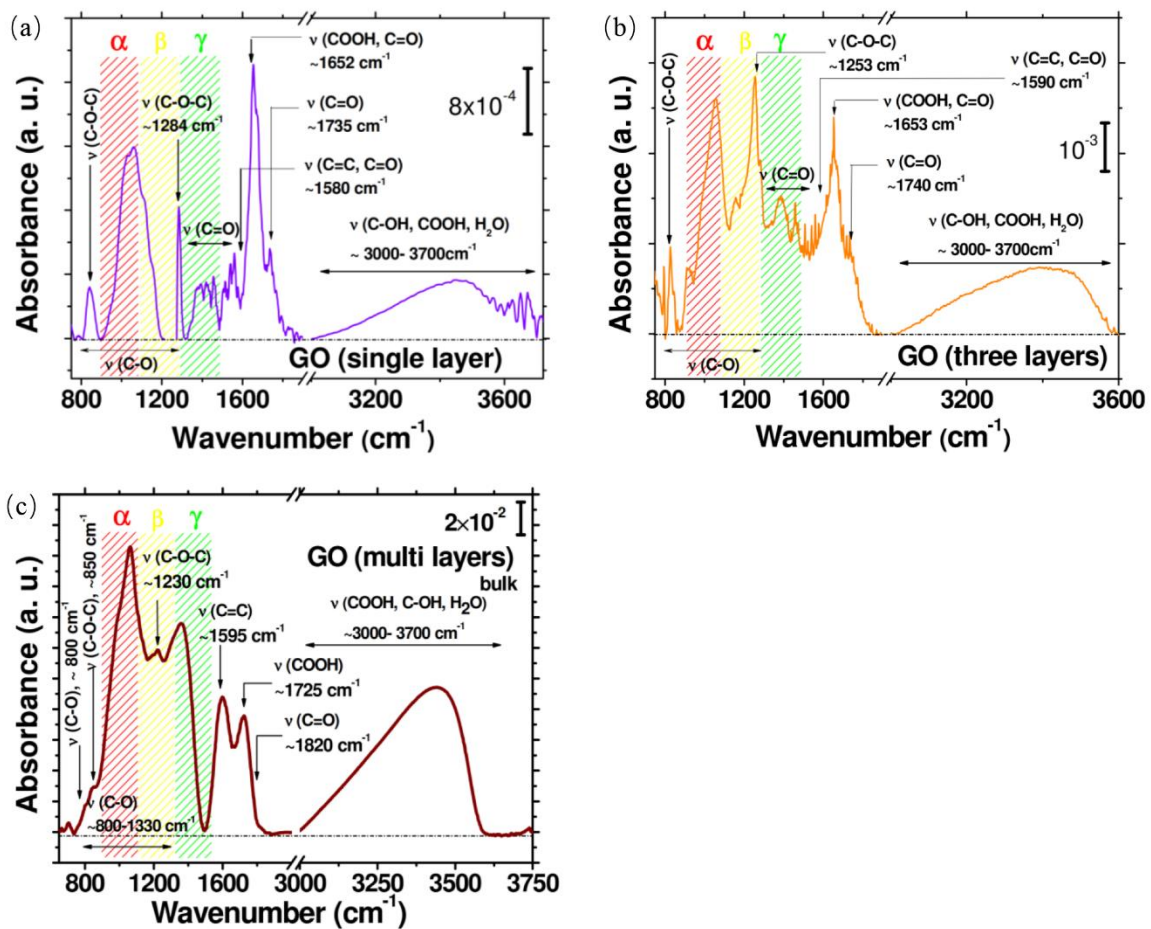
Figure 2. 5. Typical FT-IR absorbance spectrum of GO. (a) single layer, (b) 3 layers and (c) multi layers [13].

Table 2. 1. The infrared wavelength corresponds to different chemical bonds [14].

Chemical bonding	Wavenumber (cm^{-1})
C=C	1,500-1,600
hydroxyls	3,050–3,800
carboxyls	1,650–1,750
carbonyls	1,750–1,850
epoxides	1,000–1,280

2.1.3 X-ray Photoelectron Spectroscopy (XPS)

Relying on the photoelectric effect, XPS can effectively determine the elemental composition and state of the material surface, as well as the density of different electronic states. Therefore, XPS can be used as a powerful means to detect and quantify GO elements and functional groups [15]. The binding energy ($E_{binding}$) of specific material surface can be calculated through photoelectric effect equation (**Equation 2- 5**) [16].

$$E_{binding} = E_{photon} - (E_{kinetic} + \emptyset)$$

Equation 2- 5

E_{photon}: X-ray photons energy

$E_{kinetic}$: Kinetic energy of the electron

$\emptyset$: instrumental correction factor

The XPS analysis of GO usually utilizes a survey scan to explore the element composition, especially the C/O ratio or O/C ratio, and then study the functional group composition through the deconvolution of the high-resolution XPS spectra of the C 1s and the O 1s. The typical XPS

survey spectra of graphite and graphene prepared by ultrasonication are shown in **Figure 2. 6** a. Both graphite and GO contain carbon and oxygen. However, due to the functionalization of GO, the oxygen content of GO is significantly higher, and a higher oxygen content indicates a higher level of functionalization. As shown in **Figure 2. 6** b and c, the XPS C 1s spectra of graphite and GO also show significant differences. The XPS high-resolution spectra of these elements can be deconvoluted based on the parameters shown in **Table 2. 2**. The C in graphite is mainly sp^2 hybridized C-C. As shown in **Figure 2. 6** c and d, the oxygen-containing functional groups in GO are dominated by hydroxyl groups since carbonyl and carboxyl groups are further oxidized on the basis of hydroxyl groups.
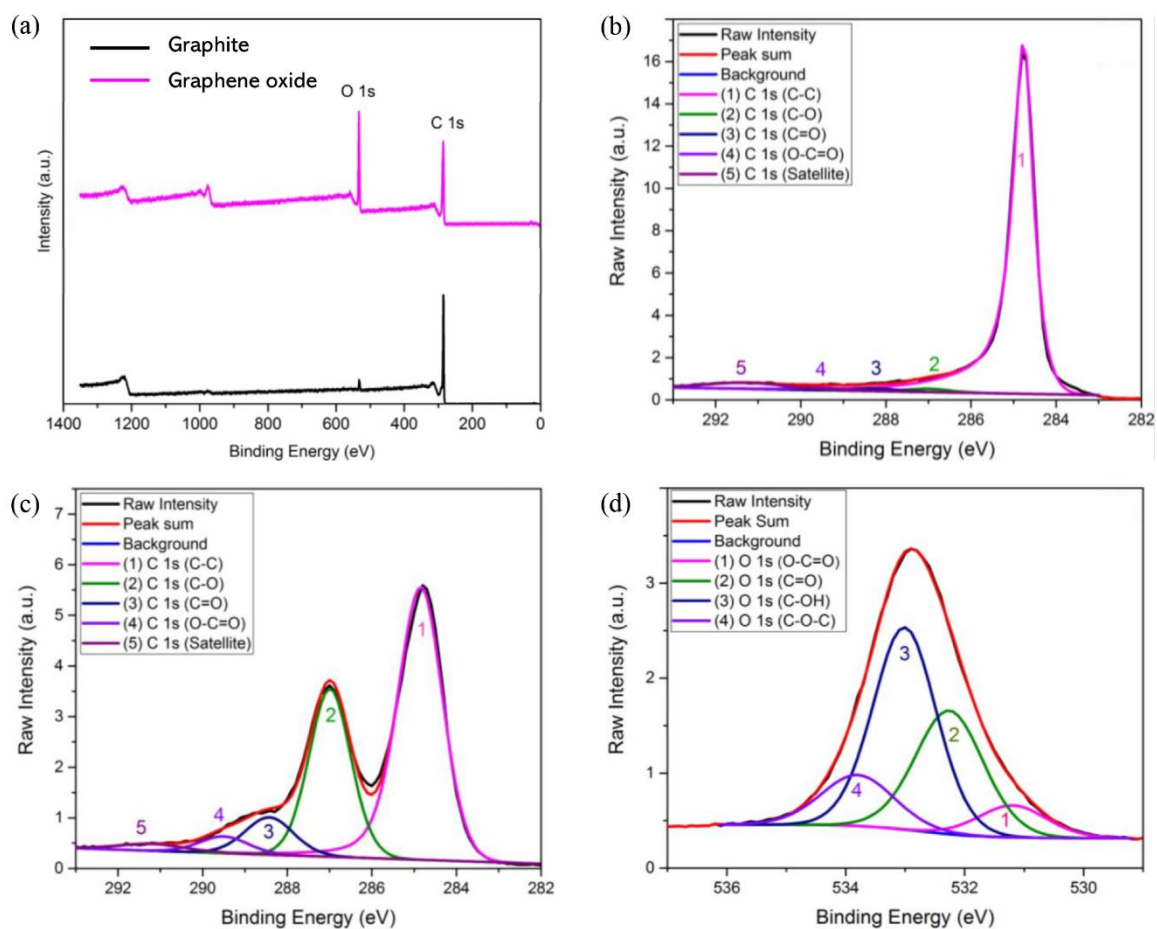
Figure 2. 6. XPS survey spectra and high-resolution elemental spectra. (a) survey spectra of graphite and graphene oxide, (b) C 1s spectra of graphite, (c) C 1s spectra of graphene oxide, (d) O 1s spectra of graphene oxide [15].

Table 2. 2. Parameters for deconvolution of XPS C 1s and O 1s spectra

Peaks	Groups	Binding energy (eV)
	C—C	~284.8
	C—O	286.8~287.0
C 1s	C=O	287.7~288.3
	O—C=O	289.1~289.7
	π- π* Satellite	290.9~292.5
	O—C=O	530.9~531.5
	C=O	531.7~532.4
O 1s	C—OH	533.0~533.3
	C—O—C	533.3~534.1

2.2 Characterization of PBI Membrane

As a matrix loaded with PA to provide a proton transfer channel, the proton conductivity of the PBI membrane plays an important role. However, the mechanical properties of the PBI membrane at high acid doping level (ADL) and the ability to block hydrogen are the preconditions for the effectiveness of PBI in HT-PEMFC. The following sections will introduce tensile testing and linear sweep voltammetry (LSV) of PBI membrane to characterize the above properties.

2.2.1 Tensile Stress and Strain

Tensile testing is performed by plotting stress-strain curves according to the relationship between force and elongation in the process of the stretch of the membrane. The typical stress-strain curve of the PBI membrane is shown in **Figure 2. 7**. The stress (σ_E) and strain (ε_S) in **Figure 2. 7** are defined by **Equation 2- 6** and **Equation 2- 7**, respectively.

$$\sigma_E[MPa] = F/(w_0 \times d_0)$$

<div align="right">*Equation 2- 6*</div>

F: axial force

w_0: width of membrane

d_0: thickness of membrane

$$\varepsilon_S [mm/mm] = (L - L_0)/L_0$$

L: length after stretch

L_0: initial length

The information available from the curve and its meaning are shown in **Table 2. 3**. The Young modulus is calculated from the slope of the initial linear stage of the curve. In addition to being affected by the mechanical properties and ADL of the PBI itself, tensile testing is also affected by temperature and humidity [17].
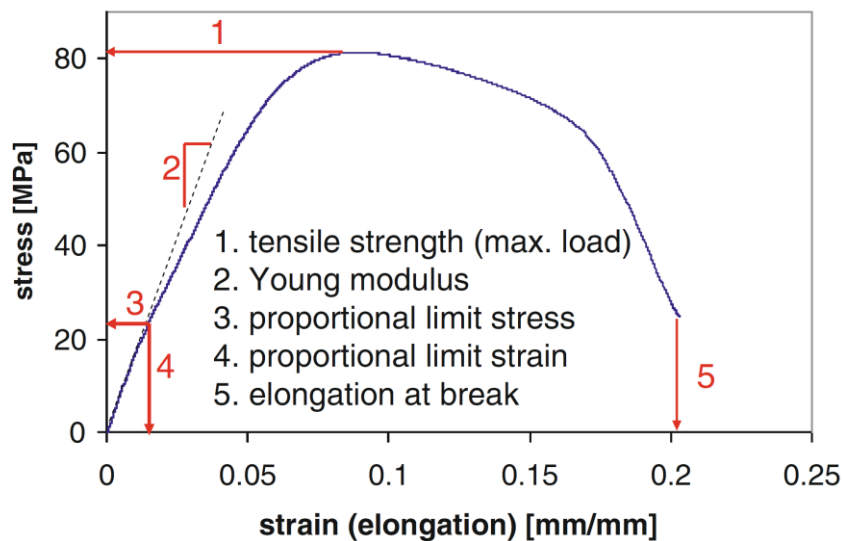
Figure 2. 7. Typical stress-strain curve of PBI membrane [17].

Table 2. 3. Information from the stress-strain curve

Parameters	Meaning
Tensile strength	Stress when elastic deformation becomes permanent
Young modulus	The tensile capacity of the material within the elastic limit
Proportional limit stress	Stress when linear deformation becomes plastic deformation
Proportional limit strain	Stress when linear deformation becomes plastic deformation
Elongation at break	--

2.2.2 Linear Sweep Voltammetry (LSV)

The crossover of hydrogen from the anode to the cathode through the membrane not only reduces the supply of electrons to the external circuit but also consumes oxygen at the cathode, which reduces the power available for the external circuit. The most intuitive impact of hydrogen crossover is to cause a significant reduction in open-circuit voltage (OCV). By creating a restricted mass transfer environment at the cathode, usually by feeding with pure nitrogen, and performing a linear sweep of the oxidation potential of the hydrogen on the cathode, the hydrogen crossover and internal short circuit can be evaluated. The typical LSV curve of PBI-membrane-based HT-PEMFC performed at 160 ℃ is shown in **Figure 2. 8**. The liner sweep potential is started from rest potential to anodic potential, and the scanning should be stopped when the potential is less than 1 V to avoid irreversible damage to the catalyst. Within a certain potential range, the current density increases linearly as the potential increases, resulting from an internal short circuit. Therefore, the internal short circuit resistance can be obtained by calculating the reciprocal slope of the linear phase of the LSV curve. By calibrating the internal short circuit, the limiting current density of hydrogen crossover ($j_{H_2\ cross}$) is

obtained, that is, the intersection of the inverted extension line of the linear part of the curve and the vertical axis. The hydrogen crossover flux can be calculated through **Equation 2- 8**.

$$\dot{n}_{H_2\ crossover} = \frac{j_{H_2\ cross} \times A_{active}}{n \times F}$$

Equation 2- 8

A_{active}: active area of fuel cell

n: the number of electrons taking part in the reaction

F: Faraday's constant
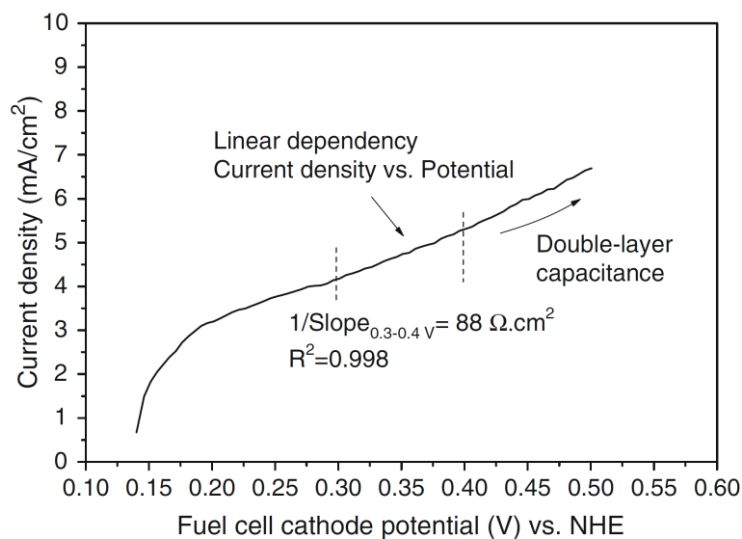
Figure 2. 8. Typical LSV curve of PBI-membrane-based HT-PEMFC. T= 160 ℃, anode: 0.3NL min^{-1} H$_2$, cathode: 0.3NL min^{-1} N$_2$ [17].

2.3 Performance Study of HT-PEMFC

2.2.1 Polarization Curves

The polarization curve is the most basic and important tool for studying the performance of PEMFC. The change of voltage with current density when PEMFC outputs power can be used

to evaluate PEMFC's reaction kinetic performance, electrochemical and physical resistance, and mass transfer performance. The typical polarization curve of PEMFC is shown in Figure 2. 9. Under the standard condition of 25℃ and atmospheric pressure, the theoretical value of OCV of PEMFC is 1.23V. The calculation process is shown in **Equation 2- 9**.

$$E = \frac{-\Delta G}{nF} = 1.23\ V$$

ΔG: Gibbs free energy of chemical reaction participate in PEMFC (ΔG=-237,340 J mol^{-1}, T=25℃)

n: number of electrons involved in hydrogen oxidation reaction or oxygen reduction reaction, 2

F: Faraday's constant (96,485 Coulombs/electron-mol)

There will be a certain gap between the actual OCV and the theoretical value. First of all, as the temperature increases, the theoretical value of Gibbs free energy will change, and the theoretically calculated value will decrease. Secondly, the irreversible voltage loss caused by the parasitic reactions will also cause the gap between the actual OCV and the theoretical value to be further widened. The factors that cause these parasitic reactions include, but are not limited to, hydrogen crossover, catalyst poisoning, internal short circuits, and the influence of feed gas bias pressure and water vapour pressure. The dominant factors causing the voltage loss at different current density stages in the polarization curve are different. The main losses are activation polarization losses in the low current density stage, ohmic losses in the medium current density, and concentration polarization losses in the high current density. The activation polarization losses are mainly related to the reaction kinetic factors of the catalyst, so it is mainly affected by the properties of activation and the physical environment of the catalyst. In

the middle current density stage, the voltage loss has a linear relationship with the increase of current density because it basically follows Ohm's law. The ohmic losses are mainly affected by the proton conductivity (membrane resistance), the resistance of the electrodes and the external circuit. Since membrane resistance is usually much larger than the electrode and external circuit resistance, the latter is usually ignored. At high current density, the concentration polarization losses are mainly related to the transmission and dispersion capacity of fuel and oxidant in the electrode. The overall performance of HT-PEMFC can be intuitively expressed by **Equation 2- 10**.

$$E = E_0 - (a + b \cdot \ln j) - R \cdot j + b \cdot \ln (1 - \frac{j}{j_{lim}})$$

E_0: OCV

a: exchange current density related parameters

b: kinetic overvoltage related Tafel slope

j: current density

j_{lim}: diffusion overvoltage related limiting current density
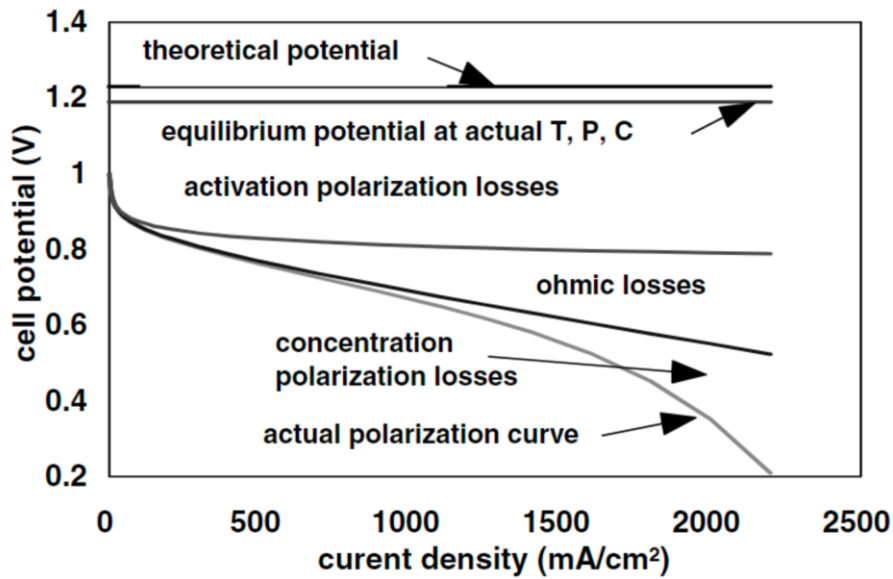
Figure 2. 9. Typical polarization curve of PEMFC [18].

2.2.2 Electrochemical Impedance Spectroscopy (EIS)

The polarization curve can intuitively express the electrochemical performance and power output of PEMFC. Exploring the factors that affect performance requires quantifying the various electronic and proton resistances in PEMFC. Since PEMFC is a complex system, there are double-layer capacitors in addition to resistors. Therefore, PEMFC cannot be expressed simply by resistance. EIS is widely used in the performance research of PEMFC to measure impedance. One of the most commonly used expressions of EIS spectra is the Nyquist curve. The typical Nyquist curves are shown in **Figure 2. 10**. The horizontal and vertical axes of the Nyquist curve represent the real and imaginary parts of the impedance, respectively. The Nyquist curve is usually fitted with a specific equivalent circuit to quantify the impedance information that the curve can express. Equivalent circuits are usually established through mathematical models, so there may be individual differences. One of the most typical equivalent circuit diagrams of PEMFC is shown in **Figure 2. 11**. The explanation of elements in equivalent circuits is shown in **Table 2. 4**. Elements in the equivalent circuit can be compared

with the Nyquist curve. The ohmic resistance, charge transfer, and mass transfer relate to the first intersection of the curve and the x-axis, the medium frequency loop, and the low-frequency loop, respectively. There is still no uniform conclusion about the definition of the high-frequency loop. The definition of high-frequency loop includes but is not limited to internal ohmic resistance, contact capacitance [19], distributed resistance [20], and anode charge transfer resistance [21].
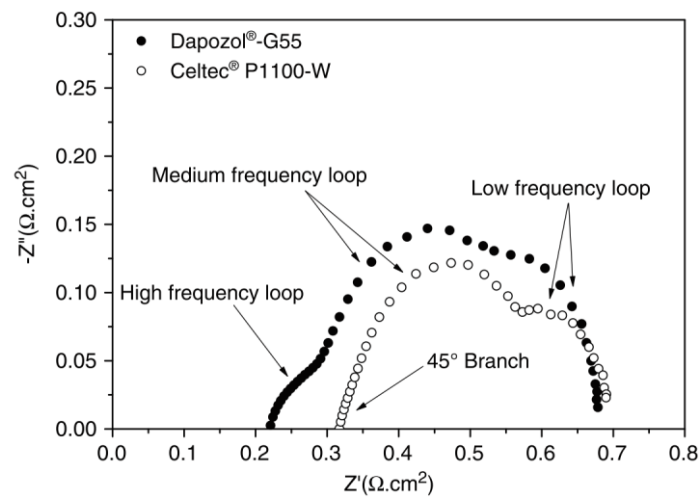
Figure 2. 10. Typical Nyquist curves of different commercial PBI membrane-based HT-PEMFC, T=160 ℃, current density = 0.2 A cm^{-2}, λ_{H_2} / λ_{Air} = 1.2/2 [17]
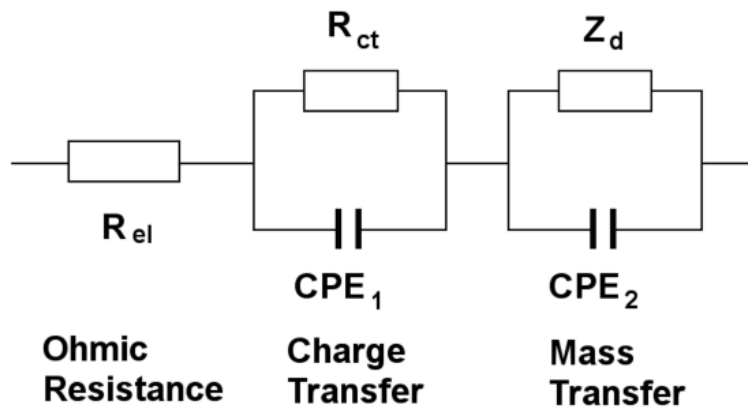
Figure 2. 11. Typical equivalent circuits of PEMFC [22].

Table 2. 4. Elements of equivalent circuits

Elements	Meaning
R_{el}	Ohmic resistance (membrane resistance) + uncompensated contact resistance (can be eliminated)
R_{ct}	Kinetic resistance (charge transfer resistance)
Z_d	Mass transfer resistance
CPE	Constant phase element

2.2.3 Cyclic Voltammetry (CV)

CV is usually used to measure the electrochemically active surface area of the PEMFC catalyst. However, in HT-PEMFC, phosphoric acid is used as the electrolyte and its fluidity may affect the measurement of CV. On the one hand, the phosphate radicals produced by the ionization of phosphoric acid leached to the surface of the catalyst are adsorbed on the surface of the catalyst to occupy its active sites [23]. On the other hand, polyphosphate or pyrophosphoric acid produced by phosphoric acid dehydration (**Equation 2- 11**) can also block the catalyst surface [24].

$$2H_3PO_4 \rightarrow H_4P_2O_7 + H_2O \text{ or } nH_3PO_4$$

$$\rightarrow H_{n+2}P_nO_{3n+1} + n - H_2O$$
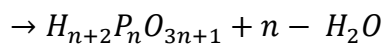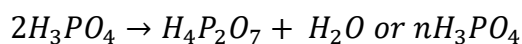
<div align="right">Equation 2- 11</div>

Therefore, the measurement of CV in HT-PEMFC is not only to explore the performance of the catalyst but also to reflect the leaching and distribution of phosphoric acid in the catalyst layer. The measurement of CV is usually carried out in the form of hydrogen stripping or carbon monoxide stripping, and hydrogen stripping is more commonly used. The hydrogen stripping method is carried out by feeding saturated nitrogen at the cathode as the working electrode and feeding the anode with hydrogen as the reference electrode and cyclic scanning

between OCV and 1V. An example of CV based on hydrogen stripping is shown in **Figure 2. 12**. The calculation of electrochemical surface area (ECSA) based on hydrogen desorption is shown in **Equation 2- 12**.

$$ECSA\left(\frac{m^2\ Pt}{g\ Pt}\right) = \frac{A_{Pt-H_2}\left(\frac{A}{V \tilde{n}cm^2}\right)}{2.1\frac{C}{m^2 Pt}\times v\left(\frac{V}{s}\right)} \times \frac{1}{L_e\left(\frac{gPt}{cm^2}\right)}$$

A_{Pt-H_2}: hydrogen desorption area

v: scan rate

L_e: Pt loading
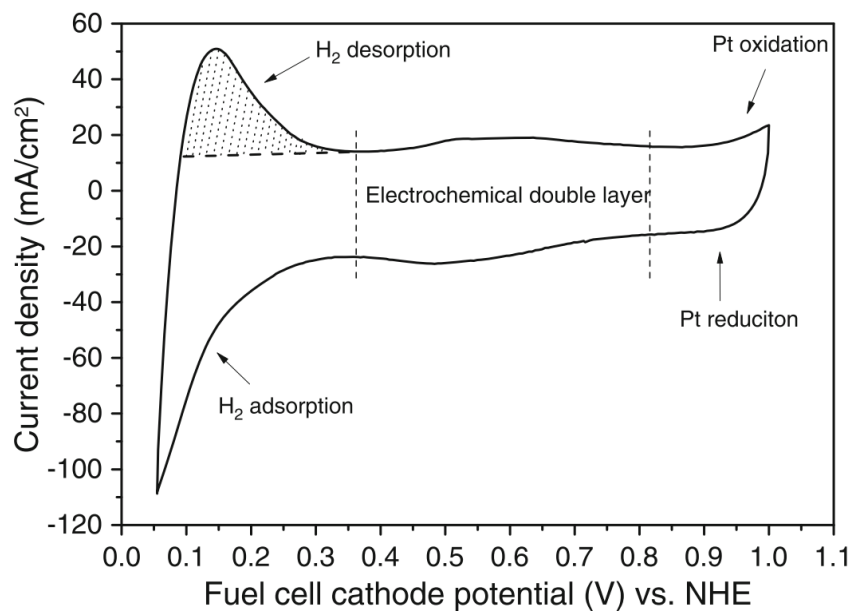
Figure 2. 12. The example of CV based on hydrogen stripping, T=160 ℃, anode: H₂=0.1 NL min⁻¹, cathode: N₂=0.1 NL min⁻¹ [17].

2.2.4 X-ray Micro-computed Tomography (CT)

X-ray CT can be used for the study of the component distribution and migration of PEMFC mostly stays on the surface, or two-dimensional level. The application of X-ray CT can realize

the imaging and quantification of the components of PEMFC on the three-dimensional level. During the X-ray CT detection process, the flow of electrons is excited from the light source to the target and partly stops abruptly after contacting the target. The energy exerted by electrons is released in the form of thermal energy and X-ray polychromatic spectrum. The remaining electron flow can pass through the object to the CCD detector and be converted into a visual signal by the scintillator to be recorded. The processing of the visual signal is based on the intensity of the beam passing through the object. The resultant intensity (I) can be calculated by **Equation 2- 12.**

$$I = I_O \exp\left[(-\mu/\rho)\rho x\right]$$

I_O: original intensity of the X-ray beam

μ: linear attenuation coefficient

ρ: density of the material

x: given distance

A 3D image can be obtained by iterating the projections obtained by continuously rotating the object. This iterative method will cause multiple projection signals to overlap and cause the image to be too bright. Filtering can solve this kind of exposure phenomenon and convert the mapping of the object into multiple 2D image volume slices and then reorganize it into a 3D tomographic image. The 3D image construction process is shown in **Figure 2. 13**.
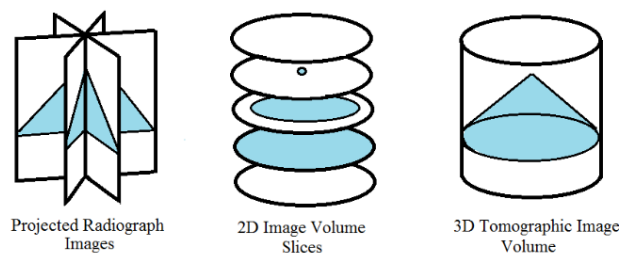
Figure 2. 13. The 3D image construction process of X-ray CT [25].

2.3 References

[1] W.S. Struve, Fundamentals of molecular spectroscopy., Wiley, 1989.

[2] J.-H. Ahn, B.H. Hong, S. Bae, H. Kim, Y. Lee, X. Xu, J.-S. Park, Y. Zheng, J. Balakrishnan, T. Lei, H. Ri Kim, Y. Il Song, Y.-J. Kim, K.S. Kim, B. Özyilmaz, S. Iijima, Roll-to-roll production of 30-inch graphene films for transparent electrodes, Nature Nanotechnology. 5 (2010) 574–578. https://doi.org/10.1038/nnano.2010.132.

[3] A.C. Ferrari, Raman spectroscopy of graphene and graphite: Disorder, electron-phonon coupling, doping and nonadiabatic effects, Solid State Communications. 143 (2007) 47–57. https://doi.org/10.1016/j.ssc.2007.03.052.

[4] Z. Ni, Y. Wang, T. Yu, Z. Shen, Raman Spectroscopy and Imaging of Graphene, Nano Res. 1 (2008) 273–291. https://doi.org/10.1007/s12274-008-8036-1.

[5] L.G. Cançado, A. Reina, J. Kong, M.S. Dresselhaus, Geometrical approach for the study of G′ band in the Raman spectrum of monolayer graphene, bilayer graphene, and bulk graphite, Physical Review B - Condensed Matter and Materials Physics. 77 (2008) 245408. https://doi.org/10.1103/PHYSREVB.77.245408/FIGURES/9/MEDIUM.

[6] Y.Y. Wang, Z.H. Ni, T. Yu, Z.X. Shen, H.M. Wang, Y.H. Wu, W. Chen, A.T.S. Wee, Raman Studies of Monolayer Graphene: The Substrate Effect, Journal of Physical Chemistry C. 112 (2008) 10637–10640. https://doi.org/10.1021/JP8008404.

[7] J.M. Englert, P. Vecera, K.C. Knirsch, R.A. Schäfer, F. Hauke, A. Hirsch, Scanning-Raman-microscopy for the statistical analysis of covalently functionalized graphene, ACS Nano. 7 (2013) 5472–5482. https://doi.org/10.1021/NN401481H/SUPPL_FILE/NN401481H_SI_001.PDF.

[8] J. Cao, P. He, M.A. Mohammed, X. Zhao, R.J. Young, B. Derby, I.A. Kinloch, R.A.W. Dryfe, Two-Step Electrochemical Intercalation and Oxidation of Graphite for the Mass Production of Graphene Oxide, Journal of the American Chemical Society. 139 (2017) 17446–17456. https://doi.org/10.1021/jacs.7b08515.

[9] E. Abouzari-Lotf, H. Ghassemi, S. Mehdipour-Ataei, A. Shockravi, Phosphonated polyimides: Enhancement of proton conductivity at high temperatures and low humidity, Journal of Membrane Science. 516 (2016) 74–82. https://doi.org/10.1016/J.MEMSCI.2016.06.009.

[10] M. Strankowski, D. Włodarczyk, Ł. Piszczyk, J. Strankowska, Polyurethane Nanocomposites Containing Reduced Graphene Oxide, FTIR, Raman, and XRD Studies, Journal of Spectroscopy. 2016 (2016). https://doi.org/10.1155/2016/7520741.

[11] D. Lin-Vien, The Handbook of infrared and raman characteristic frequencies of organic molecules, Academic Press, Boston, 1991.

[12] M.A. Hosseini, S. Malekie, N. Ebrahimi, The analysis of linear dose-responses in gamma-irradiated graphene oxide: Can FTIR analysis be considered a novel approach to examining the linear dose-responses in carbon nanostructures?, Radiation Physics and Chemistry. 176 (2020). https://doi.org/10.1016/J.RADPHYSCHEM.2020.109067.

[13] M. Acik, G. Lee, C. Mattevi, A. Pirkle, R.M. Wallace, M. Chhowalla, K. Cho, Y. Chabal, The Role of Oxygen during Thermal Reduction of Graphene Oxide Studied by Infrared Absorption Spectroscopy, J. Phys. Chem. C. 115 (2011). https://doi.org/10.1021/jp2052618.

[14] A. Bagri, C. Mattevi, M. Acik, Y.J. Chabal, M. Chhowalla, V.B. Shenoy, Structural evolution during the reduction of chemically derived graphene oxide, (2010). https://doi.org/10.1038/NCHEM.686.

[15] R. Al-Gaashani, A. Najjar, Y. Zakaria, S. Mansour, M.A. Atieh, XPS and structural studies of high quality graphene oxide and reduced graphene oxide prepared by different chemical oxidation methods, Ceramics International. 45 (2019) 14439–14448. https://doi.org/10.1016/J.CERAMINT.2019.04.165.

[16] J.F. Watts, An introduction to surface analysis by XPS and AES, Wiley, Chichester, 2002.

[17] H.A. Hjuler, D. Aili, J.O. Jensen, High temperature polymer electrolyte membrane fuel cells: Approaches, status, and perspectives, 2016. https://doi.org/10.1007/978-3-319-17082-4.

[18] F. Barbir, PEM Fuel Cells, Fuel Cell Technology. (2006) 27–51. https://doi.org/10.1007/1-84628-207-1_2.

[19] T.E. Springer, T.A. Zawodzinski, M.S. Wilson, S. Gottesfeld, Characterization of Polymer Electrolyte Fuel Cells Using AC Impedance Spectroscopy, Journal of The Electrochemical Society. 143 (1996) 587–599. https://doi.org/10.1149/1.1836485/XML.

[20] T. Romero-Castañón, L.G. Arriaga, U. Cano-Castillo, Impedance spectroscopy as a tool in the evaluation of MEA's, Journal of Power Sources. 118 (2003) 179–182. https://doi.org/10.1016/S0378-7753(03)00085-5.

[21] S.J. Andreasen, J.L. Jespersen, E. Schaltz, S.K. Kær, Characterisation and Modelling of a High Temperature PEM Fuel Cell Stack using Electrochemical Impedance Spectroscopy, Fuel Cells. 9 (2009) 463–473. https://doi.org/10.1002/FUCE.200800137.

[22] Electrochemical Impedance Spectroscopy in PEM Fuel Cells, (n.d.). https://doi.org/10.1007/978-1-84882-846-9.

[23] Q. He, X. Yang, W. Chen, S. Mukerjee, B. Koel, S. Chen, Influence of phosphate anion adsorption on the kinetics of oxygen electroreduction on low index Pt(hkl) single crystals, Physical Chemistry Chemical Physics. 12 (2010) 12544–12555. https://doi.org/10.1039/C0CP00433B.

[24] A. Orfanidi, M.K. Daletou, L. Sygellou, • Stylianos, G. Neophytides, The role of phosphoric acid in the anodic electrocatalytic layer in high temperature PEM fuel cells, (n.d.). https://doi.org/10.1007/s10800-013-0626-2.

[25] J.P. James, Micro-Computed Tomography Reconstruction and Analysis of the Porous Transport Layer in Polymer Electrolyte Membrane Fuel Cells, (2012). https://qspace.library.queensu.ca/handle/1974/7003 (accessed January 5, 2022).

3. Lab-based X-ray Micro-computed Tomography Coupled with Machine-learning Segmentation to Investigate Phosphoric Acid Leaching in High-temperature Polymer Electrolyte Fuel Cells

3.1 Manuscript Contribution

The results presented in Chapter 3 are reported in the publication "Lab-based X-ray micro-computed tomography coupled with machine-learning segmentation to investigate phosphoric acid leaching in high-temperature polymer electrolyte fuel cells, Journal of Power Sources. 509 (2021) 230347. https://doi.org/10.1016/J.JPOWSOUR.2021.230347."

My contributions in this work are as follows:

Conceptualization: Construct the overall idea of the project, propose the initial plan, and analyze the feasibility of the project.

Methodology: Prepare the membrane-electrode-assembly of the high-temperature polymer electrolyte fuel cell and test their performance and durability. Perform electrochemical characterization including electrochemical impendence spectroscopy and cyclic voltammetry. Explore the preparation method of X-ray micro-computed tomography samples. Design the sample holder for X-ray micro-computed tomography. Participate in the testing work of X-ray micro-computed tomography during the visit to Electrochemical Innovation Laboratory.

Formal analysis: Process and analyze electrochemical characterization results including polarization curves, Nyquist curves and cyclic voltammetry curves. Process X-ray micro-computed tomography data and focus primarily on slice-by-slice segmentations.

Writing-original, review and editing: Write content related to MEA preparation, performance testing, and electrochemical characterization. Final editing of the manuscript in conjunction with electrochemical characterization and the data from X-ray micro-computed tomography.

Full author list: Josh J. Bailey, Jianuo Chen, Jennifer Hack, Maria Perez-Page, Stuart M. Holmes, Dan J.L. Brett, Paul R Shearing.

Authors contribution:

Josh J. Bailey: Investigation (X-ray micro-computed tomography on high-temperature polymer electrolyte fuel cells), methodology (perform X-ray micro-computed tomography), formal analysis (machine learning), writing-original (content related to X-ray micro-computed tomography).

Jennifer Hack: Methodology (perform X-ray micro-computed tomography), formal analysis (continuous pore size distributions and tortuosity factor analysis)

Maria Perez-Page: Writing- review and editing.

Stuart M. Holmes: Writing- review and editing, supervision.

Dan J.L. Brett: Writing- review and editing, supervision.

Paul R Shearing: Writing- review and editing, supervision.

Lab-based X-ray Micro-computed Tomography Coupled with Machine-learning Segmentation to Investigate Phosphoric Acid Leaching in High-temperature Polymer Electrolyte Fuel Cells

Josh J. Bailey [a,b], Jianuo Chen [c], Jennifer Hack [a], Maria Perez-Page [c], Stuart M. Holmes [c], Dan J.L. Brett [a], Paul R Shearing [a,*]

[a] Electrochemical Innovation Laboratory, Department of Chemical Engineering, University College London, WC1E 7JE, United Kingdom

[b] School of Chemistry and Chemical Engineering, Queen's University Belfast, Belfast, BT7 1NN, United Kingdom

[c] School of Chemical Engineering and Analytical Science, The University of Manchester, M13 9PL, United Kingdom

*Corresponding author: p.shearing@ucl.ac.uk; +44 (0)20 7679 3783

3.2 Abstract

A machine-learning-based approach is used to segment 14 X-ray computed-tomography datasets acquired by lab-based scanning of laser-milled, high-temperature polymer electrolyte fuel cell samples mounted in a 3D-printed sample holder. Two modes of operation, one with constant current load and the other with current cycling, are explored and their impact on microstructural change is correlated with electrochemical performance degradation. Constant-current testing shows the overall quantity of phosphoric acid in the gas diffusion layers is effectively unchanged between 50 and 100 hours of operation but that inter-electrode distribution becomes less uniform. Current-cycling tests reveal similar quantities of phosphoric acid but a different intra-electrode distribution. Membrane swelling appears more pronounced after current-cycling tests and in both cases, significant catalyst layer migration is observed. The present analysis provides a lab-based approach to monitoring microstructural degradation in high-temperature polymer electrolyte fuel cells and provides a more accessible and more statistically robust platform for assessing the impact of phosphoric acid mitigation strategies.

3.3 Keywords

High-temperature polymer electrolyte fuel cell; Phosphoric acid leaching; X-ray micro-computed tomography; Machine-learning segmentation; Accelerated stress testing.

3.4 Introduction

High-temperature proton exchange membrane fuel cells (HT-PEMFC) are typically composed of polybenzimidazole (PBI) membranes doped with phosphoric acid (PA) [1], wherein the polymer backbone provides mechanical integrity, and the acid endows the membrane electrode assembly (MEA) with relatively high proton conductivity (>0.1 S.cm^{-1}) at elevated operating temperatures (150-200 °C) [2]. Compared with their low-temperature polymer electrolyte membrane fuel cell (LT-PEMFC) analogues, typically containing hydrated perfluorosulphonic acid (often, Nafion) membranes, HT-PEMFCs are not limited to being run at 80 °C (ambient pressure) as they do not need to retain water in liquid form to be suitably hydrated for their ionic conductivity. Along with mitigating water management issues, the higher operating temperature of HT-PEMFCs also suppresses the impact of fuel impurities; where LT-PEFCs are constrained mostly to running on only pure hydrogen streams, HT-PEMFC systems have been developed with much greater CO tolerance [3]. Although the oxygen reduction reaction at the cathode is hindered by the presence of phosphate anions at the Pt catalyst surface [4][5], HT-PEMFCs have a lower sensitivity to the sorts of contaminants found in steam reformates (H_2S as well as CO), this opens up the opportunity for combined heat and power or auxiliary power unit applications [2]. Moreover, at these higher temperatures, the electrochemical reaction kinetics are improved versus their LT-PEFCs as exchange current density increases exponentially with temperature [6].

For sufficient proton conductivity, both in the membrane and in the catalyst layers (CL), a large concentration of PA is required [7]. Although it has been shown that the maximum protonation degree of PBI by PA is reached with a doping level of 2 acid molecules per repeat unit[8], often acid doping levels of up to 6-16 are realized [9][10][11], leading to a majority of acid molecules being free and highly mobile. This encourages high proton conductivity (pure H_3PO_4 has a conductivity of around 0.650 S.cm^{-1}) [12] but can impede electrode reactions if the phosphate

anion adsorbs at the active sites, and/or it increases mass transfer losses if gas permeation is made more difficult [7]. It has been shown that PA distribution is effectively independent of how it is introduced, but that its quantity influences the achievable performance of the HT-PEMFC MEA [7].

For many years, PA redistribution was investigated by cell-averaged methods, such as by post-mortem analysis [7][13] or electrochemical techniques [7][14][15][16][17][18]. Recently, further insight has been provided by synchrotron X-ray radiographic imaging, in both in-plane [19][20][21][22] and through-plane [23] modes. In-plane X-ray radiography identified reversible membrane swelling upon current draw [19][20][22] and attributed increased transmission in the membrane to the dilution of PA by product water [19][20][22] or crossover processes [20][22]. Through-plane studies suggested that chemical conversion of PA was accompanied by a redistribution of its derivatives as dilution alone would not explain the transmission differences observed. The work revealed heterogeneity in PA distribution after operation above 0.35 A.cm^{-2}, with transmission changes greater under flow-field channels than under ribs [23]. Unfortunately, in this work, it was not possible to identify if these changes originated from PA redistribution or inhomogeneous membrane swelling, highlighting the drawback common to all the radiographic investigations - the lack of the third dimension.

X-ray computed tomography (CT) involves the acquisition of radiographic projections that are collected by incrementally rotating samples, positioned between a source and detector, through regularly spaced angles. The full set of projections are processed using mathematical back-projection algorithms to give a three-dimensional reconstruction of the X-ray attenuation coefficient distribution within the sample. Eberhardt *et al.* demonstrated the first tomographic investigation of HT-PEMFCs, developing grayscale-concentration calibration curves for quantifying PA in the gas diffusion layer (GDL), CL and membrane [24]. The work compared MEAs immersed in known concentrations of PA, correlating local grayscale to bulk PA

concentration and its concentration in "PA + C" mixtures, whose grayscale peaks overlapped in the image histograms for all concentrations. The authors conceded that at low PA concentrations, PA and "PA + C" peaks were not separable, such that PA volume in the GDL of wet samples was estimated by a slice-by-slice subtraction method versus the GDL of a different dry sample. All images were of non-operated components at room temperature, thus the quantities of PA in the GDLs were not representative of real operation. Follow-up *operando* studies targeted PA re-distribution under dynamic load conditions [25], monitoring PA distribution in the anode GDL as a function of current density. Increasing current density from 0.2 to 0.8 A.cm^{-2} coincided with PA flowing into the anode GDL, and a continuous path of PA between membrane and flow-field was observed after 15 min. GDL and flow-field immediately lost PA upon lowering the current, implying an inverse process at play. The original condition was not re-established, with some PA lost from the electrolyte reservoir, potentially contributing to long-term degradation. "Electrochemical pumping", similar to that in phosphoric acid fuel cells [26], was reported to be behind PA migration from cathode to anode, resultant from $H_2PO_4^-$ migration in this direction. The average increase in grayscale on the anode side, with a small decrease on the cathode, is consistent with the pumping mechanism, but the increase in grayscale value (greater absorption) in the membrane was counter to the behaviour in prior radiographic studies [19][21][20][22].

Recently, Halter *et al.* investigated PA leaching over two current cycles, linking PA content to mass transport losses, approximating flooding times and highlighting CL cracks as the determining factor for PA egress from the membrane [27], as supported by work by Chevalier *et al.*[28]. The latter work used synchrotron X-ray CT to produce inputs for a pore network model (PNM) [29], combining with an invasion percolation algorithm [30] to predict PA mass and invasion patterns, matching well to experiment [7]. However, only one sample with an unrealistically thick CL was studied.

Although synchrotron experiments have revealed important insights into PA (re-) distribution, beamtime access is limited, time constraints mean that only a few samples are investigated in each study, and the high flux risks radiation damage to membranes. Fortunately, the recent application of lab-based X-ray micro-CT in materials science [31], among other fields [32][33], has allowed for approaches to imaging HT-PEMFC in a more accessible fashion, albeit with polychromatic radiation and lower flux. An early example investigated CL morphologies from different fabrication routes but without information on PA distribution [34]. Schonvogel *et al.* explored the use of accelerated stress tests (AST), one of which was used in this work (0.6 to 1.0 A cm^{-2} cycling), but their X-ray micro-CT images were simply used to identify CL crack, without any segmentation of the acquired tomograms, nor comprehensive analysis of the MEA in three dimensions [35]. More recent work by Halter *et al.* used PA injection methods, which rely on subtractive imaging ("dry" subtracted from "wet" images), to investigate the influence of PA concentration and temperature on the wetting behaviour of PA on GDL materials by capillary pressure and contact angle measurements [36], quantifying the capillary pressure required to see PA breakthrough the entire gas diffusion electrode (GDE), albeit for their specific materials selection and not from PA introduced into the GDE *in-situ*. A follow-up *operando* study of PA migration in HT-PEMFCs with two different CL morphologies correlated their previous *ex-situ* injection work with real *operando* performance [37], showing that even at the low current densities of 0.2 A.cm^{-2}, PA is present in CL cracks, but increases significantly at higher current densities of 0.8 A.cm^{-2}.

The focus of the present study is on improving the implementation of accessible, lab-based X-ray micro-CT in the study of HT-PEMFCs, with a focus on monitoring PA migration. The investigations make use of the AST procedure introduced recently [35], wherein load cycling between 0.6 and 1.0 A.cm^{-2} is used to accelerate PA leaching and allow for semi-quantitative determinations to be made from high-resolution, segmentable tomograms. Emphasis is placed

on increasing the statistical robustness of X-ray lab-based CT, leveraging its greater longitudinal availability versus the synchrotron, as well as mitigating poorer contrast by acquiring tomograms from several replicates with optimised scanning parameters. The results indicate that the AST used is sufficient to bring about PA migration that can be reliably identified by lab-based micro-CT and paves the way for lab-based investigations of PA leaching mitigations in state-of-the-art HT-PEMFC microstructures.

3.5 Materials and Methods

3.5.1 HT-PEMFC

Materials

The samples were fabricated by coating two commercial GDLs with in-house prepared MPLs and CLs, before hot-pressing around a PA-doped commercial PBI membrane. The GDL used was a 280-µm-thick carbon paper (TGPH 090, Toray) containing 5 wt% polytetrafluoroethylene (PTFE). The MPL ink constituted 90 wt% Ketjen black (EC-300J, AkzoNobel) and 10 wt% PTFE (Sigma Aldrich) in iso-propanol (IPA), giving a Ketjen black MPL loading of 1 mg.cm^{-2}. The CL ink was prepared by blending 80 wt% Pt/C catalyst (60% Pt loading, Fisher Scientific) and 20 wt% PTFE in a 2:3 mixture of de-ionized water and IPA. The 30-µm-thick PBI membrane (Fumapem® AP-30, Fumatech) was doped with PA by immersing in 85 wt% orthophosphoric acid (PA, Fisher Scientific) at 140 °C for 6 h. The doped membranes were vacuum-dried at 80 °C for 3 h to remove moisture and calculate the acid doping level (ADL). The ADL was calculated according to **Equation 3- 1**.

$$ADL = \frac{W_{PA}}{M_{PA}} / \frac{W_{PBI}}{M_{PBI}}$$

<div align="right">Equation 3- 1</div>

where W_{PA} and W_{PBI} are the wt% content of PA and PBI, respectively, and M_{PA} and M_{PBI} are the molar mass of PA and the polymer repeat unit, respectively. For all membranes, the ADL

was approximately 11.5, representative of other literature preparations [9][10][11].

Assembly

The MPL was spray-coated onto each GDL using nitrogen, and the solvent removed by heating at 120 °C for 10 s between each coat, after which each MPL-coated GDL was sintered at 300 °C for 3 h. Subsequently, the CL ink was sprayed on the MPL, and the solvent similarly removed, giving a final CL loading of 1 $mg_{Pt}.cm^{-2}$. The samples were assembled by sandwiching the membrane between GDEs, using 150-μm-thick PTFE gaskets, hot-pressing the assembly at 140 °C for 270 s, with a constant pressure of 80 psi. The electrodes were square with an active area of 225 mm^2 in all cases.

Electrochemical methods

The hot-pressed samples were assembled into a single-cell 4 x 4 cm^2 test rig, designed in-house, compressed with 0.5 N.m torque and operated at 150 °C. Polarisation curves were collected, and electrochemical impedance spectroscopy (EIS) was performed for Sample Sets A and B, with the addition of cyclic voltammetry (CV) for Sample Set B. Using a potentiostat (E5000, Gamry), polarisation curves and EIS measurements were collected with 100 $mL.min^{-1}$ of dry hydrogen on the anode and dry oxygen on the cathode, and CV used 33.4 $mL.min^{-1}$ dry hydrogen on the anode and 140 $mL.min^{-1}$ dry nitrogen on the cathode. The cathode of each MEA served as the working electrode, where the anode served as the counter and reference electrode in a typical 2-electrode set-up.

Once the open-circuit voltage (OCV) stabilised, ten polarisation curves were collected by discharging from OCV to 0.1 V in 0.1 A steps with 5 s dwell time, and the final polarisation curve taken as the steady-state condition. Galvanostatic EIS was performed at 0.5 A (0.22 $A.cm^{-2}$) across a frequency range of 10,000 to 0.1 Hz, with a perturbation current of 10 mA. CV was performed between 0.05 and 0.5 V with a scan rate of 100 $mV.s^{-1}$ and the hydrogen

desorption curve used to calculate the electrochemical surface area (ECSA) of the catalyst on the working electrode side using **Equation 3- 2**.

$$\text{ECSA}(cm^2{}_{Pt}/g_{Pt}) = \text{Charge}(\mu C.cm^{-2})/[210(\mu C.cm^{-2}{}_{Pt}) \times \text{Catalyst Loading}(g_{Pt}.cm^{-2})$$

<div align="right">Equation 3- 2</div>

Sample Set A underwent lifetime testing by running each cell at constant current, at the value associated with an initial voltage of ~0.6 V, for up to 100 h. A single cell was characterised immediately after hot-pressing, again after 50 h of operation, and finally after having operated for 100 h in total. X-ray CT characterisation was carried out for identically fabricated cells after 0, 50 and 100 h of operation. Sample Set B underwent accelerated stress testing (AST) which consisted of repeated chronopotentiometry – 4-minute operation at 0.6 A.cm^{-2} followed by 16-minute operation at 1.0 A.cm^{-2}, for a total of 6 h [35]. The cells were held at OCV for ten minutes between each cycle, and the cycle repeated a total of 11 times, such that the entire testing regime lasted approximately 70 h. X-ray CT characterisation was carried out on identically prepared pristine samples and the AST samples.

3.5.2 X-ray micro-CT

Sample preparation

A laser micro-machining tool (A Series/Compact System, Oxford Lasers) was used to mill multiple circular discs of either 1.5 or 2 mm from the active area at ~0.8 W and at a scan speed of ~ 1 mm s^{-1}, and 2-3 iterations. This size was chosen as a balance between improved signal-to-noise for a given exposure time and the need for a representative volume[38][39]. To ensure laser milling did not affect the sample discs more than mechanical cleavage, similar half-cell samples were prepared; a laser-milled and a mechanically hole-punched disc, each 1.5 mm in diameter, both immersed in 85 wt% PA at room temperature for 10 s. Volume renderings and XZ-orthoslices are shown in **Figure S3. 1** for comparison, illustrating that the

delicate microstructure is in fact more deformed by mechanical cleavage than by laser micro-machining. Sub-volumes (0.16 mm^3) from the two GDLs gave similar porosities (54% and 49% for mechanical and laser, respectively), indicating a similar PA content in both.

To improve the statistical robustness of the resulting tomographic analysis, a procedure for scanning multiple subsamples from each sample MEA was developed. An in-house sample holder (jig), compatible with the X-ray CT instrument's sample stage, was designed in SolidWorks (Dassault Systèmes), 3D-printed using a Form 3 (Formlabs) 3D printer, and each disc was individually placed into the recess of one jig part, before building into a stack and securing within the X-ray CT sample holder chuck. For Sample Set A, the samples were cut out completely before being placed in jig parts; in the process, the 'anode side' and 'cathode side' information for the operated samples was lost. However, for Sample Set B, two rather than three iterations of milling were used to leave the discs just intact such that each could be gently coaxed into the recess from the bulk MEA, retaining the 'anode side' facing upwards for all samples. CAD and optical images of the 3D-printed jig are shown in **Figure S3. 2**. The advantage of this design is that acquisition for multiple samples (5-10) can be set up all at once in a multi-recipe scan, utilising overnight periods, despite scan times of only 2-4 hours per sample.

Image Acquisition

An X-ray micro-CT instrument (Zeiss Xradia 520 Versa, Carl Zeiss) was used for all scanning in this study, equipped with a polychromatic source with a tube voltage range of 30-160 kV. A 4× objective was chosen to give ~1 µm voxel dimension with a ca. 2 mm field-of-view at reasonable source-to-sample and sample-to-detector distances. Preliminary scanning was conducted to evaluate the degree to which PA could be discerned from other materials, hence "half cells" (GDL/MPL/CL) were fabricated and scanned both "dry" (pristine) and "wet" (85

wt% PA).
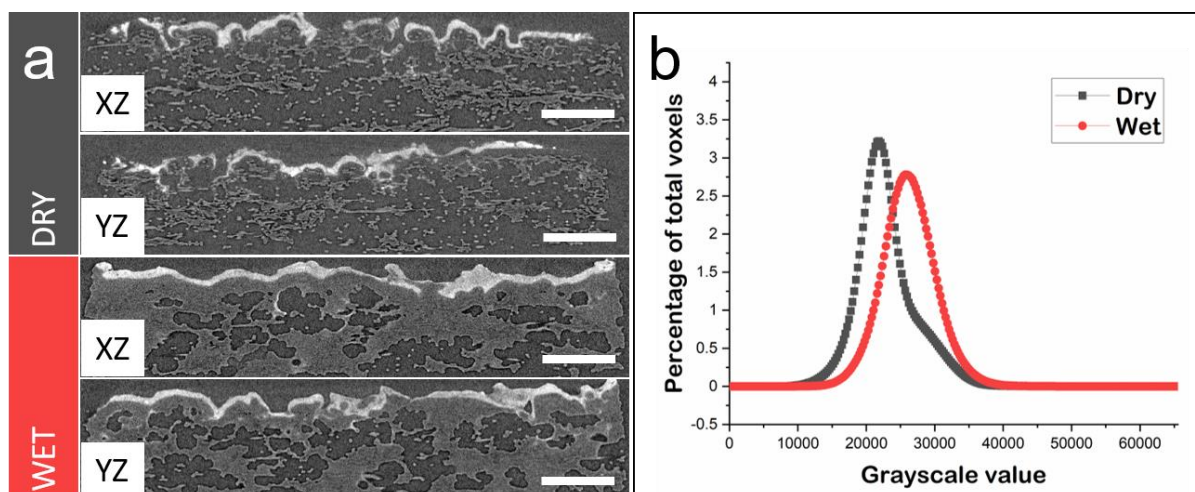
Figure 3. 1.(a) XZ- and YZ-orthoslices of dry and wet "half-cells" comprising GDL, MPL and CL. (b) Histogram comparison between sub-volumes taken from the GDL of each volume. All scalebars denote 200 µm.

Figure 3. 1a shows two-dimensional slices (orthoslices) from X-ray CT tomograms of half-cells imaged in "dry" and "wet" (laser-milled disc shown in **Figure S3. 1**) states. Previously, synchrotron tomographic imaging with a monochromatic 20 kV beam was shown to give distinguishable peaks for carbon fibres and binder in dry samples, but not in wet samples saturated with low concentration PA [24]. **Figure 3. 1**b shows a similar trend is observed where a higher grayscale shoulder in the dry sample is obscured in the wet sample where the presence of PA effectively renders the fibres, binder and PA one phase. It should be noted that this is the case even at relatively high PA concentration (~85 wt%) as here a lab-based polychromatic X-ray beam with a peak energy of 80 kV (as used in previous studies[35],[40]) has been used. Lower peak energies were selected for further scanning, a trade-off between improving contrast and retaining adequate flux for sufficient signal-to-noise ratio. X-ray acquisition parameters used in this study are shown in **Table S3. 1**, the key differences being highlighted in **Table 3. 1**.

Table 3. 1. Key X-ray CT acquisition parameters used in this study.

Sample Set	X-ray voltage (kV)	Voxel size (μm)	Exposure time (s)	Projection Number	Scan time per sample (h)
Half-cells	80	1.09	8	801	1.8
A	60	0.95	14	1101	4.3
B (Pristine)	40	1.01	25	401	2.8
B (AST)	50	1.01	25	501	3.5

For Sample Set A, the X-ray parameters were internally consistent, but the X-ray energy was lowered between the sets to improve contrast and consequently, the exposure time was increased to retain good signal-to-noise. The Sample Set B pristine (0 h) samples were scanned with low energy of 40 kV and minimal projections, both of which were increased slightly for AST samples to improve data quality, retaining the same voxel dimension. Generally, the number of projections was lowered versus the half-cell scans to facilitate shorter scans, whilst retaining adequate image quality. Slightly larger diameter discs (2.0 versus 1.5 mm) were used to ensure that all replicates had the "anode side" facing upwards as this was practically more difficult with smaller discs. Therefore, the optimised parameters allow for seven to eight scans of 2-mm-diameter HT-PEMFC discs with sufficient data quality for segmentation, within a 24 h period.

Data Processing

Each set of collected radiographs was reconstructed using a proprietary version of the Feldkamp-Davis-Kress (FDK) cone-beam algorithm [41] in XMReconstructor (Carl Zeiss). Each tomogram was processed in the same way to minimise variation: the data was transformed to be planar and cropped to produce cuboidal volumes. 3D renderings of these tomograms are shown in **Figure 3. 2**. From the series of tomograms comprising each sample set, the largest cuboidal sub-volume was extracted that avoided the inclusion of air external to the cylindrical sample; for Sample Set A this was $1070 \times 1070 \times 525$ voxels (0.533 mm^3), for Sample Set B

this was either $1013 \times 1013 \times 507$ voxels (Pristine) or $1015 \times 1015 \times 508$ voxels (AST) (both also 0.533 mm^3). XZ- orthoslices from each of the subvolume tomograms from Sample Set A and Sample Set B are shown in **Figure S3. 3** and **Figure S3. 4**, respectively. Each tomogram was filtered twice, first with a 3D non-local means filter (search window=10 pixels; local neighbourhood=3 pixels) which dramatically reduced the noise. Secondly, to enhance the feature edges, a 3D unsharp masking filter (edge size=9 pixels; edge contrast=0.9) was applied.

To perform segmentations in a robust and time-efficient manner, particularly given the high number of tomograms involved, segmentation was performed using a two-stage, semi-automated approach, harnessing the power of machine-learning based segmentation (using freeware, Ilastik [42]) to perform the majority of voxel allocation, combined with a localised approach (performed in Avizo [43]) for membrane identification, phase separation and final adjustments. In the first stage, the machine-learning step achieves a ternary segmentation: high grayscale is allocated to the CL, low grayscale is allocated to Pore, and intermediate grayscales are allocated to a combined GDL/MPL/Membrane (and PA where applicable) phase. Subsequently, a localised procedure is used to segment Membrane from the other phases, as it is indistinguishable in grayscale value at 40-60 keV, and the resultant segmented volume was further divided into anode and cathode sides for Sample Set B, with *a priori* knowledge. An example of raw, filtered and segmented orthoslices from a single Sample Set A tomogram is shown in **Figure S3. 5**.
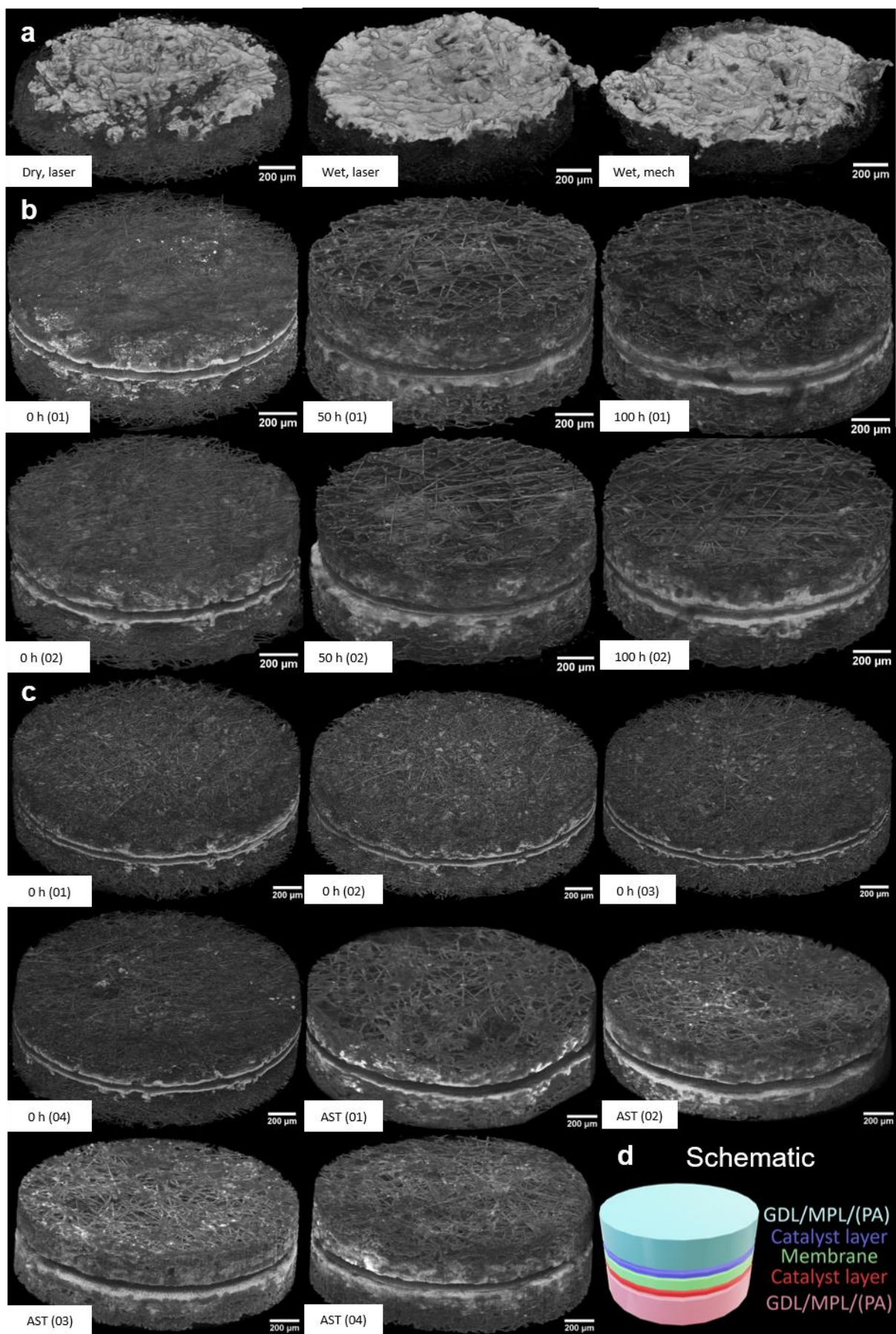
Figure 3. 2. Volume renderings of processed tomograms from (a) half-cell tests and (b) lifetime tests on Sample Set A; c) AST tests on Sample Set B; d) Schematic illustrating the different layers of all samples.

The processed volumes are imported into Ilastik as 2D TIFF stacks, selecting all pre-defined "features" (convolutional kernels) [42], and performing an initial user training by manually "painting" a small portion of the central slice in the *XZ*-direction. An initial machine-learning segmentation is computed and displayed, which allows the user to interact with the result to suggest further refinements before an updated segmentation is proposed. The initial training input, initial suggested segmentation, additional training and updated segmentation for the same central slice of a single tomogram is shown in **Figure S3. 6** as an illustration. Additional interaction by the user can be carried out on additional slices any orientation, specifically targeting areas of high uncertainty and regions that appear under or over-segmented from the first pass. For Sample Set A, training was undertaken on the central *XZ*-slice (20 min), and additions were made on the same slice (20 min) and a slice in the other directions (10 mins each) to give a result within one hour of interacting with the data. For Sample Set B, despite lower signal-to-noise ratio, only 30 min was required to provide a similarly visually acceptable segmentation.

Stage two consisted of importing the output from Ilastik, along with the raw image, into Avizo and manually segmenting the membrane from the GDL, since the membrane is spatially separate from the other features but possesses similar grayscale. This segmentation was achieved by first using the outer edge of the pre-segmented CL to create a "Mask" phase. The combination of this phase and CL acted as an effective barrier, such that voxels with the grayscale values selected for segmentation using the "Magic Wand" tool would remain within the boundary of the "Mask+CL" region. The "Magic Wand" was used to select many narrow grayscale regions, which slowly built up the membrane phase. Finally, interpolation between slices, in either the *xz-* or *yz*-planes, was performed to fill any gaps, and the final segmentation was manually adjusted to smooth the membrane edges. Attempting a quaternary segmentation with the machine-learning approach proved problematic, leading to an under- or over-

segmentation of GDL. Once this two-stage segmentation was complete, the two sides of the membrane were labelled separately, and final adjustments made to amend any major residual misallocations by manual re-allocation.

Data Analysis

Phase fraction calculations were computed in Avizo by simple voxel counting, and represent a proportion of the total volume, unless otherwise stated. The phase fraction for unoperated samples represents the carbonaceous phases that constitute the GDL and MPL, whereas the analogous phase fraction for operated samples represents these phases plus migrated PA. Clear distinction of PA from the carbonaceous phases was not possible with a polychromatic (40-60 keV) X-ray beam, and comparisons were drawn across samples, both for bulk and slice-by-slice analysis. It is worth noting that no lab-based system has yet shown sufficient contrast for direct segmentation and instead, complex *operando* set-ups have been required in order to subtract "dry" from "wet" images [27][44]. Here, we leverage the multi-sample, high-throughput procedure to provide statistically more robust estimates of PA distribution as a function of fuel cell operation. Volume-specific surface areas (VSSA) are calculated by producing surfaces from the voxel reconstructions and dividing the summated area by the total volume of that specific phase.

To probe PA penetration into the GDL, a slice-by-slice (Z-direction) analysis was undertaken for all volumes. As PA penetrated deep into the GDL, and to avoid the uncertainty caused by variations in MPL phase fraction, the first and last 150 slices were also used to calculate average phase fractions for pore and GDL(/PA) for comparisons between unoperated and operated cells in the "strictly GDL region". Measurements of membrane thicknesses were performed by taking the full-width at half-maximum (FWHM) approach to the central peak, and inter-CL distances were peak-to-peak maxima distances. To characterise the pore domain,

tortuosity factor in the z-direction (τ_z) and continuous pore size distributions (cPSD) calculations were performed in TauFactor [45] and ImageJ, respectively. Tortuosity factor (τ) in this formulation is defined in **Equation 3- 1**:

$$D^{eff} = D \, \frac{\varepsilon}{\tau}$$

Where ε is the porosity in this study, D is the intrinsic diffusivity of whichever gas is flowing in the pores, and D^{eff} is the effective diffusivity given by the presence of the solid phase. cPSD calculations follow an algorithm developed by Münch *et al.* that involves the determination of the amount of pore volume that can be filled with spheres of given radius, characterising a continuous pore volume as if it were composed of a distribution of these spheres. The reader is referred to [46] for more detail and a mathematical description of the algorithm.

Given both the greater solid density in the MPL region and its almost complete filling in operated samples, GDL regions were selected by choosing an appropriate slice number from the slice-by-slice analysis of each dataset. For the pristine samples, this value was taken at the elbow-point of the CL, where there was a noticeable change in CL "area", typically ~200 slices (**Figure 3. 5**). For the aged samples, because of the greater intrusion of the PA into the pores, values were chosen where the GDL/MPL (PA) phase fraction equaled the pore phase, typically ~150 slices. This ensured that the complete flooding of pores near the CL did not distort the values for pore size and tortuosity of the GDL/MPL. Importantly, attempts to quantify τ_z through entire GDEs often gave very high or even infinite values due to low or no percolation at the imaged resolution such that focus was given to residual percolated volumes after PA leaching. After extraction of the subvolumes from both the top and bottom of each sample, the datasets were binarized to form "solid" and "pore" phases, before application of the tortuosity factor and cPSD procedures. Where "± errors" are reported, the standard error of the mean is given, equivalent to the sample standard deviation divided by the square root of the number of

measurements made.

3.6 Results and Discussion

3.6.1 Sample Set A

100 h of operation at constant current was monitored by taking voltage readings throughout, measuring polarisation curves at 0, 50 and 100 h, and performing EIS before and after operation (**Figure 3. 3**). **Figure 3. 3**a clearly shows that operating at a fixed current density is accompanied by significant degradation (20 mV between 20 h and 100 h) within a relatively short duration, which is equivalent to 10% voltage loss in less than 250 h (where the current US DoE target is 5000 h [47]). This early-stage degradation corresponds to a loss of ca. 200 μV.h^{-1} which is an order of magnitude greater than previous durability studies [48][49]. This may be because the cell in this work is considerably smaller than those examined in the literature such that detrimental edge effects may be enhanced. Additionally, the tests presented here are shorter term (100 h versus 800-1000 h in the literature), such that a plateau in voltage after 100 h would imply an over-estimation of degradation. Finally, and potentially most importantly, the doping procedure (85 wt% orthophosphoric acid at 140 °C for 6 h) and level (ADL = 11.5) were specifically chosen to exacerbate PA leaching for electrochemical and microstructural analysis, rather than using a polyphosphoric route [48] shown to give improved physicochemical properties [50] or a lower doping level (e.g. ADL = 3.5 [49]). The polarisation curves display the same trend, with maximum current densities of 407 mW.cm^{-2} at 0 h, 390 mW.cm^{-2} at 50 h and 365 mW.cm^{-2} at 100 h (average -0.4 mW cm^{-2} h^{-1}). The complex plane plot in **Figure 3. 3**c illustrates that the ohmic contribution to impedance is approximately unaffected by operation, but that there is an appreciable increase from 0.31 to 0.35 Ω.cm^2 (~13%) in the sum of charge transfer resistance and mass transfer resistance, also evident at low and high current densities, respectively, in the polarisation curves shown in **Figure 3. 3**b. Attributing losses specifically to either or both of the anode and cathode is beyond the scope

of this work.

Figure 3. 3. Electrochemical data pertaining to Sample Set A, (a) Voltage-time plot for the duration of operation; (b) Polarisation curves (black) and power density curves (red) for 0 h (line), 50 h (dashed) and 100 h (dotted); (c) Complex plane plots for 0 and 100 h.

A single *XZ*-orthoslice from filtered and segmented tomograms for each sample is shown in **Figure 3. 4**. The defined fibrous structure of the GDL is evident in both 0-h-samples (**Figure 3. 4** a,c), attributable to a lack of observable PA in any of the micron-sized pores. Although hot-pressing can lead to a small quantity of PA escaping the MEA, the porous microstructure of the GDL-MPL layers is still visibly empty. This is not the case in either the 50- or 100-h-samples, where significant quantities of PA have migrated into the porous microstructure, in both cases partially but appreciably filling the MPL and GDL layers.

Figure 3. 4. X-ray CT data pertaining to Sample Set A: Filtered XZ-orthoslices from (a), (c) 0 h tomograms; (e), (g) 50 h tomograms; i), k) 100 h tomograms; Corresponding segmented XZ-orthoslices from b, d) 0 h tomograms; f, h) 50 h tomograms; j, l) 100 h tomograms.

From the segmented datasets, phase fractions are calculated for seven phases - three phases for top and bottom (CL, Pore, and combined GDL-MPL – and PA where applicable) plus the membrane. PA cannot be reliably segmented from the GDL, but bulk phase fractions from operated and unoperated samples, shown in **Table 3. 2** and **Figure S3. 7**, provide an estimate of the leached PA, with the full global phase fraction results shown in **Table S3. 2**. In 0-h-samples, the GDL/MPL phase accounts for 14-15% of the total volume, consistent for both sides and samples, providing a baseline against which to compare operated samples. Notably, the VSSA was 0.33 & 0.31 μm^{-1} and 0.34 & 0.33 μm^{-1} for the top & bottom of 0 h (01) and 0 h (02), respectively; this high level of similarity representing successful segmentation that captures the same morphology of material, regardless of side or sample. In both the 50-h-samples and 100-h-samples, there is a significant increase in this phase fraction, due to PA leaching. For 50-h-samples, the average GDL/MPL/PA phase fraction increases to 24% and 28% for the top and bottom, respectively, which represents an average sample increase of $11.2 \pm 1.6\%$ by volume (~0.06 mm^3 in absolute terms) at one electrode. Similarly, for 100-h-samples, the same phase fraction shows an increment of $10.0 \pm 2.4\%$ by volume (~0.05 mm^3) versus 0-h-samples, although there is greater variation in the replicates compared with the 50-h-case (26% and 24% versus 26% and 26% for the 100-h- and 50-h-cases, respectively). The results of an analysis of the first and last 150 slices (GDL only) are shown in **Table S3. 3**. The average phase fraction when excluding the MPL region increases from 0.30 (0 h) to 0.55 (50 and 100 h), equating to a concomitant filling of ~35% and 40% for 50 h and 100 h (due to a small difference in CL distribution). Both the full electrode and GDL-only analysis imply that between 0 and 50 h, a substantial amount of PA egresses from the membrane and CL into the pore space of the GDL/MPL, consistent with literature that suggests GDL flooding reaches a steady-state in just a few hours [25]. Although this quantity does not increase substantially in the following 50 h, the data suggests an increasing heterogeneity in PA distribution with time,

such that the impact of longer-term testing on PA distribution requires further investigation.

Table 3. 2. Global GDL/MPL/(PA) phase fraction for each sample and comparisons versus the pristine state.

Electrode	GDL/MPL/(PA) Phase fraction				
	0 h Mean	50 h Mean	100 h Mean	50 h vs 0h	100 h vs 0h
Top	15.3%	23.7%	28.7%	8.4%	13.4%
Bottom	14.0%	28.0%	20.6%	14.0%	6.7%
Mean	14.6 ± 0.4%	25.8 ± 1.5%	24.7 ± 2.4%	11.2 ± 1.6%	10.0% ± 2.4%

To inspect the degree of PA egress, slice-by-slice analysis was conducted (**Figure 3. 5**), plotting each phase's area fraction from the bottom (Layer 1) to the top (Layer 535). Note that each layer is ~0.95 µm thick. First, it is observed that the membrane thickness (FWHM) increases a little with operation time, from ~45-48 µm (0 h, **Figure 3. 5** a,b), to ~49-51 µm (50 h, **Figure 3. 5** c,d), to ~52-56 µm (100 h, **Figure 3. 5** e,f), although these small increments with only duplicate data require further investigation to confirm. The CL areal fraction peak tends to move further from the membrane with operation time, and an increased overall magnitude and greater magnitude in each curve's "tail" is observed, depicting increasing penetration of Pt into the GDL with operation. Of course, there is no physical reason to suspect that the true quantity of Pt increases as a function of operating time; instead, the bulk phase fraction increase is an artefact of the fact that even small quantities of very electron-dense Pt appear appreciably bright in the tomograms to be allocated as such. Thus, Pt migration that is not complete but involves migratory and residual metal yields an effective increase in measured CL phase fraction. It is also observed that the CL peaks after 100 h are taller and narrower, suggestive of inner Pt that is close to the membrane migrating outwards to amass at the newly established interface, as well as Pt migration into the GDE, although this requires more experimentation to confirm. Overall, the observed Pt migration may explain the greater activation losses seen in the operated cells' polarization curves in **Figure 3. 3**b. Membrane thickness and inter-CL distance data are given in **Table S3. 3**.

Figure 3. 5. Slice-by-slice plots for Sample Set A, showing the area fraction for each of the seven phases from the bottom (Layer 1) to the top (Layer 535) for (a) 0 h (01); (b) 0 h (02); (c) 50 h (01); (d) 50 h (02); (e) 100 h (01); (f) 100 h (02).

Importantly, the curves pertaining to the GDL/MPL phase (0 h, **Figure 3. 5**a,b)) and GDL/MPL/PA composite phase (50 h, **Figure 3. 5**c,d and 100 h, Figure 3. 5e,f) present different shapes. In **Figure 3. 5**a,b, there are peaks for both sides attributable to the MPL region, followed by an average of ~30% carbonaceous volume. However, in **Figure 3. 5**c,d, there are

128

broader and higher peaks just after the MPL, *and* secondary, taller peaks towards the top and bottom of the GDL (where the flow-fields had been). In this case, from GDL-only calculations, the average GDL/MPL/PA phase fraction is ~55%. Despite very similar values in bulk quantity in 100-h-samples (also ~55%), the distribution can be seen (**Figure 3. 5**e,f) to differ, versus 50-h-samples (**Figure 3. 5**c,d). In the 100-h-case, one of the sides retains the double peak, whereas the other has a much less significant peak towards the flow-field end and there is a large discrepancy between the amount of PA on both sides. As this analysis only captures the residual PA inside the GDL/MPL, further work to inspect the volume of PA that escapes *via* the flow-field is planned using an *in-situ* set-up.

The impact on the porous network was investigated by both cPSD and tortuosity factor measurements for each GDL layer of all six samples. The cPSD results are summarised in **Table 3. 3**. There is little difference in the average (r_{50}) pore sizes between the two sides of the unoperated MEAs. For 50-h-samples this remains the same with a small increase in intrasample difference for 100-h-samples. However, there is a significant measured difference in pore r_{50} between the unoperated cells (12.6 ± 0.2 µm) and operated cells (15.5 ± 0.2 µm and 15.7 ± 0.4 µm for 50 h and 100 h, respectively). These changes represent average increases of 23% and 25% for 50 h and 100 h, respectively. Given the inundation of the GDL with PA, and the greater mass transport losses seen in **Figure 3. 3**, it might appear counterintuitive that the average pore size increases for the operated cells. However, there is a wide PSD for the unoperated cells, including many small pores that are mainly filled in the operated cases, causing the median value to increase. Moreover, it is not just the pore size that is important, but also the connectivity and "constrictivity" of the pore throats that must be considered. It is also worth noting that although the solid phase r_{50} values for the "dry" fibres for both sides of both 0-h-samples are very similar (4.4-4.7 µm), much greater magnitude and variation is observed for both operated samples due to the inclusion of PA in the solid phase and its uneven

distribution across the two sides of the membrane.

Table 3. 3. Summary of Pore cPSD results for Sample Set A

Sample	Electrode	Pore r_{50} (μm)	Mean Pore r_{50} (μm)	Top/Bot. Pore r_{50} (μm)
0 h (01)	Top	12.2	12.4	0.98
	Bottom	12.5		
0 h (02)	Top	13.2	12.8	1.06
	Bottom	12.4		
0 h Mean	Top	12.7	12.6 ± 0.2	1.02
	Bottom	12.4		
50 h (01)	Top	14.9	15.2	0.97
	Bottom	15.4		
50 h (02)	Top	15.4	15.7	0.96
	Bottom	16.1		
50 h Mean	Top	15.2	15.5 ± 0.2	0.97
	Bottom	15.7		
100 h (01)	Top	16.2	15.4	1.11
	Bottom	14.6		
100 h (02)	Top	15.5	16.0	0.93
	Bottom	16.6		
100 h Mean	Top	15.8	15.7 ± 0.4	1.01
	Bottom	15.6		

The z-tortuosity factor (through-plane) results of the binarized GDL volumes are shown in **Table 3. 4**. Despite the increasing r_{50} upon operation, there is a significant increase in tortuosity factor from 4.5 ± 0.8 in 0-h-samples to 10.6 ± 3.2 in 50-h-samples. The mean pore τ_z of 100-h-samples is also greater than in the unoperated cells but there is a significant difference between each GDL per sample.

Table 3. 4. Summary of z-tortuosity factor (τ_z) results for Sample Set A

Sample	Electrode	Pore τ_z	Connectivity	Mean Pore τ_z	Top/Bot. Pore τ_z
0 h (01)	Top	4.33	99.7%	4.0	1.20
	Bottom	3.61	99.7%		
0 h (02)	Top	4.42	99.6%	5.0	0.81
	Bottom	5.49	99.8%		
0 h Mean	Top	4.38	99.7%	4.5 ± 0.4	0.96
	Bottom	4.55	99.8%		
50 h (01)	Top	11.2	95.7%	10.7	1.10
	Bottom	10.2	97.0%		
50 h (02)	Top	6.53	95.6%	10.4	0.46
	Bottom	14.3	95.9%		
50 h Mean	Top	8.87	95.7%	10.6 ± 1.6	0.72
	Bottom	12.3	96.5%		
100 h (01)	Top	9.34	88.0%	7.2	1.86
	Bottom	5.02	96.8%		
100 h (02)	Top	11.5	88.8%	7.2	3.90
	Bottom	2.95	98.6%		
100 h Mean	Top	10.4	88.4%	7.2 ± 2.0	2.61
	Bottom	3.99	97.8%		

Although the pore τ_z is approximately equal for both sides of both 0-h-samples, the variance in this value increases with operation time. The pore network in the 50 h (01) sample appears to have been uniformly hindered with PA distributed similarly on both sides, but despite a similar connectivity, the 50 h (02) sample is more severely affected by PA in the bottom electrode than the top. In 100-h-samples, there is an even larger discrepancy in the pore τ_z on either side of the membrane, and in this case, this is matched by a concomitant drop in connectivity. The increased resistance to gas permeation between the current collector side and the membrane side in one GDL of each of the 100-h-samples correlates with the increase in mass transport polarisation losses shown in **Figure 3. 3**c.

3.6.2 Sample Set B

To improve the statistical significance of the data collected, and by using a standard AST available in the recent literature [35], a second set of samples was investigated in quadruplicate. Electrochemical testing was performed both on the pristine cell (0 h) and after the 70-h of load cycling between 0.6 and 1.0 A.cm^{-2} of the same. Voltage readings were taken throughout, as well as measuring pre- (0 h) and post- (AST) polarisation curves, along with EIS and CV curves,

shown in **Figure 3. 6**. XCT samples were taken from the AST sample and compared with a separate 0 h sample made following the same procedure and material batch.
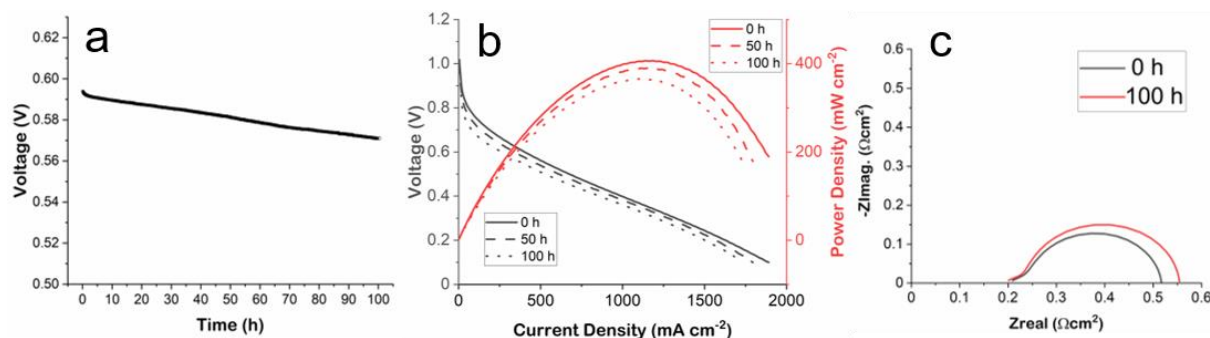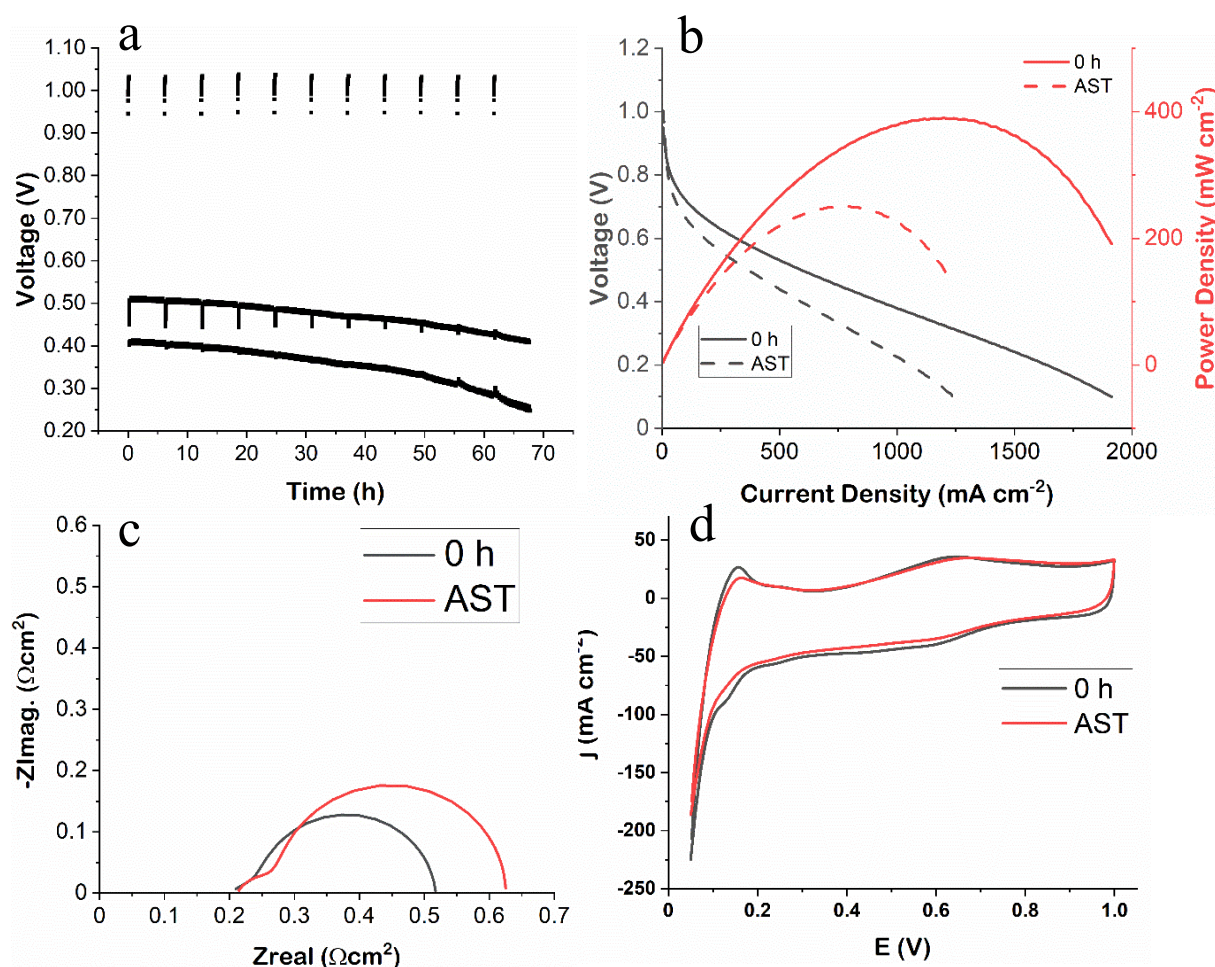

Figure 3. 6. Electrochemical data pertaining to Sample Set B, (a) Voltage-time plot for the duration of operation; (b) Polarisation curves (black) and power density curves (red) for 0 h (line) and AST (dashed); (c) complex plane plot for before (black) and after (red) AST; (d) Cyclic voltammograms for before (black) and after (red) AST.

A significant decline in performance is clearly observable in the voltage drop seen at either current density (**Figure 3. 6**a), 10 mV at 0.6 A.cm^{-2} and 16 mV at 1.0 A.cm^{-2} over ~70 h, similar in magnitude to the voltage drops observed in Sample Set A. All three 'regimes' in the polarisation curves (**Figure 3. 6**b) and in the magnitude of the semi-circular arcs in the complex plane plot (**Figure 3. 6**c) also signal significant performance degradation. The greater activation and mass transport losses seen in the polarisation curve are reflected in the emergence of an observable mid-frequency arc in the complex plane plot and an increase from

132

0.31 to 0.41 $\Omega.cm^2$ in overall polarisation resistance (~32% increase). There is minimal increase in the DC ohmic resistance (high-frequency intercept), which is thought to be due to more than sufficient PA doping in PBI such that a certain degree of PA leaching does not have a significant impact on the conductivity of the membrane. However, an ohmic loss increase is more apparent in the polarisation curve. This may be due to acid leaching and catalyst migration causing the dead region between catalyst layer and membrane to become larger, whilst the membrane resistance is only minimally impacted.

The CV curves shown in **Figure 3. 6**d illustrate a small drop in ECSA, measured to be 55.4 $cm^2.mg^{-1}$ in the 0 h cell and 50.0 $cm^2.mg^{-1}$ in the AST cell, representing a ~10% decrease, accounting for increased activation losses. The sum of charge transfer resistance and mass transfer resistance in the pristine cell is 0.29 $\Omega.cm^2$, very similar to that seen for Sample Set A (0.31 $\Omega.cm^2$), which increases to 0.38 $\Omega.cm^2$ after the AST, representing a ~31% increase. The membrane swelling, Pt migration and PA egress from the membrane (**Figure 3. 7**) qualitatively capture the correlation of microstructural change with these indicators of electrochemical performance decline. However, the degradation effects observed here are likely compound effects arising from multiple, independent degradation mechanisms. Unlike LT-PEFCs, which have established ASTs to target specific modes of degradation, HT-PEMFCs still lack standardised AST protocols. Thus, future work should aim to develop such targeted ASTs, which would allow for direct correlation between electrochemical degradation and morphological changes in the MEA components observed by X-ray CT.
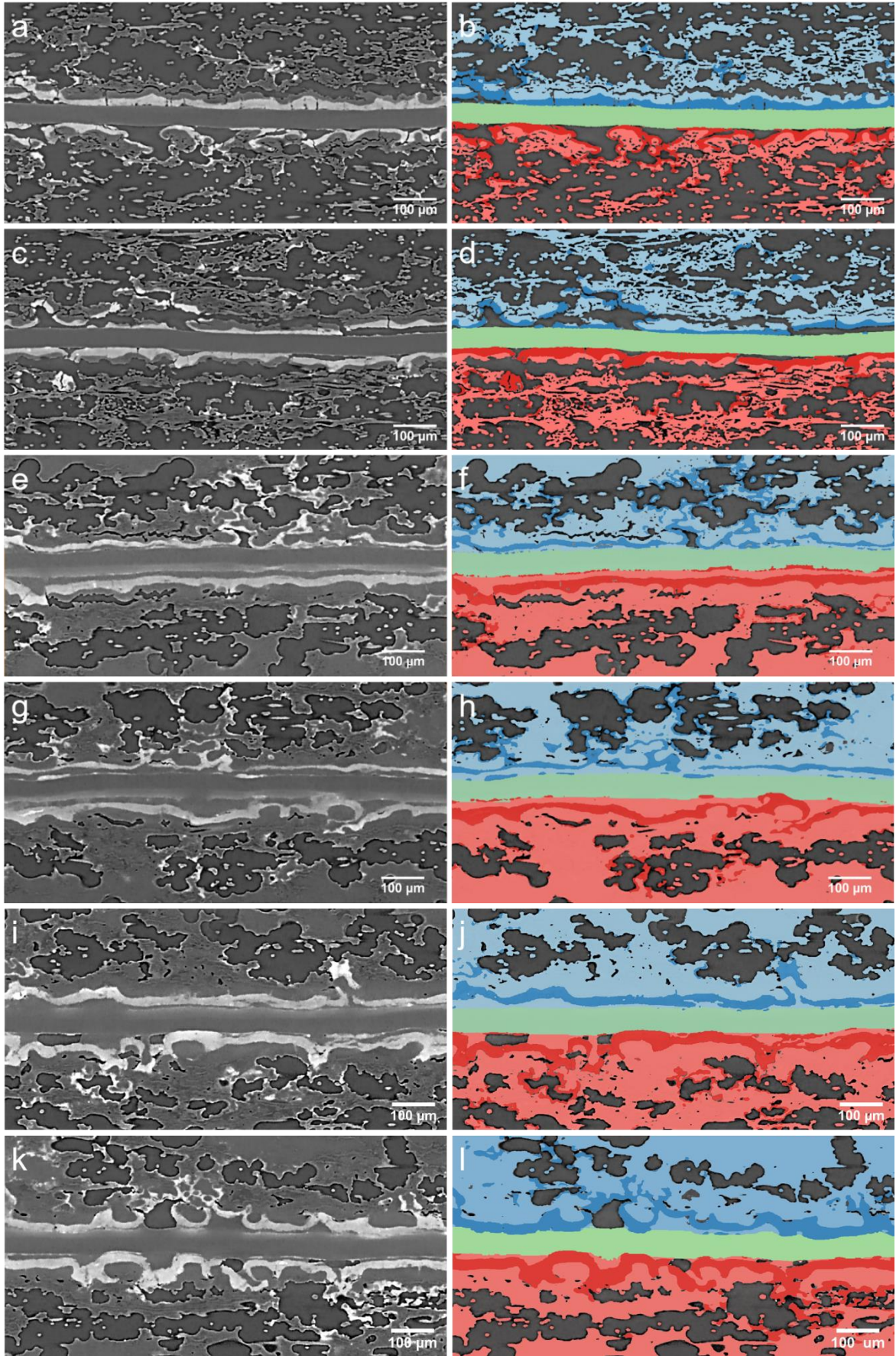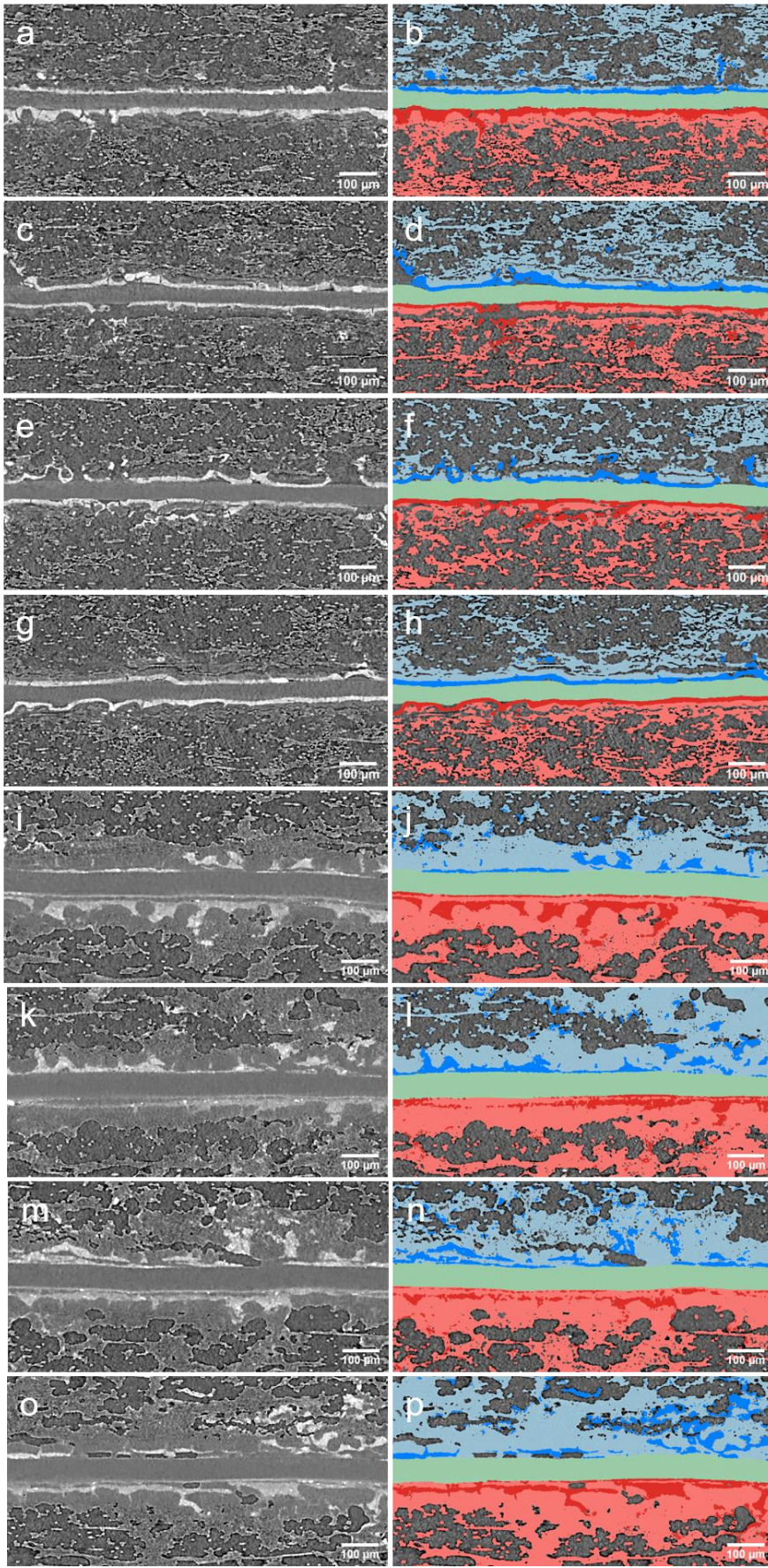
Figure 3. 7. X-ray CT data pertaining to Sample Set B: Filtered XZ-orthoslices from (a), (c), (e), (g) 0 h tomograms; (b), (d), (f), (h) Corresponding segmented XZ-orthoslices from 0 h tomograms and from (i), (k), (m), (o) AST tomograms; (j), (l), (n), (p) Corresponding segmented XZ-orthoslices from AST tomograms.

The segmented volumes were analysed quantitatively, both globally and by a slice-by-slice method. The full results from this analysis are given in **Table S3. 4** and a summary of the GDL/MPL (unoperated) and GDL/MPL/PA (operated) composite phase fractions are shown in **Table 3. 3**. Importantly, the average phase fraction for the PA-free carbonaceous phase is $15.2 \pm 0.4\%$, which is consistent with the value observed previously for Sample Set A 0-h-samples ($14.6 \pm 0.4\%$), highlighting that the sample-to-sample variation is <5% (~0.6% in absolute phase fraction).

Table 3. 5. Global GDL/MPL/(PA) phase fractions from 0 h (unoperated) and AST (operated) cells, per electrode for each replicate and mean values

Sample	Electrode	GDL/MPL/(PA) phase fraction	Mean
0 h (01)	Anode	15.9%	16.7%
	Cathode	17.5%	
0 h (02)	Anode	15.5%	15.1%
	Cathode	14.7%	
0 h (03)	Anode	15.1%	15.4%
	Cathode	15.7%	
0 h (04)	Anode	13.8%	13.8%
	Cathode	13.7%	
0 h Mean	Anode	15.1%	15.2 ± 0.4%
	Cathode	15.4%	
AST (01)	Anode	20.1%	21.3%
	Cathode	22.5%	
AST (02)	Anode	25.3%	24.0%
	Cathode	22.6%	
AST (03)	Anode	22.6%	23.2%
	Cathode	23.8%	
AST (04)	Anode	21.8%	22.2%
	Cathode	22.7%	
AST Mean	Anode	22.4%	22.7% ± 0.3%
	Cathode	22.9%	

The equivalent mean and standard error of the mean values for the AST samples were 22.7% and ~0.3%, demonstrating a significant filling of the porous region of the MPL and GDL with leached PA (almost one-third of the pore phase flooded). The mean difference between the two sets (7.4 ± 0.5%) represents an average volumetric increase of ~0.04 mm^3 in each electrode, similar in magnitude to the lifetime testing of Sample Set A (0.05-0.06 mm^3). It is perhaps surprising that this AST, which incorporates current cycling, leads to a similar amount of PA in the GDL/MPL as operating at a single current density for a similar number of hours (50-100 versus 70 h); suggesting that there is a saturation limit, the current cycling has little added effect over operation time, or that switching between these two current densities has some compensatory effect [51]. More research is required at the flow-field level to understand if in fact the AST causes greater PA egress through the gas channels, whilst nevertheless leaving

similar residual PA in the porous electrodes.

The results of areal slice-by-slice analysis are presented in **Figure 3. 8**. The average measured membrane thicknesses (FWHM) show a more pronounced increase than that observed in lifetime testing, from 44 ± 2 µm in 0-h-samples (**Figure 3. 8** a,b,c,d) to 63 ± 1 µm in AST-samples (**Figure 3. 8** e,f,g,h), representing on average a 44% increase, far more significant than the internal variation in either case (see **Table S3. 5**). The irreversible swelling observed with this AST is greater in magnitude than the reversible swelling observed in early radiographic studies (20%) [19]. This observation is also contrary to the MEA shrinkage seen in early tomographic literature [25] and indeed implies a volumetric increase despite PA egress. Although only small changes in membrane thickness were detected *in-situ* by a distance sensor in recent work [35], the authors highlight that with the production of large amounts of water at high current densities, protolysis and PA dilution are expected. The impact of *post-mortem* electrochemical testing can be effectively ruled out since these are thought to result in a shrinkage [35], and the same electrochemical tests were carried out for the pristine and operated samples in this study. However, due to the *ex-situ* nature of the investigation, forming small discs for X-ray CT investigation may allow MEA mechanical stresses built up during operation to be relieved by sample sectioning, leading to *post-mortem* deformation. This possibility will be further investigated by lab-based *in-situ* measurements in future work.

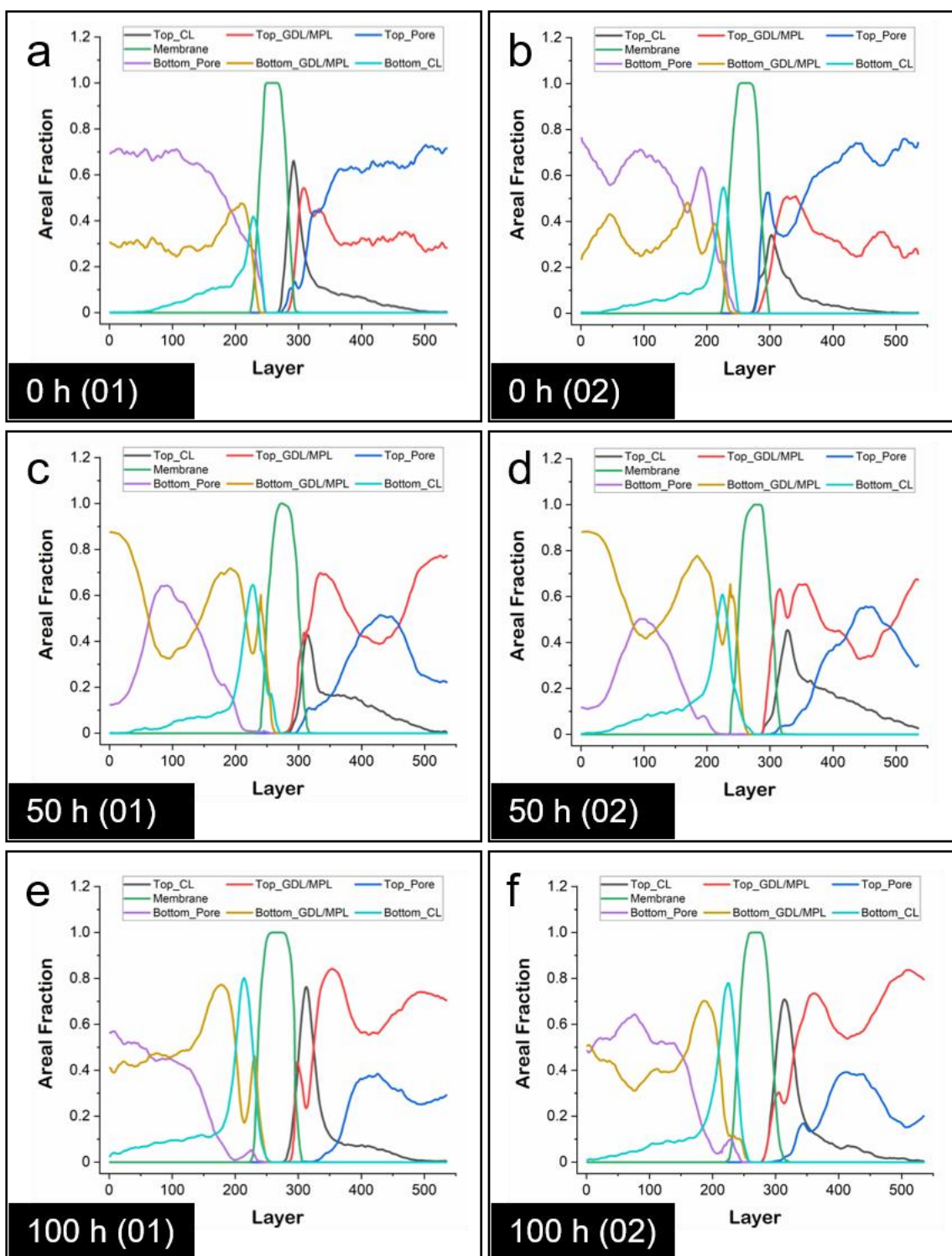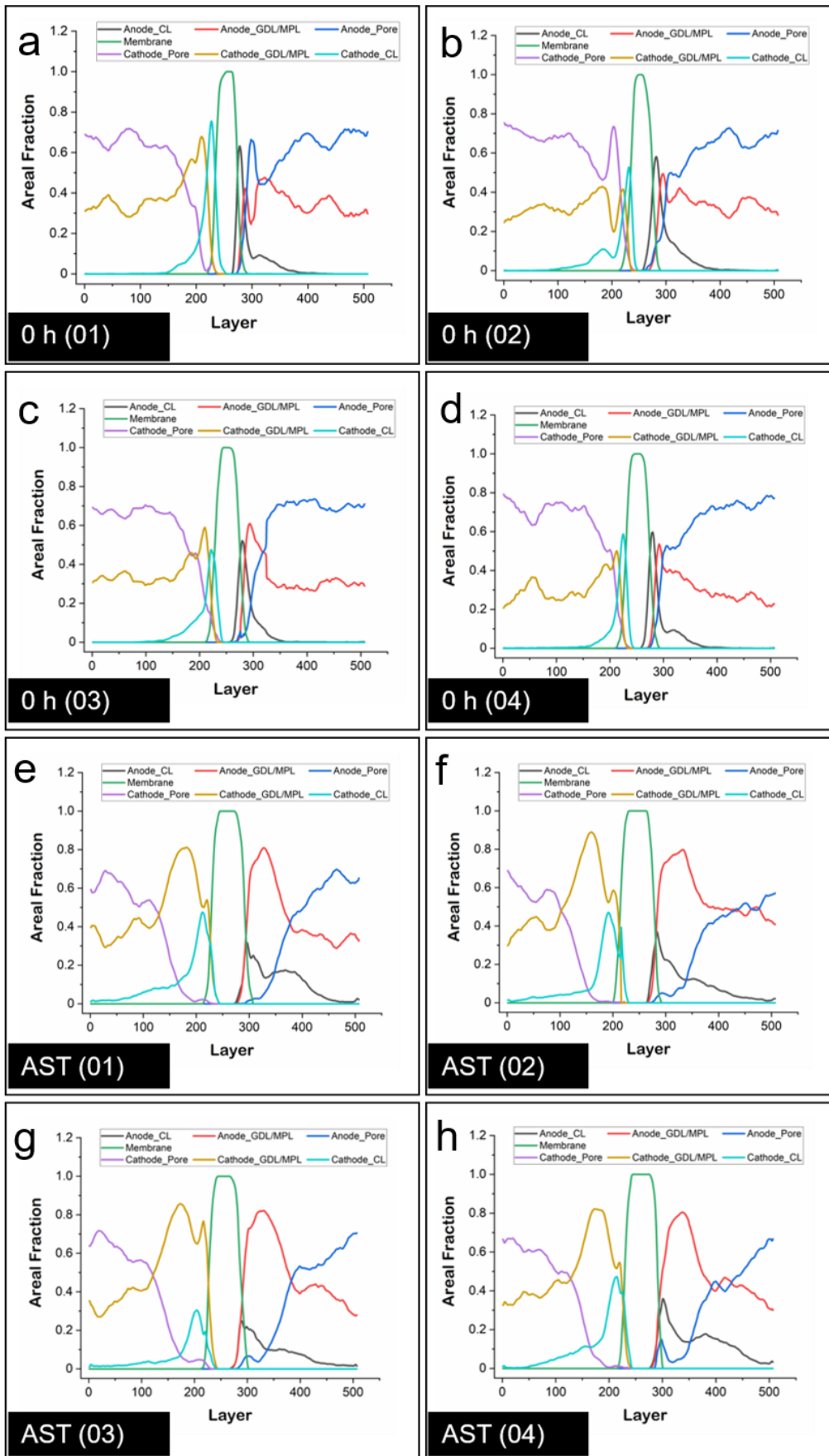*Figure 3. 8. Slice-by-slice plots for Sample Set B*, showing the area fraction for each of the seven phases from the cathode *(Layer 1) to the anode (Layer 506)* for (a) 0 h (01); (b) 0 h (02); (c) 0 h (03); (d) 0 h (04); (e) AST (01); (f) AST (02); (g) AST (03); (h) AST (04).

138

The behaviour of the CL during the AST is also noteworthy. Given that membrane swelling likely accounts for between 14 and 24 µm, if CL migration behaviour during the AST matches the lifetime testing regime, an increase in inter-CL distance of the order of 38 – 48 µm is expected. Indeed, the average inter-CL peak distance in the 0-h- (**Figure 3. 8** a,b,c,d) and AST-samples (**Figure 3. 8** e,f,g,h) is 54 ± 3 µm and 88 ± 3 µm, respectively, representing a change of between 28 and 41 µm. However, unlike for Sample Set A, the distances between CL peaks and the centre of the membrane are not the same for each electrode in Sample Set B, with a significantly greater migration of the cathode CL (50 µm) than the anode CL (37 µm) (see

Table S3. 6), suggesting cathodic CL degradation may be greater than anodic CL degradation under the AST regime studied. This would, however, require a more in-depth EIS study or a 3-electrode set-up to experimentally verify, which is beyond the scope of this work.

With regards to PA migration into the MPL/GDL region, the eight samples present a coherent picture which is different from that observed during lifetime testing. In the unoperated cells (**Figure 3. 8** a,b,c,d), there is a peak close to the membrane, after the CL, representing the denser MPL layer. After this, the carbonaceous phase fraction generally falls, averaging between 0.27 and 0.34 across all sides and all replicates (overall average 0.30, as for 0-h-samples in Sample Set A). However, in the operated cells (**Figure 3. 8** e,f,g,h), rather than the bimodal distribution seen in most electrodes in 50-h- and 100-h-samples, the AST samples present a single large peak at the location attributable to the MPL, without the secondary peak towards where the flow-fields had been. In fact, in all cases there is a depletion of PA as one moves further out from the initial MPL peak. This has been quantified in **Table S3. 8** as the average phase fraction across the first and last 150 slices, where the GDL/MPL/(PA) phase fraction is increased from 0.30 to 0.42 in the GDL region (~41%), a smaller proportional increase versus the entire electrode change (~49%). This may indicate a larger build-up in the MPL region, but that perhaps the PA observed at the outer edges in the lifetime operated cells

had escaped *via* the flow-field, giving a similar residual increase in PA content. Such a hypothesis would require imaging of the flow-field and/or monitoring of the exhaust gases to confirm.

cPSD and τ_z measurements were also performed on both electrodes of each sample, with the cPSD summary shown in **Table 3. 6**. First, the mean pore size ($r_{50} = 12.6 \pm 0.4$ µm) compares very well with the unoperated cells in Sample Set A ($r_{50} = 12.6 \pm 0.2$ µm), as is expected for these nominally equivalent cells. Again, it is clear there is very little discrepancy between each electrode in these pristine cells. However, there is a small pore size increase after AST, attributable to the greater filling of smaller pores. However, this effect is thought to be less pronounced than that seen during lifetime testing due to the greater concentration of egressed PA in the MPL region which is effectively removed from the analysed volumes here. Therefore, it is likely only the smaller number of small pores found in the GDL being filled that causes the observed change.

Table 3. 6. Summary of Pore cPSD results for Sample Set B

Sample	Electrode	Pore r_{50} (µm)	Mean Pore r_{50} (µm)	An./Cat. Pore r_{50} (µm)
0 h (01)	**Anode**	12.0	11.9	1.01
	Cathode	11.8		
0 h (02)	**Anode**	11.5	11.5	1.00
	Cathode	11.5		
0 h (03)	**Anode**	11.7	13.8	1.01
	Cathode	11.6		
0 h (04)	**Anode**	13.1	13.3	0.97
	Cathode	13.5		
0 h Mean	**Anode**	12.6	12.6 ± 0.4	1.00
	Cathode	12.6		
AST (01)	**Anode**	13.3	14.0	0.91
	Cathode	14.6		
AST (02)	**Anode**	13.7	14.1	0.95
	Cathode	14.5		
AST (03)	**Anode**	12.9	13.4	0.92
	Cathode	13.9		
AST (04)	**Anode**	12.3	13.2	0.87
	Cathode	14.1		
AST Mean	**Anode**	13.0	13.7 ± 0.3	0.91
	Cathode	14.3		

The final column of **Table 3. 6** indicates that the average pore size is slightly larger on the cathode side than the anode side, although the interpretation of this result is best examined in conjunction with the tortuosity factor results shown in **Table 3. 7**.

Table 3. 7. Summary of z-tortuosity factor (τ$_z$) results for Sample Set B

Sample	Electrode	Pore τ_z	Connectivity	Mean Pore τ_z	Top/Bot. Pore τ_z
0 h (01)	Anode	3.34	99.6%	3.2	1.07
	Cathode	3.11	99.5%		
0 h (02)	Anode	3.06	99.7%	3.0	1.05
	Cathode	2.92	99.7%		
0 h (03)	Anode	2.55	99.9%	2.8	0.84
	Cathode	3.02	99.8%		
0 h (04)	Anode	2.86	99.9%	2.7	1.13
	Cathode	2.52	99.9%		
0 h Mean	Anode	2.95	99.7%	2.9 ± 0.1	1.02
	Cathode	2.89	99.7%		
AST (01)	Anode	3.92	96.9%	3.6	1.21
	Cathode	3.20	97.8%		
AST (02)	Anode	4.68	96.6%	4.4	1.12
	Cathode	4.17	97.9%		
AST (03)	Anode	5.13	97.9%	4.8	1.17
	Cathode	4.38	97.4%		
AST (04)	Anode	5.70	97.0%	4.6	1.60
	Cathode	3.54	98.4%		
AST Mean	Anode	4.85	97.1%	4.3 ± 0.3	1.26
	Cathode	3.83	97.9%		

Indeed, a significant increase in tortuosity factor is observed, as well as a consistently higher tortuosity factor for the anode side. Importantly, if the binarized volume is allowed to extend any further towards the MPL region, it rises exponentially for all AST samples, again highlighting significant filling of the MPL. There is also lower connectivity in all AST cases than in the pristine cases, mostly marginally lower in the former on the anode side than the cathode side. From solely the quantity of PA in each GDL, this result would not be apparent, as in most cases the GDL/MPL/(PA) phase fraction is lower on the anode side. Nonetheless, the tortuosity factor calculations run on the binarized GDL layers suggest that either at the GDL/MPL and/or the GDL/flow-field interface, there is greater flooding of PA on the anode side than the cathode side, more greatly hindering gas transport on this electrode. Further investigation to probe the mechanism and establish whether "electrochemical pumping" in this direction is the dominant factor will be the focus of future work.

3.7 Conclusions

Lifetime and accelerated stress testing of HT-PEMFCs have been undertaken, correlating their

microstructure and electrochemical performance by combining lab-based X-ray micro-CT and machine-learning segmentation. Statistically significant changes in the membrane, CL and MPL/GDL, particularly in regard to PA leaching, can be detected and well-characterised without a synchrotron. Although the low-flux, polychromatic lab-source precludes direct *ex-situ* determination of PA location, a multi-sample approach allows ready access to data that can be reliably segmented to yield insights into global and layer-by-layer PA distribution. The following conclusions can be drawn:

i.   A laser micro-machining sample preparation route has been developed that can be implemented to provide sufficiently small discs to yield adequate image quality for reliable segmentation by a novel machine-learning based approach. By careful selection of milling parameters, MEA orientation can be retained, giving rise to greater insights into PA leaching anisotropy.

ii.   High-fidelity segmented volumes allow for analysis of membrane width, Pt catalyst migration, PA leaching and concomitant changes in the pore networks.

iii.   Duplicate lifetime testing shows that the quantity of GDL/MPL-held PA was little changed between 50 h and 100 h, corroborating reports that a steady-state is established within the first few hours. Nonetheless, PA re-distribution likely continues on the order of tens of hours, leading to non-uniform filling. Observed mass transfer polarisation losses correlate well with the recorded microstructural change.

iv.   Slice-by-slice analysis of the volumes operated at constant current density identified a bimodal distribution of leached PA, with maxima in the MPL region and towards the outer GDL edge, towards where the flow-fields had been. cPSD and tortuosity factor analysis suggested that smaller pores were filled preferentially, and that with longer operation, a greater disparity in pore network connectivity and tortuosity factor between the two electrodes evolved.

143

v. Quadruplicate accelerated stress testing showed a similar quantity of leached PA residing in the GDL but with a single, larger maximum at the MPL. This concentration of PA served as a greater barrier to gas transport than the similar quantity of PA in the other tests, resulting in a more significant mass transfer polarisation loss.

vi. cPSD analysis of the GDL region highlighted a less pronounced filling of smaller pores but importantly the z-tortuosity factor was observed to increase, and pore connectivity to decrease, after the AST.

vii. It was also observed that the AST had a much more pronounced impact on membrane swelling and led to less uniform Pt migration across electrodes. However, as discussed in relation to the electrochemical results of Sample Set B, the AST used here likely results in several degradation mechanisms occurring at once. Thus, we stress the need to create standardised, targeted ASTs that are specific to each degradation mechanism and timescale, which would allow for better correlation between electrochemical degradation and changes in MEA morphology observed by X-ray CT.

It is hoped that more research will focus not only on improving the statistical robustness of X-ray CT measurements in electrochemical devices, but that this study has also underlined that a greater understanding of how PA re-distributes within and exits a real cell will help in the design of improved HT-PEMFCs. Indeed, the platform developed here has been applied to the application of a PA leaching mitigation approach, which will be the focus of a follow-up publication.

3.8 Acknowledgements

3.9 References:

[1]   J.S. Wainright, J. -T. Wang, D. Weng, R.F. Savinell, M. Litt, Acid-Doped Polybenzimidazoles: A New Polymer Electrolyte, Journal of The Electrochemical Society. 142 (1995) L121–L123. https://doi.org/10.1149/1.2044337.

[2]   Q. Li, J.O. Jensen, R.F. Savinell, N.J. Bjerrum, High temperature proton exchange membranes based on polybenzimidazoles for fuel cells, Progress in Polymer Science. 34 (2009) 449–477. https://doi.org/10.1016/J.PROGPOLYMSCI.2008.12.003.

[3]   Q. Li, R. He, J.-A. Gao, J.O. Jensen, N.J. Bjerrum, The CO Poisoning Effect in PEMFCs Operational at Temperatures up to 200°C, Journal of The Electrochemical Society. 150 (2003) A1599. https://doi.org/10.1149/1.1619984.

[4]   Q. He, X. Yang, W. Chen, S. Mukerjee, B. Koel, S. Chen, Influence of phosphate anion adsorption on the kinetics of oxygen electroreduction on low index Pt(hkl) single crystals, Physical Chemistry Chemical Physics. 12 (2010) 12544–12555. https://doi.org/10.1039/C0CP00433B.

[5]   A. Kamat, M. Herrmann, D. Ternes, O. Klein, U. Krewer, S. Scholl, Experimental investigations into phosphoric acid adsorption on platinum catalysts in a high temperature PEM Fuel cell, Fuel Cells. 11 (2011) 511–517. https://doi.org/10.1002/fuce.201000102.

[6]   R. Zeis, Materials and characterization techniques for high-temperature polymer electrolyte membrane fuel cells, Beilstein Journal of Nanotechnology. 6 (2015) 68–83. https://doi.org/10.3762/bjnano.6.8.

[7]   C. Wannek, I. Konradi, J. Mergel, W. Lehnert, Redistribution of phosphoric acid in membrane electrode assemblies for high-temperature polymer electrolyte fuel cells,

International Journal of Hydrogen Energy. 34 (2009) 9479–9485. https://doi.org/10.1016/j.ijhydene.2009.09.076.

[8] R. Bouchet, E. Siebert, Proton conduction in acid doped polybenzimidazole, Solid State Ionics. 118 (1999) 287–299. https://doi.org/10.1016/s0167-2738(98)00466-4.

[9] K.A. Perry, K.L. More, E.A. Payzant, R.A. Meisner, B.G. Sumpter, B.C. Benicewicz, A comparative study of phosphoric acid-doped m-PBI membranes, Journal of Polymer Science Part B: Polymer Physics. 52 (2014) 26–35. https://doi.org/10.1002/POLB.23403.

[10] J. Chen, M. Perez-Page, Z. Ji, Z. Zhang, Z. Guo, S. Holmes, One step electrochemical exfoliation of natural graphite flakes into graphene oxide for polybenzimidazole composite membranes giving enhanced performance in high temperature fuel cells, Journal of Power Sources. 491 (2021) 229550. https://doi.org/10.1016/j.jpowsour.2021.229550.

[11] N. Üregen, K. Pehlivanoğlu, Y. Özdemir, Y. Devrim, Development of polybenzimidazole/graphene oxide composite membranes for high temperature PEM fuel cells, International Journal of Hydrogen Energy. 42 (2017) 2636–2647. https://doi.org/10.1016/j.ijhydene.2016.07.009.

[12] C. Korte, Phosphoric Acid, an Electrolyte for Fuel Cells – Temperature and Composition Dependence of Vapor Pressure and Proton Conductivity, in: D.S. and B. Emonts (Ed.), Fuel Cell Science and Engineering: Materials, Processes, Systems and Technology, Wiley-VCH GmbH & Co. KGaA, Weinheim, Germany, 2012: pp. 335–359.

[13] Y. Oono, A. Sounai, M. Hori, Influence of the phosphoric acid-doping level in a polybenzimidazole membrane on the cell performance of high-temperature proton exchange membrane fuel cells, Journal of Power Sources. 189 (2009) 943–949.

https://doi.org/10.1016/j.jpowsour.2008.12.115.

[14] K. Kwon, T.Y. Kim, D.Y. Yoo, S.G. Hong, J.O. Park, Maximization of high-temperature proton exchange membrane fuel cell performance with the optimum distribution of phosphoric acid, Journal of Power Sources. 188 (2009) 463–467. https://doi.org/10.1016/j.jpowsour.2008.11.104.

[15] K. Wippermann, C. Wannek, H.F. Oetjen, J. Mergel, W. Lehnert, Cell resistances of poly(2,5-benzimidazole)-based high temperature polymer membrane fuel cell membrane electrode assemblies: Time dependence and influence of operating parameters, Journal of Power Sources. 195 (2010) 2806–2809. https://doi.org/10.1016/j.jpowsour.2009.10.100.

[16] S. Galbiati, A. Baricci, A. Casalegno, R. Marchesi, Sensitivity analysis of a polybenzimidazole-based polymer fuel cell and insight into the effect of humidification Samuele, INTERNATIONAL JOURNAL OF ENERGY RESEARCH. 38 (2014) 780–790. https://doi.org/10.1002/er.

[17] N. Pilinski, M. Rastedt, P. Wagner, Investigation of Phosphoric Acid Distribution in PBI Based HT-PEM Fuel Cells, ECS Transactions. 69 (2015) 323–335. https://doi.org/10.1149/06917.0323ecst.

[18] K. Kwon, J.O. Park, D.Y. Yoo, J.S. Yi, Phosphoric acid distribution in the membrane electrode assembly of high temperature proton exchange membrane fuel cells, Electrochimica Acta. 54 (2009) 6570–6575. https://doi.org/10.1016/j.electacta.2009.06.031.

[19] W. Maier, T. Arlt, C. Wannek, I. Manke, H. Riesemeier, P. Krüger, J. Scholta, W. Lehnert, J. Banhart, D. Stolten, In-situ synchrotron X-ray radiography on high temperature polymer electrolyte fuel cells, Electrochemistry Communications. 12 (2010)

1436–1438. https://doi.org/10.1016/j.elecom.2010.08.002.

[20]   W. Maier, T. Arlt, K. Wippermann, C. Wannek, I. Manke, W. Lehnert, D. Stolten, Investigation of HT-PEMFCs by means of synchrotron X-ray radiography and electrochemical impedance spectroscopy, ECS Transactions. 41 (2011) 1413–1422. https://doi.org/10.1149/1.3635672.

[21]   R. Kuhn, J. Scholta, P. Krüger, C. Hartnig, W. Lehnert, T. Arlt, I. Manke, Measuring device for synchrotron X-ray imaging and first results of high temperature polymer electrolyte membrane fuel cells, Journal of Power Sources. 196 (2011) 5231–5239. https://doi.org/10.1016/j.jpowsour.2010.11.025.

[22]   W. Maier, T. Arlt, K. Wippermann, C. Wannek, I. Manke, W. Lehnert, D. Stolten, Correlation of synchrotron X-ray radiography and electrochemical impedance spectroscopy for the investigation of HT-PEMFCs, Journal of the Electrochemical Society. 159 (2012) F398–F404. https://doi.org/10.1149/2.024208jes.

[23]   A. Tobias, M. Wiebke, C. Tötzke, C. Wannek, H. Markötter, F. Wieder, J. Banhart, W. Lehnert, I. Manke, Synchrotron X-ray radioscopic in situ study of high-temperature polymer electrolyte fuel cells - Effect of operation conditions on structure of membrane, Journal   of   Power   Sources.   246   (2014)   290–298. https://doi.org/10.1016/j.jpowsour.2013.07.094.

[24]   S.H. Eberhardt, F. Marone, M. Stampanoni, F.N. Büchi, T.J. Schmidt, Quantifying phosphoric acid in high-temperature polymer electrolyte fuel cell components by X-ray tomographic microscopy, Journal of Synchrotron Radiation. 21 (2014) 1319–1326. https://doi.org/10.1107/S1600577514016348.

[25]   S.H. Eberhardt, M. Toulec, F. Marone, M. Stampanoni, F.N. Büchi, T.J. Schmidt, Dynamic Operation of HT-PEMFC: In-Operando Imaging of Phosphoric Acid Profiles

and (Re)distribution, Journal of The Electrochemical Society. 162 (2015) F310–F316. https://doi.org/10.1149/2.0751503jes.

[26]   H.R. Kunz, Lessons Learned from Phosphoric Acid Electrolyte Fuel Cell Development Pertinent to PEMFCs, ECS Transactions. 11 (2019) 1447–1460. https://doi.org/10.1149/1.2781058.

[27]   J. Halter, F. Marone, T.J. Schmidt, Breaking through the Cracks : On the Mechanism of Phosphoric Acid Migration in High Temperature Polymer Electrolyte Fuel, 165 (2018) 1176–1183. https://doi.org/10.1149/2.0501814jes.

[28]   S. Chevalier, M. Fazeli, F. Mack, S. Galbiati, I.T.D. If, A. Bazylak, R. Zeis, Role of the microporous layer in the redistribution of phosphoric acid in high temperature PEM fuel cell gas diffusion electrodes, Electrochimica Acta. 212 (2016) 187–194. https://doi.org/10.1016/j.electacta.2016.06.121.

[29]   J. Gostick, M. Aghighi, J. Hinebaugh, T. Tranter, M.A. Hoeh, H. Day, B. Spellacy, M.H. Sharqawy, A. Bazylak, A. Burns, W. Lehnert, A. Putz, OpenPNM: A Pore Network Modeling Package, Computing in Science and Engineering. 18 (2016) 60–74. https://doi.org/10.1109/MCSE.2016.49.

[30]   D. Wilkinson, J.F. Willemsen, Invasion percolation: A new form of percolation theory, Journal of Physics A: Mathematical and General. 16 (1983) 3365–3376. https://doi.org/10.1088/0305-4470/16/14/028.

[31]   L. Vásárhelyi, Z. Kónya, Kukovecz, R. Vajtai, Microcomputed tomography–based characterization of advanced materials: a review, Materials Today Advances. 8 (2020) 1–13. https://doi.org/10.1016/j.mtadv.2020.100084.

[32]   S. Carmignato, W. Dewulf, R. Leach, Industrial X-ray computed tomography, 2017.

https://doi.org/10.1007/978-3-319-59573-3.

[33] V. Cnudde, B. Masschaele, M. Dierick, J. Vlassenbroeck, L. Van Hoorebeke, P. Jacobs, Recent progress in X-ray CT as a geosciences tool, Applied Geochemistry. 21 (2006) 826–832. https://doi.org/10.1016/j.apgeochem.2006.02.010.

[34] F. Mack, M. Klages, J. Scholta, L. Jörissen, T. Morawietz, R. Hiesgen, D. Kramer, R. Zeis, Morphology studies on high-temperature polymer electrolyte membrane fuel cell electrodes, Journal of Power Sources. 255 (2014) 431–438. https://doi.org/10.1016/j.jpowsour.2014.01.032.

[35] D. Schonvogel, M. Rastedt, P. Wagner, M. Wark, A. Dyck, Impact of Accelerated Stress Tests on High Temperature PEMFC Degradation, Fuel Cells. 16 (2016) 480–489. https://doi.org/10.1002/fuce.201500160.

[36] J. Halter, T. Gloor, B. Amoroso, T.J. Schmidt, F.N. Büchi, Wetting properties of porous high temperature polymer electrolyte fuel cells materials with phosphoric acid, Physical Chemistry Chemical Physics. 21 (2019) 13126–13134. https://doi.org/10.1039/c9cp02149c.

[37] J. Halter, N. Bevilacqua, R. Zeis, T.J. Schmidt, F.N. Büchi, The impact of the catalyst layer structure on phosphoric acid migration in HT-PEMFC – An operando X-ray tomographic microscopy study, Journal of Electroanalytical Chemistry. 859 (2020) 113832. https://doi.org/10.1016/j.jelechem.2020.113832.

[38] J. Hack, P.A. García-Salaberri, M.D.R. Kok, R. Jervis, P.R. Shearing, N. Brandon, D.J.L. Brett, X-ray Micro-Computed Tomography of Polymer Electrolyte Fuel Cells: What is the Representative Elementary Area?, Journal of The Electrochemical Society. 167 (2020) 013545. https://doi.org/10.1149/1945-7111/ab6983.

[39] I. V. Zenyuk, D.Y. Parkinson, L.G. Connolly, A.Z. Weber, Gas-diffusion-layer structural properties under compression via X-ray tomography, Journal of Power Sources. 328 (2016) 364–376. https://doi.org/10.1016/j.jpowsour.2016.08.020.

[40] K. Yezerska, A. Dushina, F. Liu, M. Rastedt, P. Wagner, A. Dyck, M. Wark, Characterization methodology for anode starvation in HT-PEM fuel cells, International Journal of Hydrogen Energy. 44 (2019) 18330–18339. https://doi.org/10.1016/j.ijhydene.2019.05.114.

[41] L.A. Feldkamp, L.C. Davis, J.W. Kress, Practical cone-beam algorithm, J. Opt. Soc. Am. A. 1 (1984) 612–619. https://doi.org/10.1364/JOSAA.1.000612.

[42] C. Sommer, C. Straehle, U. Kothe, F.A. Hamprecht, Ilastik: Interactive learning and segmentation toolkit, Proceedings - International Symposium on Biomedical Imaging. (2011) 230–233. https://doi.org/10.1109/ISBI.2011.5872394.

[43] T.F. Scientific, Avizo Software 9 User's Guide, 2018.

[44] J. Halter, N. Bevilacqua, R. Zeis, T.J. Schmidt, F.N. Büchi, The impact of the catalyst layer structure on phosphoric acid migration in HT-PEMFC – An operando X-ray tomographic microscopy study, Journal of Electroanalytical Chemistry. (2020) 113832. https://doi.org/10.1016/j.jelechem.2020.113832.

[45] S.J. Cooper, A. Bertei, P.R. Shearing, J.A. Kilner, N.P. Brandon, TauFactor: An open-source application for calculating tortuosity factors from tomographic data, SoftwareX. 5 (2016) 203–210. https://doi.org/10.1016/j.softx.2016.09.002.

[46] B. Münch, L. Holzer, Contradicting Geometrical Concepts in Pore Size Analysis Attained with Electron Microscopy and Mercury Intrusion, Journal of the American Ceramic Society. 91 (2008) 4059–4067. https://doi.org/10.1111/j.1551-

2916.2008.02736.x.

[47] DoE Fuel Cell Targets, (2020).

[48] S. Yu, L. Xiao, B.C. Benicewicz, Durability Studies of PBI-based High Temperature PEMFCs, Fuel Cells. 8 (2008) 165–174. https://doi.org/10.1002/FUCE.200800024.

[49] C. Wannek, B. Kohnen, H.F. Oetjen, H. Lippert, J. Mergel, Durability of ABPBI-based MEAs for high temperature PEMFCs at different operating conditions, Fuel Cells. 8 (2008) 87–95. https://doi.org/10.1002/fuce.200700059.

[50] L. Xiao, H. Zhang, E. Scanlon, L.S. Ramanathan, E.W. Choe, D. Rogers, T. Apple, B.C. Benicewicz, High-temperature polybenzimidazole fuel cell membranes via a sol-gel process, Chemistry of Materials. 17 (2005) 5328–5333. https://doi.org/10.1021/cm050831+.

[51] J. Halter, S. Thomas, S.K. Kær, T.J. Schmidt, F.N. Büchi, The influence of phosphoric acid migration on the performance of high temperature polymer electrolyte fuel cells, Journal of Power Sources. 399 (2018) 151–156. https://doi.org/10.1016/j.jpowsour.2018.07.090.

3.10 Supplementary Information

3.10.1 Supplementary Figures
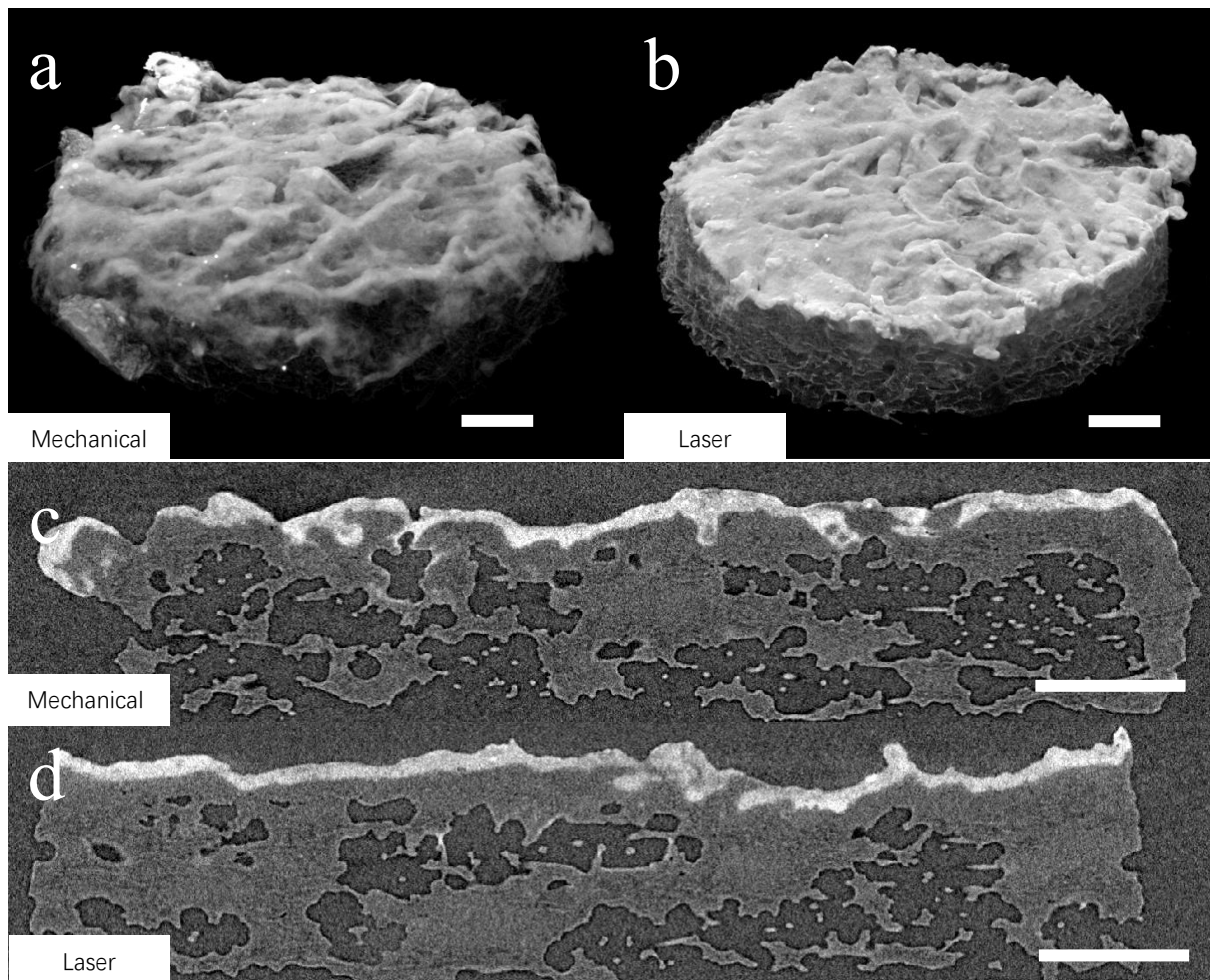
Figure S3. 1. Volume renderings (a,b) and XZ-orthoslices (c,d) from raw tomograms of (a,c) disc cut by hole punch and (b,d) disc cut by laser milling. All scalebars denote 200 μm.
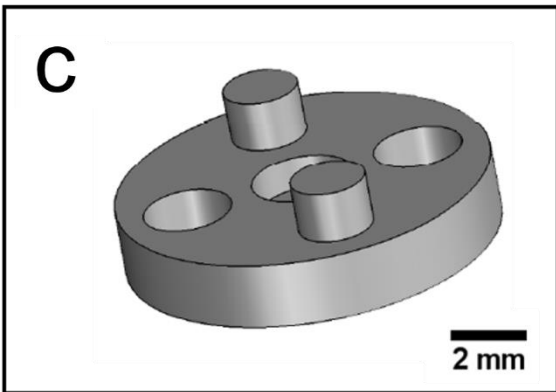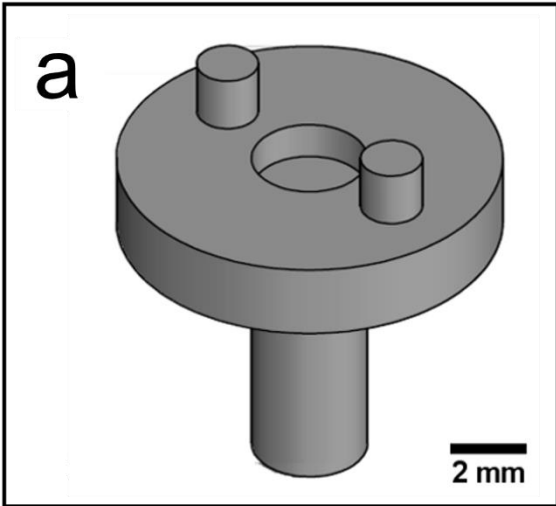
Figure S3. 2. (a) CAD drawing for 3D-printed chuck piece; (b) Photograph of assembled jig clamped in chuck of X-ray CT sample holder; (c) CAD drawing for 3D-printed sample disc holder
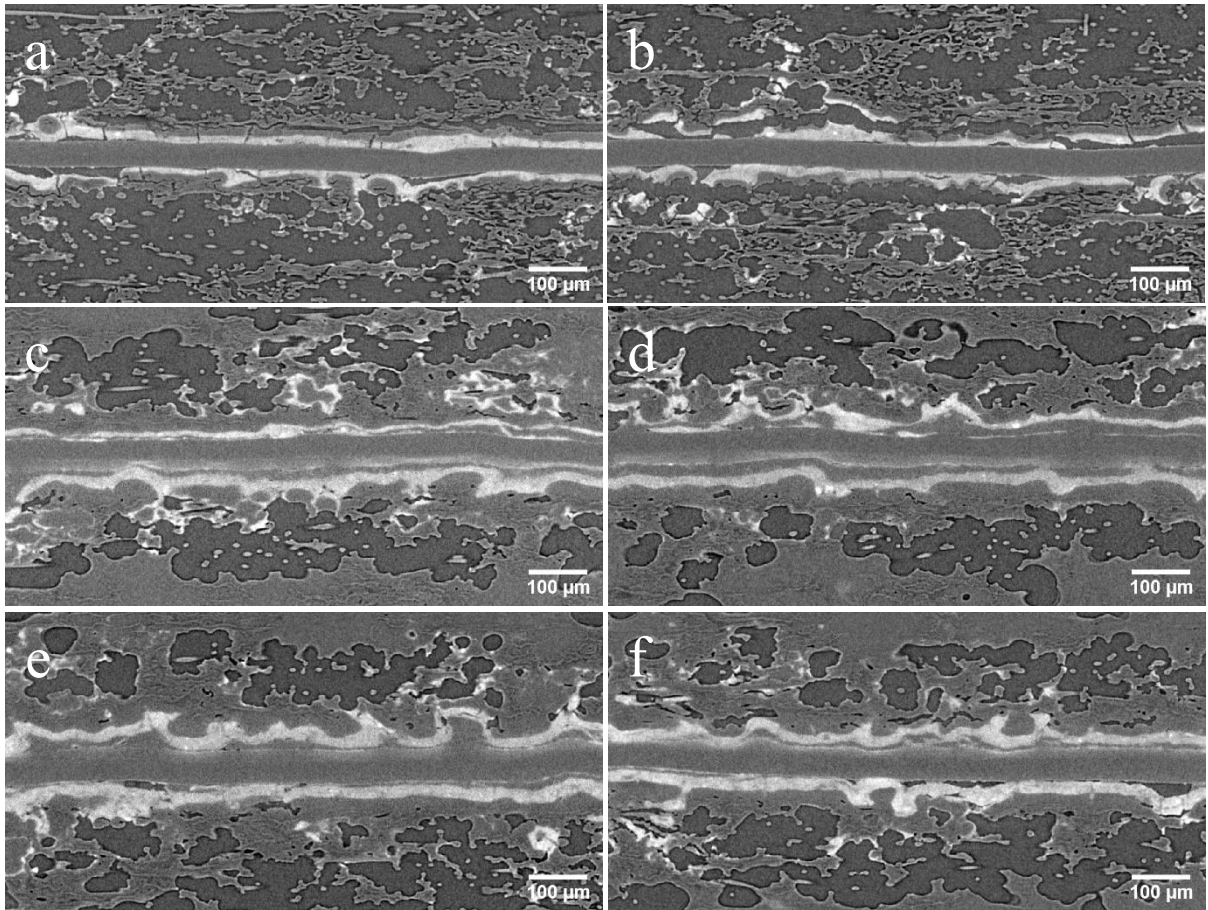
Figure S3. 3. Raw XZ-orthoslices from a, b) 0 h; c, d) 50 h; e, f) 100 h tomograms
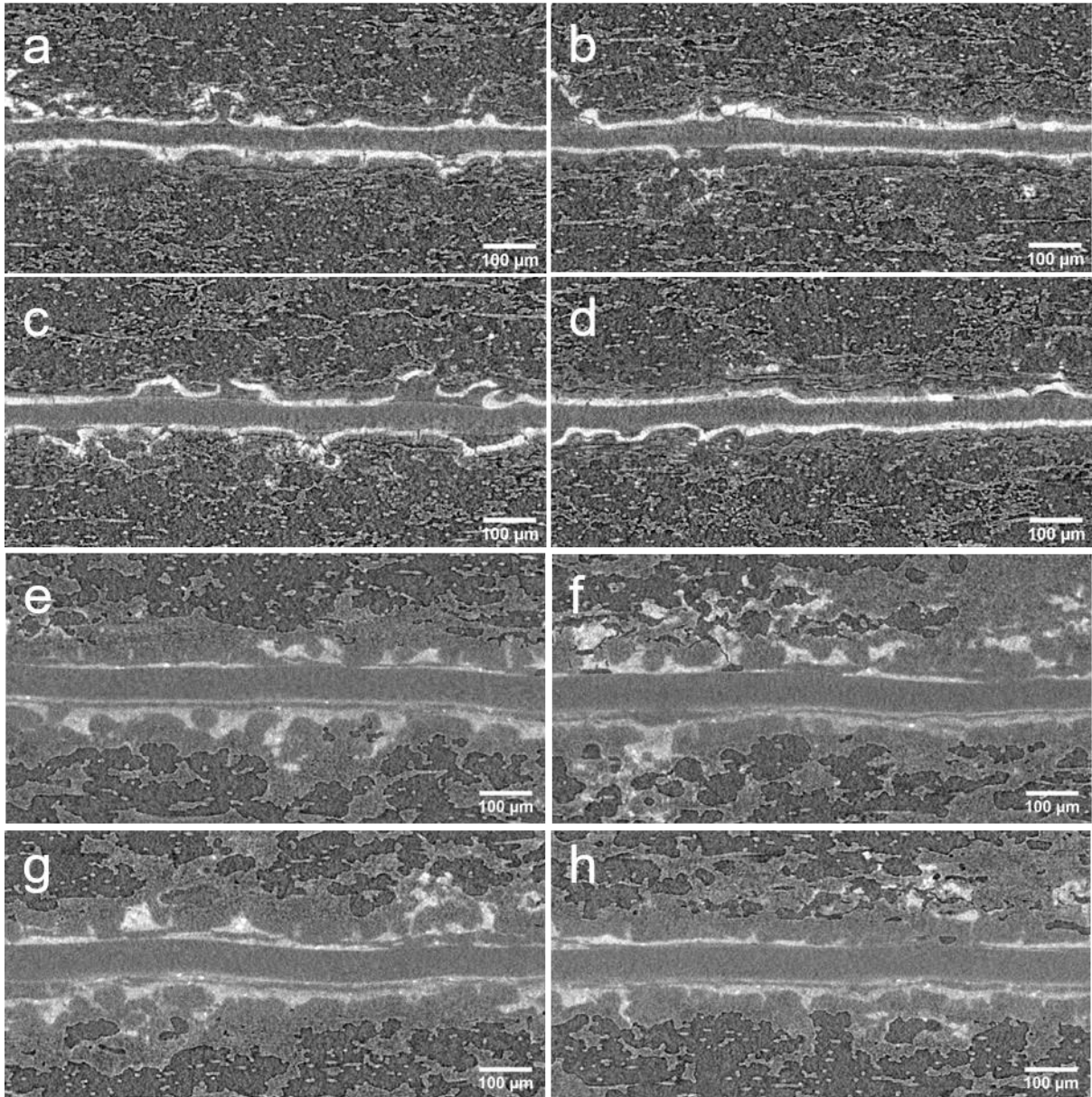
Figure S3. 4. Raw XZ-orthoslices from a, b c, d) 0 h; e, f, g, h) AST tomograms.
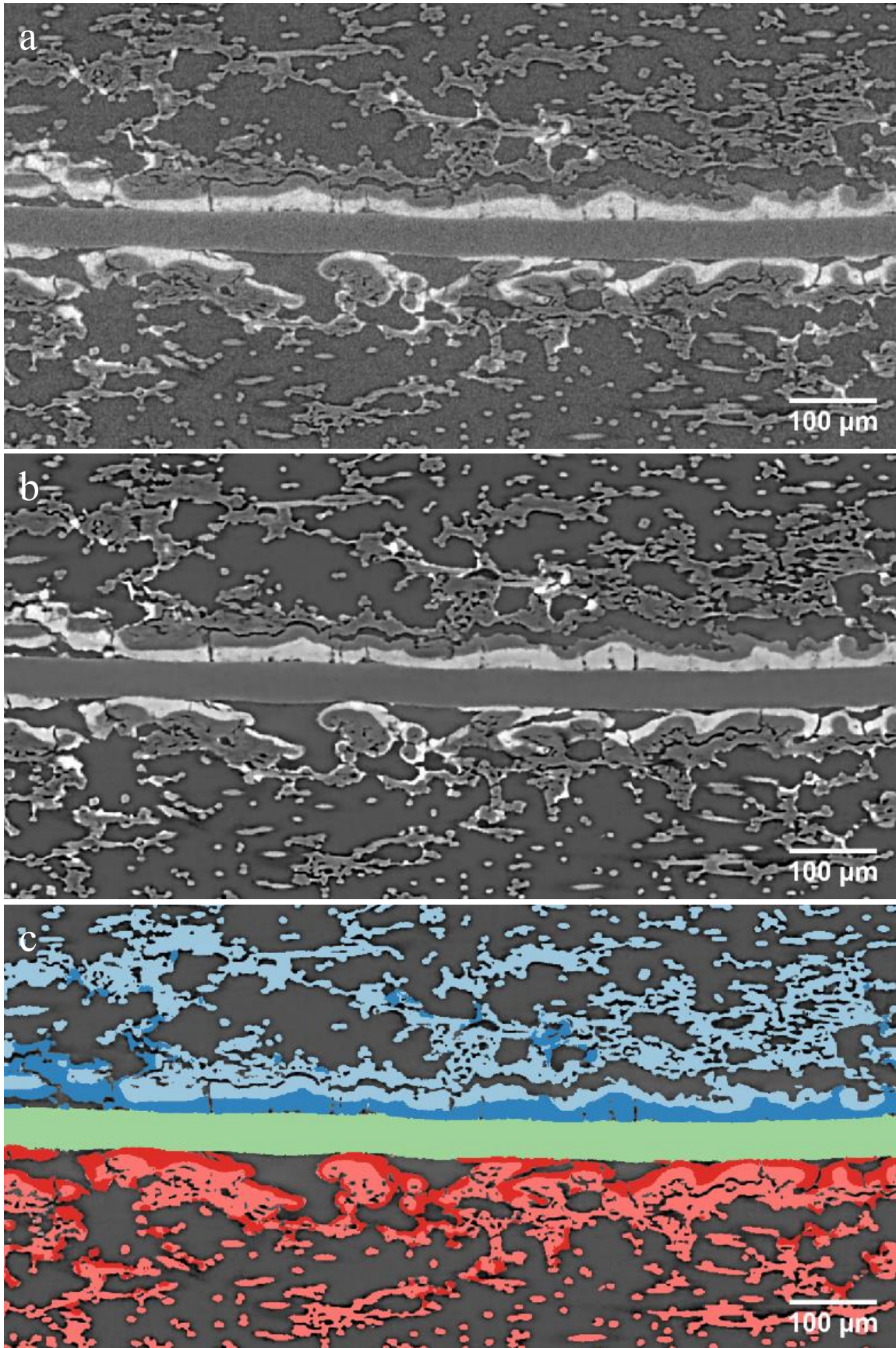
Figure S3. 5. Single orthoslices from tomogram of Sample Set A 0h-sample, (a) raw image; (b) filtered image; (c) segmented image.

157
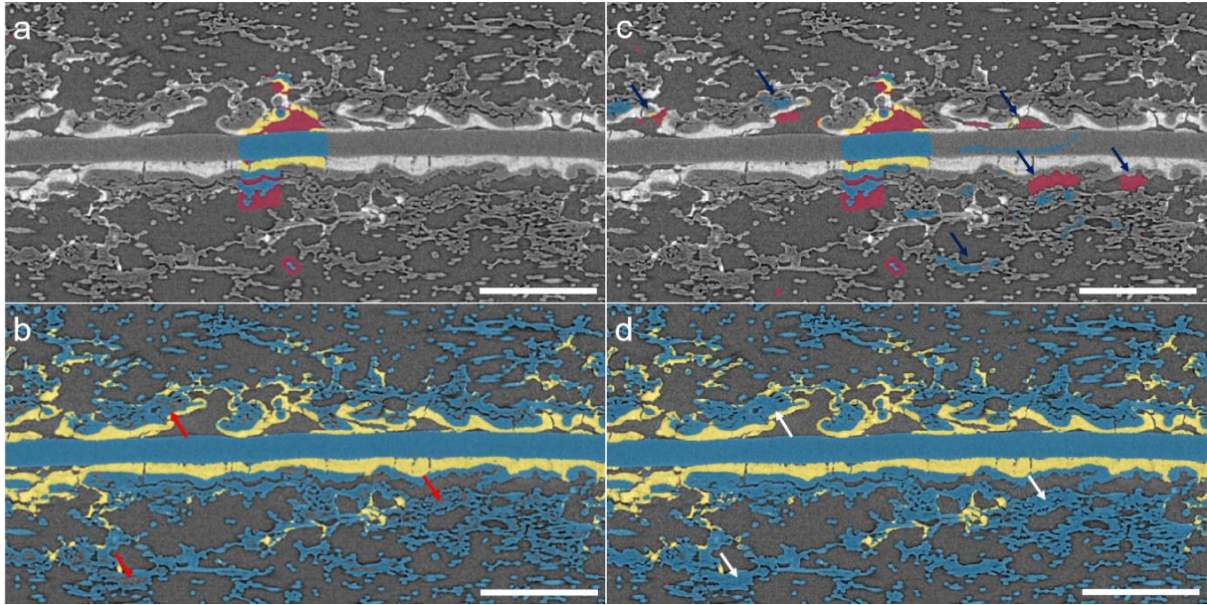
Figure S3. 6. Central XZ-orthoslice from Sample Set A 0h sample showing (a) the initial training input; (b) the initial proposed segmentation (under-segmentation marked with red arrows); (c) additional training data added (main additions marked with blue arrows); (d) updated segmentation (highlighting improvements with white arrows)
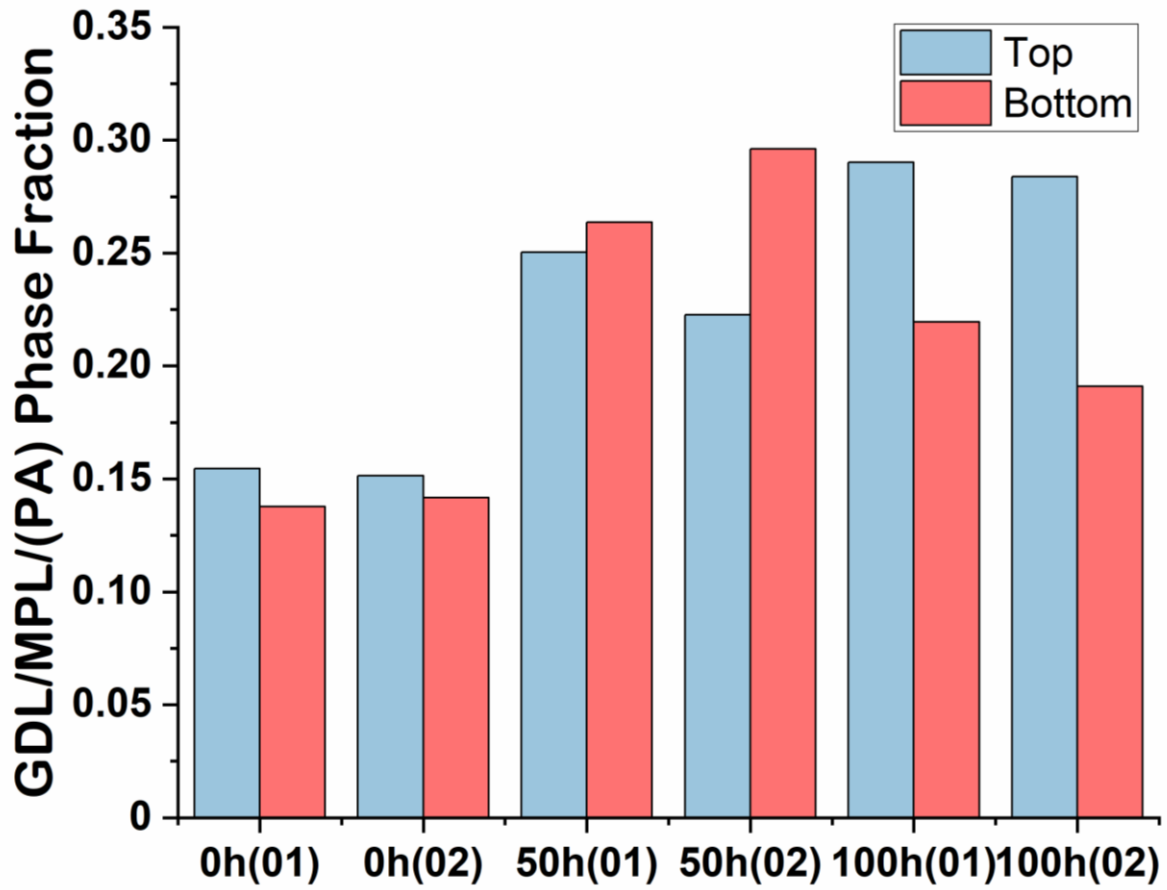
Figure S3. 7. Plot of GDL/MPL/(PA) phase fraction for Sample Set A, for two sides of each sample
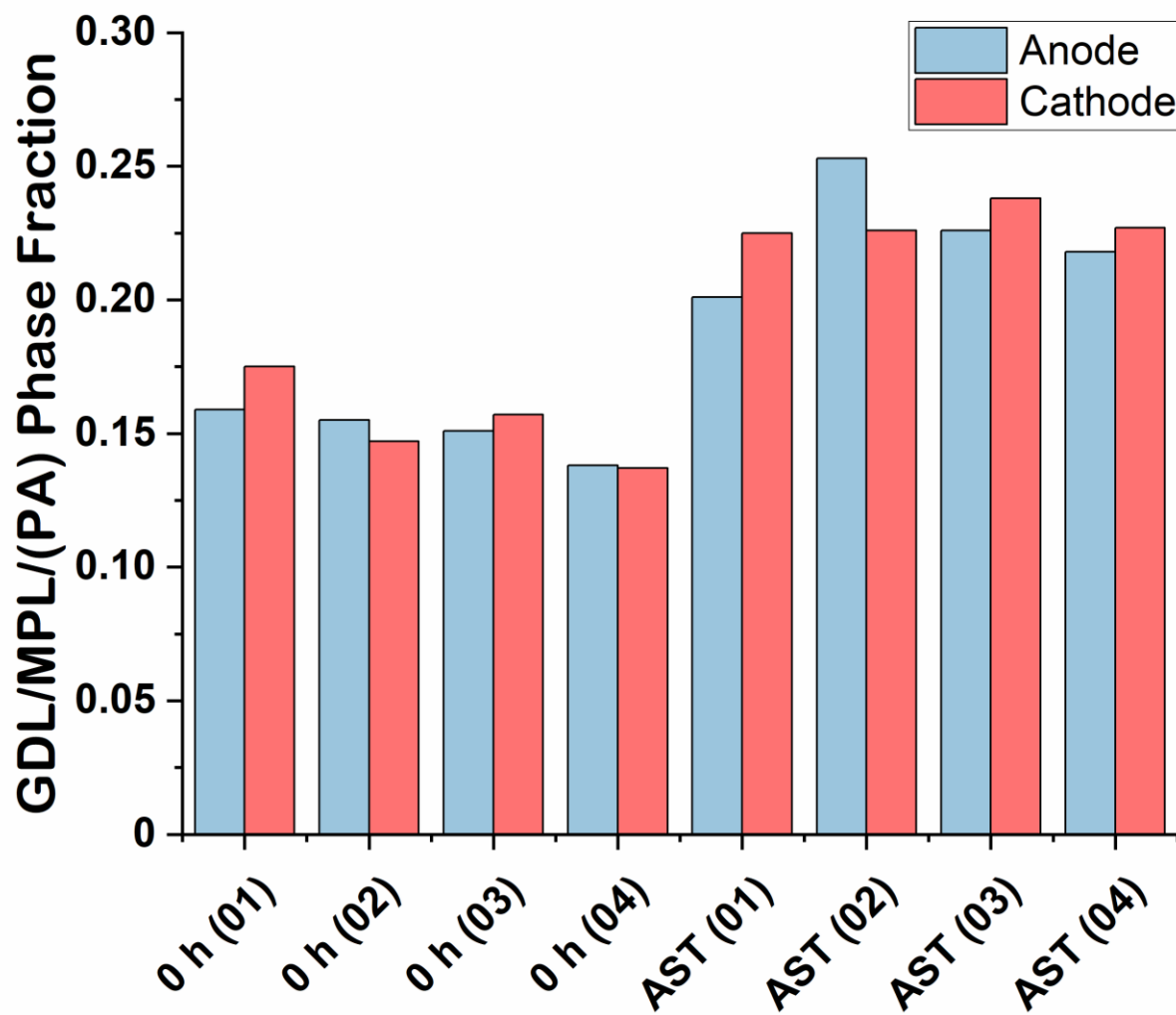
Figure S3. 8. Plot of GDL/MPL/(PA) phase fraction for Sample Set B, for anode and cathode sides of each sample

3.10.2 Supplementary Tables

Table S3. 1. Full list of X-ray CT acquisition parameters in this study

Batch	Sub-sample	Cutting	Sample diameter	X-ray voltage	X-ray power	Binning	Voxel dimension	Exposure time	Projection #	Scan time
unit			mm	kV	W	-	μm	s	-	h
Half Cell Tests	0 h	Manual	1.5	80	7	1	1.09	8	801	1.8
Half Cell Tests	0 h	Laser	1.5	80	7	1	1.09	8	801	1.8
Half Cell Tests	85 wt% PA	Laser	1.5	80	7	1	1.09	8	801	1.8
Sample Set A	0 h_1	Laser	1.5	60	5	1	0.95	14	1101	4.3
Sample Set A	0 h_2	Laser	1.5	60	5	1	0.95	14	1101	4.3
Sample Set A	48 h_1	Laser	1.5	60	5	1	0.95	14	1101	4.3
Sample Set A	48 h_2	Laser	1.5	60	5	1	0.95	14	1101	4.3
Sample Set A	100 h_1	Laser	1.5	60	5	1	0.95	14	1101	4.3
Sample Set A	100 h_2	Laser	1.5	60	5	1	0.95	14	1101	4.3
Sample Set B	0 h_1	Laser	2.0	40	3	1	1.01	25	401	2.8
Sample Set B	0 h_2	Laser	2.0	40	3	1	1.01	25	401	2.8
Sample Set B	0 h_3	Laser	2.0	40	3	1	1.01	25	401	2.8
Sample Set B	0 h_4	Laser	2.0	40	3	1	1.01	25	401	2.8
Sample Set B	AST_1	Laser	2.0	50	4	1	1.01	25	501	3.5
Sample Set B	AST_2	Laser	2.0	50	4	1	1.01	25	501	3.5
Sample Set B	AST_3	Laser	2.0	50	4	1	1.01	25	501	3.5
Sample Set B	AST_4	Laser	2.0	50	4	1	1.01	25	501	3.5

Table S3. 2. Phase fractions for each of the seven phases for Sample Set A

Phase	Phase Fraction (%) for Sample Set A								
	0 h (01)	0 h (02)	0 h Mean	50 h (01)	50 h (02)	50 h Mean	100 0h (01)	100 h (02)	100 h Mean
Top CL	5.2	3.3	4.3	5.5	7.2	6.4	6.3	6.8	6.5
Top GDL/MPL/(PA)	15.5	15.1	15.3	25.0	22.3	23.7	29.0	28.4	28.7
Top PORE	26.5	28.2	27.4	13.3	14.0	13.7	9.8	9.7	9.8
MEMBRANE	8.7	9.4	9.0	9.3	9.9	9.6	10.7	10.2	10.4
Bottom PORE	26.4	25.1	25.8	14.2	10.4	12.3	14.1	18.2	16.2
Bottom GDL/MPL/(PA)	13.8	14.2	14.0	26.4	29.6	28.0	22.0	19.1	20.5
Bottom CL	4.0	4.7	4.3	6.2	6.5	6.3	8.2	7.5	7.9

Table S3. 3. GDL.MPL/(PA) phase fractions for outer 150 layers of Sample Set A (representing global GDL results)

Electrode	GDL/MPL/(PA) Phase Fraction								
	0 h (01)	0 h (02)	0 h Mean	50 h (01)	50 h (02)	50 h Mean	100 h (01)	100 h (02)	100 h Mean
Top	0.31	0.29		0.56	0.46		0.66	0.68	
Bottom	0.29	0.32	0.30 ± 0.02	0.55	0.63	0.55 ± 0.07	0.46	0.40	0.55 ± 0.14
Mean	0.30	0.31		0.55	0.54		0.56	0.54	

Table S3. 4. All measurements from slice-by-slice analysis of Sample Set A

Sample	Membrane thickness (μm)	Mean per sample (μm)	Distance between CL peaks (μm)	Mean per sample (μm)
0 h (01)	45	47 ± 3	61	67 ± 8
0 h (02)	48		72	
50 h (01)	49	50 ± 1	83	90 ± 11
50 h (02)	51		98	
100 h (01)	55	54 ± 2	94	90 ± 5
100 h (02)	52		86	

Table S3. 5. All cPSD measurements for Sample Set A

Sample	Electrode	Phase	r_{50} (µm)	Mean Pore r_{50} (µm)	Top/Bottom Pore r_{50} (µm)
0 h (01)	Top	Pore	12.2	12.4	0.98
		Solid	4.42		
	Bottom	Pore	12.5		
		Solid	4.44		
0 h (02)	Top	Pore	13.2	12.8	1.06
		Solid	4.73		
	Bottom	Pore	12.4		
		Solid	4.48		
0 h mean	Top	Pore	12.7	**12.6**	**1.02**
		Solid	4.57		
	Bottom	Pore	12.5		
		Solid	4.46		
50 h (01)	Top	Pore	14.9	15.2	0.97
		Solid	14.1		
	Bottom	Pore	15.4		
		Solid	15.3		
50 h (02)	Top	Pore	15.4	15.7	0.96
		Solid	14.3		
	Bottom	Pore	16.1		
		Solid	28.7		
50 h mean	Top	Pore	15.2	**15.5**	**0.97**
		Solid	14.2		
	Bottom	Pore	15.7		
		Solid	22.0		
100 h (01)	Top	Pore	16.2	15.4	1.11
		Solid	23.0		
	Bottom	Pore	14.6		
		Solid	10.0		
100 h (02)	Top	Pore	15.5	16.0	0.93
		Solid	20.5		
	Bottom	Pore	16.6		
		Solid	10.9		
100 h mean	Top	Pore	15.8	**15.7**	**1.01**
		Solid	21.8		
	Bottom	Pore	15.6		
		Solid	10.5		

Table S3. 6. Phase fractions for each of the seven phases for Sample Set B

Phase	Phase fraction (%) for Sample Set B									
	0 h (01)	0 h (02)	0 h (03)	0 h (04)	0 h Mean	AST (01)	AST (02)	AST (03)	AST (04)	AST Mean
Anode CL	2.9	3.8	2.8	3.2	3.2	5.0	4.8	3.8	5.9	4.5
Anode GDL/MPL/(PA)	15.9	15.5	15.1	13.8	15.1	20.1	25.3	22.6	21.8	21.0
Anode PORE	27.1	26.7	28.0	28.9	27.7	17.7	15.3	17.1	15.2	18.6
MEMBRANE	7.9	8.0	9.2	9.0	8.5	12.3	12.5	11.7	12.1	11.4
Cathode PORE	24.7	28.2	26.3	28.6	26.9	17.2	14.6	17.8	17.2	18.7
Cathode GDL/MPL/(PA)	17.5	14.7	15.7	13.7	15.4	22.5	22.6	23.8	22.7	21.4
Cathode CL	3.9	3.1	2.9	2.7	3.2	5.2	4.8	3.2	5.2	4.3

Table S3. 7. Summary of measurements from slice-by-slice analysis of Sample Set B

Sample	Membrane thickness (μm)	Mean per sample (μm)	Distance between CL peaks (μm)	Mean per sample (μm)
0 h (01)	40		52	
0 h (02)	41	44 ± 2	52	54 ± 1
0 h (03)	46		57	
0 h (04)	46		56	
AST (01)	64		85	
AST (02)	65	63 ± 1	92	88 ± 2
AST (03)	61		86	
AST (04)	63		88	

Table S3. 8. Average CL-Membrane distances for each electrode and each sample

Sample Set	Sample	Electrode	Average Membrane Centre - CL Peak distance (µm)	Mean per sample (µm)
A	0 h	Top	35 ± 4	33 ± 8
		Bottom	31 ± 4	
	50 h	Top	43 ± 9	45 ± 11
		Bottom	48 ± 1	
	100 h	Top	45 ± 1	45 ± 7
		Bottom	45 ± 6	
B	0 h	Anode	27 ± 4	27 ± 7
		Cathode	27 ± 4	
	AST	Anode	50 ± 5	44 ± 8
		Cathode	37 ± 3	

Table S3. 9. GDL.MPL/(PA) phase fractions for outer 150 layers of Sample Set B (representing global GDL results)

Sample	Cathode	Anode	Average
0 h (01)	0.34	0.30	0.32
0 h (02)	0.31	0.28	0.30
0 h (03)	0.32	0.29	0.31
0 h (04)	0.28	0.27	0.27
0 h Mean	**0.31**	**0.28**	**0.30**
AST (01)	0.40	0.36	0.38
AST (02)	0.48	0.48	0.48
AST (03)	0.41	0.41	0.41
AST (04)	0.41	0.41	0.41
AST Mean	**0.43**	**0.42**	**0.42**

4. The Performance and Durability of High-temperature Proton Exchange Membrane Fuel Cells Enhanced by Single-layer Graphene

4.1 Manuscript Contribution

The results presented in Chapter 4 are reported in the publication "The performance and durability of high-temperature proton exchange membrane fuel cells enhanced by single-layer graphene, Nano Energy. 93 (2022) 106829. https://doi.org/10.1016/J.NANOEN.2021.106829."

My contributions in this work are as follows:

Investigation: Propose the concept of monolayer graphene to control phosphoric acid leaching based on the characteristics of graphene and phosphoric acid migration in high-temperature hydrogen proton exchange membrane fuel cells.

Methodology: Preparation of polybenzimidazole membranes. Preparation, electrochemical performance testing, and durability testing of pristine membrane-electrode-assembly based on pure polybenzimidazole membrane and sing layer graphene-loaded MEAs at a different position.

Formal analysis: Evaluation of single-layer graphene coverage on electrodes by Raman spectroscopy mapping. Process and analyze electrochemical characterization results including polarization curves, Nyquist curves, cyclic voltammetry curves and linear sweep voltammetry curves. Process X-ray micro-computed tomography data and focus primarily on slice-by-slice segmentations.

Writing-original: Writing of the original draft of manuscript.

Full author list: Jianuo Chen, Josh J. Bailey, Liam Britnell, Maria Perez-Page, Madhumita Sahoo, Zhe Zhang, Andrew Strudwick, Jennifer Hack, Zunmin Guo, Zhaoqi Ji, Philip Martin, Dan J.L. Brett, Paul R. Shearing, Stuart M. Holmes

Authors contribution:

Josh J. Bailey: Methodology (perform X-ray micro-computed tomography), formal analysis (machine learning), writing- review & editing

Liam Britnell: Methodology (transfer of single layer graphene between different substrate)

Maria Perez-Page: Project administration, writing-review & editing

Madhumita Sahoo: Project administration, writing-review & editing

Zhe Zhang: Methodology (Raman spectroscopy and mapping)

Andrew Strudwick: Methodology (growth of single layer graphene on copper foil)

Jennifer Hack: Methodology (perform X-ray micro-computed tomography), formal analysis (continuous pore size distributions and tortuosity factor analysis)

Zunmin Guo: Methodology (electrochemical performance testing)

Zhaoqi Ji: Methodology (electrochemical performance testing)

Philip Martin: Supervision, writing-review editing

Dan J.L. Brett: Supervision, writing-review editing

Paul R Shearing: Supervision, writing-review editing

Stuart M. Holmes: Supervision, project administration, funding acquisition, writing-review editing.

The Performance and Durability of High-temperature Proton Exchange Membrane Fuel Cells Enhanced by Single-layer Graphene

Jianuo Chen [a], Josh J. Bailey [b,d], Liam Britnell [c], Maria Perez-Page [a], Madhumita Sahoo [a], Zhe Zhang [a], Andrew Strudwick [c], Jennifer Hack [b], Zunmin Guo [a], Zhaoqi Ji [e], Philip Martin [a], Dan J.L. Brett [b], Paul R. Shearing [b], Stuart M. Holmes [a,]*

[a] Department of Chemical Engineering and Analytical Science, The University of Manchester, M13 9PL, United Kingdom

[b] Electrochemical Innovation Laboratory, Department of Chemical Engineering, University College London, WC1E 7JE, United Kingdom

[c] Graphene Engineering Innovation Centre, The University of Manchester, M3 3BB, United Kingdom

[d] School of Chemistry and Chemical Engineering, Queen's University Belfast, United Kingdom, BT7 1NN, United Kingdom

[e] School of Automotive Engineering, Harbin Institute of Technology, 264209, China

Corresponding author: Stuart M. Holmes, stuart.holmes@manchester.ac.uk

4.2 Abstract

Single-layer graphene (SLG) obtained by chemical vapour deposition is applied between membrane and electrodes by a wet chemical transfer method to study its effect on the performance and durability of polybenzimidazole membranes in high-temperature proton exchange membrane fuel cells (HT-PEMFCs). After accelerated stress testing (AST), the membrane electrode assembly (MEA) loaded with SLG at different positions exhibits higher peak power density, lower electrode resistances, and larger electrochemical active surface area than pure polybenzimidazole membranes with high phosphoric acid doping levels. The peak power density of the MEAs with both cathode and anode loaded with SLG is 480 mW cm^{-2} after AST, while those based on pure membranes is 249 mW cm^{-2}. Lab-based X-ray micro-computed tomography combined with Raman spectroscopic mapping was applied for the first time to study the effect of SLG on controlling phosphoric acid leaching. In addition, samples containing SLG on an ultra-thin membrane (7.5 µm) were also tested to explore its influence on hydrogen crossover. After 100 hours of galvanostatic discharging, the hydrogen crossover of samples loaded with single-layer graphene on the anode does not exceed 1.75×10^{-4} mol s^{-1}, which is much lower than that of MEAs made using pure ultra-thin membranes (8.16×10^{-4} mol s^{-1}).

4.3 Keywords

4.4 Introduction

Graphene is a two-dimensional carbon nanomaterial with a hexagonal lattice structure [1]. Single-layer graphene (SLG) can block the penetration of almost all molecules and atoms including hydrogen atoms under ambient conditions [2]. Unlike its atomic form, hydrogen ions can easily penetrate graphene with a low tunnelling barrier giving SLG a high proton conductivity. The barrier to proton transport through graphene could be lower than 1.2–2.2 eV, and the resistivity of SLG to proton can be lower than 10^{-3} Ω cm^2 when the temperature reaches 250°C [3][4]. In addition, catalytic metal nanoparticles may enhance the proton transport capability of graphene by virtue of their high affinity for protons [2]. The presence of SLG is extremely minor, even negligible, to weaken the proton conductivity of the proton exchange membrane [5][6][7]. Protons can form an intermediate case between the electrons and atoms of graphene to pass through by simply tunnel [3] [8]. Transmembrane proton transport is driven by electrical polarization across the graphene layer via electrolyte solutions [9]. Combined with the above properties, SLG also has good chemical stability and excellent thermal stability, making it a promising material for proton exchange membrane fuel cells (PEMFC) [10][11].

Although the various properties of graphene have indicated its great potential value for PEMFCs, especially its high selectivity and proton conductivity, it has only successfully been applied to direct methanol fuel cells (DMFC) [5]. The conduction of protons by typical low-temperature PEFMC based on perfluorosulfonic acid (PFSA) membranes is based on the hydration of the sulfonate group at the end of its side chain to generate ionic sites [12]. The replenishment of moisture in PFSA membranes usually depends on the humidification of the gas. Therefore, the application of SLG in PEMFCs based on PFSA polymers is very likely to cause the transmission of water into the membrane to be blocked and affect the proton conductivity of the membrane [13]. Additionally, it is still a challenge to produce large-area, high-quality, low-defect SLG and transfer it to a specific substrate, which limits the application

of SLG in fuel cells [5].

Different from the low-temperature PEMFC, high-temperature (HT-)PEMFC based on polybenzimidazole (PBI) and phosphoric acid (PA) conducts protons by the Grotthuss mechanism, whereby the charge carriers jump across an extended hydrogen bond network established between PBI and PA [14]. Under this mechanism, the fuel cell is no longer so dependent on humidity and the operating temperature can be higher than 100 °C [15]. Therefore, the performance of PA-doped PBI membranes largely depends on the acid doping level (ADL). However, PA leaching will inevitably occur during the operation of HT-PEMFCs [16]. In addition to being mechanically squeezed, diffusion causes PA to leach out from the membrane, when the fuel cell starts and the current increases, PA has been shown to migrate from the cathode to the anode under the influence of "electrochemical pumping" [17][18][19]. Moreover, PA can bleed out from the membrane since PA can be dissolved in the water produced at the cathode [20]. Excessive leaching of PA can cause the blockage of the gas diffusion layer (GDL), poisoning of the catalyst and decrease of the PA content in the membrane, thereby increasing the mass transfer resistance, reducing the activity of the oxygen reduction reaction (ORR), and reducing the proton conductivity of the membrane, respectively [21][22][23][24]. Furthermore, weak mechanical properties of the membrane caused by high ADL and the use of ultra-thin PBI membranes (below 20 µm) may cause significant hydrogen crossover and greatly reduce the performance of the PBI membrane [25][26][27].

Based on the proton conduction mechanism of HT-PEMFC, the performance of PBI does not depend excessively on the entry of external substances such as water. In addition, the relatively high temperature of HT-PEMFC operation is conducive to the high proton conductivity of SLG [5] [10]. Combining these characteristics, SLG is expected to become a barrier between the membrane and the catalyst layer (CL) in HT-PEMFC to prevent hydrogen crossover and excessive PA leaching.

This work aims to explore the effect of the addition of SLG, on HT-PEMFC electrochemical performance, durability, and electrochemically active surface area (ECSA) under lifetime testing or accelerated stress testing (AST). Chemical vapor deposition (CVD) method which can prepare SLG with large area, good compatibility, less disorder and fewer defects was applied [28][29][30][31][32][33][34]. The SLG is designed as a molecular sieve to prevent hydrogen crossover and excessive PA leaching from the membrane to the electrodes.

4.5 Experimental Section

4.5.1 SLG-based MEA Preparation

The preparation of membranes and electrodes, and acid doping are shown in supporting information. SLG generation was achieved by CVD onto polycrystalline copper using methane and hydrogen as precursor gases [35][36]. The transfer of SLG to the electrode was performed by a wet chemical transfer method and a poly(methyl methacrylate) (PMMA) layer was used as the support material for the graphene [37]. The surface of SLG prepared by CVD on a copper sheet was spin-coated with a PMMA layer. A 0.1 M ammonium persulfate aqueous solution was used to etch away the copper sheet to form a SLG-PMMA film. The detached SLG-PMMA film was washed with de-ionised water and floated on the surface of the water. The transfer of SLG-PMMA to an amorphous carbon electrode was achieved by lifting out the electrode from under the floating SLG-PMMA film. After drying at room temperature, PMMA was finally removed under acetone rinsing. The transfer of SLG and the structure of MEA are shown schematically in **Figure 4. 1**.
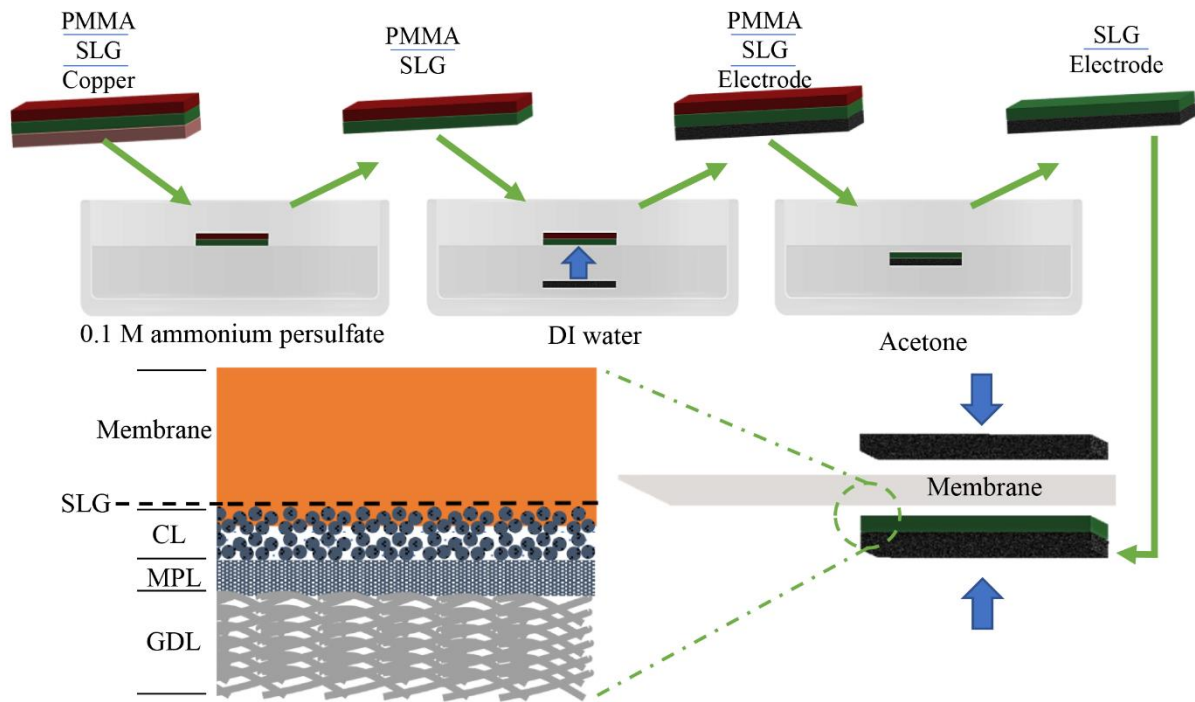
Figure 4. 1. The transfer of SLG and the structure of membrane-electrode-assembly

4.5.2 Characterization of SLG and Electrode Coverage

Raman spectroscopy of the SLG loaded on the copper foil was performed using a Renishaw inVia™ Qontor® confocal microscope system with a 532-nm-wavelength laser. Raman acquisition of the SLG on the electrodes was carried out with the Renishaw inVia utilizing a 785-nm-wavelength laser to prevent laser damage to the catalyst surface and to reduce any fluorescence. A laser spot size of 2 μm was achieved by applying a pinhole. The coverage of SLG on electrodes was evaluated by mapping the catalyst surface and calculating the integrated peak intensity of the 2D peak.

4.5.3 Electrochemical Characterization, Performance Study and MEA Durability Test

The prepared MEAs were assembled into an in-house fuel cell rig and operated at 150 °C with

100 mL min^{-1} dry H_2 and 100 mL min^{-1} dry O_2. A GAMRY E5000 potentiostat was used to measure linear sweep voltammetry (LSV), electrochemical impedance spectroscopy (EIS) and cyclic voltammetry (CV). Accelerated stress test (AST) is performed alternately at 0.6 A cm^{-2} (4 min) and 1A cm^{-2} (16 min), and the open-circuit voltage (OCV) is operated for 10 min every 6 h. The specific parameters of electrochemical characterization are shown in supporting information.

4.5.4 Characterization of PA Distribution and MEA Component Migration

A method combining lab-based X-ray CT and machine-learning segmentation has recently been established in our previous work [38]. Circular samples with a diameter of 2 mm were milled out from MEAs by a laser micro-machining method [39] and placed on a 3D-printed multi-layer jig for X-ray CT measurement. The structure of the jig is shown in **Figure S4. 1**. A Zeiss Xradia 520 Versa (Carl Zeiss) X-ray micro-CT instrument, equipped with polychromatic source and 30 to 160 kV tube voltage, was utilized to scan all samples. The specific parameters for XCT image acquisition are shown in **Table S4. 1**.

Raman mapping of MEA cross-sections was carried out using a Renishaw inVia with a 785 nm laser. MEAs were manually cut by a scalpel to expose the cross-section. The resultant spectra were baseline-corrected and normalized. The free PA peak (~911 cm^{-1}) intensity was used to form the concentration maps and the distribution curves.

4.6 Results and Discussion

4.6.1 SLG Coverage of Electrodes

A typical Raman spectrum of graphene prepared by CVD onto copper foil is shown in **Figure 4. 2**a. The Raman spectrum only showed a G peak and a narrow 2D peak at Raman shifts of 1590 cm^{-1} and 2680 cm^{-1}, respectively. The intensity ratio of the 2D peak to the G peak (I_{2D}/I_G)

was ca. 2.5, which indicates that the graphene is monolayer [40][41][42][43]. 20×20 µm Raman mapping with 64 points in 5 arbitrary areas across a macroscopic sample of A5 size was carried out. The I_{2D}/I_G of all of the spectra exhibit the same as the Raman spectrum shown in Figure 2a indicating that the graphene prepared by CVD was effectively defect-free SLG with 100% coverage of the copper foil. The graphene on the copper foil is transferred by the wet chemical transfer method. It has been shown through Raman spectroscopy that the graphene on the copper foil is a single-layer graphene. The wet chemical transfer method still maintains the graphene on the target substrate as a single layer [37]. Therefore, the thickness of graphene on the electrode surface is assumed to be about 0.335~1nm [40][41][42][43].

Although the SLG maintains good integrity on the copper sheet, SLG is prone to cracking and defect generation during the transfer from the copper sheet to the target substrate [44]. The Raman spectrum of the catalyst surface is shown as the orange curve in **Figure 4. 2**b. Raman spectrum on the electrode surface basically has no 2D peak. This may be attributed to the relatively weak energy of the 785 nm laser, which is not powerful enough to observe the relatively weak 2D peaks in graphite [45]. The Raman spectrum of the catalyst surface with SLG is shown in the blue curve in **Figure 4. 2**b. Due to the use of electrodes with graphite-related materials as the substrate for the Raman spectroscopy, subject to the influence of the G and D peaks of the graphite materials, it is difficult for the Raman spectra of graphene on the catalyst surface to be fully consistent with the characteristics of SLG. However, the relatively strong narrow 2D peak characteristic of SLG is not completely covered by the signal from the substrate. Therefore, the 2D peak area can be used as a strong basis for whether the electrode is covered with SLG. Raman spectroscopic mapping of the 2D peak of two regions on the surface of the SLG-loaded electrode is shown in **Figure 4. 2**c (Region 1) and d (Region 2). The heterogeneous distribution area of the 2D peak has obvious boundaries. The blue area is regarded as the area without graphene. The SLG coverage shown by Raman mapping in Region

1 and Region 2 is approximately 75% and 45%, respectively, indicating the distribution of SLG in different regions may be vary to differing extents. Through multi-region Raman mapping, the average coverage of SLG on the electrode surface was measured to be ca. 55±5%.
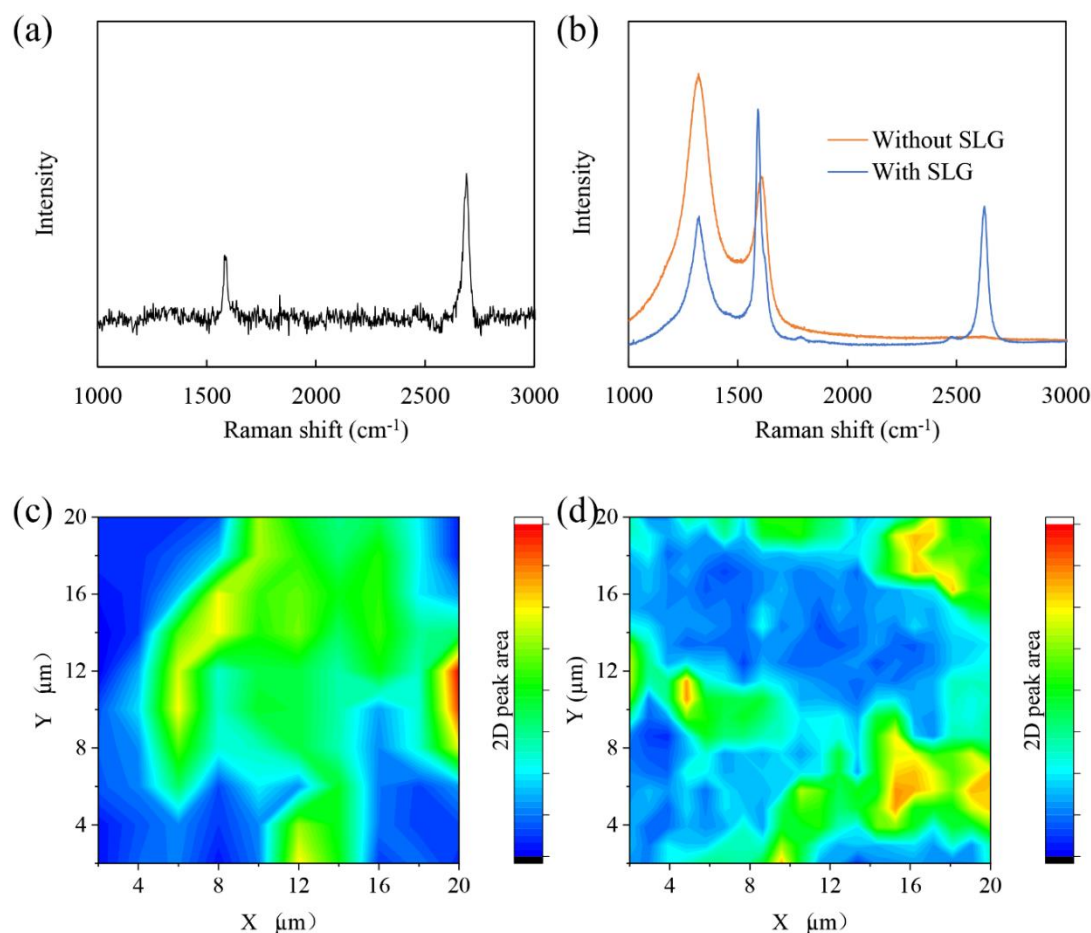
Figure 4. 2. Raman spectrum and Raman mapping (785nm laser) of SLG on different substrates, (a) Raman spectrum of SLG on copper foil, (b) Raman spectra of electrode surface with (blue line) and without (orange line) SLG, (c) Raman mapping of electrode surface region 1, (d) Raman mapping of electrode surface region 2.

4.6.2 Impact of SLG on PA leaching

Electrochemical Characterization

To explore the impact of SLG on HT-PEMFC performance and durability, SLG was loaded on the anode, or cathode, or both sides. For all membranes, the ADL was approximately 11.5. MEAs without SLG, SLG on the anode, SLG on the cathode, and SLG on both sides are denoted PBI, AS, CS, and ACS, respectively. The naming of MEAs under different conditions

is shown in **Table 4. 1**. The initial measurement of MEAs is shown in **Figure 4. 3**. The peak

power density of various MEAs is shown in **Table 4. 1**. From the perspective of power density

curves, PBI-I and CS-I have similar performance, while AS-I and ACS-I have similar but lower

performance. The application of SLG did not improve the performance of HT-PEMFC in the

initial measurement, such that AS and ACS performed worse than the pristine MEAs. The

difference in the performance of MEAs reflected by polarization curves in the initial

measurement begins to appear at the low current density stage, which is mainly associated with

activation polarization losses [46]. In the low current density stage, AS-I and ACS-I showed

the most rapid voltage loss, followed by PBI-I and CS-I. The middle current density stage is

dominated by ohmic losses, as the current density increases, the change in this difference is not

obvious. Thus, ohmic losses is not the main cause of the difference in voltage loss [46].

Table 4. 1. MEA nomenclature, electrochemical performance, and resistances

Name	SLG load	Condition	Peak power density (mW cm^{-2})	Ohmic resistance (mΩ cm^2)	Charge transfer + mass transfer resistance (mΩ cm^2)
PBI-I	No SLG	Before operation	404	201	307
AS-I	Anode side	Before operation	330	205	394
CS-I	Cathode side	Before operation	399	229	276
ACS-I	Both sides	Before operation	321	263	348
PBI-F	No SLG	After AST	249	199	414
AS-F	Anode side	After AST	367	205	355
CS-F	Cathode side	After AST	365	221	320
ACS-F	Both sides	After AST	480	205	308

The performance indicated by the final measurement of different MEAs after AST showed in

Figure 4. 3b represents a significant change compared to initial measurements. ACS-F had the

highest peak power density of 480 mW cm^{-2}. AS-F and CS-F had similar peak power densities

of 367 mW cm^{-2} and 365 mW cm^{-2}, while the peak power density of CS-F appeared at a lower

current density. PBI-F showed the lowest peak power density, which was 249 mW cm^{-2}. From

the voltage loss at different current density stages, PBI-F had the largest activation polarization losses, ohmic losses and concentration polarization losses.

The performance changes are directly reflected by the voltage changes at different current densities during the AST shown in **Figure 4. 3**c. The upper, middle, and lower curves of each MEA represent the OCV, the voltage at 0.6 A cm^{-2} and the voltage at 1 A cm^{-2}, respectively. During the AST, the MEA based on a pure PBI membrane maintained a stable OCV, but the voltage at different current densities continued to drop significantly. This is generally considered to be caused by factors such as corrosion, deactivation, or migration of the internal components of the MEA, and established test methods have been shown to accelerate these aging processes [47][48][49]. In addition, the detrimental edge effects caused by the small electrode size and the high ADL may also accelerate the voltage drop versus other literature examples [38]. The voltage changes at different current densities are shown in **Figure 4. 4**. The voltage loss of the MEA based on a pure PBI membrane at a high current density of 1 A cm^{-2} is more obvious than that at 0.6 A cm^{-2}, 43.3% and 23.6%, respectively. Different from PBI, the voltage of AS and ACS at different current densities increased versus the initial stage, rather than decreasing. This difference is reflected in the first 6-h cycle shown in the inset in **Figure 4. 3**c. The performance of PA-based HT-PEMFC continues to improve can be explained by favourable PA redistribution, the removal of impurities, or the formation of new catalytic sites that lead to the activation [50][51]. Although the initial voltage of AS and ACS was slightly lower than that of PBI at different current densities, these values surpass that of PBI after about 7 h of AST. After 24 h, the voltage of AS remained effectively constant, while the voltage of ACS increased throughout the entire 70-h test. Although the voltage of CS continued to drop during AST, its drop is only about a quarter of that of PBI. To further test the durability of ACS, an additional 70 h of AST was run. The voltage changes at different current densities during the AST from 70 to 140 h are shown in **Figure S4. 2**. In the additional AST, the voltage of the

ACS at different current densities maintained a slow rise in the first 25 h. After that, the voltages remained relatively stable. At the end of the additional AST of ACS (named ACS-E), the peak power density of ACS-E reached 511 mW cm^{-2}. The polarization curve and power density curve of ACS-E are shown in **Figure S4. 3**.

Nyquist curves of initial and final measurement are shown in **Figure 4. 3**d and e, respectively. The equivalent circuit for fitting is shown in **Table 4. 2**. The resistance between the intercept on the real Z-axis at high and low frequencies is interpreted as the sum of charge transfer resistance and mass transfer resistance of the anode and cathode, hereafter referred to as $\Delta R_{Charge+Mass}$ [52][53][54][55][56]. The various resistances reflected by intercepts on the real Z-axis in the Nyquist curves are summarized in **Table 4. 1**. PBI-I and AS-I had very similar Ohmic resistance, which indicates that placing SLG between the anode and the PBI membrane does not cause significant hindrance to protons conduction, potentially benefitting from excellent proton conductivity of SLG and high operating temperature [2][3]. Unlike AS-I, CS-I has lightly larger ohmic resistance and ACS-I have significantly larger ohmic resistances compared to PBI-I. That may be due to SLG blocking water generated at the cathode from entering the electrolyte in a short time to hydrate and positively influence membrane conductivity [56]. Since the coverage of the SLG on the electrode is limited, long-term operation at high current density provides the possibility for the water produced at the cathode to enter the electrolyte and hydrate it. Thus, PBI-F, AS-F, CS-F and ACS-F all have closer ohmic resistance. It is worth noting that the ohmic resistance of ACS-I is significantly larger than that of CS-I, and the ohmic resistance of ACS-I before and after AST changes more than that of CS-I. This may be due to the fact that the performance of ACS in the initial stage is much lower than that of CS, resulting in that the water production of ACS-I after initial activation is much smaller than that of CS-I, so that the ohmic resistance of ACS-I is larger than that of CS-I. The difference in the impedance of each MEA is more reflected in

179
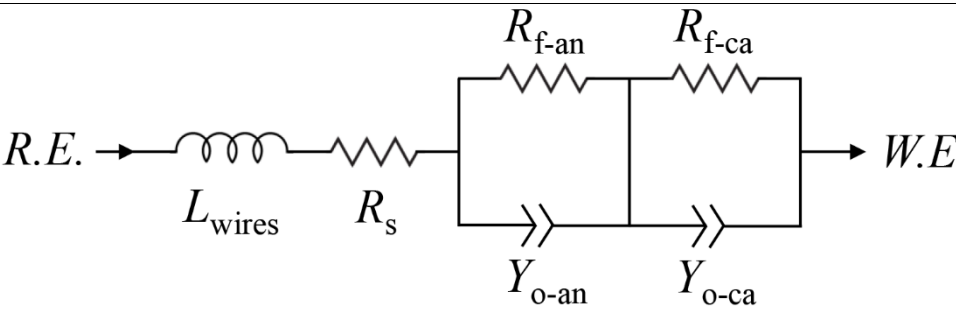
$\Delta R_{Charge+Mass}$. The relationship between the magnitude of $\Delta R_{Charge+Mass}$ in the initial measurement of different MEAs is AS-I > ACS-I > PBI-I > CS-I. However, this relationship is completely changed in final measurement. In the final measurement, the relationship between the $\Delta R_{Charge+Mass}$ of each MEA is PBI-F > AS-F > CS-F > ACS-F. The value and change of $\Delta R_{Charge+Mass}$ may be affected by various factors such as PA migration, catalyst migration and corrosion, and the complex environment in electrodes.

The initial and final CV curves with calculated ECSA are shown in **Figure 4. 3**f and g, respectively. Since the leaching of PA into the CL will poison platinum at high temperatures, and the adsorption of phosphate anions on the catalyst surface will block catalyst active sites, *in-situ* CV measurement of HT-PEMFC is not rigorous like the low-temperature PEMFC [22][23] [57]. The aforementioned influence of PA on the catalyst causes distortion of the CV curves such that the peak of the CV curve becomes very small [22]. The distortion of this CV peak is fully reflected in the CV curves of PBI-I and AS-I. The ECSA of PBI-I and AS-I were only 55.5 cm^2 mg^{-1} and 55.2 cm^2 mg^{-1}, respectively, and the ECSA of them dropped further after AST. However, the ECSA of the cathode of CS-I and ACS-I, is much larger than that of PBI-I and AS-I. The ECSA of the cathode of CS-I and ACS-I were 388.1 cm^2 mg^{-1} and 302.4 cm^2 mg^{-1}, respectively, which is almost 7 times that of PBI-I and AS-I. This indicates that the protection of the surface of the catalyst by SLG at the cathode is immediate. While SLG has high proton conductivity and electronic conductivity, it forms a certain isolation between PA and the surface of the catalyst that may prevent excessive phosphate anions from adsorbing onto the surface of the catalyst, thereby increasing ECSA. As for the ECSA of CS-I is higher than ACS-I, it may be due to the osmotic pressure of phosphoric acid in the membrane with SLG on both sides should be higher than when SLG is used on one side or SLG is not used on both sides. Therefore, ACS is easier to leach appropriate amount of phosphoric acid at the cathode than CS. In other words, the ACS may have more phosphoric acid covering the catalyst

at the cathode. Although the ECSA of CS-F (248 cm^2 mg^{-1}) and ACS-F (185.8 cm^2 mg^{-1}) both declined compared with their respective initial values, they were still much larger than the ECSA of PBI-F (50.0 cm^2 mg^{-1}) and AS-F (50.8 cm^2 mg^{-1}). The protective capability of the catalyst by SLG is still present after AST.

Table 4. 2. The equivalent circuit and the definition of parameters

Equivalent circuit	
L_{wires} (H)	Inductance of cables
R_s (ohm)	Ohmic resistance
R_{f-an} (ohm)	Charge transfer resistance of anode
Y_{o-an} (S s^a)	Constant phase element of anode
R_{f-ca} (ohm)	Charge transfer resistance of cathode
Y_{o-ca} (S s^a)	Constant phase element of cathode
a	Dimensionless exponent
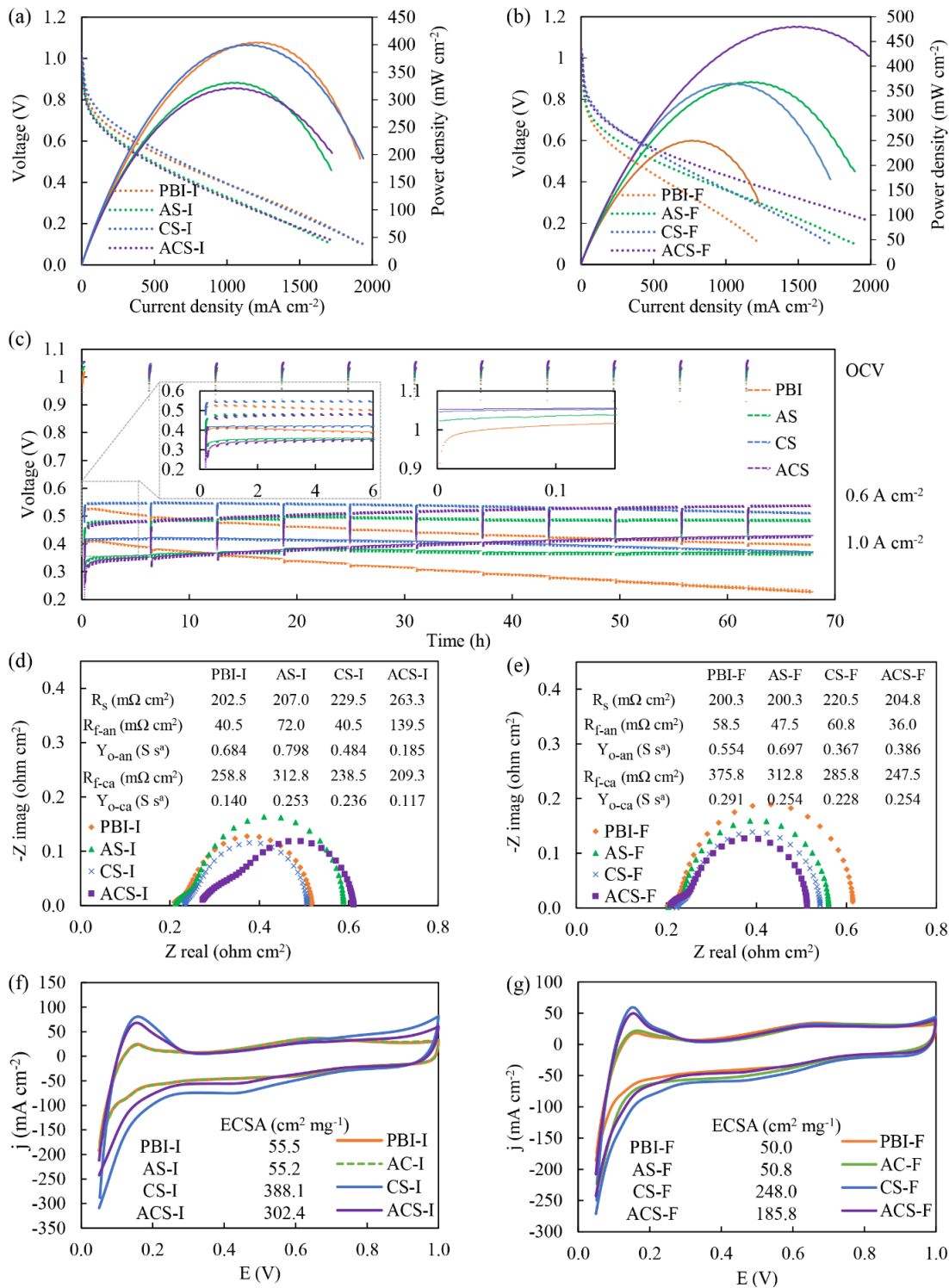
Figure 4. 3. Electrochemical characterization: (a) initial measurement of polarization curves and power density curves (150 ℃, anode: 100 mL min⁻¹ hydrogen, 1 mg cm⁻² Pt; Cathode: 100 mL min⁻¹ oxygen, 1 mg cm⁻² Pt), (b) final measurement of polarization curves and power density curves, (c) AST process, (d) initial measurement of Nyquist curves, (e) final measurement of Nyquist curves, (f) initial measurement of CV curves and (g) final measurement of CV curves (150 ℃, anode: 100 mL min⁻¹ hydrogen; Cathode: 33.4 mL min⁻¹ nitrogen)

182
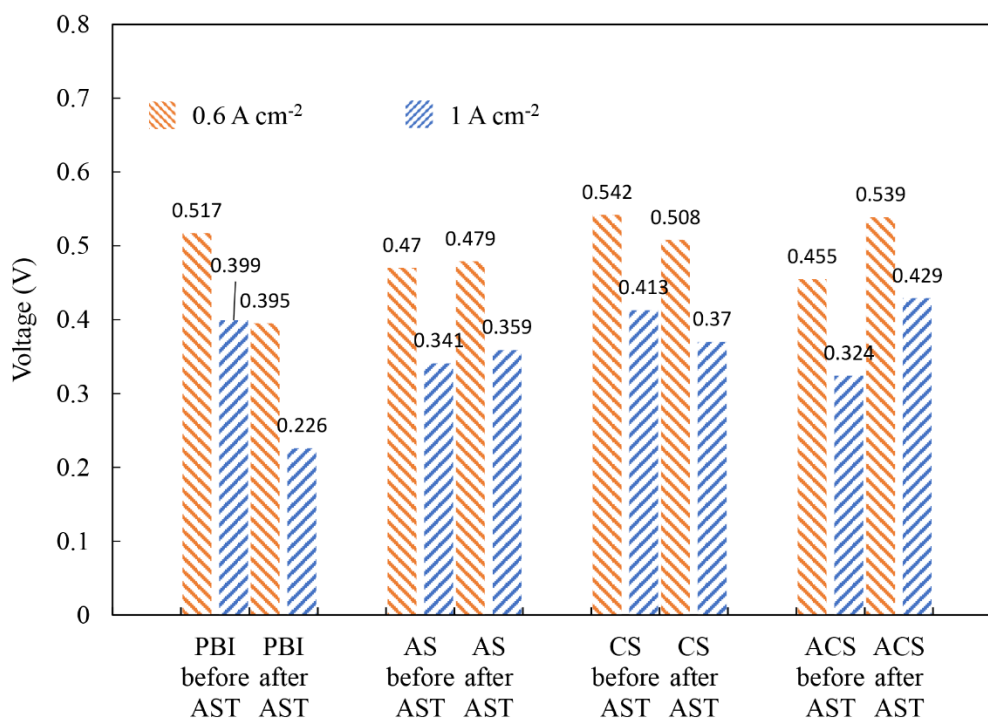
Figure 4. 4. The voltage changes under different current densities before and after AST

X-ray CT

Typical 3D X-ray CT segmentations of MEA and GDL of each sample are shown in **Figure 4. 5**. Since the lab-based X-ray CT in this work is unable to distinguish between (microporous layer) MPL, GDL and PA, the yellow and green phases shown in **Figure 4. 5**a, c, e, g and i represent a mixture of MPL, GDL and PA of anode and cathode, respectively. GDL/MPL/(PA) composite phase may contain carbon materials, polytetrafluoroethylene (PTFE) binder, and PA. Although limited by the degree of discrimination, the distribution of the GDL/MPL/(PA) phase in the segmented XZ-orthoslice and filtered XZ-orthoslice of layer 506 in **Figure 4. 5**a and c are significantly different. Compared with the pristine MEA, the yellow and green phases in the PBI-F tomogram show significant expansion, which is also accompanied by a decrease in the porosity represented by the black area. The expansion of GDL/MPL/(PA) composite phase indirectly indicates the leaching of PA, which has been demonstrated in our previous work by comparing tomograms of 'wet' electrodes soaked in PA with 'dry' electrodes [38]. This

phenomenon can be more intuitively reflected in the phase fraction parameters of the GDL/MPL/(PA) composite phase shown in **Table 4. 3**. The voxels of the GDL/MPL/(PA) phases in the anode and cathode of the pristine MEA account for 15.7% and 16.1% of the total $1015 \times 1015 \times 508$ voxels. However, in PBI-F, the phase fractions of Anode GDL/MPL/(PA) phase and Cathode GDL/MPL/(PA) phase reached 22.7% and 22.6%, respectively. The CL has the greatest average X-ray attenuation coefficient due to the electron-dense Pt contained within, and thus appears brightest in orthoslice in **Figure 4. 5**. Combined with the resolution used, chosen to capture a representative volume element, means the distribution of PA in the catalyst is not resolvable. However, it is not difficult to infer that the swelling of GDL/MPL/(PA) composite phase from the pristine MEA to the post-AST MEA in the electrode indicates PA leached through the CL and MPL to reach the GDL. The degree of PA migration also indicates that it is most likely the CL is saturated with PA by the end of the AST. According to the tomographic images in **Figure 4. 5**e, g and i and the phase fraction data in **Table 4. 3**, it can be inferred that SLG significantly reduces the degree of PA leaching after AST. The phase fraction of the anode of AS-F is smaller than that of the cathode, being 17.4% and 21.2%, while the phase fraction of the anode of CS-F is greater than that of the cathode, being 23.7% and 19.4%, respectively. According to slice-by-slice plots of area fraction from Layer 1 to Layer 506 in the *z*-direction of AS-F and CS-F shown in **Figure 4. 5**k and l, the above differences are mainly reflected in layers 100 to 200 and layers 300 to 400. The high phase fraction of GDL/MPL/(PA) is accompanied by the low phase fraction of pore. In the same way, the GDL/MPL/(PA) phase fraction of the anode and cathode sides of the MEA of ACS-F are relatively small, and the porosity is relatively large.

PA leaching may not only immerse the CL but also drive the migration of the catalyst. This can be seen from the X-ray CT segmentation of the CL phase of pristine MEA and PBI-F

shown in **Figure 4. 5**b and d. By comparing the catalyst distribution of the SLG-loaded MEA in **Figure 4. 5**f, h, j, k, l and m, the migration of the catalyst and the migration of PA are linked to a certain extent. The CL phase is more concentrated at the junction of the membrane and the electrode on the side of the electrode with SLG than on the side of the electrode without SLG.

Legend: Anode GDL/MPL/(PA) ■ Anode CL ■ Membrane ■ Cathode CL ■ Cathode GDL/MPL/(PA) ■

Plot legends: Anode_CL ── Anode_GDL/MPL/(PA) ── Anode_Pore ── Membrane ── Cathode_Pore ── Cathode_GDL/MPL/(PA) ── Cathode_CL ──
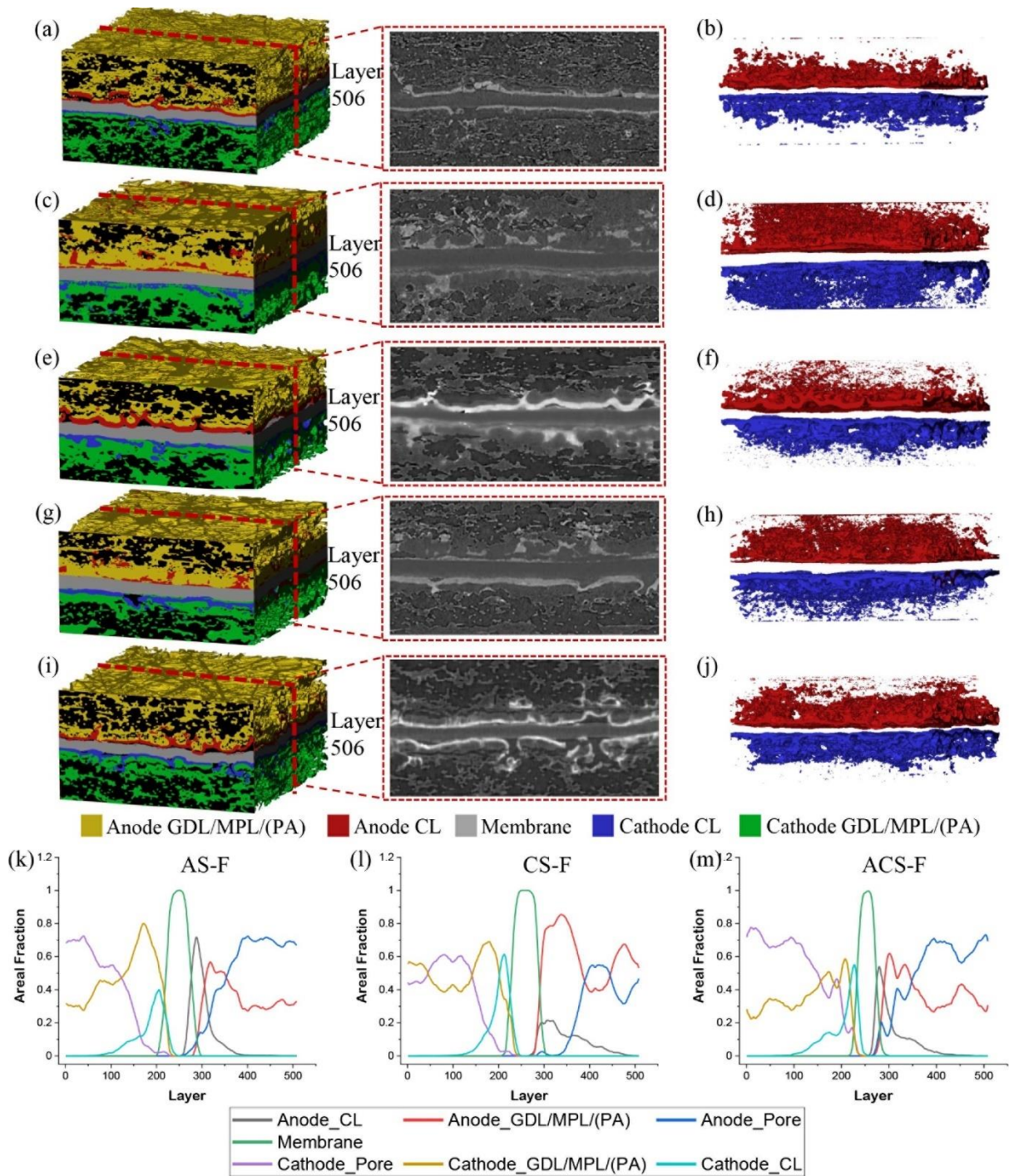
Figure 4. 5. 3D X-ray CT segmentation of (a) pristine MEA with unsegemted orthoslice of layer 506, (b) pristine CL, (c) PBI-F MEA with unsegemted orthoslice of layer 506, (d) PBI-F CL, (e) AS-F MEA with unsegemted orthoslice of layer 506, (f) AS-F CL, (g) CS-F MEA with unsegemted orthoslice of layer 506, (h) CS-F CL, (i) ACS-F MEA with unsegemted orthoslice of layer 506 and (j) ACS-F CL. Slice-by-slice plots of area fraction from Layer 1 to Layer 506 in the Z-direction of (k) AS-F, (l) CS-F and (m) ACS-F

Table 4. 3. Global GDL/MPL/(PA) of phase fraction of MEAs

Sample	Electrode	GDL/MPL/(PA) phase fraction	Mean
Pristine MEA	Anode	15.7%	15.9 ± 0.4%
	Cathode	16.1%	
PBI-F	Anode	22.7%	22.7% ± 0.3%
	Cathode	22.6%	
AS-F	Anode	17.4%	19.3 ± 1.3%
	Cathode	21.2%	
CS-F	Anode	23.7%	21.55 ± 3.6%
	Cathode	19.4%	
ACS-F	Anode	16.3%	16.3 ± 0.4%
	Cathode	16.2%	

Raman Spectroscopy

X-ray CT describes the migration of components in HT-PEMFC from morphology, and Raman may prove it from a chemical point of view. Raman spectroscopy can detect the signal of free PA in the high ADL PBI membrane when the Raman shift is around 911 cm^{-1}[56] [58]. The Raman spectrum of PA-doped PBI membranes is shown in **Figure 4. 6**a. The Raman spectroscopic mapping of free PA peak area of PBI-I, PBI-F, AS-F, CS-F and ACS-F in the 2D form is shown in **Figure 4. 6**b, c, f and h, respectively. Since Raman spectroscopic mapping is obtained by scanning the cross-sections of different samples, the thickness of each component of each sample may be different. Therefore, it is difficult to explain the migration of PA in different MEAs by comparing the size and dimension of PA distribution. However, by comparing the Raman spectroscopic mapping of PBI-I and PBI-F, free PA has a clear boundary before AST but this changes after AST. Compared with PBI-I, the free PA boundary of PBI-F shows a step-like decline from membrane to electrodes and this is more obvious in the cathode than the anode. In addition, by observing 2D Raman spectroscopic maps of AS-F, CS-F and ACS-F, the boundary of free PA on the SLG side of these MEAs is closer to the boundary between the membrane and the electrode by comparing with the 2D Raman mapping

of PBI-F. The difference in the distribution of free PA in PBI-I and PBI-F as well as the influence of SLG on the migration of free PA can be shown more visually by 3D Raman spectroscopic mapping. The Raman spectroscopic mapping of PBI-I, PBI-F, AS-F, CS-F and ACS-F in the 3D form is shown in **Figure 4. 6**d, e, i, j and k, respectively. In contrast to the 2D mapping, the boundary of free PA of PBI-I was steeper than that of PBI-F in 3D mapping. Similarly, SLG also steepened the phosphate boundary on the additive side. The different ranges of intensity may have an impact on the degree of convergence of the PA boundary in Raman spectroscopic mappings. However, comparing the ratio of the average slope of the PA boundary between anode and cathode in 3D Raman spectroscopic mappings, hereafter referred to as $|S_{Anode/Cathode}|$, can more rigorously illustrate the influence of SLG on PA migration. $|S_{Anode/Cathode}|$ of PBI-F, AS-F and CS-F are 4.48, 7.14 and 2.11, respectively. Assuming the PA leaching situation on the side of the electrode without SLG remains unchanged, the free PA boundary on the side with SLG function on AS-F and CS-F will be steeper than that of PBI-F. The $|S_{Anode/Cathode}|$ of ACS-F of 2.14 is similar to PBI-I of 2.91. Therefore, SLG has a buffering effect on PA leaching on its active side, which is observable by Raman spectroscopic mapping of different MEAs cross-sections. As for the obvious difference between the cathode and the anode shown in Raman spectroscopic mapping of PBI-F and AS-F, or because the uneven distribution of PA caused by the action of the "electrochemical pump" and the driving effect of the water produced by the cathode on PA [17][18] [20].
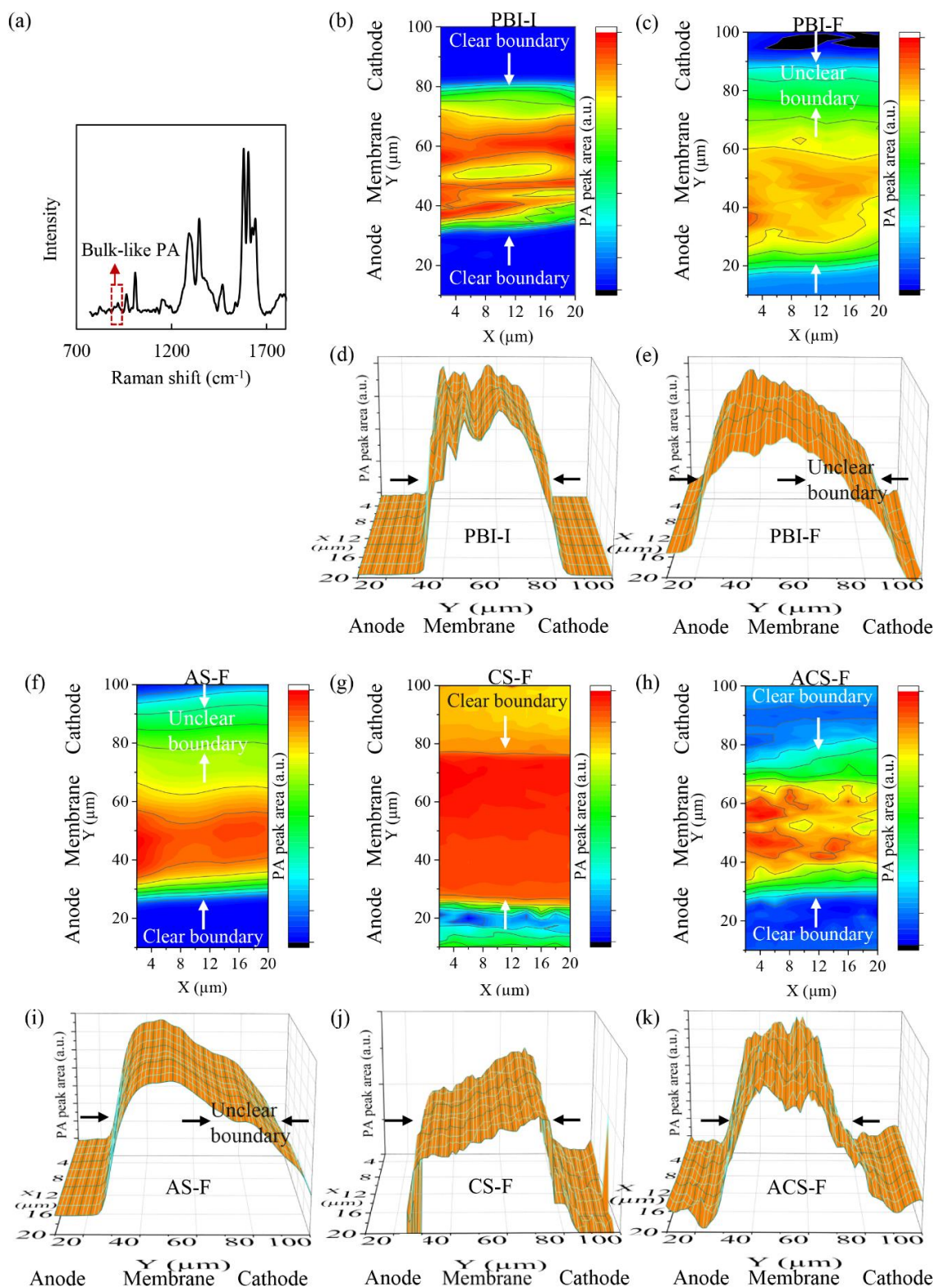
Figure 4. 6. Raman spectrum and Raman mapping at 785 nm, (a) Raman spectrum of PA-doped PBI membrane showing free PA at 911 cm⁻¹, Raman mapping of the free PA peak at 911 cm⁻¹, (b) PBI-I in 2D, (c) PBI-F in 2D, (d) PBI-I in 3D, (e) PBI-F in 3D, (f) AS-F in 2D, (g) CS-F in 2D, (h) ACS-F in 2D, (i) AS-F in 3D, (j) CS-F in 3D, (k) ACS-F in 3D

4.6.3 Mechanism

The following mechanism for how SLG acts in an HT-PEMFC is proposed. The hydrogen oxidation reaction (HOR) and the ORR, which involve catalytic active reaction processes, mainly occur at the three-phase boundary composed of electrolyte (PA), catalyst and gas [59][60]. Therefore, the three-phase boundary directly affects the charge transfer resistance and the activation loss in the polarization curve, and its size plays a vital role in the performance. As shown in **Figure 4. 7**, the green line represents the three-phase boundary of a specific cross-section of the MEA. When PA is not leached from the PBI membrane at all, the three-phase boundary is simply the interface between the membrane and the catalyst (approximately planar under ideal circumstances). With the proper amount of PA leaching from the membrane into the CL, the three-phase boundary can be envisaged as changing from the straight green line to the wavy green line, which makes the three-phase boundary larger. This is also one of the reasons for the activation of HT-PEMFC [50][51]. However, when PA excessively migrates into the GDL, the CL is submerged and driven to migrate, and the pores in the GDL are blocked, affecting gas transport. In these situations, the charge transfer resistance and mass transfer resistance of the MEA increase. Since the SLG prepared by CVD has good mechanical properties and good large-scale integrity, it has a good buffering effect on PA, which can be observed in X-ray CT, Raman mapping and CV. At the same time, SLG has ultra-high proton conductivity, so it does not significantly affect the transmission of protons while preventing the leaching of PA, which is reflected in the EIS analysis. In summary, SLG can perform proton transfer and acts as a boundary between PA and catalyst to protect the catalyst from being soaked so that gas can reach it. Therefore, SLG can act as part of the three-phase boundary. In addition, due to the limited coverage of the SLG on electrodes, PA can still be leached out between the gaps in SLG coverage to provide a favourable distribution of PA in the vicinity of the membrane (shown in the bottom-right image in **Figure 4. 7**). This is conducive to the

expansion of the three-phase boundary. As mentioned above, there are different mechanisms for the leaching of phosphoric acid at the anode and cathode. During the AST process, the continuous application of higher current density and the alternating changes of the current will cause the PA to move from the cathode to the anode under the drive of the 'electrochemical pump' [17][18][19]. At the cathode, the production of water will also cause the leaching of phosphoric acid [20]. Therefore, the appropriate amount of PA leaching at the cathode though the gap of SLG occurs at the initial stage after initial activation and is less affected by the AST process compared to the anode. It is worth noting that in the initial stage, the difference in impedance of different MEAs is mainly reflected in the R_{f-an} of AS-I and ACS-I is much larger than that of CS-I and PBI-I. This results in the performance of CS-I being better than AS-I and ACS-I. With the progress of AST, the PA of AS-I and ACS-I gradually leached from the gaps of SLG to form a sawtooth-shaped phosphoric acid distribution, which increased the three-phase boundary and gradually improved the performance. This can be reflected by the impedance changes of AS and ACS before and after AST. Since CS cannot control the excessive PA leaching at anode, the performance gradually declines. In AS, the performance improvement caused by the further appropriate PA leaching at anode may be countered by the performance degradation caused by the excessive PA at cathode. Therefore, the performance of AS in the later stage of AST no longer increases, while the performance of ACS continues to increase.
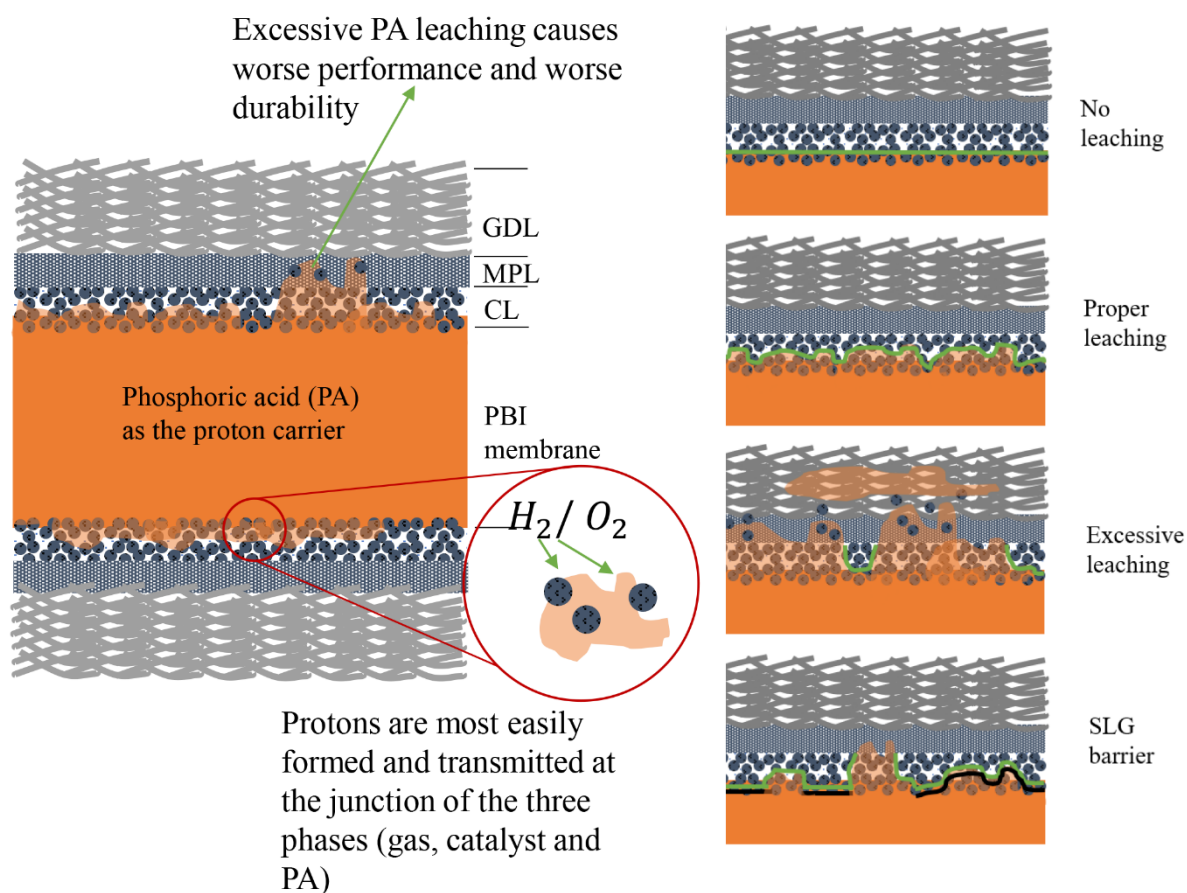
Figure 4. 7. The proposed mechanism behind the positive effect of SLG on HT-PEMFC performance

4.6.3 Impact of SLG on Hydrogen Crossover

To explore the effect of SLG on hydrogen crossover of ultra-thin PBI (UT-PBI) membranes, a PBI membrane with a thickness of 7.7 μm was prepared, and the SLG was added between anode and membrane (UT-AS). To avoid the strong influence of AST on PA leaching, UT-PBI and UT-AS were tested under a constant current of 600 mA instead of the AST. The polarization curves and power density curves of MEAs based on ultra-thin PBI membrane under different conditions are shown in **Figure 4. 8**. I and F stand for initial measurement and final measurement after 100 h testing, respectively. The ultra-thin nature of the membrane allowed for a large amount of hydrogen permeation, which gave an OCV for UT-PBI-I of only 0.57 V. Nevertheless, reducing the thickness of the membrane also reduces membrane resistance, which can be seen in the relatively low ohmic loss in the medium current density

stage. This gave a relatively high maximum power density of UT-PBI-I (464 mW cm^{-2}), even higher than the maximum power density of PBI-I (404 mW cm^{-2}). The OCV for UT-AS-I of 0.80 V was significantly higher than that of UT-PBI-I, indicating that SLG had a significant blocking effect on hydrogen crossover. Although UT-PBI and UT-AS both had relatively high ADL, the ultra-thin nature made their overall PA content relatively low. Although this is helpful to avoid the side effects of excessive PA leaching, SLG may prevent the only PA in the PBI membrane from proper leaching to the electrode, leading to a dead zone between the membrane and the electrode, and the appearance of these dead zones will affect proton conduction [50][51]. The 100-hour test of UT-PBI and UT-AS is shown in **Figure 4. 8**b. The voltage of UT-PBI continued to drop over time. In **Figure 4. 8**a, the polarization curve of UT-PBI-F is almost a downward shift of the polarization curve of UT-PBI-I, and the OCV of UT-PBI-F dropped from 0.57 V at the initial measurement to 0.48 V. Therefore, the continuous drop in voltage of UT-PBI during the test was largely due to the gradual increase in hydrogen crossover. Unlike UT-PBI, the voltage of UT-AS continued to rise during the test. This is most likely caused by the activation of the MEA due to the reduction of the dead zone during operation [50][51]. The OCV for UT-AS-F was effectively the same as that of UT-AS-I, which shows that there is no significant increase in hydrogen crossover during the operation of UT-AS. In addition, due to activation, the performance of UT-AS-F was significantly improved compared to UT-AS-I. The maximum power density of UT-AS-F reached 513 mW cm^{-2}, which is better than all aforementioned MEAs. The blocking effect of SLG on hydrogen crossing can be further reflected in the LSV curve shown in **Figure 4. 8**c. The limiting current density from the LSV curves and the calculated hydrogen crossover flux are shown in **Table 4. 4**. SLG had a certain blocking effect on the hydrogen crossover of ultra-thin PBI, and it continued to play a role throughout testing. Although SLG failed to produce an OCV at the normal level (usually considered to be 1 V), UT-AS still showed excellent performance in view of the low ohmic

resistance of the ultra-thin PBI membrane.

Table 4. 4. Hydrogen crossover flux of UT-PBI and UT-AS

MEA	$j_{H_2\ Cross}$ (mA cm^{-2})	$\dot{n}H_2\ Crossover$ (mol s^{-1})
UT-PBI-I	21	2.45×10^{-4}
UT-PBI-F	70	8.16×10^{-4}
UT-AS-I	14	1.63×10^{-4}
UT-AS-F	15	1.75×10^{-4}
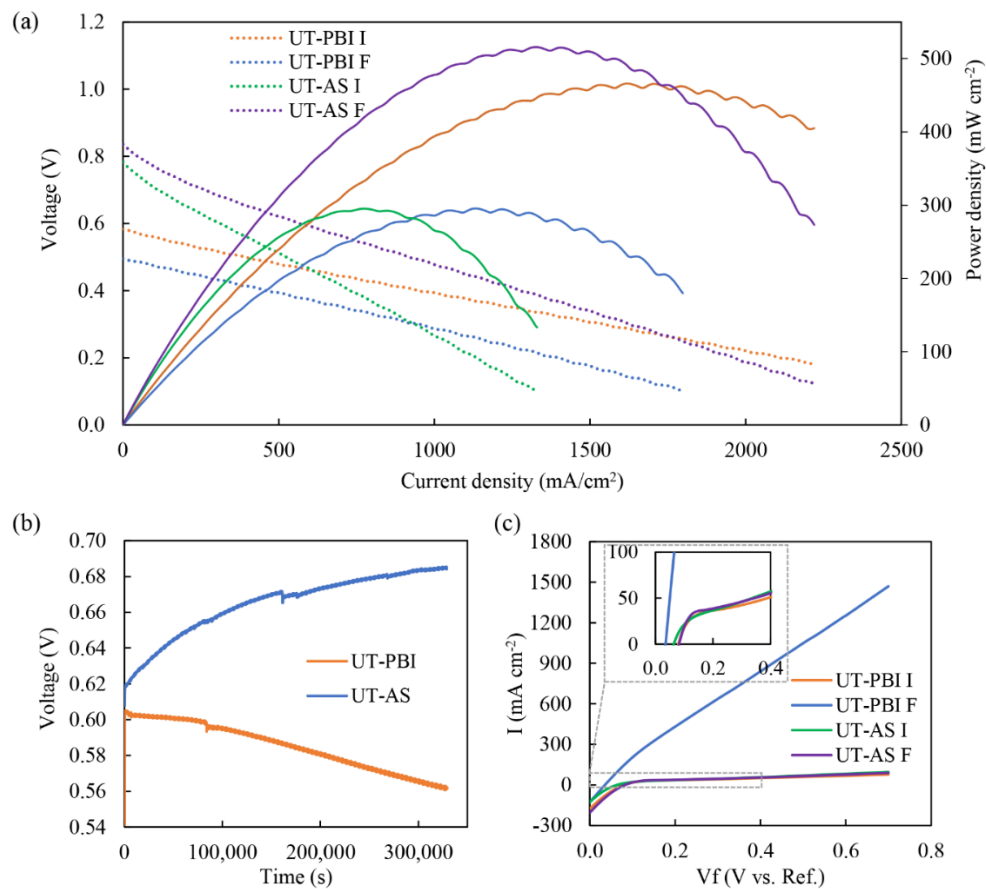
Figure 4. 8. Electrochemical characterization of UT-PBI and UT-AS: (a) polarization curves and power density curves (150 ℃, anode: 100 mL min⁻¹ hydrogen, 1 mg cm⁻² Pt; Cathode: 100 mL min⁻¹ oxygen, 1 mg cm⁻² Pt), (b) constant-current (600 mA) discharging curves, (c) LSV curves (150 ℃, anode: 100 mL min⁻¹ hydrogen; Cathode: 100 mL min⁻¹ nitrogen)

4.7 Conclusions

Large-size and high-quality SLG prepared by CVD was added between the membrane and anode, the cathode and both sides to study the effect of SLG on the performance and durability of PA-doped PBI membrane-based HT-PEMFC. The average coverage of the SLG on the

194

electrode estimated by Raman spectroscopic mapping was about 55%±5%. The performance of AS-I and ACS-I, reflected by their peak power densities of 330 mW cm^{-2} and 321 mW cm^{-2}, respectively, was significantly lower than that of PBI-I (404 mW cm^{-2}). However, when the SLG is only placed on the cathode side, its effect on the initial stage performance in terms of its peak power density is not obvious (399 mW cm^{-2} for CS-I). Although the SLG did not contribute to the power output in the initial stage of the test, the *in-situ* ECSA of the cathode of the MEA with SLG loaded on the cathode was significantly higher than that of the PBI-I. The introduction of SLG may slow down the activation of MEAs in the initial stage caused by advantageous PA leaching.

During AST, the performance of the MEA based on pure PBI membrane decreased significantly over time. This may be due to excessive PA leaching caused by the high ADL in the PBI affecting the three-phase boundary. The application of SLG significantly improved the durability of MEA in the AST process. The peak power density of CS-F was 365 mW cm^{-2}, which is significantly higher than that of PBI-F. For AS and ACS, the voltage at each current density during the AST process did not drop but increased, resulting in ACS-F showing the highest peak power density of 480 mW cm^{-2} across all MEAs. The resistance, ECSA, phase fraction and free PA boundary of different MEAs show that SLG can effectively control the PA leaching, maintaining a large three-phase boundary and protecting the CL.

The application of SLG can effectively limit hydrogen crossover. After 100 h of constant-current testing, hydrogen crossover of UT-AS-F and UT-PBI-F were 1.75×10^{-4} mol s^{-1} and 8.16×10^{-4} mol s^{-1}, respectively, with UT-AS-F exhibiting excellent performance with a peak power density of 513 mW cm^{-2}.

4.8 Declaration of Competing Interest

The authors declare that they have no known competing financial interests or personal relationships that could have appeared to influence the work reported in this paper.

4.9 Acknowledgment

4.10 References:

[1]   Y. Zhu, S. Murali, W. Cai, X. Li, … J.S.-A., undefined 2010, Graphene and graphene oxide: synthesis, properties, and applications, Wiley Online Library. 22 (2010) 3906–3924. https://doi.org/10.1002/adma.201001068.

[2]   S. Hu, M. Lozada-Hidalgo, F.C. Wang, A. Mishchenko, F. Schedin, R.R. Nair, E.W. Hill, D.W. Boukhvalov, M.I. Katsnelson, R.A.W. Dryfe, I. V. Grigorieva, H.A. Wu, A.K. Geim, Proton transport through one-atom-thick crystals, Nature. 516 (2014) 227–230. https://doi.org/10.1038/nature14015.

[3]   M. Miao, M.B. Nardelli, Q. Wang, Y. Liu, First principles study of the permeability of graphene to hydrogen atoms, Physical Chemistry Chemical Physics. 15 (2013) 16132–16137. https://doi.org/10.1039/C3CP52318G.

[4]   M. Perez-Page, … M.S.-A.M., undefined 2019, Single layer 2D crystals for electrochemical applications of ion exchange membranes and hydrogen evolution catalysts, Wiley Online Library. 6 (2019). https://doi.org/10.1002/admi.201801838.

[5]   S.M. Holmes, P. Balakrishnan, V.S. Kalangi, X. Zhang, M. Lozada-Hidalgo, P.M. Ajayan, R.R. Nair, S.M. Holmes, P. Balakrishnan, V.S. Kalangi, R.R. Nair, X. Zhang, P.M. Ajayan, M. Lozada-Hidalgo, 2D Crystals Significantly Enhance the Performance of a Working Fuel Cell, Advanced Energy Materials. 7 (2017) 1601216. https://doi.org/10.1002/AENM.201601216.

[6]   X.H. Yan, R. Wu, J.B. Xu, Z. Luo, T.S. Zhao, A monolayer graphene – Nafion sandwich membrane for direct methanol fuel cells, Journal of Power Sources. 311 (2016) 188–194. https://doi.org/10.1016/J.JPOWSOUR.2016.02.030.

[7]   W. Jia, B. Tang, P. Wu, Novel Slightly Reduced Graphene Oxide Based Proton

Exchange Membrane with Constructed Long-Range Ionic Nanochannels via Self-Assembling of Nafion, ACS Applied Materials and Interfaces. 9 (2017) 22620–22627. https://doi.org/10.1021/ACSAMI.7B06117/SUPPL_FILE/AM7B06117_SI_001.PDF.

[8] L. Britnell, R. V. Gorbachev, R. Jalil, B.D. Belle, F. Schedin, M.I. Katsnelson, L. Eaves, S. V. Morozov, A.S. Mayorov, N.M.R. Peres, A.H. Castro Neto, J. Leist, A.K. Geim, L.A. Ponomarenko, K.S. Novoselov, Electron Tunneling through Ultrathin Boron Nitride Crystalline Barriers, Nano Letters. 12 (2012) 1707–1710. https://doi.org/10.1021/NL3002205.

[9] S. Bukola, K. Beard, C. Korzeniewski, J.M. Harris, S.E. Creager, Single-Layer Graphene Sandwiched between Proton-Exchange Membranes for Selective Proton Transmission, ACS Applied Nano Materials. 2 (2019) 964–974. https://doi.org/10.1021/ACSANM.8B02270/SUPPL_FILE/AN8B02270_SI_002.XLSX.

[10] M. Perez-Page, M. Sahoo, S.M. Holmes, Single Layer 2D Crystals for Electrochemical Applications of Ion Exchange Membranes and Hydrogen Evolution Catalysts, Advanced Materials Interfaces. 6 (2019) 1801838. https://doi.org/10.1002/ADMI.201801838.

[11] V. Eswaraiah, S.S. Jyothirmayee Aravind, S. Ramaprabhu, Top down method for synthesis of highly conducting graphene by exfoliation of graphite oxide using focused solar radiation, Journal of Materials Chemistry. 21 (2011) 6800–6803. https://doi.org/10.1039/C1JM10808E.

[12] S.J. Peighambardoust, S. Rowshanzamir, M. Amjadi, Review of the proton exchange membranes for fuel cell applications, International Journal of Hydrogen Energy. 35 (2010) 9349–9384. https://doi.org/10.1016/J.IJHYDENE.2010.05.017.

[13]   S.A. Vilekar, R. Datta, The effect of hydrogen crossover on open-circuit voltage in polymer electrolyte membrane fuel cells, Journal of Power Sources. 195 (2010) 2241–2247. https://doi.org/10.1016/J.JPOWSOUR.2009.10.023.

[14]   Y.-L. Ma, J.S. Wainright, M.H. Litt, R.F. Savinell, Conductivity of PBI Membranes for High-Temperature Polymer Electrolyte Fuel Cells, Journal of The Electrochemical Society. 151 (2004) A8. https://doi.org/10.1149/1.1630037/META.

[15]   H. Su, S. Pasupathi, B. Bladergroen, V. Linkov, B.G. Pollet, Optimization of gas diffusion electrode for polybenzimidazole-based high temperature proton exchange membrane fuel cell: Evaluation of polymer binders in catalyst layer, International Journal of Hydrogen Energy. 38 (2013) 11370–11378. https://doi.org/10.1016/J.IJHYDENE.2013.06.107.

[16]   S.H. Eberhardt, F. Marone, M. Stampanoni, F.N. Büchi, T.J. Schmidt, Operando X-ray Tomographic Microscopy Imaging of HT-PEFC: A Comparative Study of Phosphoric Acid Electrolyte Migration, Journal of The Electrochemical Society. 163 (2016) F842–F847. https://doi.org/10.1149/2.0801608JES/XML.

[17]   S.H. Eberhardt, M. Toulec, F. Marone, M. Stampanoni, F.N. Büchi, T.J. Schmidt, Dynamic Operation of HT-PEFC: In-Operando Imaging of Phosphoric Acid Profiles and (Re)distribution, Journal of The Electrochemical Society. 162 (2015) F310–F316. https://doi.org/10.1149/2.0751503JES/XML.

[18]   H.R. Kunz, Lessons Learned from Phosphoric Acid Electrolyte Fuel Cell Development Pertinent to PEMFCs, ECS Transactions. 11 (2007) 1447–1460. https://doi.org/10.1149/1.2781058/META.

[19]   S. Yerramalla, A. Davari, A. Feliachi, T. Biswas, Modeling and simulation of the

dynamic behavior of a polymer electrolyte membrane fuel cell, Journal of Power Sources. 124 (2003) 104–113. https://doi.org/10.1016/S0378-7753(03)00733-X.

[20]   S. Yu, L. Xiao, B.C. Benicewicz, Durability Studies of PBI-based High Temperature PEMFCs, Fuel Cells. 8 (2008) 165–174. https://doi.org/10.1002/FUCE.200800024.

[21]   S.H. Eberhardt, F. Marone, M. Stampanoni, F.N. Büchi, T.J. Schmidt, Quantifying phosphoric acid in high-temperature polymer electrolyte fuel cell components by X-ray tomographic microscopy, Journal of Synchrotron Radiation. 21 (2014) 1319–1326. https://doi.org/10.1107/S1600577514016348.

[22]   S. Galbiati, A. Baricci, A. Casalegno, R. Marchesi, Degradation in phosphoric acid doped polymer fuel cells: A 6000 h parametric investigation, International Journal of Hydrogen Energy. 38 (2013) 6469–6480. https://doi.org/10.1016/J.IJHYDENE.2013.03.012.

[23]   Q. He, X. Yang, W. Chen, S. Mukerjee, B. Koel, S. Chen, Influence of phosphate anion adsorption on the kinetics of oxygen electroreduction on low index Pt(hkl) single crystals, Physical Chemistry Chemical Physics. 12 (2010) 12544–12555. https://doi.org/10.1039/C0CP00433B.

[24]   Z. Guo, M. Perez-Page, J. Chen, Z. Ji, S.M. Holmes, Recent advances in phosphoric acid–based membranes for high–temperature proton exchange membrane fuel cells, Journal of Energy Chemistry. 63 (2021) 393–429. https://doi.org/10.1016/j.jechem.2021.06.024.

[25]   H.L. Lin, Y.C. Chou, T.L. Yu, S.W. Lai, Poly(benzimidazole)-epoxide crosslink membranes for high temperature proton exchange membrane fuel cells, International Journal of Hydrogen Energy. 37 (2012) 383–392.

https://doi.org/10.1016/J.IJHYDENE.2011.09.049.

[26] J. Yang, W. Liao, Y. Liu, M. Murugananthan, Y. Zhang, Degradation of Rhodamine B using a Visible-light driven Photocatalytic Fuel Cell, Electrochimica Acta. 144 (2014) 7–15. https://doi.org/10.1016/J.ELECTACTA.2014.08.036.

[27] G. Liu, H. Zhang, J. Hu, Y. Zhai, D. Xu, Z. gang Shao, Studies of performance degradation of a high temperature PEMFC based on H3PO4-doped PBI, Journal of Power Sources. 162 (2006) 547–552. https://doi.org/10.1016/J.JPOWSOUR.2006.07.008.

[28] P. Blake, P.D. Brimicombe, R.R. Nair, T.J. Booth, D. Jiang, F. Schedin, L.A. Ponomarenko, S. V. Morozov, H.F. Gleeson, E.W. Hill, A.K. Geim, K.S. Novoselov, Graphene-Based Liquid Crystal Device, Nano Letters. 8 (2008) 1704–1708. https://doi.org/10.1021/NL080649I.

[29] J. Xu, D.K. Dang, V.T. Tran, X. Liu, J.S. Chung, S.H. Hur, W.M. Choi, E.J. Kim, P.A. Kohl, Liquid-phase exfoliation of graphene in organic solvents with addition of naphthalene, Journal of Colloid and Interface Science. 418 (2014) 37–42. https://doi.org/10.1016/J.JCIS.2013.12.009.

[30] J.N. Coleman, M. Lotya, A. O'Neill, S.D. Bergin, P.J. King, U. Khan, K. Young, A. Gaucher, S. De, R.J. Smith, I. V. Shvets, S.K. Arora, G. Stanton, H.Y. Kim, K. Lee, G.T. Kim, G.S. Duesberg, T. Hallam, J.J. Boland, J.J. Wang, J.F. Donegan, J.C. Grunlan, G. Moriarty, A. Shmeliov, R.J. Nicholls, J.M. Perkins, E.M. Grieveson, K. Theuwissen, D.W. McComb, P.D. Nellist, V. Nicolosi, Two-dimensional nanosheets produced by liquid exfoliation of layered materials, Science. 331 (2011) 568–571. https://doi.org/10.1126/SCIENCE.1194975/SUPPL_FILE/COLEMAN.SOM.PDF.

[31] J.J. Liu, S. Liu, N.G. Morgenthaler, M.D.S. Wong, S. Tavintharan, C.F. Sum, S.C. Lim, Association of plasma soluble α-klotho with pro-endothelin-1 in patients with type 2 diabetes, Atherosclerosis. 233 (2014) 415–418. https://doi.org/10.1016/J.ATHEROSCLEROSIS.2014.01.024.

[32] A. Reina, X. Jia, J. Ho, D. Nezich, H. Son, V. Bulovic, M.S. Dresselhaus, K. Jing, Large area, few-layer graphene films on arbitrary substrates by chemical vapor deposition, Nano Letters. 9 (2009) 30–35. https://doi.org/10.1021/NL801827V/SUPPL_FILE/NL801827V_SI_003.PDF.

[33] S. Bae, H. Kim, Y. Lee, X. Xu, J.S. Park, Y. Zheng, J. Balakrishnan, T. Lei, H. Ri Kim, Y. Il Song, Y.J. Kim, K.S. Kim, B. Özyilmaz, J.H. Ahn, B.H. Hong, S. Iijima, Roll-to-roll production of 30-inch graphene films for transparent electrodes, Nature Nanotechnology 2010 5:8. 5 (2010) 574–578. https://doi.org/10.1038/nnano.2010.132.

[34] K.S. Novoselov, V.I. Fal'Ko, L. Colombo, P.R. Gellert, M.G. Schwab, K. Kim, A roadmap for graphene, Nature 2012 490:7419. 490 (2012) 192–200. https://doi.org/10.1038/nature11458.

[35] C. Mattevi, H. Kim, M. Chhowalla, A review of chemical vapour deposition of graphene on copper, Journal of Materials Chemistry. 21 (2011) 3324–3334. https://doi.org/10.1039/C0JM02126A.

[36] X. Li, W. Cai, J. An, S. Kim, J. Nah, D. Yang, R. Piner, A. Velamakanni, I. Jung, E. Tutuc, S.K. Banerjee, L. Colombo, R.S. Ruoff, Large-area synthesis of high-quality and uniform graphene films on copper foils, Science. 324 (2009) 1312–1314. https://doi.org/10.1126/SCIENCE.1171245/SUPPL_FILE/LI.SOM.PDF.

[37] K.S. Vasu, E. Prestat, J. Abraham, J. DIx, R.J. Kashtiban, J. Beheshtian, J. Sloan, P.

Carbone, M. Neek-Amal, S.J. Haigh, A.K. Geim, R.R. Nair, Van der Waals pressure and its effect on trapped interlayer molecules, Nature Communications 2016 7:1. 7 (2016) 1–6. https://doi.org/10.1038/ncomms12168.

[38]   J.J. Bailey, J. Chen, J. Hack, M. Perez-Page, S.M. Holmes, D.J.L. Brett, P.R. Shearing, Lab-based X-ray micro-computed tomography coupled with machine-learning segmentation to investigate phosphoric acid leaching in high-temperature polymer electrolyte fuel cells, Journal of Power Sources. 509 (2021) 230347. https://doi.org/10.1016/J.JPOWSOUR.2021.230347.

[39]   J.J. Bailey, T.M.M. Heenan, D.P. Finegan, X. Lu, S.R. Daemi, F. Iacoviello, N.R. Backeberg, O.O. Taiwo, D.J.L. Brett, A. Atkinson, P.R. Shearing, Laser-preparation of geometrically optimised samples for X-ray nano-CT, Journal of Microscopy. 267 (2017) 384–396. https://doi.org/10.1111/JMI.12577.

[40]   A. Ferrari, D.B.-N. nanotechnology, undefined 2013, Raman spectroscopy as a versatile tool for studying the properties of graphene, Nature.Com. (n.d.). https://idp.nature.com/authorize/casa?redirect_uri=https://www.nature.com/articles/nnano.2013.46&casa_token=wmOfAbk96JIAAAAA:nrbsuCyCILshde8R5FQlCD4v4OQgn_Ezd-AClHgBFq1SnD9iBDs5Ixh1AGdu_T0GK_C5daZVxmKSoynayw (accessed February 5, 2022).

[41]   A.C. Ferrari, Raman spectroscopy of graphene and graphite: Disorder, electron–phonon coupling, doping and nonadiabatic effects, Solid State Communications. 143 (2007) 47–57. https://doi.org/10.1016/J.SSC.2007.03.052.

[42]   L.M. Malard, M.A. Pimenta, G. Dresselhaus, M.S. Dresselhaus, Raman spectroscopy in graphene, Physics Reports. 473 (2009) 51–87. https://doi.org/10.1016/J.PHYSREP.2009.02.003.

[43] Z. Ni, Y. Wang, T. Yu, Z. Shen, Raman spectroscopy and imaging of graphene, Nano Research 2008 1:4. 1 (2010) 273–291. https://doi.org/10.1007/S12274-008-8036-1.

[44] C.N.R. Rao, A.K. Sood, K.S. Subrahmanyam, A. Govindaraj, Graphene: The New Two-Dimensional Nanomaterial, Angewandte Chemie International Edition. 48 (2009) 7752–7777. https://doi.org/10.1002/ANIE.200901678.

[45] R. Yivlialin, L. Brambilla, G. Bussetti, M. Tommasini, A.L. Bassi, C.S. Casari, M. Passoni, F. Ciccacci, L. Duò, C. Castiglioni, Evolution of the graphite surface in phosphoric acid: an AFM and Raman study, Beilstein Journal of Nanotechnology 7:180. 7 (2016) 1878–1884. https://doi.org/10.3762/BJNANO.7.180.

[46] V. Gurau, F. Barbir, H. Liu, An Analytical Solution of a Half-Cell Model for PEM Fuel Cells, Journal of The Electrochemical Society. 147 (2000) 2468. https://doi.org/10.1149/1.1393555/META.

[47] Accelerated Testing Method for PEM Fuel Cell based Uninterrupted Power Supply Systems, Meeting Abstracts (Electrochemical Society). (2007). https://doi.org/10.1149/MA2007-02/9/596.

[48] Y. Zhai, H. Zhang, G. Liu, J. Hu, B. Yi, Degradation Study on MEA in $H3PO4/PBI$ High-Temperature PEMFC Life Test, Journal of The Electrochemical Society. 154 (2006) B72. https://doi.org/10.1149/1.2372687.

[49] D. Schonvogel, M. Rastedt, P. Wagner, M. Wark, A. Dyck, Impact of Accelerated Stress Tests on High Temperature PEMFC Degradation, Fuel Cells. 16 (2016) 480–489. https://doi.org/10.1002/FUCE.201500160.

[50] S. Galbiati, A. Baricci, A. Casalegno, G. Carcassola, R. Marchesi, On the activation of polybenzimidazole-based membrane electrode assemblies doped with phosphoric acid,

International Journal of Hydrogen Energy. 37 (2012) 14475–14481. https://doi.org/10.1016/J.IJHYDENE.2012.07.032.

[51] M. Boaventura, A. Mendes, Activation procedures characterization of MEA based on phosphoric acid doped PBI membranes, International Journal of Hydrogen Energy. 35 (2010) 11649–11660. https://doi.org/10.1016/J.IJHYDENE.2010.03.137.

[52] P. Zoltowski, A new approach to measurement modelling in electrochemical impedance spectroscopy, Journal of Electroanalytical Chemistry. 375 (1994) 45–57. https://doi.org/10.1016/0022-0728(94)13406-5.

[53] S. Andreasen, J. Jespersen, E. Schaltz, S.K.-F. Cells, undefined 2009, Characterisation and modelling of a high temperature PEM fuel cell stack using electrochemical impedance spectroscopy, Wiley Online Library. 9 (2009) 463–473. https://doi.org/10.1002/fuce.200800137.

[54] X. Yuan, H. Wang, J. Colin Sun, J. Zhang, AC impedance technique in PEM fuel cell diagnosis—A review, International Journal of Hydrogen Energy. 32 (2007) 4365–4380. https://doi.org/10.1016/J.IJHYDENE.2007.05.036.

[55] N. Wagner, Characterization of membrane electrode assemblies in polymer electrolyte fuel cells using a.c. impedance spectroscopy, Journal of Applied Electrochemistry. 32 (2002) 859–863. https://doi.org/10.1023/A:1020551609230.

[56] M. Mamlouk, K. Scott, Analysis of high temperature polymer electrolyte membrane fuel cell electrodes using electrochemical impedance spectroscopy, Electrochimica Acta. 56 (2011) 5493–5512. https://doi.org/10.1016/J.ELECTACTA.2011.03.056.

[57] A. Orfanidi, M.K. Daletou, L. Sygellou, S.G. Neophytides, The role of phosphoric acid in the anodic electrocatalytic layer in high temperature PEM fuel cells, Journal of

Applied Electrochemistry. 43 (2013) 1101–1116. https://doi.org/10.1007/S10800-013-0626-2/FIGURES/13.

[58]   F. Conti, A. Majerus, V. Di Noto, C. Korte, W. Lehnert, D. Stolten, Raman study of the polybenzimidazole–phosphoric acid interactions in membranes for fuel cells, Physical Chemistry Chemical Physics. 14 (2012) 10022–10026. https://doi.org/10.1039/C2CP40553A.

[59]   P. Kurzweil, Brennstoffzellentechnik, Brennstoffzellentechnik. (2016). https://doi.org/10.1007/978-3-658-14935-2.

[60]   J. Zhang, PEM fuel cell electrocatalysts and catalyst layers: fundamentals and applications, 2008. https://doi.org/10.1007/978-1-84800-936-3.

4.11 Supplementary Information

PBI membrane preparation

The preparation of PBI membranes was carried out by a modified solution casting method. The PBI ionomer (Fumion® AP-30, Fumatech) was dissolved in dimethylacetamide (DMAc) and stirred in an oil bath at 80 °C for 6 h to prepare a 2 wt% PBI/DMAc solution. The PBI/DMAc solution was placed in an oven at 80 °C for 12 h and then placed at 130 °C under vacuum for 3 h to remove the bulk of the DMAc solvent.

PA doping

The PA doping of PBI was achieved by immersing the in-house membranes or 30 μm thick commercial PBI membranes (Fumapem® AP-30, Fumatech) in 85% orthophosphoric acid (Fisher Chemical) for 6 h at a temperature of 140 °C. The ADL was calculated according to **Equation S4-1**.

Preparation of electrodes

The electrodes were made by coating a microporous layer (MPL), followed by the catalyst layer (CL), onto Toray carbon paper (TGPH 090, 280 μm) through a spraying method. The specific preparation method is shown in supporting information. The MPL inks were prepared by blending Ketjen black (90 wt%, EC-300J, AkzoNobel) and polytetrafluoroethylene (PTFE, 10 wt%, Aldrich) in iso-propanol (IPA). The Ketjen black loading of the MPL was 1 mg cm^{-2}. Sintering of MPL coated carbon paper was carried out in an oven at 300°C for 3 h. CL inks were prepared by blending 80 wt% Pt/carbon catalyst (Fisher Scientific, 60% Pt loading) and 20wt% PTFE in a mixture of deionized water and IPA. The spraying process of MPL inks and CL inks is accompanied by heating in a furnace at 120°C to remove the solvent. The Pt loading on electrodes was 1 mg cm^{-2} and the electrode area was 1.5 cm × 1.5 cm.

Assembly of membrane-electrode-assembly

The assembly of PA-doped membrane and electrodes was completed by using PT44FE film (0.15 mm) as gaskets and hot pressing at 140 °C and 80 psi for 4 min. Since the SLG was attached to the CL surface of the electrode, after hot pressing, the SLG was located between the CL and the membrane.

Electrochemical characterization

During the operation of LSV, 100 ml min^{-1} of dry hydrogen and nitrogen were passed through the anode and cathode, respectively. The LSV curves were obtained by gradually increasing the voltage from 0 to 700 mV with a scan rate of 1 mV s^{-1} and a step size of 2 mV. The hydrogen crossover flux was calculated according to **Equation S4-2**.

Galvanostatic EIS was performed at 0.5 A from 10 kHz to 0.1 Hz to acquire Nyquist plots. The measurement of CV was carried out with the anode and cathode fed with 33.4 ml min^{-1} hydrogen and 140 ml min^{-1} oxygen, respectively. During the CV measurement, the potential of the working electrode is cyclically scanned between 0.05 V and 1 V at a scan rate of 100 mV s^{-1}. The equation used to calculate ECSA is shown in **Equation S4-3**.

X-ray CT data processing

The data was extracted, cropped to $1015 \times 1015 \times 508$ voxels and converted to 8-bit to reduce the computational load and remove any external air. To make the boundary between phases clearer, a 3D non-local means filter, and a 3D unsharp masking filter were applied to denoise and sharpen the image. The segmentation of each phase in the MEA was completed by a combination of manual machine-learning training in Ilastik and some manual, slice-by-slice correction in the XZ direction in Avizo. The phase fraction was calculated according to simple voxel counting in Avizo.

Supplementary Equations:

ADL calculation:

$$ADL = (W_{PA}/M_{PA})/(W_{PBI}/M_{PBI})$$

W_{PA}: phosphoric acid content

M_{PA}: molar mass of the PA

W_{PBI}: PBI content

M_{PBI}: molar mass of the polymer repeat unit

Hydrogen crossover flux calculation:

$$\dot{\eta}H_2\ Crossover = j_{H_2\ Cross} \times A/(n \times F)$$

$\dot{\eta}H_2\ Crossover$: hydrogen crossover flux (mol s^{-1})

$j_{H_2\ Cross}$: limiting current density (mA cm^{-2})

A: fuel cell active area (cm^2)

n: the number of electrons taking part in the reaction (2e$^-$ per H$_2$ molecule)

F: Faraday's constant (96,485 C mol^{-1})

ECSA calculation:

$$ECSA\ (cm^2{}_{Pt}\ g_{Pt}{}^{-1}) = Charge(\mu C\ cm^{-2})/[210(\mu C\ cm^{-2}{}_{Pt}) \times Catalyst\ Loading(g_{Pt}\ cm^{-2})]$$

Supplementary Figures:

Figure S4. 1. 3D CAD of X-ray CT sample holders
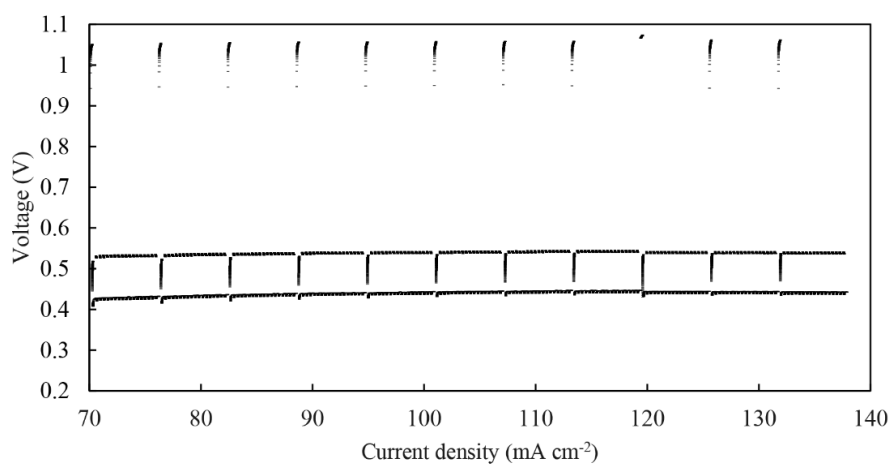
Figure S4. 2. Additional AST of ACS
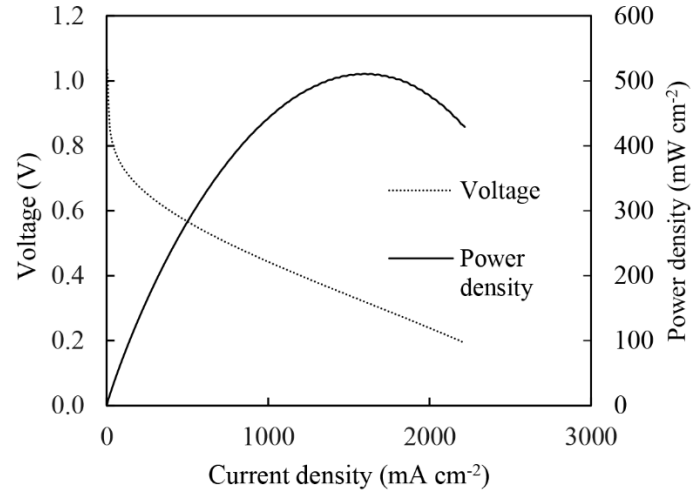
Figure S4. 3. Polarization curve and power density of ACS-E

Supplementary Tables:

Table S4. 1. X-ray CT acquisition parameters

	Pristine MEAs	AST MEAs
X-ray voltage (kV)	40	50
Voxel dimension (μm)	1.01	1.01
X-ray power (W)	3	4
Binning	1	1
Exposure time (s)	25	25
Number of projections	401	501
Scan time (h)	2.8	3.5

5. One-Step Electrochemical Exfoliation of Natural Graphite Flakes into Graphene Oxide for Polybenzimidazole Composite Membranes Giving Enhanced Performance in High-Temperature Fuel Cells

5.1 Manuscript Contribution

The results presented in Chapter 5 are reported in the publication "One step electrochemical exfoliation of natural graphite flakes into graphene oxide for polybenzimidazole composite membranes giving an enhanced performance in high-temperature fuel cells, Journal of Power Sources. 491 (2021) 229550. https://doi.org/10.1016/j.jpowsour.2021.229550."

My contributions in this work are as follows:

Investigation: Investigated the feasibility of electrochemical exfoliation using natural graphite flakes as raw material to prepare graphene or graphene oxide. Case study of reactor design for electrochemical exfoliation to prepare graphene of graphene oxide.

Methodology: Designed and manufactured the 3D-printed reactor. Preparation of polybenzimidazole membranes. Prepared electrochemically exfoliated graphene (oxide). Characterize electrochemically exfoliated graphene (oxide) through Raman, scanning electron microscopy, transmission electron microscopy, fourier-transform infrared spectroscopy, X-ray photoelectron spectroscopy and thermogravimetric analysis. Preparation, electrochemical performance testing, and durability testing of pristine membrane-electrode-assembly based on pure polybenzimidazole membrane and polybenzimidazole/graphene oxide composite membranes.

Formal analysis: Processed and analyzed the characterization results of electrochemically exfoliated graphene (oxide). Processed and analyzed electrochemical characterization results including polarization curves, Nyquist curves, and linear sweep voltammetry curves.

Writing-original: Writing of the original draft of manuscript.

Full author list: Jianuo Chen, Maria Perez-Page, Zhaoqi Ji, Zhe Zhang, Zunmin Guo, Stuart Holmes

Authors contribution:

Maria Perez-Page: Project administration, writing-review & editing Methodology

Zhaoqi Ji: Methodology (electrochemical performance testing)

Zhe Zhang: Methodology (Raman spectroscopy and mapping)

Zunmin Guo: Methodology (electrochemical performance testing)

Stuart M. Holmes: Supervision, project administration, funding acquisition, writing-review editing.

One Step Electrochemical Exfoliation of Natural Graphite Flakes into Graphene Oxide for Polybenzimidazole Composite Membranes Giving Enhanced Performance in High Temperature Fuel Cells

Jianuo Chen, ††Maria Perez-Page, Zhaoqi Ji, Zhe Zhang, Zunmin Guo, †Stuart Holmes

Department of Chemical Engineering and Analytical Science, University of Manchester, Oxford Road, Manchester, M13 9PL, United Kingdom.

†, †† **Corresponding author**

E-mail addresses: stuart.holmes@manchester.ac.uk (Stuart M. Holmes)

maria.perez-page@manchester.ac.uk (Maria Perez-Page)

5.2 Abstract

In this work, a 3D-printed reactor was designed to enable natural graphite flakes to be used for electrochemical exfoliation to quickly obtain graphene oxide. Graphite foil as a typical raw material of electrochemical exfoliation was also exfoliated for comparison. Under the same conditions (10V, 1mol/L ammonium sulfate solution as electrolyte), the graphene products obtained by one-step electrochemical exfoliation using natural graphite flakes based on the reactor, have a significantly higher degree of oxidation than products obtained using graphite foil (the oxygen content is increased by 50.2%). In addition, the oxidation degree can be further increased by increasing the electrolyte concentration or reaction time. This design achieves one-step exfoliation using natural graphite flakes to obtain graphene oxide with tunable oxygen content in short time without using any strong oxidants or strong acids. The as-prepared electrochemically exfoliated graphene oxide (EGO) was used to prepare polybenzimidazole (PBI)/ graphene oxide (GO) composite membranes for high-temperature polymer electrolyte membrane fuel cells (HTPEMFC). The 0.5%, 1% and 2% EGO loadings in the PBI membrane increased the peak power density by 13.8%, 24.4 % and 29.2 %, respectively.

5.3 Keywords

5.4 Introduction

Graphene oxide, which presents the 2D honeycomb structure similar to pristine graphene, contains in its structure, functional groups such as carboxyl, hydroxyl and carbonyl groups. In addition to some of the properties similar to graphene, the presence of these functional groups creates some additional properties of GO such as hydrophilicity, which makes this material easily dispersible in water and in some organic solvents which facilitates processing [1]. These oxygen-containing functional groups can also be covalently linked to polymers or small molecules to tune surface functionalization [2][3][4]. Graphene oxide has begun to play a significant role in many fields such as electrochemical energy devices [5][6], polymer composites [7][8], and sensors [9][10].

The properties of GO make it a promising material for PEMFC, especially in polymer composites [11][12][13][14][15]. As the most typical polymer used in the membrane of phosphoric acid-based HTPEMFC, PBI is affected by factors such as phosphoric acid (PA) leaching, thermal stability and mechanical performance degradation at high temperatures [16][17]. In addition, the phosphoric acid loading of PBI negatively affects mechanical properties [18]. The proton conductivity of the PA-based PBI membrane depends on the network of PA in the PBI matrix [19]. Therefore, less phosphoric acid loading or phosphoric acid leaching will affect the proton conductivity of the PBI membrane. Thanks to functional groups, GO can solve the above-mentioned issues as GO has a trapping effect on PA to prevent its leaching [20]. The functional group of GO can facilitate hopping of protons on external surfaces and establishment of three-dimensional proton transfer channels to improve conductivity [15] [21][22][23][24]. The hydrogen bond in GO plays a vital role in the improvement of conductivity. Although phosphoric acid has relatively low acidity, it has stronger hydrogen bonding forming ability and amphoteric characteristics than other acids [15][25][26]. In addition, graphene materials are also expected to improve the thermal stability

216

and mechanical properties of PBI [14].

GO can be synthesised by treating natural graphite with strong oxidants ($KMnO_4$, $NaNO_3$ and concentrated H_2SO_4) via chemical exfoliation methods, being modified Hummers' method the most popular [27][28]. However, the safety and environmental issues caused by the use of strong oxidants together with the long and tedious process of these traditional methods cannot be underestimated [29]. In addition, the traditional method of producing chemical exfoliation is very time-consuming.

Electrochemical exfoliation of graphite has been proposed as a promising method to produce graphene, having some valuable advantages such as reduced environmental impact, fast, high yield, low cost and ease of scale-up [30][31][32][33][34][35][36][37]. Electrochemical exfoliation uses graphite materials as the anode, which inevitably makes the graphene partially oxidized, hence, most research has been focused on reducing the degree of oxidation to obtain a graphene material with properties similar to pristine graphene [38]. However, as mentioned above, compared with pristine graphene, graphene oxide has its unique efficacy due to the functional groups leading to specific applications. Therefore, using electrochemical exfoliation to obtain graphene oxide with a higher degree of oxidation has also recently been on the research agenda [37].

Without pretreatments such as bonding or extrusion, natural graphite flakes are not suitable for direct use in electrochemical exfoliation to obtain large-scale graphene products because of the small flake size [39]. Most of the electrochemical exfoliation methods published so far use graphite foil [37] [40], highly oriented pyrolytic graphite [32], graphite rods [41] or graphite pellets [42] as raw materials. Most of these graphite materials have been obtained by processing graphite flakes using methods such as chemical treatment, thermal treatment or mechanical compression [43]. The different manufacturing processes and morphology of these raw

materials are likely to affect the properties of exfoliated products [44][45]. Because the preparation of graphite foil requires a complex process, the price of solid packed graphite such as graphite foil has reached 25 to 100 times of natural graphite flakes [46]. It can be seen that using natural graphite as a raw material to replace these graphite-processed products for electrochemical exfoliation has great commercial value. There are some works trying to use electrochemical exfoliation to prepare GO, but these works still cannot avoid the use of strong acids or strong oxidants, and the prepared GO has low oxygen content and low yield [36][47].

In this work, we have designed and manufactured a 3D printed reactor for the electrochemical exfoliation of natural graphite flakes to produce electrochemically exfoliated graphene oxide (EGO) using ammonium sulphate as the electrolyte. The reactor enables rapid exfoliation of natural graphite flakes at low voltage to obtain high yield EGO. Reactor-produced material from natural graphite flakes obtains GO with greater oxidation. In order to explore the effects of the reactor to control the variables, another unprocessed natural graphite, vein graphite, was also used as a raw material for comparison. The as-prepared EGO was applied to the PBI membrane composites of HTPEMFC to explore efficacy in fuel cells.

5.5 Experimental Section

5.5.1 Exfoliation Reactor Design

The raw materials used for electrochemical exfoliation in this work are natural graphite flakes (Alfa Aesar, -10 mesh, 99.9%), graphite foil (Alfa Aesar, 0.5mm thick) and vein graphite (Asbury carbon, US). The appearance of these materials is shown in **Figure S5. 1**. Unlike graphite foil and vein graphite, natural graphite flakes are in the form of crumbs, so they must undergo a certain form of assembly to perform mass exfoliation while the graphite foil and vein graphite can be directly connected to the current and immersed in the electrolyte to act as an anode. Therefore, the 3D printing-based reactor is designed to mount natural graphite flakes

into a collective.

The overall structure of the reactor is shown in **Figure 5. 1**a. The reactor consists of two main parts that can be observed in **Figure 5. 1**b and c. The base of the reactor is immersed inside of a beaker and the graphite flakes are placed on the top of the holder and covered by the perforated cover, which has the shape of an inverted funnel. The cover and base are connected by mortise and tenon with each other and can be locked or separated by rotation. The cover is connected to a plug to seal the reactor and the two springs apply pressure to the graphite flakes, as can be observed in the section view in **Figure 5. 1**a, the wall at the bottom of the cover has an angle of 10° to the horizontal. The holes on the cover have a diameter of 0.5 mm which is subject to the printing resolution of the 3D printer. Copper foil (Wruth electronics UK) is used to connect electrically the graphite flakes with the external circuit. The copper sheet penetrates the plug along the wall of the plug to the bottom and is kept in contact with the graphite by the force of springs. A platinum (Pt) wire (Goodfellow. UK) is used as the counter electrode. The electrolyte is added into the beaker, the liquid level of the solution is higher than the holes of the cover and lower than the bottom part of copper foil to ensure graphite acts as the anode in the electrochemical system rather than the copper. The special structure of the reactor and the placement of the platinum electrode change the anode and cathode from original vertical parallel to horizontal parallel, which allows the generated bubbles to escape with their own buoyancy instead of adhering to the surface of the material to block the further process of the reaction. The engineering drawings of each part of the design are shown in **Figure S5. 2**. The plug, the cover and the base are manufactured by 3D printer. The materials used for 3D printing are acrylonitrile butadiene styrene (ABS) and polyethylene terephthalate glycol (PETG). These 3D printed materials are resistant to high temperature, mechanically strong and resistant to weak acids and bases.
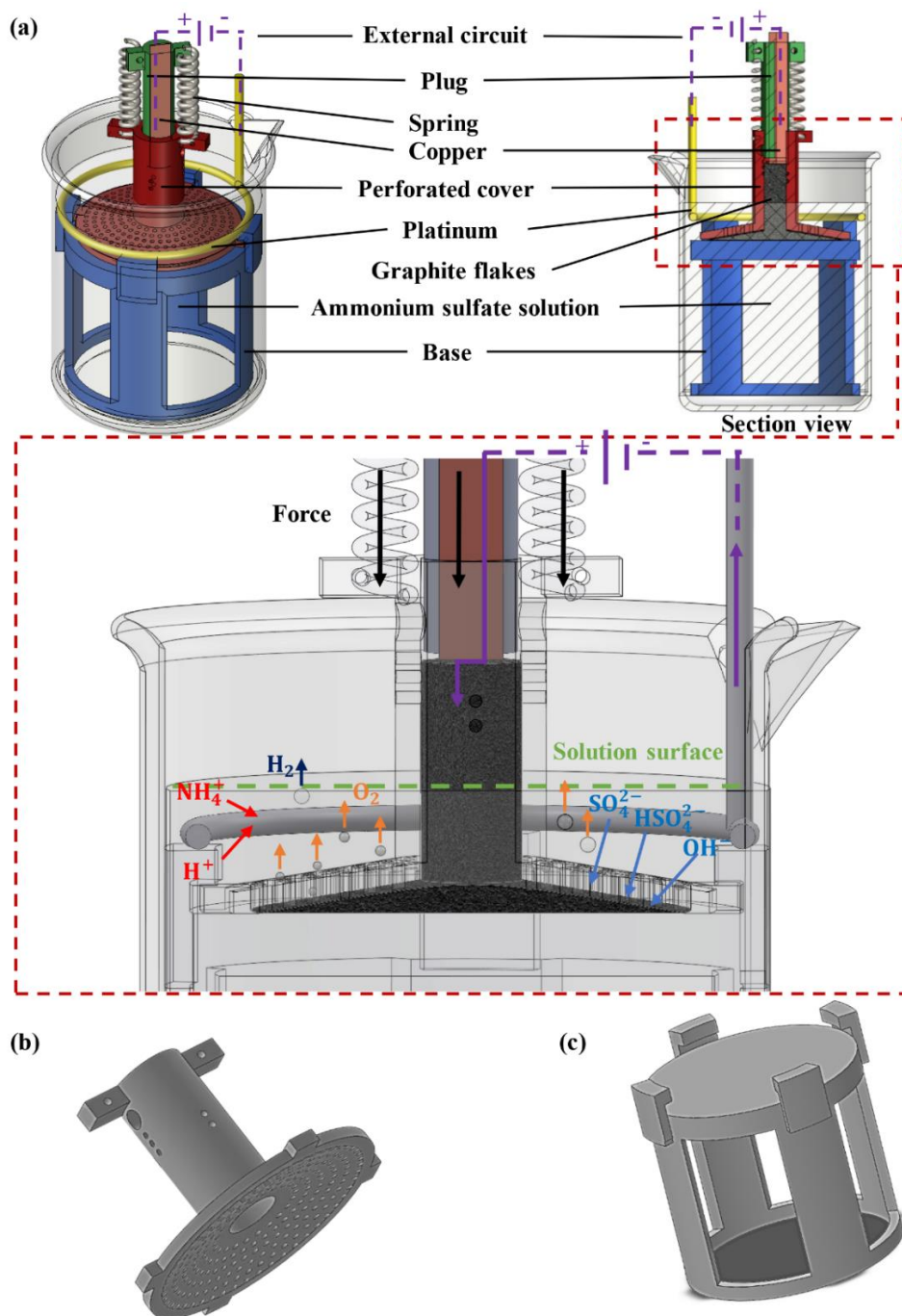
Figure 5. 1. Structure of the reactor, (a) overall design and section view, (b) structure of the perforated cover, (c) structure of the base

5.5.2 Synthesis of Electrochemical Exfoliated Graphene Oxide.

A diagram of the EGO preparation method is shown in **Figure S5. 3**. Graphite materials were

exfoliated by a single step electrochemical exfoliation. 0.1-1M aqueous solution of ammonium

sulphate (Sigma UK) has been used as the electrolyte. In the case of the graphite flakes, which

were exfoliated using the reactor, the natural graphite flakes are filled into the reactor and

immersed inside the ammonium sulphate solution. Then they acted as a working electrode by connecting to the positive electrode of a power supply through the copper foil. Alternatively, a piece of graphite foil with the dimension 1.5 cm × 4.5 cm or vein graphite working as a working electrode, has been immersed into a beaker with the electrolyte, and they were held by a clamp. Platinum was used as a counter electrode. The voltage remains constant at 10V during exfoliation. Different from graphite foil, the exfoliation process based on the reactor and natural graphite flakes can last longer. Due to the mechanical assistance of the reactor, although the size of the hole on the reactor is much larger than GO, the GO after exfoliation becomes muddy, and most of the GO will be retained in the reactor and continue to contact the current under the force of the spring to participate in the reaction.

During this process, the current gradually rises and eventually remains stable. For all kinds of products, the exfoliated products were washed 3 to 5 times by vacuum filtration with DI water until the washing liquid was neutral, pH = 7. This process removes ammonium sulphate residues. The filtered mixture was dispersed in deionized water and sonicated for 10 minutes to complete the exfoliation and to obtain a homogeneous dispersion. Lastly, the product is centrifuged at 1500 rpm for 15 minutes to separate graphite and graphene.

5.5.3 Characterization of EGO.

To evaluate the obtained EGO quality, the structure and different properties of the produced material have been evaluated. The contact angle of exfoliated graphene oxide was measured by Holmarc's contact angle meter. Films were vacuum-filtered from dispersion contact angle measurement. The electrical conductivity of EGO was measured by a four-probe station (Jandel Engineering, Linslade, UK) equipped with a 2182 A nano voltmeter and a 6220 current source (Keithley Instruments, Cleveland, OH, USA) at room temperature and ambient atmosphere. To

measure the electrical conductivity, the EGO dispersion obtained was vacuum filtered into a thin film and then placed in a vacuum chamber to dry overnight to remove moisture.

Raman spectroscopy and Raman mapping were performed on Horiba LabRAM Evolution with 633nm laser and ×50 SLWD VIS objective lens ranging from 1000 cm^{-1} to 3000 cm^{-1}. The Raman mapping is acquired by measuring 1600 (40×40) points in 10μm × 10μm area. The samples for Raman spectroscopy were prepared by drop-casting the EGO water dispersion onto a silicon wafer. The crystal structure was studied by X-ray Diffraction (XRD) with a PANalytical X'Pert Pro X'Celerator diffractometer. The minimum step size is 0.001 2 Theta (degree). The XRD sample preparation is similar to Raman's sample preparation, but a load of graphene on the silicon wafer is larger.

To evaluate EGO morphology, Scanning Electron Microscope (SEM) and Transmission electron microscopy (TEM) have been performed. SEM was carried out on a Tescan Mira3 SC. The beam energy was 5.0kV and the imaging mode is the secondary electron. TEM images were obtained by JEOL JEM 2100. TEM samples were prepared by dispersing EGO in ethanol, dropping the dispersion on Lacey carbon film and drying in air at room temperature and atmospheric pressure. To evaluate the number of layers of the EGO obtained, Atomic Force Microscope (AFM) was performed on PSIA XE-100.

To measure and evaluate the number of functional groups present in the EGO obtained, Fourier-Transform Infrared Spectroscopy (FTIR), X-ray photoelectron spectroscopy (XPS) and thermogravimetric analysis (TGA) were performed. TGA also allows the studying of thermal resistance. FTIR was conducted in a Tensor 27 ranging from 400 cm^{-1} to 2000 cm^{-1}in transmission mode. The resolution, scan time was 16 cm^{-1} and 32 scans respectively. The samples for FTIR measurement were prepared by drying the graphene dispersion into a few microns thick films by using a vacuum suction filter. The TGA was performed on

Discovery TGA 550. The heating rate was 10°C/min. Air is used as the carrier gas for TGA and the flow rate was 25 mL/min. The sample was prepared by grinding the dried graphene and placing them in alumina pans. XPS analysis was performed using a Thermo NEXSA XPS fitted with a mono chromated Al kα X-ray source (1486.7 eV), 3 multichannel resistive plates, a spherical sector analyser, and 128 channel delay line detectors.

5.5.4 Synthesis of PBI Membrane and PBI/EGO Composite Membranes

20wt% PBI/DMAc solution (PBI performance product, USA) was cast on a glass plate by a doctor's blade. DMAc was evaporated off, in the oven at 60°C overnight, followed by vacuum drying at 130°C for 3 hours. In order to remove residual DMAc, the cast PBI membrane was boiled in deionized water for one hour and then vacuum dried at 80°C for one hour to remove water. The PBI/EGO composite solution was obtained by mixing 1wt% FL-0.1-1/DMAc solution with PBI/DMAc solution and stirring with an overhead stirrer for three hours. The subsequent preparation process of the composite membrane is the same as that of the pure PBI membrane.

5.5.5 Preparation of Membrane Electrode Assemblies

The PBI membrane is soaked in 85% Orthophosphoric acid (Fisher Chemical) at room temperature for 48 hours. The calculation method of doping level is shown in supporting information (**Equation S5- 1**). The electrodes were prepared by spraying Microporous layer ink which is consisted of 90wt% Ketjen black (EC-300J, AkzoNobel) and 10wt% PTFE (Sigma Aldrich) on a Toray carbon paper (TGPH 090, 280 microns), then followed by spraying catalyst layer which is consisted of 80wt% Pt/carbon catalyst (Fisher Scientific, 60% Pt loading) and 20wt% Polytetrafluoroethylene (PTFE) as the binder. The Pt loading on electrodes is 1mg/cm^2. The electrodes area is 1.5cm*1.5cm. MEA is finally made by hot pressing (140℃, 80psi and 4.5 minutes) and uses 0.15mm PTFE film as gaskets.

5.5.6 Characterization and Performance Study of PBI Membranes and PBI/EGO Membranes Based MEAs

For Raman measurement, the sample MEA was measured with the Renishaw inVia confocal Raman microscope. The experiments were carried out with a 785nm CW laser (400mW), a 100× objective lens. TGA was performed from room temperature to 800℃ with a 10℃/min heating rate in air, to study the thermal stability of membranes. The stress-strain behaviour of PA doped membranes was tested by a tensile test instrument (INSTRON 3344) at a strain rate of 1mm min^{-1} at room temperature. SEM was performed on Quanta 650 with 5kV beam energy. MEAs were tested in a homemade fuel cell set up with the 100ml/min flow rates of oxygen and hydrogen. Polarization curves, Electrochemical Impedance Spectroscopy (EIS) and linear sweep voltammetry (LSV) were performed by GAMRY E5000. EIS was performed at a constant current operating environment (0.5A) from 10000 Hz to 0.1 Hz. LSV was performed when the anode and cathode connect to 100ml/min hydrogen and 100ml/min nitrogen, respectively. During the LSV measurement, the voltage increases from 0 to 550mV with 1mV/s scan rate and 2mV step size. Accelerated stress test (AST) is performed alternately at 0.6A cm^{-2} (4 minutes) and 1Acm^{-2} (16 minutes), and the open-circuit voltage is operated for 10 minutes every 6 hours [48].

5.6 Results and Discussion

5.6.1 Characterization of Raw Materials for Electrochemical Exfoliation

To better understand the electrochemical exfoliation reaction of graphite, an initial characterization of graphite raw materials used was carried out. As mentioned, graphite foils are made of natural graphite after physical, chemical and mechanical treatment. This can be seen from SEM images of graphite foil, natural graphite flakes and vein graphite, which can be

observed in **Figure 5. 2**a, b and c respectively. The graphite foil has a different morphological structure from natural graphite flakes and vein graphite. The graphite foil has a large-sized layered structure, but its surface has obvious compression characteristics, and the graphite layer has a large number of folds. The base surface of this type of graphite foil is usually considered to be formed by stacking micron-sized graphitized platelets in a disordered manner, and therefore will have flaws such as wrinkling, overlapping, or folding. Unlike graphite foil, natural graphite flakes have a relatively flat layered structure. The layers of natural graphite flakes are tightly wrapped with each other [49]. The morphological structure of vein graphite is basically the same as that of natural graphite flakes. Vein graphite is also a kind of natural graphite. Its block structure is naturally formed without binders [39].
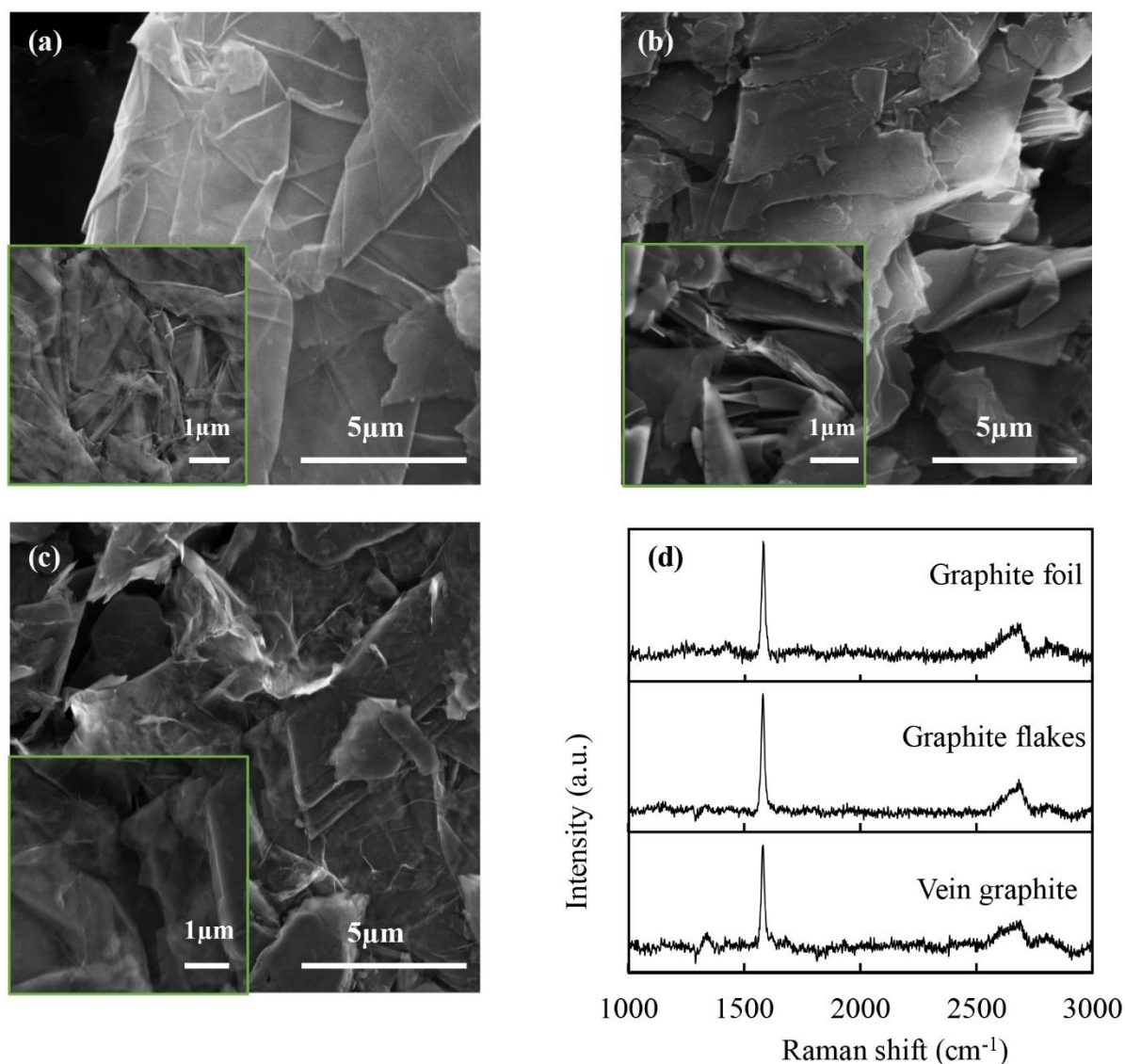
Figure 5. 2. Characterization of graphite: (a) SEM image of graphite foil; (b) SEM image of natural graphite flakes; (c) SEM image of vein graphite, (d) Raman spectroscopy of graphite foil, natural graphite flakes and vein graphite

Raman spectra of graphite foil, natural graphite flakes and vein graphite are shown in **Figure 5. 2**d. For graphite and graphene materials, Raman spectroscopy is an effective tool for evaluating defects or structural quality of carbon lattices, mainly achieved by analysing the position, shape and the relationship of three main peaks. The defect-activated D peak, attributed to functional groups or structural disorder, appears around 1328 cm^{-1} to 1340 cm^{-1}. The G peak corresponding to the phonon mode in-plane vibration of sp^2 carbon atoms appears near

1572 cm^{-1} to 1599 cm^{-1}. The 2D peak, which is the second-order of D peak, indicating the characteristic of few-layer graphene appears at 2648 cm^{-1} to 2694 cm^{-1} [50]. The ratio between the intensity of D peak and G peak (I_D/I_G) indicates the extent of disorder and defects [51]. The structural quality of these graphite materials does not show a significant difference. The D peak of natural graphite flakes can be basically ignored. The D peak of graphite foil is also not obvious. Vein graphite has the most obvious D peak by comparison. Although the processing of graphite foil has caused a change in its morphological structure, its lattice structural quality is not significantly changed according to Raman.

5.6.2 Characterization of EGO

With 0.1M ammonium sulfate as the electrolyte and a voltage of 10V, vein graphite quickly cracked due to its fragile structure and the lack of mechanical assistance. In a short period of time, a large number of fragments sink to the bottom under the action of gravity. Therefore, it is difficult to perform continuous electrochemical exfoliation using vein graphite to obtain graphene products. The feasibility of electrochemical exfoliation and product characterization are mainly carried out with graphite foil and natural graphite flakes.

Natural graphite flakes (in the reactor) and graphite foil were subjected to electrochemical exfoliation under the same conditions (applied voltage of 10V, 0.1M ammonium sulphate solution as electrolyte, and duration of 1 hour), to obtain graphene-like products. Under such conditions, the products obtained using graphite foil and natural graphite flakes as raw materials are named FO-0.1-1 and FL-0.1-1, respectively. A reactor with a cover diameter of 4 cm can be filled with approximately 1200 mg of graphite flakes. The mass of the graphite foil used for exfoliation is approximately 900 mg. Due to the special structure of the reactor, part of the graphite flakes are not immersed in the electrolyte to ensure that the copper foil connected to the external circuit is not immersed in the electrolyte. This part of the graphite

flakes that have not participated in the reaction can be easily recovered and filled into the next batch. It is difficult to reuse the graphite foil that has been reduced in consumption to obtain large-volume products. The consumption of graphite flakes and graphite foil in the final reactor is about 800mg and 700mg, respectively. After one hour of reaction followed by dispersion and centrifugation, the final product yields were 90% and 75% of the consumption of graphite flakes and graphite foil, respectively.

EGO from different graphite materials (FO-0.1-1 and FL-0.1-1) were dispersed in DI water and DMAc to a concentration of 0.6 mg·mL^{-1} by sonication. The dispersions were used to observe the stability of EGO in DI water. The effects after settling for different times are shown in **Figure 5. 3**a. The dispersion of FL-0.1-1 in water and DMAc is more stable than FO-0.1-1. To prove stronger hydrophilicity for FL-0.1-1, contact angle measurements have been conducted for both materials, showing a larger contact angle for FO-0.1-1 with a value of 88.6^o while the value obtained for FL-0.1-1 is 64.7^o. The easier dispersion in water and DMAc is advantageous for the further processing and functionalization of graphene-based materials. The higher the polarity of the graphene surface, the easier it is to disperse in water and DMAc. This property mainly depends on the degree of functionalization of graphene during the oxidation process [52]. Another proof of the larger amount of functionalization obtained with natural graphite flakes during the exfoliation in the reactor, is the colour that both dispersions show at the same concentration, as can be observed in **Figure 5. 3**b. The diluent of FO-0.1-1 dispersion (0.08mg mL^{-1}) is light grey and the diluent of FL-0.1-1 dispersion (0.08mg mL^{-1}) is brown/yellow, which is usually the colour for GO when it is obtained by a traditional chemical exfoliation [53].
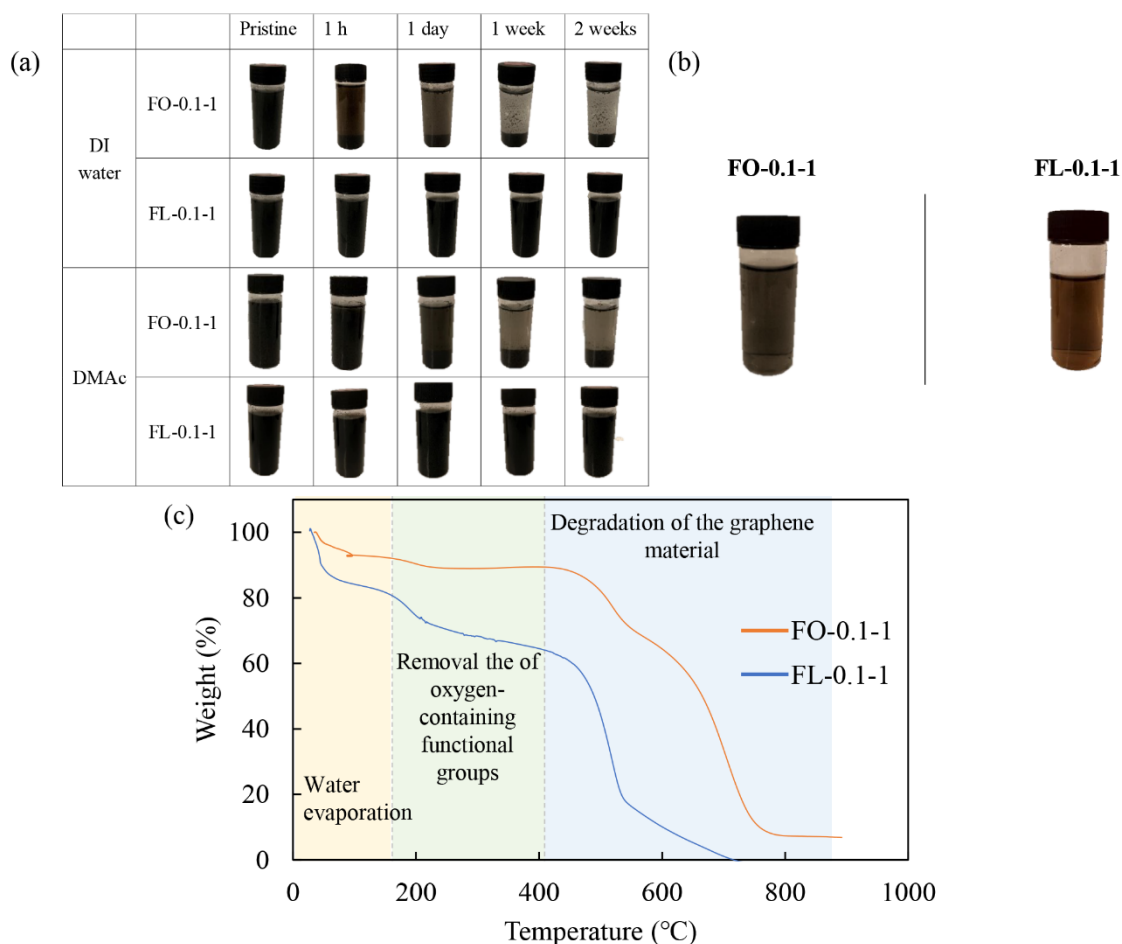
Figure 5. 3. (a)The effects after settling of FO-0.1-1and FL-0.1-1 in water and DMAc, (b) Diluted EGO dispersion of FO-0.1-1 and FL-0.1-1 in DI water, (c) TGA curves of FL-0.1-1 and FO-0.1-1

Electrical conductivity is measured by a 4-probe method. The calculation formula of conductivity is shown in Equation S5- 2(supporting information). The detailed parameters are shown in Table S5. 1 (supporting information). FL-0.1-1 (261 S m^{-1}) has significantly lower conductivity than FO-0.1-1 (9115 S m^{-1}). As mentioned, the structure of graphene makes it have very good electrical conductivity. However, the introduction of the disordered structure due to the different oxygen functional groups present in GO will significantly change the electronic properties [54][55].

The thermal stability for both samples, FL-0.1-1 and FO-0.1-1, has been also evaluated. TGA

analysis has been conducted in air and the results obtained are shown in **Figure 5. 3**c. From TGA results, it can be concluded the thermal stability for the samples is significantly different. In addition to that, information about the amounts of functional groups present on the samples can be also obtained. The weight of FO-0.1-1 remained relatively stable until about 500°C. For FL-0.1-1, more significant water loss in the initial stage due to its higher hydrophilicity making it less likely to be dried at room temperature [56]. There is also a relatively rapid weight drop of FL-0.1-1 around 200℃, which is generally considered to be a mass loss due to the pyrolysis or reduction of the oxygen-containing functional group [57][58]. The weight loss of around 20% can be measured for FL-0.1-1 while only 4% for FO-0.1-1.

Fourier-transform infrared (FTIR) spectroscopy is a tool for analysing chemical bonding in materials [59]. For FO-0.1-1 and FL-0.1-1, the chemical bonds found mainly include $C = C$ (1574 cm^{-1}, 1645 cm^{-1},1671cm^{-1} ; Stretching vibration of sp^2 carbon), C-O (1023 cm^{-1}, 1209-1275 cm^{-1}; Stretching vibration of the hydroxyl group), $C = O$ (1728 cm^{-1}; Stretching vibration of a ketone, ester, aldehyde or carboxyl group) and O-H (1363-1389 cm^{-1}) [32]. The spectral positions of these chemical bonds are shown in **Figure 5. 4**a. The existence of these chemical bonds proves the generation of oxygen-containing functional groups. Therefore, under the specific conditions of this work, no matter whether graphite foil or graphite flakes are used, the anodic electrochemical exfoliation will cause oxidation, which is the disadvantage of using anodic electrochemical exfoliation to prepare pristine graphene [38].
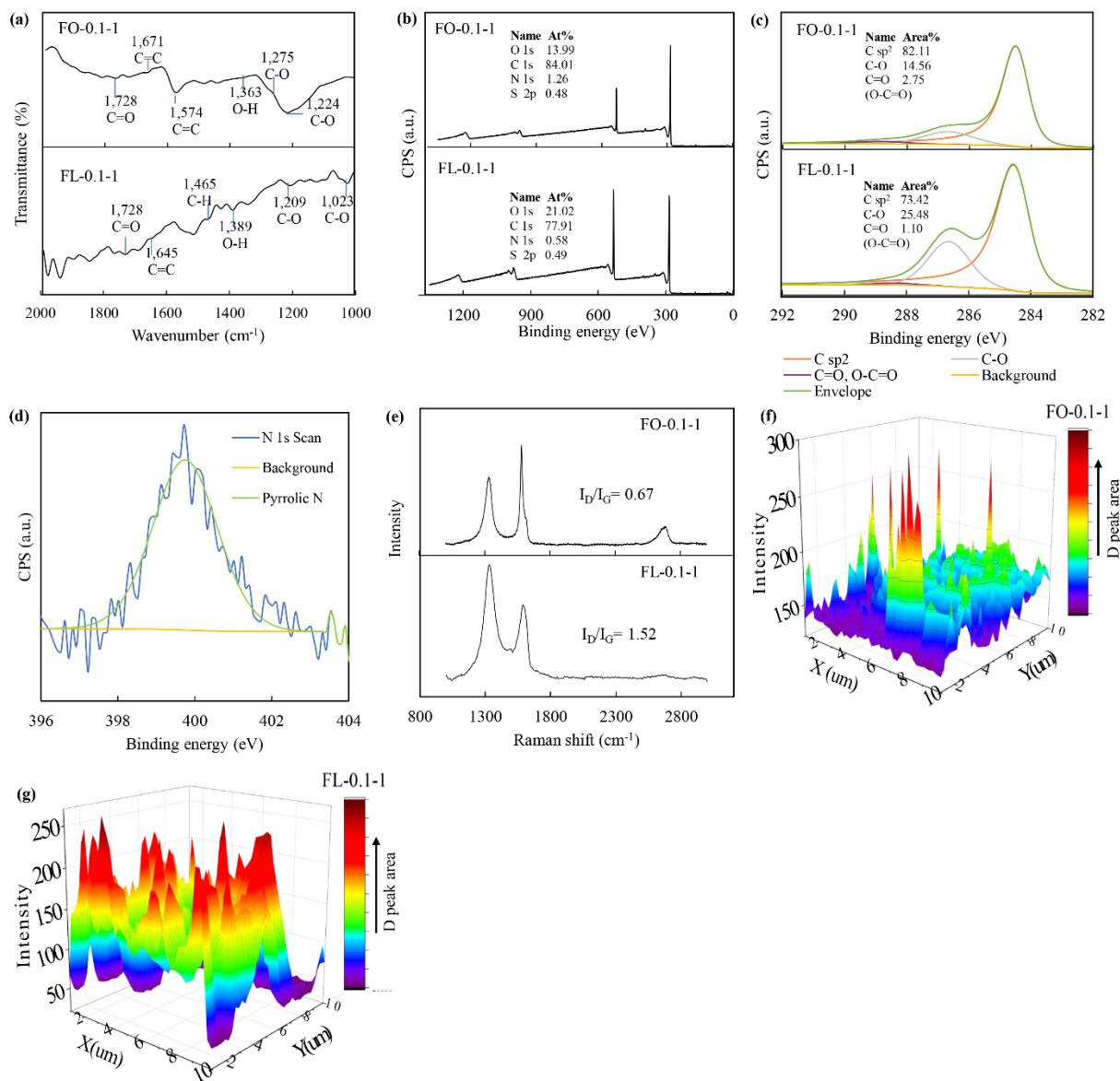
*Figure 5. 4. Chemical bonding and elemental characterizations: (a) **FT-IR spectra of** FO-0.1-1 and FL-0.1-1, (b) XPS survey spectra of FO-0.1-1 and FL-0.1-1, (c) XPS C 1s spectra of FO-0.1-1 and FL-0.1-1, (d) XPS spectra of N 1s of FL-0.1-1, (e) Raman spectra of FO-0.1-1 and FL-0.1-1, (f) D peak Raman mapping of FO-0.1-1, (g) D peak Raman mapping of FL-0.1-*

231

To obtain further detail about the chemical composition and elemental content of different EGO samples, XPS has been performed. XPS survey and the C1 XPS spectra of FO-0.1-1 and FL-0.1-1 are shown in **Figure 5. 4**b and c. It can be seen from the XPS survey spectra of both samples that the oxygen content of FL-0.1-1 is significantly higher than that of FO-0.1-1 being 21.02% and 13.99% respectively. If the O/C ratios are compared, there is also a significant difference between both samples being 0.177 for FO-0.1-1 and 0.274 for FL-0.1-1. The difference in oxygen content illustrates the difference in the degree of oxidation of the two graphene products. Although FO-0.1-1 has a certain amount of oxygen content and local oxidation, it is generally regarded as pristine graphene made by electrochemical exfoliation, although its O/C ratio is slightly higher than the theoretical threshold of graphene oxide O/C ratio (0.167) [30][32][38][40]. However, FL-0.1-1 is considered to be graphene oxide by virtue of its oxygen content [36][37] [47].

The C 1s spectra of FO-0.1-1 and FL-0.1-1 are shown in **Figure 5. 4**c. The C 1s spectra peaks can be deconvoluted into C-C (sp^2), C-O, and C=O at 284.5 eV, 285.3 eV, 287.8 eV respectively [30] [37] [60]. The C 1s spectra fitting results correspond to FT-IR. The oxidation reaction during exfoliation is shown in **Figure S5. 4**. It can be seen from the oxidation step of graphite in the exfoliation process that the hydroxyl group is the group that is most easily carried on the surface of graphene. The C-O content is 14.56% for FO-0.1-1 while 25.48 for FL-0.1-1.

According to the XPS spectra, there is 0.58% Nitrogen (N) in FL-0.1-1. The nitrogen can only come from the ammonium sulfate used in the electrochemical exfoliation. The XPS N 1s spectra of FL-0.1-1 is shown in **Figure 5. 4**d. The N 1s spectra peaks can be deconvoluted into pyrrolic N at 400 eV [61]. The mechanism of nitrogen doping during electrochemical exfoliation has been proposed by previous publications [62]. Pyrrolic nitrogen is exactly the type of nitrogen on PBI. It can be used to capture phosphoric acid molecules to improve the

conductivity of the membrane [63].

Raman spectra of each exfoliated graphene are shown in **Figure 5. 4**e. As mentioned earlier, I_D/I_G indicates the extent of disorder and defects. It is worth noting that the I_D/I_G the ratio of FL-0.1-1 is significantly larger than that of FO-0.1-1 presenting a ratio of 0.67 for FO-0.1-1 while 1.52 for FL-0.1-1. Based on the hydrophilicity, thermal stability and conductivity of the samples mentioned above, as well as the results exhibited by XPS and FT-IR, it is reasonable to believe that the ratio difference is due to the different extent of defects caused by the introduction of oxygen-containing functional groups. Corresponding to XPS, the Raman spectrum of FL-0.1-1 is more in line with the characteristics of the Raman spectrum of graphene oxide. The measured I_D/I_G ratio may be slightly higher than the value corresponding to the oxygen-containing functional group, which may be due to the smaller size of EGO [64]. However, since the EGO obtained under different conditions has similar sizes, it has little effect on the comparison of the content of oxygen-containing functional groups.

Raman mapping of the D peak for samples FO-0.1-1 and FL-0.1-1 is represented in **Figure 5. 4**f and **Figure 5. 4**g in a 3D diagram which can better display the distribution of defects. Mapping a square area of 10×10 µm in the centre of graphene flake. The red area indicates the area with a higher D peak. From the mapping obtained, it can observe that FL-0.1-1 has a more uniform defect distribution; in contrast, defects of FO-0.1-1 are only distributed at the edge of the slice. Compared to foil, natural graphite flakes in the reactor have more time to be slowly oxidized instead of just being exfoliated quickly. The uniform distribution of oxygen-containing functional groups also makes graphene obtained by exfoliation of natural graphite flakes have better dispersion stability in water.

The flake size of as-synthesised graphene oxide was evaluated by SEM while the thickness was measured by AFM and TEM as can be shown in **Figure 5. 5**. The dimensional overview

of the FL-0.1-1 sheet on a silicon wafer is shown in **Figure 5. 5**a and the dimension distribution of FL-0.1-1 is shown in **Figure 5. 5**b. The dimension of FL-0.1-1 is relatively small compared to FO-0.1-1 whose SEM image is shown in **Figure 5. 5**c and dimension distribution is shown in **Figure 5. 5**d. Most FL-0.1-1 sheets are between 1 and 3 µm, with an average of about 2.5 µm, while the mean flake size of FO-0.1-1 is around 5µm. There are also very few EGO sheets larger than 10 µm in size shown in **Figure 5. 5**e. The smaller size of FL-0.1-1 is probably due to the longer contact current of the graphene material, and thus the longer participation in exfoliation. The thickness of single-layer graphene is generally considered to be equivalent to the interlayer distance of graphite, 0.34 nm [56]. However, considering the factors such as the generation of defects, nitrogen doping, the addition of functional groups, and the enhancement of hydrophilicity, the thickness of graphene oxide increases compared to graphene, which is usually defined as 1nm [56][65]. A typical AFM image of FL-0.1-1 is shown in **Figure 5. 5**f, and the AFM overview image of FL-0.1-1 on silicon wafer is shown in **Figure S5. 5**. As shown in the graph of graphene oxide layer number distribution of FL-0.1-1, **Figure 5. 5**g, the number of layers of FL-0.1-1 is mainly distributed between 1 to 9 layers, most of which are 3 layers, and the average number of layers is about 3.66 layers. Figure 5. 5h shows the TEM image for the FL-0.1-1 sample. The flakes observed are transparent which indicates that the flake of FL-0.1-1 are thin. Further observation through selected area diffraction reveals that the diffraction patterns of some samples (**Figure 5. 5**i) show a typical six-fold symmetry and the brightness of the 0-110 plane is higher than that of the 0-120 plane, which indicates the existence of single-layer graphene oxide [66]. As the thickness distribution of FO-0.1-1 shown in **Figure 5. 5**d, FO-0.1-1 is mainly based on 2nm and 3nm thick. Although FO-0.1-1 is closer to graphene than graphene oxide, it is still partially oxidized and may have wrinkles, which can correspond to XPS and SEM. Therefore, the definition of the thickness of the monolithic layer in FO-0.1-1 is tricky. The typical AFM image of FO-0.1-1 is shown in **Figure S5. 6**.
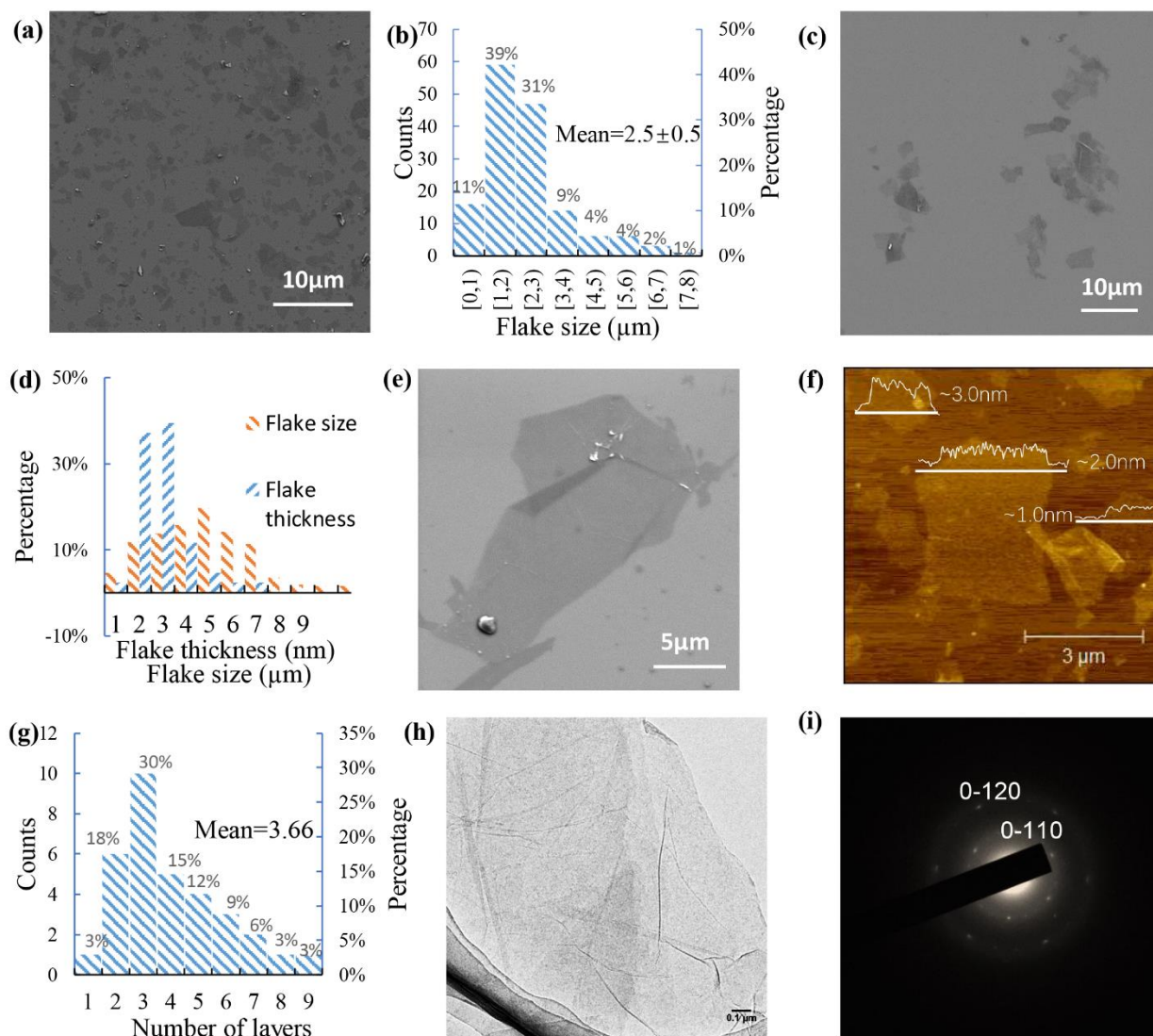
Figure 5. 5. Morphological and Structural Characterizations: (a) SEM overview image of FL-0.1-1; (b) flakes size distribution of FL-0.1-1; (c) SEM overview image of FO-0.1-1; (d) flakes size distribution and thickness distribution of FO-0.1-1; (e)large size sheet of FL-0.1-1; (f) AFM image of FL-0.1-1; (g) thickness distribution FL-0.1-1; (h) TEM image of FL-0.1-1; (i) Selected area electron diffraction (SAED) of FL-0.1-1

It can be seen from the above comparison that the graphene materials obtained by electrochemical exfoliation of different raw graphite materials are different. In order to further explore which variables, such as raw materials and mechanical assistance of the reactor, caused these differences, the reactor has been also used to exfoliate graphite foil. Graphite foils were divided into small pieces and fed into the reactor. This exfoliation process also uses 0.1M ammonium sulfate solution as electrolyte and is carried out at 10V. The graphene product

obtained in 1 hour is so called FOR-0.1-1. The specific procedure and results are shown in supporting information (**Figure S5. 7** and **Figure 5. 5**).

Table 5. 1 shows the reaction conditions and product parameters when using different methods, raw materials, and whether the new reactor was used. CGO represents the graphene generated by traditional chemical exfoliation, Hummers' methods. From the data shown in Table 1, it is not difficult to find that the graphene oxide obtained by using electrochemical exfoliation in this work has a slight gap compared with the Hummers method in terms of hydrophilicity and oxidation degree. However, this work achieves a good connection between the reactor and graphite flakes. Compared to Hummers methods, it greatly reduces the reaction time and does not use any harmful environmental oxidants to produce high yield graphene oxide with a certain degree of oxidation. Compared to the typical electrochemical exfoliation using graphite foil as a raw material, it reduces the cost of raw materials while increasing the degree of oxidation and does not significantly weaken the exfoliation. Compared with the current relatively advanced method of using electrochemical exfoliation to produce graphene oxide [37] (two-step electrochemical exfoliation based on graphite foil), the method of this work eliminates the use of concentrated sulfuric acid and has a higher oxygen content, and uses natural graphite to reduce costs.

Table 5. 1. Comparison of reaction process and product parameters of different exfoliating methods [67][68][69] [37]

	CGO	EGO (This work) (Graphite foil without reactor)	EGO (This work) (Graphite foil with reactor)	EGO (This work) (Graphite flakes with reactor)	Exfoliated graphite (This work)	EGO (two-step exfoliation)
Raw material	Natural graphite flakes	Graphite foil	Graphite foil	Natural graphite flakes	Vein graphite	Graphite foil
Reaction time	More than 1 week	1 hour	1 hour	1 hour	--	30 minutes -40 minutes
Chemical used	$KMnO_4$ H_2SO_4 $NaNO_3$ H_2O_2	0.1 M $(NH_4)SO_4$	0.1 M $(NH_4)SO_4$	0.1 M $(NH_4)SO_4$	0.1 M $(NH_4)SO_4$	Concentrated H_2SO_4 0.1 M $(NH_4)SO_4$
Mean flakes size (μm)	6-25	5	5	2.5	graphite	3.12
Average layers/thickness	1-5	2.95nm	--	3.66	graphite	--
O/C ratio (XPS)	0.33 - 0.5	0.177	0.247	0.274		0.217
Water contact angle	61.8° - 11.6°	88.6°	--	64.7°	graphite	--
Yield	~100%	78%	25%	90%	<1%	71%

The degree of oxidation of this graphene oxide can be further increased by increasing the electrolyte concentration or reaction time. The products characteristics obtained under different conditions are shown in **Table 5. 2**. The specific Raman and XPS spectra are shown in **Figure S5. 9** and **Figure S5. 10**. It can be seen from **Table 5. 2** that when the reaction time is increased from 1 hour to 2 hours and then to 3 hours, the conductivity of the obtained product gradually decreases, I_D/I_G ratio increases sequentially, and the O/C ratio and C-O content also increase. Changes in all these parameters indicate an increase in oxidation. Similarly, when the electrolyte concentration is increased from 0.1 M to 0.5 M and then to 1 M, each parameter shows an increase. As the exfoliation previously assumed, the samples exfoliated from natural graphite flakes with reactor obtain more oxygen-containing group since it has been exposed to current and bias for a longer time, resulting in more opportunities for hydroxide to be loaded onto the graphene surface. The most oxidized of these samples, FL-1.0-1, has an O/C ratio of 0.3.

Table 5. 2. Characteristics of exfoliated graphene oxide obtained from different electrolyte concentration and reaction time

Name	Reaction time (h)	Concentration of solution (mol/L)	σ (S m^{-1})	I_D/I_G (Raman)	2D peak (Raman cm^{-1})	O/C atomic ratio (XPS)	C-O Content (XPS %)
FL-0.1-1	1	0.1	261	1.52	2677	0.274	25.48
FL-0.1-2	2	0.1	250	1.55	2670	0.276	32.43
FL-0.1-3	3	0.1	243	1.65	2676	0.302	36.42
FL-0.5-1	1	0.5	251	1.66	2653	0.302	29.88
FL-1.0-1	1	1.0	241	1.69	2661	0.307	32.22

5.6.3 Mechanism of Reactor Based Electrochemical Exfoliation

Based on experimental results and characterization, a reasonable assumption for the electrochemical exfoliation mechanism in the reactor can be suggested. XRD patterns of natural graphite flake and exfoliated graphene oxide with different exfoliation time are shown in **Figure 5. 6**a, and the schematic diagram of proposed mechanism is shown in **Figure 5. 6**b.
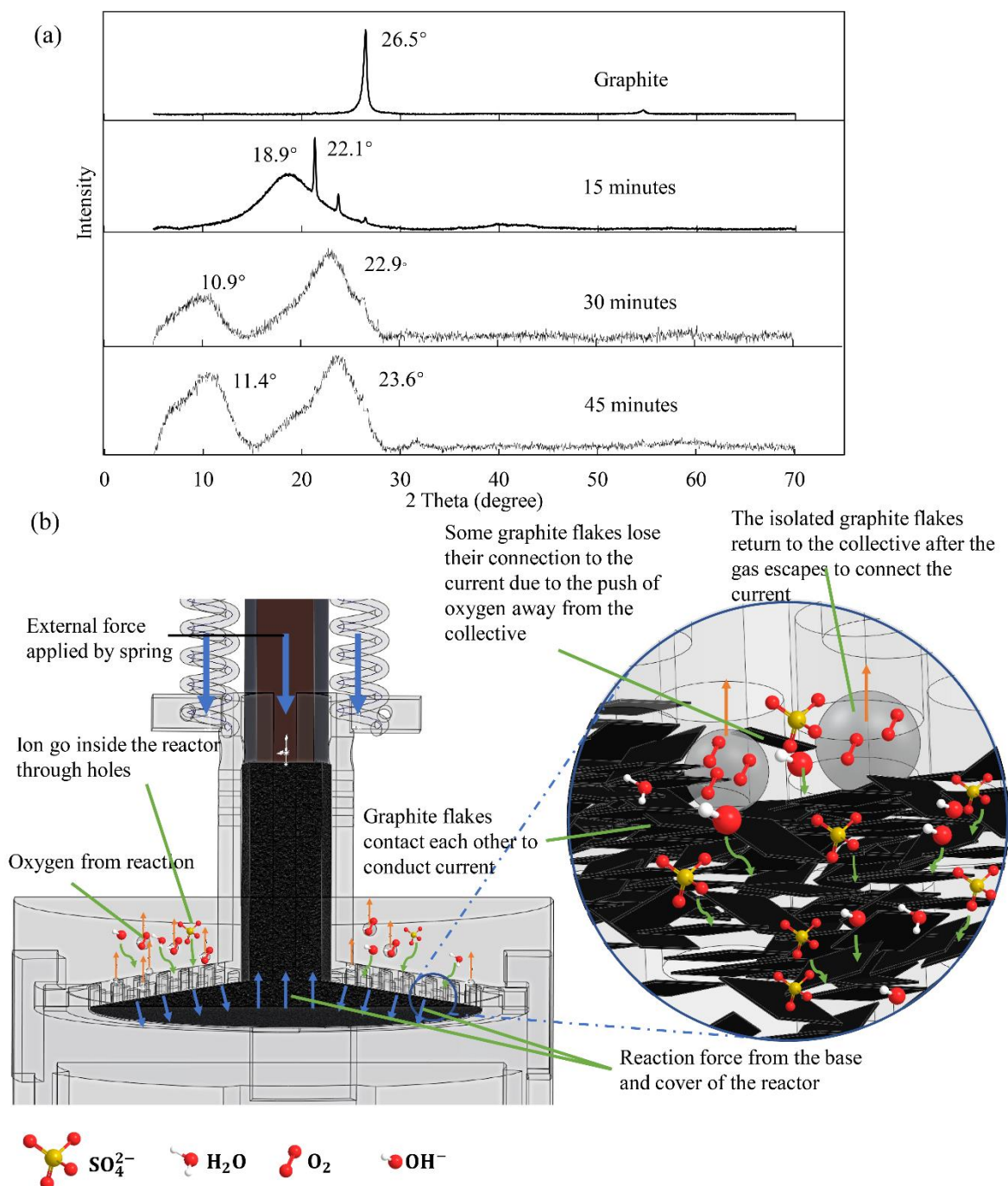
Figure 5. 6. Electrochemical exfoliation mechanism based on graphite and 3D printed reactor：(a) XRD patterns of natural graphite flake and exfoliated graphene oxide with 15minutes, 30 minutes and 45 minutes reaction, (b) Reactor mechanical structure related operation mechanism

A graphite intercalation compound (GIC) refers to a system where a reactant is inserted into the graphite interlayer under the action of an intercalator and bonds with the carbon atoms in the interlayer wall to form a compound that will not damage the structure of the graphite layer

[70]. The number of stages is defined as the number of graphene layers between two intervening layers, and the corresponding substance is called stage n GIC [71]. The formation of low stage GIC is an important prerequisite for the generation of graphene oxide because one of the important steps of the oxidation process is achieved by the replacement of the intercalating agent with an oxidizing agent [37]. As the XRD patterns shown in **Figure 5. 6**a, after 15 minutes of reaction, the sharpest peak of graphite (G-phase characteristic peak 002) shifted from 26.5 ° to 22.1 °, which illustrates the formation of a stage 1 GIC [72][73][74]. The broad peak of 18.9 ° appearing in the XRD pattern after 15 minutes reaction indicates that graphite is further oxidized and the interlayer distance becomes larger [75]. This data indicates that the natural graphite flakes in the reactor were not directly exfoliated in the initial stage but intercalated and oxidized. As the schematic diagram shows in **Figure 5. 6**b, the interconnection between the graphite flakes is achieved by squeezing the graphite flakes by the external force applied by the spring and the reaction force of the inner wall of the reactor. As was shown by SEM, graphite foil is made by expanded graphite and the internal interlayer of each single graphite flake is relatively tight. However, there is a certain gap between the natural graphite flakes despite the external force of the squeeze. When the oxygen bubbles generated by reaction on the graphite surface are large enough, some of the surrounding graphite flakes will be pushed away from the collective by the bubbles, losing their connection to the current. Therefore, the reaction will stop on the surface or inside these isolated flakes. At the same time, the graphite flakes that have not left the collective are still connected to the current and continue to react generating new oxygen bubbles. When oxygen escapes from the pores of the reactor, the previously separated flakes return to the collective due to the squeezing effect of the external force and the connection with the current is re-established to continue the reaction. In short, at the same time of the reaction, there will always be some graphite flakes in the pause state of the reaction due to the push of the bubbles. This partial isolation of some graphite flakes once

the oxygen has accumulated makes the speed of the oxygen generated inside the reactor lower than when using graphite foil as the working electrode. This phenomenon can be observed during the experiment. This can also be reflected by the change in current over time when using the reactor and graphite foil to do exfoliation with the same voltage (10V) and the same electrolyte concentration, being the current needed for graphite foil significant larger than for graphite flakes as can be observed in **Figure S5. 11**. The slower oxygen generation speed makes the graphene sheet peel off more slowly, also makes the hydroxyl groups more inclined to combine with the electrons to form functional groups on the graphite surface to balance the generation and consumption of electrons. The oxidation reaction during exfoliation is shown in **Figure S5. 4**. Therefore, in the initial stage of the reaction, the most reactions that occur on and inside the graphite flakes are oxidation and anion intercalation rather than direct stripping (shown in **Figure S5. 12**).

The formation of GIC causes graphite to expand. This expansion allows the further intercalation of the sulphate ions, sulphur oxide, and oxygen generated through oxidation from nucleophilic water within the interlayer gap of graphite and makes the graphite layer peel off [37][76]. As shown in **Figure 5. 6**a, as the reaction progressed to 30 minutes or even 45 minutes, two main peaks appeared in XRD patterns around 11 ° and 23 °, respectively. Among them, the peak appearing around 11 ° indicates the formation of graphene oxide with higher oxidation degree [37][77], and the peak appearing around 23 ° indicates the formation of graphene oxide with lower oxidation degree or unoxidized pristine graphene [78][79]. The content relationship between the two can be expressed by the peak area ratio of their corresponding peaks [46]. At 45 minutes, the area ratio of the first peak to the second peak is significantly greater than that at 30 minutes (0.76 for 45 minutes and 0.40 for 30 minutes). This shows that over time, even if the graphene sheet is peeled off, it may be oxidized by reconnecting to the current under the squeeze of external force. This is due to the use of the reactor so that the exfoliated graphene

remains inside the reactor

5.6.4 Characterization and performance of EGO/PBI composite membranes

A pure PBI membrane and PBI membranes with 0.5wt%, 1wt% and 2wt% EGO loadings were prepared to explore the effect of EGO on PBI membrane performance. The acid doping level (ADL) of membranes is around 9.7 mol PA per repeat unit PBI. The change in the weight of membranes overtime during the phosphoric acid doping process is shown in **Figure S5. 13**. The thickness of these membranes after phosphoric acid doping is about 126-140 μm. The Raman spectra of the PBI membrane and PBI/1%EGO composite membrane is shown in **Figure 5. 7**a. The difference between the Raman spectra of EGO/PBI composite membrane and the Raman spectra of pure PBI is the peak at 1300cm^{-1} and 1600cm^{-1}. The ratio of PBI/EGO peaks at these positions to other peaks increases. This is most likely due to the influence of the D peak and G peak of EGO. This shows the presence of graphene oxide in PBI. The effect of EGO on the thermal stability of PBI was evaluated by TGA in the air atmosphere as shown in **Figure 5. 7**b. The weight loss of all membranes is mainly reflected in two stages, namely the degradation of water and DMAc before the temperature rises to 200°C, and the decompose of the PBI backbone around 750°C. The TGA curves of all membranes show similarity within the allowable measurement error range and maintain good thermal stability before 600°C, which is due to the excellent thermal stability of the aromatic backbone of PBI and is not significantly affected by GO doping [15][24][80]. The reinforcing effect of EGO on PA doped PBI membranes are evaluated by tensile stress-strain behaviour as shown in **Figure 5. 7**c. Although Young's modulus of these PA doped membranes is basically the same, they are all around 46 MPa. PBI/EGO composite membranes have greater tensile strength and elongation at break than pure PBI membranes. As the content of EGO increases, the maximum stress becomes larger and the maximum strain decreases. The enhancement of mechanical properties could be caused by the transfer of the force in the PBI matrix to the EGO nanosheet and the strong

interaction between EGO and PBI [14][23].

The polarization curves and power density curves of these membranes based MEAs are shown in **Figure 5. 7**d. From the perspective of the polarization curves, compared to the PBI membrane loaded with EGO, the voltage loss of the MEA is based on the pure PBI membrane in the medium current density stage, that is, the ohmic loss is significantly larger. This is also reflected in the Nyquist curve shown in **Figure 5. 7**e. The comparison of membrane resistance is: PBI ($287m\Omega$ cm^2) > PBI/0.5%EGO ($204m\Omega$ cm^2) > PBI/ 1% EGO ($192m\Omega$ cm^2) > PBI/ 2% EGO ($160m\Omega$ cm^2). The increase in membrane conductivity can ultimately be reflected in the power density (shown in **Figure 5. 7**d). The peak power density of PBI/0.5%EGO ($378mW$ cm^{-2}), PBI/1%EGO ($413mW$ cm^{-2}) and PBI/2%EGO ($429mW$ cm^{-2}) is 13.8%, 24.4% and 29.2% higher than that of PBI ($332mW$ cm^{-2}), respectively. The improvement of the performance after adding EGO can be explained as the abundant functional groups in EGO strengthening the interaction between the membrane and phosphoric acid and establishing a better hydrogen bond network to improve the conductivity of the membrane [81]. In addition, nitrogen doping can provide an anchor point for the phosphoric acid, the hydrogen bond formed by the epoxy and carboxyl groups on the EGO can also help the proton hoping to improve conductivity [81].
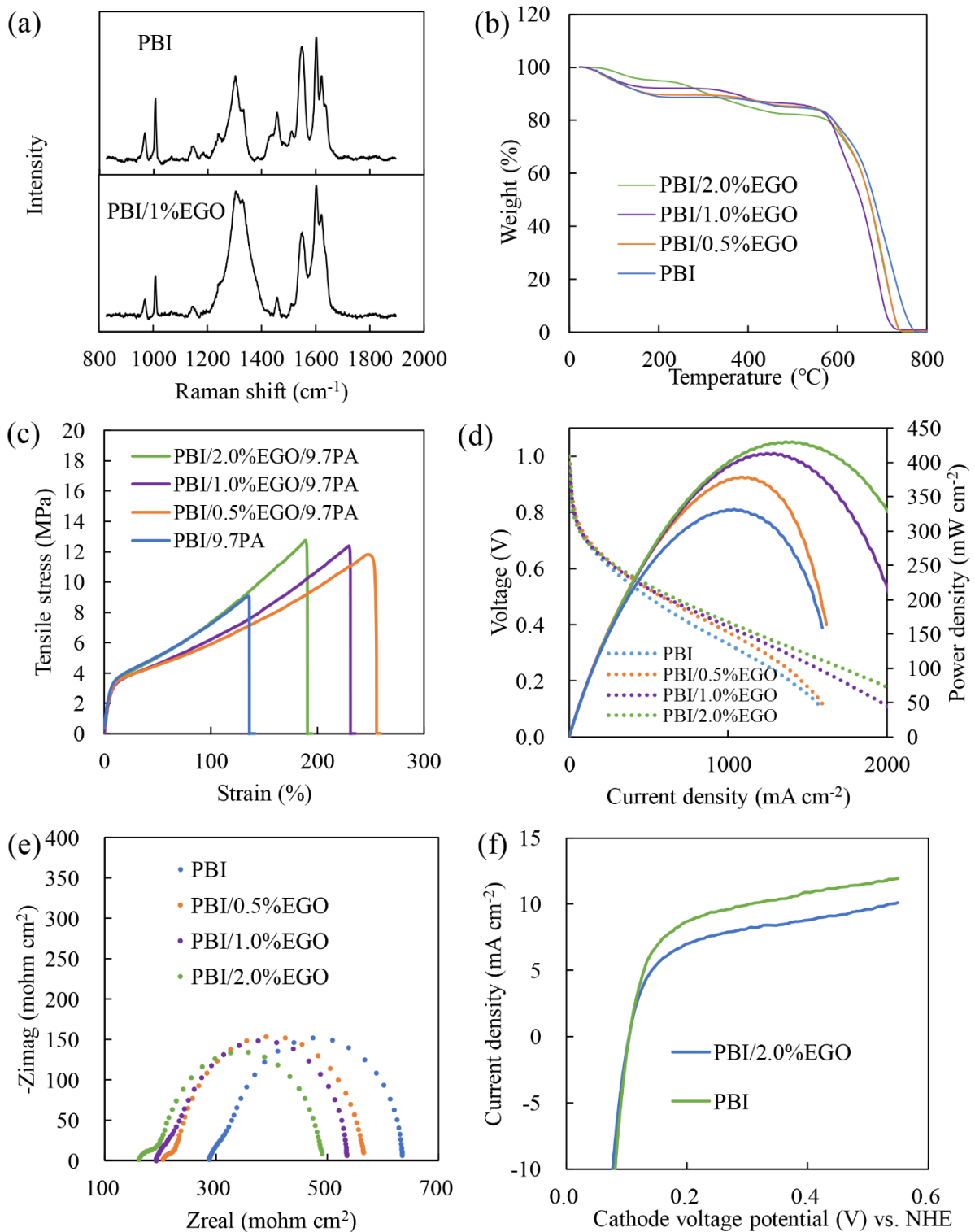
Figure 5. 7. Characterization and performance study of PBI and PBI/EGO membranes: (a) Raman, (b) TGA (c) stress-strain behavior, (d) polarization curves and power density curves (150℃, anode: 100ml min^{-1} hydrogen, 1mg cm^{-2} Pt; Cathode: 100ml min^{-1} oxygen, 1mg cm^{-2} Pt), (e) Nyquist curves and (f) LSV of PBI and PBI/EGO membranes

LSV is an effective tool for detecting hydrogen crossover and electron crossover between anode and cathode through the membrane of PEMFC [82][83]. The LSV curves of pure PBI

membrane and PBI membrane with the highest EGO content (PBI/2%EGO) are shown in

Figure 5. 7f. By taking the reciprocal of the linear fitting slope near 0.4V of the LSV curve, it

can be seen that the short-circuit resistance of pure PBI membrane and PBI/2%EGO are 129 Ω

cm^2 and 123 Ω cm^2 respectively. The short-circuit resistance of PBI/2%EGO is slightly smaller

than that of pure PBI may be due to the electronic conductivity of EGO itself or reduction at

high temperatures. However, this difference is not obvious. This is due to the interaction

between PBI and EGO functional groups, which inhibits the reduction of EGO at high

temperatures and prevents EGO from becoming more conductive reduced EGO [81]. In

addition, the as-prepared EGO has been shown to have a smaller size to avoid short circuits

caused by EGO penetrating both sides of the PBI membrane. According to LSV curves, the

limit current density of PBI and PBI/2%EGO is approximately 7.5 mA cm^{-2} and 5.5 mA cm^{-2},

respectively. According to **Equation S5- 3**, the hydrogen crossover of PBI and PBI/2% EGO

are 8.7 x 10^{-8} mol s^{-1} and 6.4 x 10^{-8} mol s^{-1}, respectively. This indicates that PBI may have a

larger hydrogen crossover compared to PBI/2%EGO. This may be due to the graphene material

blocking the permeation of hydrogen. However, the intercept of the two curves on the Y-axis

is not obvious, so it is tricky to accurately analyse the specific amounts of crossover of

hydrogen through the two LSV curves.
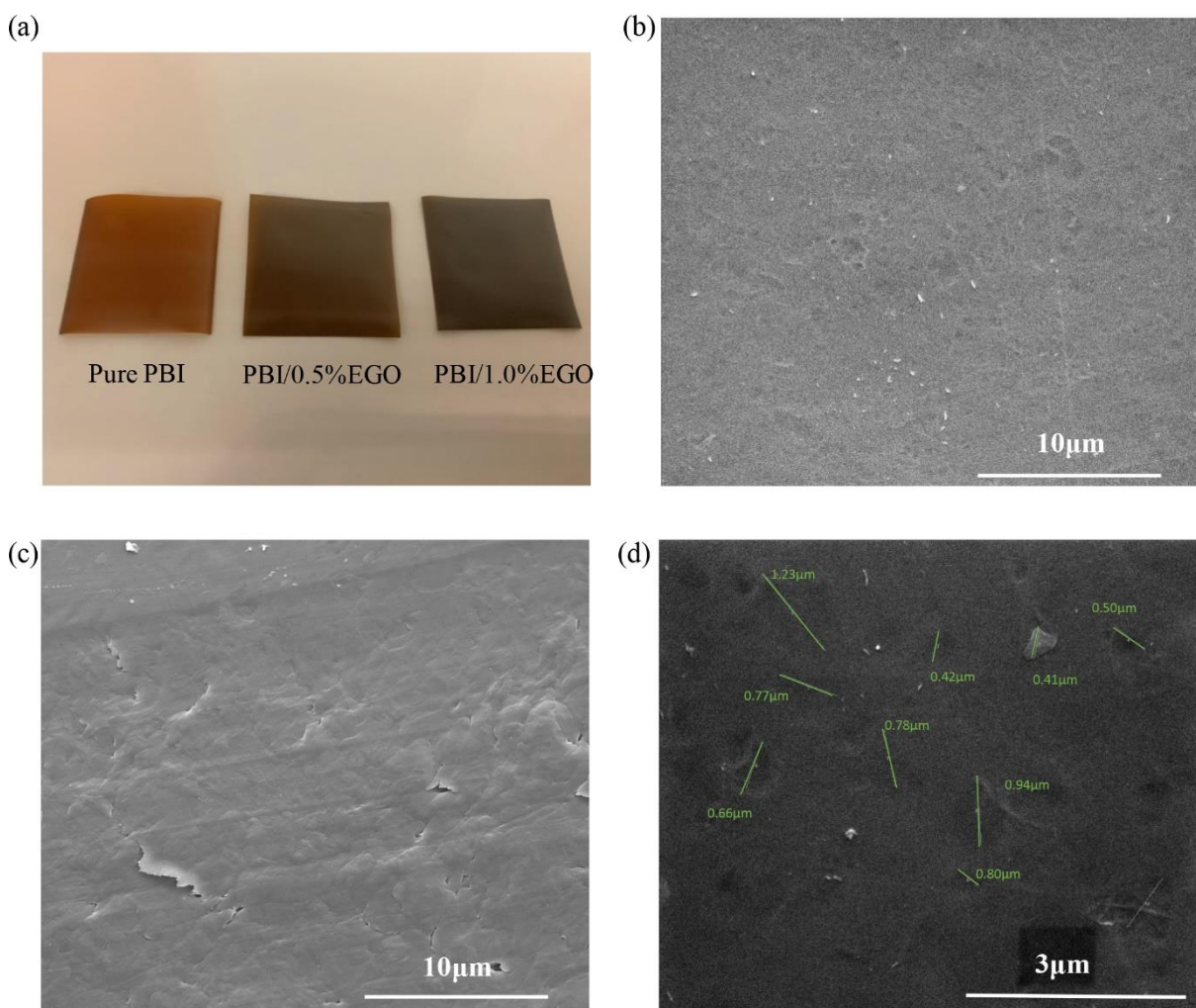
Figure 5. 8. Appearance and SEM images of PBI and PBI/EGO composite membranes: (a) appearance of pure PBI, PBI/0.5%EGO and PBI/1.0%EGO, (b) SEM image of PBI/1.0% EGO surface ×5000, (c) SEM image of PBI/1.0% EGO cross-section ×5000, (d) SEM image of PBI/1.0% EGO surface ×20000

The performance comparison between EGO prepared by electrochemical exfoliation in this work and GO prepared by Hummers' methods doped in PBI is shown in **Table 5. 3**. Previous literature have proposed that the application potential of GO/PBI composite membranes in high-temperature PEM fuel cells depends on factors such as better proton conductivity or mechanical properties of the membrane. However, the research on the performance of specific GO/PBI composite membrane-based fuel cells that can be used for reference is very limited. This may be related to the fact that the GO without further functionalization is prone to agglomerate during the evaporation of the 2wt% PBI/DMAc solution (typical concentration

used in literature), making the distribution of GO not uniform [21]. The PBI/DMAc solution with a concentration of 20wt% (high viscosity) and a doctor blade method was used in this work to make the distribution of GO more uniform. This can be reflected by the appearance and the SEM diagrams of PBI membranes with different EGO loadings which are shown in **Figure 5. 8**. As shown in **Figure 5. 8**a, with the increase of EGO loading, the colour of the membranes gradually changed from light brown to dark brown, and the colour change was very uniform. It can be seen from the SEM images of the surface and cross-section of PBI/1.0%EGO (shown in **Figure 5. 8**b and c, respectively) that PBI/1.0%EGO is quite homogeneous and the surface of PBI/1.0%EGO is very flat. The size and distribution of EGO in the PBI membrane can be represented by **Figure 5. 8**d. The size of EGO is about 0.4 to 1µm. This small size is conducive to the uniform distribution of EGO in PBI membranes. Üregen et al. and Xu et al. tested the performance of Hummers' method made GO / PBI composite membrane in high-temperature PEM fuel cells [21][81]. Although the GO/PBI composite membranes used in their work have the same GO loading and similar peak power density, there are obvious differences in their peak power density improvement compared to their pure PBI (22.5% and 72% respectively), which may be attributed to the poor performance of pure PBI (about 200mW/cm^2) in the work of Xu et al. In recently published works, the peak power density of high-temperature fuel cells based on pure PBI membranes are mostly between 270-390mW cm^{-2} at 150°C [84][85][86]. Yang et al. tried to use Triazole modified graphene oxide to dope in PBI and got good peak power density at a higher temperature (180°C), but it was only 6% higher than pure PBI [23]. Although PBI/2%EGO membrane prepared in our work uses lower operating temperature and lower PA doping level, compared to GO made by Hummers' method, the doping of EGO prepared in this work shows similar or higher power density and improvement compared to pure PBI membranes. Besides, the benefits of electrochemical exfoliation such as reduced environmental impact, fast, high yield, low cost should not be

underestimated. In addition, the PBI/2%EGO composite membrane prepared in this work showed better stability in AST. After running for nearly 70 hours AST by chronopotentiometry scan between 0.6A cm^{-2} and 1A cm^{-2}, The voltage of PBI/2%EGO composite membrane based MEA at 0.6A cm^{-2} and 1A cm^{-2} dropped by 11.4% and 16.5%, while pure PBI membrane based MEA dropped by 16.9% and 33.3%, respectively. The AST of PBI/2%EGO and pure PBI are shown in **Figure S5. 14**. The better durability may be due to the PBI/EGO composite membrane having better thermal stability, mechanical property, and ability to slow down the leaching of phosphoric acid.

Table 5. 3. The performance comparison between EGO prepared by electrochemical exfoliation in this work and GO prepared by Hummers' method [81][21][23]

GO type	GO preparation	GO Loading (wt%)	ADL	Working temperature (℃)	Peak power density (mW/cm^2)	Improvement compared to pure PBI
Pure GO (this work)	Electrochemical Exfoliation	2	9.7	150℃	429	29.2%
Pure GO	Hummers' method	2	13	165℃	380	22.5%
Pure GO	Hummers' method	2	11	175℃	380	72%
Triazole modified graphene oxide	Modified Hummers' method	1.2	12.2	160℃	~450	~6%

5.7 Conclusions

In summary, a 3D printing-based reactor is designed to use natural graphite flakes for electrochemical exfoliation to obtain large yields of graphene oxide. This process is implemented using only ammonium sulphate salt solution and no strong acid or strong oxidant. Characterization of the graphene oxide shows that the GO exfoliated from natural graphite flakes mainly consists of two-three layers and has a smaller size, compared with products obtained using graphite foil under the same conditions (10V and 1M Ammonium sulphate solution as electrolyte). The oxidation degree of the product exfoliated from natural graphite flakes with the reactor is higher. According to Raman mapping, its functional group distribution is not only distributed on the edge like exfoliated products from foil, being more uniformly distributed on the graphene. In addition, for the graphene oxide exfoliated from natural graphite flakes with the new reactor, by increasing the electrolyte concentration or increasing the reaction time, the electronic conductivity will decrease; defect level and the oxygen content will increase. These indicate that increasing the reaction time or electrolyte concentration will increase the degree of oxidation. The comparison experiment and the method of controlling variables prove that natural graphite flakes and the reactor cause the difference between graphene products obtained by exfoliating two different raw materials, due to the different exfoliating mechanisms caused by the combination of natural graphite flakes and the special structure of the reactor. The as-prepared EGO is applied in PBI membrane composites to improve the performance of high-temperature PEMFC. PBI/EGO has better proton conductivity. The maximum power density of PBI/0.5%EGO ($378mW\ cm^{-2}$), PBI/1%EGO ($413mW\ cm^{-2}$) and PBI/2%EGO ($429mW\ cm^{-2}$) is 13.8%, 24.4% and 29.2% higher than that of PBI ($332mW\ cm^{-2}$), respectively. In addition, EGO improves the mechanical behaviour, and durability under AST of PBI.

5.8 Declaration of Competing Interest

The authors declare that they have no known competing financial interests or personal relationships that could have appeared to influence the work reported in this paper.

5.9 Acknowledgment

5.10 References:

[1]   D. Konios, M.M. Stylianakis, E. Stratakis, E. Kymakis, Dispersion behaviour of graphene oxide and reduced graphene oxide, Journal of Colloid and Interface Science. 430 (2014) 108–112. https://doi.org/10.1016/J.JCIS.2014.05.033.

[2]   D.R. Dreyer, S. Park, C.W. Bielawski, R.S. Ruoff, The chemistry of graphene oxide, Chemical Society Reviews. 39 (2009) 228–240. https://doi.org/10.1039/B917103G.

[3]   S. Eigler, A. Hirsch, S. Eigler, A. Hirsch, Chemistry with Graphene and Graphene Oxide—Challenges for Synthetic Chemists, Angewandte Chemie International Edition. 53 (2014) 7720–7738. https://doi.org/10.1002/ANIE.201402780.

[4]   Z. Sun, D.K. James, J.M. Tour, Graphene Chemistry: Synthesis and Manipulation, The Journal of Physical Chemistry Letters. 2 (2011) 2425–2432. https://doi.org/10.1021/JZ201000A.

[5]   T. Bayer, R. Selyanchyn, S. Fujikawa, K. Sasaki, S.M. Lyth, Spray-painted graphene oxide membrane fuel cells, Journal of Membrane Science. 541 (2017) 347–357. https://doi.org/10.1016/J.MEMSCI.2017.07.012.

[6]   A.S. Pushkarev, I. V. Pushkareva, S.A. Grigoriev, V.N. Kalinichenko, M.Y. Presniakov, V.N. Fateev, Electrocatalytic layers modified by reduced graphene oxide for PEM fuel cells, International Journal of Hydrogen Energy. 40 (2015) 14492–14497. https://doi.org/10.1016/J.IJHYDENE.2015.05.093.

[7]   H.K. Jang, H.I. Kim, T. Dodge, P. Sun, H. Zhu, J. Do Nam, J. Suhr, Interfacial shear strength of reduced graphene oxide polymer composites, Carbon. 77 (2014) 390–397. https://doi.org/10.1016/J.CARBON.2014.05.042.

[8]   M. Li, C. Gao, H. Hu, Z. Zhao, Electrical conductivity of thermally reduced graphene

oxide/polymer composites with a segregated structure, Carbon. 65 (2013) 371–373. https://doi.org/10.1016/J.CARBON.2013.08.016.

[9]   Y. Jin, E.P. Boon, L.T. Le, W. Lee, Fabric-infused array of reduced graphene oxide sensors for mapping of skin temperatures, Sensors and Actuators A: Physical. 280 (2018) 92–98. https://doi.org/10.1016/J.SNA.2018.06.043.

[10]   W. Ren, S. Mura, J.M.K. Irudayaraj, Modified graphene oxide sensors for ultra-sensitive detection of nitrate ions in water, Talanta. 143 (2015) 234–239. https://doi.org/10.1016/J.TALANTA.2015.05.073.

[11]   U.R. Farooqui, A.L. Ahmad, N.A. Hamid, Graphene oxide: A promising membrane material for fuel cells, Renewable and Sustainable Energy Reviews. 82 (2018) 714–733. https://doi.org/10.1016/J.RSER.2017.09.081.

[12]   H. Zarrin, D. Higgins, Y. Jun, Z. Chen, M. Fowler, Functionalized Graphene Oxide Nanocomposite Membrane for Low Humidity and High Temperature Proton Exchange Membrane Fuel Cells, Journal of Physical Chemistry C. 115 (2011) 20774–20781. https://doi.org/10.1021/JP204610J.

[13]   H.A. Hjuler, D. Aili, J.O. Jensen, High temperature polymer electrolyte membrane fuel cells: Approaches, status, and perspectives, High Temperature Polymer Electrolyte Membrane Fuel Cells: Approaches, Status, and Perspectives. (2016) 1–545. https://doi.org/10.1007/978-3-319-17082-4.

[14]   M.W. Ahmad, B. Dey, G. Sarkhel, D.S. Bag, A. Choudhury, Exfoliated graphene reinforced polybenzimidazole nanocomposite with improved electrical, mechanical and thermal properties, Materials Chemistry and Physics. 223 (2019) 426–433. https://doi.org/10.1016/J.MATCHEMPHYS.2018.11.026.

[15] E. Abouzari-Lotf, M. Zakeri, M.M. Nasef, M. Miyake, P. Mozarmnia, N.A. Bazilah, N.F. Emelin, A. Ahmad, Highly durable polybenzimidazole composite membranes with phosphonated graphene oxide for high temperature polymer electrolyte membrane fuel cells, Journal of Power Sources. 412 (2019) 238–245. https://doi.org/10.1016/J.JPOWSOUR.2018.11.057.

[16] S. Yu, L. Xiao, B.C. Benicewicz, Durability Studies of PBI-based High Temperature PEMFCs, Fuel Cells. 8 (2008) 165–174. https://doi.org/10.1002/FUCE.200800024.

[17] J.H. Liao, Q.F. Li, H.C. Rudbeck, J.O. Jensen, A. Chromik, N.J. Bjerrum, J. Kerres, W. Xing, Oxidative Degradation of Polybenzimidazole Membranes as Electrolytes for High Temperature Proton Exchange Membrane Fuel Cells, Fuel Cells. 11 (2011) 745–755. https://doi.org/10.1002/FUCE.201000146.

[18] J. Yang, W. Liao, Y. Liu, M. Murugananthan, Y. Zhang, Degradation of Rhodamine B using a Visible-light driven Photocatalytic Fuel Cell, Electrochimica Acta. 144 (2014) 7–15. https://doi.org/10.1016/J.ELECTACTA.2014.08.036.

[19] M.F.H. Schuster, W.H. Meyer, M. Schuster, K.D. Kreuer, Toward a New Type of Anhydrous Organic Proton Conductor Based on Immobilized Imidazole, Chemistry of Materials. 16 (2004) 329–337. https://doi.org/10.1021/CM021298Q.

[20] C. Xue, J. Zou, Z. Sun, F. Wang, K. Han, H. Zhu, Graphite oxide/functionalized graphene oxide and polybenzimidazole composite membranes for high temperature proton exchange membrane fuel cells, International Journal of Hydrogen Energy. 39 (2014) 7931–7939. https://doi.org/10.1016/J.IJHYDENE.2014.03.061.

[21] C. Xu, Y. Cao, R. Kumar, X. Wu, X. Wang, K. Scott, A polybenzimidazole/sulfonated graphite oxide composite membrane for high temperature polymer electrolyte

membrane fuel cells, Journal of Materials Chemistry. 21 (2011) 11359–11364. https://doi.org/10.1039/C1JM11159K.

[22] A. Verma, K. Scott, Development of higherature PEMFC based on heteropolyacids and polybenzimidazole, Journal of Solid State Electrochemistry. 14 (2010) 213–219. https://doi.org/10.1007/S10008-008-0678-0/FIGURES/8.

[23] J. Yang, C. Liu, L. Gao, J. Wang, Y. Xu, R. He, Novel composite membranes of triazole modified graphene oxide and polybenzimidazole for high temperature polymer electrolyte membrane fuel cell applications, RSC Advances. 5 (2015) 101049–101054. https://doi.org/10.1039/C5RA16554G.

[24] J. Kim, K. Kim, T. Ko, J. Han, J.C. Lee, Polybenzimidazole composite membranes containing imidazole functionalized graphene oxide showing high proton conductivity and improved physicochemical properties, International Journal of Hydrogen Energy. 46 (2021) 12254–12262. https://doi.org/10.1016/J.IJHYDENE.2020.02.193.

[25] E. Abouzari-Lotf, H. Ghassemi, S. Mehdipour-Ataei, A. Shockravi, Phosphonated polyimides: Enhancement of proton conductivity at high temperatures and low humidity, Journal of Membrane Science. 516 (2016) 74–82. https://doi.org/10.1016/J.MEMSCI.2016.06.009.

[26] V. Atanasov, D. Gudat, B. Ruffmann, J. Kerres, Highly phosphonated polypentafluorostyrene: Characterization and blends with polybenzimidazole, European Polymer Journal. 49 (2013) 3977–3985. https://doi.org/10.1016/J.EURPOLYMJ.2013.09.002.

[27] L. Staudenmaier, Verfahren zur Darstellung der Graphitsäure, Berichte Der Deutschen Chemischen Gesellschaft. 31 (1898) 1481–1487.

https://doi.org/10.1002/CBER.18980310237.

[28] N.I. Zaaba, K.L. Foo, U. Hashim, S.J. Tan, W.W. Liu, C.H. Voon, Synthesis of Graphene Oxide using Modified Hummers Method: Solvent Influence, Procedia Engineering. 184 (2017) 469–477. https://doi.org/10.1016/J.PROENG.2017.04.118.

[29] C. Siegfried Eigler, M. Enzelberger-Heim, S. Grimm, P. Hofmann, W. Kroener, A. Geworski, C. Dotzer, M. Röckert, J. Xiao, C. Papp, O. Lytken, H.-P. Steinrück, P. Müller, A. Hirsch, S. Eigler, S. Grimm, C. Dotzer, A. Hirsch, M. Enzelberger-Heim, P. Hofmann, W. Kroener, A. Geworski, P. Müller, M. Röckert, J. Xiao, C. Papp, O. Lytken, H. Steinrück, Wet Chemical Synthesis of Graphene, Advanced Materials. 25 (2013) 3583–3587. https://doi.org/10.1002/ADMA.201300155.

[30] K. Parvez, Z.S. Wu, R. Li, X. Liu, R. Graf, X. Feng, K. Müllen, Exfoliation of graphite into graphene in aqueous solutions of inorganic salts, Journal of the American Chemical Society. 136 (2014) 6083–6091. https://doi.org/10.1021/JA5017156/SUPPL_FILE/JA5017156_SI_001.PDF.

[31] A.J. Cooper, N.R. Wilson, I.A. Kinloch, R.A.W. Dryfe, Single stage electrochemical exfoliation method for the production of few-layer graphene via intercalation of tetraalkylammonium cations, Carbon. 66 (2014) 340–350. https://doi.org/10.1016/J.CARBON.2013.09.009.

[32] C.Y. Su, A.Y. Lu, Y. Xu, F.R. Chen, A.N. Khlobystov, L.J. Li, High-quality thin graphene films from fast electrochemical exfoliation, ACS Nano. 5 (2011) 2332–2339. https://doi.org/10.1021/NN200025P/SUPPL_FILE/NN200025P_SI_003.ZIP.

[33] S. Tian, S. Yang, T. Huang, J. Sun, H. Wang, X. Pu, L. Tian, P. He, G. Ding, X. Xie, One-step fast electrochemical fabrication of water-dispersible graphene, Carbon. 111

(2017) 617–621. https://doi.org/10.1016/J.CARBON.2016.10.044.

[34] M.K. Punith Kumar, M. Nidhi, C. Srivastava, Electrochemical exfoliation of graphite to produce graphene using tetrasodium pyrophosphate, RSC Advances. 5 (2015) 24846–24852. https://doi.org/10.1039/C5RA01304F.

[35] A.M. Abdelkader, I.A. Kinloch, R.A.W. Dryfe, High-yield electro-oxidative preparation of graphene oxide, Chemical Communications. 50 (2014) 8402–8404. https://doi.org/10.1039/C4CC03260H.

[36] B. Gurzęda, P. Florczak, M. Kempiński, B. Peplińska, P. Krawczyk, S. Jurga, Synthesis of graphite oxide by electrochemical oxidation in aqueous perchloric acid, Carbon. 100 (2016) 540–545. https://doi.org/10.1016/J.CARBON.2016.01.044.

[37] J. Cao, P. He, M.A. Mohammed, X. Zhao, R.J. Young, B. Derby, I.A. Kinloch, R.A.W. Dryfe, Two-Step Electrochemical Intercalation and Oxidation of Graphite for the Mass Production of Graphene Oxide, Journal of the American Chemical Society. 139 (2017) 17446–17456.

https://doi.org/10.1021/JACS.7B08515/SUPPL_FILE/JA7B08515_SI_001.PDF.

[38] F. Sharif, A.S. Zeraati, P. Ganjeh-Anzabi, N. Yasri, M. Perez-Page, S.M. Holmes, U. Sundararaj, M. Trifkovic, E.P.L. Roberts, Synthesis of a high-temperature stable electrochemically exfoliated graphene, Carbon. 157 (2020) 681–692. https://doi.org/10.1016/J.CARBON.2019.10.042.

[39] M. Wissler, Graphite and carbon powders for electrochemical applications, Journal of Power Sources. 156 (2006) 142–150. https://doi.org/10.1016/J.JPOWSOUR.2006.02.064.

[40] A. Ambrosi, M. Pumera, Electrochemically Exfoliated Graphene and Graphene Oxide

for Energy Storage and Electrochemistry Applications, Chemistry – A European Journal. 22 (2016) 153–159. https://doi.org/10.1002/CHEM.201503110.

[41] J. Liu, C.K. Poh, D. Zhan, L. Lai, S.H. Lim, L. Wang, X. Liu, N. Gopal Sahoo, C. Li, Z. Shen, J. Lin, Improved synthesis of graphene flakes from the multiple electrochemical exfoliation of graphite rod, Nano Energy. 2 (2013) 377–386. https://doi.org/10.1016/J.NANOEN.2012.11.003.

[42] Z. Tian, P. Yu, S.E. Lowe, A.G. Pandolfo, T.R. Gengenbach, K.M. Nairn, J. Song, X. Wang, Y.L. Zhong, D. Li, Facile electrochemical approach for the production of graphite oxide with tunable chemistry, Carbon. 112 (2017) 185–191. https://doi.org/10.1016/J.CARBON.2016.10.098.

[43] M. Piao, G. Kim, G.P. Kennedy, S. Roth, U. Dettlaff-Weglikowska, Preparation and characterization of expanded graphite polymer composite films for thermoelectric applications, Physica Status Solidi (B). 250 (2013) 2529–2534. https://doi.org/10.1002/PSSB.201300078.

[44] I.M. Afanasov, D. V. Savchenko, S.G. Ionov, D.A. Rusakov, A.N. Seleznev, V. V. Avdeev, Thermal conductivity and mechanical properties of expanded graphite, Inorganic Materials. 45 (2009) 486–490. https://doi.org/10.1134/S0020168509050057.

[45] M.B. Dowell, R.A. Howard, Tensile and compressive properties of flexible graphite foils, Carbon. 24 (1986) 311–323. https://doi.org/10.1016/0008-6223(86)90232-0.

[46] S.E. Lowe, G. Shi, Y. Zhang, J. Qin, S. Wang, A. Uijtendaal, J. Sun, L. Jiang, S. Jiang, D. Qi, M. Al-Mamun, P. Liu, Y.L. Zhong, H. Zhao, Scalable Production of Graphene Oxide Using a 3D-Printed Packed-Bed Electrochemical Reactor with a Boron-Doped Diamond Electrode, ACS Applied Nano Materials. 2 (2019) 867–878.

https://doi.org/10.1021/ACSANM.8B02126/SUPPL_FILE/AN8B02126_SI_001.PDF.

[47] P. Yu, Z. Tian, S.E. Lowe, J. Song, Z. Ma, X. Wang, Z.J. Han, Q. Bao, G.P. Simon, D. Li, Y.L. Zhong, Mechanically-assisted electrochemical production of graphene oxide, Chemistry of Materials. 28 (2016) 8429–8438. https://doi.org/10.1021/ACS.CHEMMATER.6B04415/SUPPL_FILE/CM6B04415_SI _001.PDF.

[48] D. Schonvogel, M. Rastedt, P. Wagner, M. Wark, A. Dyck, Impact of Accelerated Stress Tests on High Temperature PEMFC Degradation, Fuel Cells. 16 (2016) 480–489. https://doi.org/10.1002/FUCE.201500160.

[49] J.M. Munuera, J.I. Paredes, S. Villar-Rodil, M. Ayán-Varela, A. Pagán, S.D. Aznar-Cervantes, J.L. Cenis, A. Martínez-Alonso, J.M.D. Tascón, High quality, low oxygen content and biocompatible graphene nanosheets obtained by anodic exfoliation of different graphite types, Carbon. 94 (2015) 729–739. https://doi.org/10.1016/J.CARBON.2015.07.053.

[50] A.C. Ferrari, Raman spectroscopy of graphene and graphite: Disorder, electron–phonon coupling, doping and nonadiabatic effects, Solid State Communications. 143 (2007) 47–57. https://doi.org/10.1016/J.SSC.2007.03.052.

[51] L.M. Malard, M.A. Pimenta, G. Dresselhaus, M.S. Dresselhaus, Raman spectroscopy in graphene, Physics Reports. 473 (2009) 51–87. https://doi.org/10.1016/J.PHYSREP.2009.02.003.

[52] W. Jia, B. Tang, P. Wu, Novel Slightly Reduced Graphene Oxide Based Proton Exchange Membrane with Constructed Long-Range Ionic Nanochannels via Self-Assembling of Nafion, ACS Applied Materials and Interfaces. 9 (2017) 22620–22627.

https://doi.org/10.1021/ACSAMI.7B06117/SUPPL_FILE/AM7B06117_SI_001.PDF.

[53]   M.J. Fernández-Merino, J.I. Paredes, S. Villar-Rodil, L. Guardia, P. Solís-Fernández, D.
        Salinas-Torres, D. Cazorla-Amorós, E. Morallón, A. Martínez-Alonso, J.M.D. Tascón,
        Investigating the influence of surfactants on the stabilization of aqueous reduced
        graphene oxide dispersions and the characteristics of their composite films, Carbon. 50
        (2012) 3184–3194. https://doi.org/10.1016/J.CARBON.2011.10.039.

[54]   V.M. Pereira, F. Guinea, J.M.B. Lopes Dos Santos, N.M.R. Peres, A.H. Castro Neto,
        Disorder induced localized states in graphene, Physical Review Letters. 96 (2006)
        036801. https://doi.org/10.1103/PHYSREVLETT.96.036801/FIGURES/3/MEDIUM.

[55]   I. Jung, D.A. Dikin, R.D. Piner, R.S. Ruoff, Tunable electrical conductivity of individual
        graphene oxide sheets reduced at "Low" temperatures, Nano Letters. 8 (2008) 4283–
        4287. https://doi.org/10.1021/NL8019938/SUPPL_FILE/NL8019938_SI_001.PDF.

[56]   M.J. McAllister, J.L. Li, D.H. Adamson, H.C. Schniepp, A.A. Abdala, J. Liu, M.
        Herrera-Alonso, D.L. Milius, R. Car, R.K. Prud'homme, I.A. Aksay, Single Sheet
        Functionalized Graphene by Oxidation and Thermal Expansion of Graphite, Chemistry
        of Materials. 19 (2007) 4396–4404. https://doi.org/10.1021/CM0630800.

[57]   X. Jiang, Y. Cao, P. Li, J. Wei, K. Wang, D. Wu, H. Zhu, Polyaniline/graphene/carbon
        fiber ternary composites as supercapacitor electrodes, Materials Letters. 140 (2015) 43–
        47. https://doi.org/10.1016/J.MATLET.2014.10.162.

[58]   J. Shen, Y. Hu, C. Li, C. Qin, M. Ye, Synthesis of Amphiphilic Graphene Nanoplatelets,
        Small. 5 (2009) 82–85. https://doi.org/10.1002/SMLL.200800988.

[59]   P.R. Griffiths, J.A. De Haseth, Introduction to Vibrational Spectroscopy, Chemical
        Analysis. 171 (2007) 1–18. https://doi.org/10.1002/9780470106310.CH1.

[60] S. Yang, A.G. Ricciardulli, S. Liu, R. Dong, M.R. Lohe, A. Becker, M.A. Squillaci, P. Samorì, K. Müllen, X. Feng, Ultrafast Delamination of Graphite into High-Quality Graphene Using Alternating Currents, Angewandte Chemie International Edition. 56 (2017) 6669–6675. https://doi.org/10.1002/ANIE.201702076.

[61] L. Lai, J.R. Potts, D. Zhan, L. Wang, C.K. Poh, C. Tang, H. Gong, Z. Shen, J. Lin, R.S. Ruoff, Exploration of the active center structure of nitrogen-doped graphene-based catalysts for oxygen reduction reaction, Energy & Environmental Science. 5 (2012) 7936–7942. https://doi.org/10.1039/C2EE21802J.

[62] F. Lou, M.E.M. Buan, N. Muthuswamy, J.C. Walmsley, M. Ronning, D. Chen, One-step electrochemical synthesis of tunable nitrogen-doped graphene, Journal of Materials Chemistry A. 4 (2016) 1233–1243. https://doi.org/10.1039/C5TA08038J.

[63] R. Zeis, Materials and characterization techniques for high-temperature polymer electrolyte membrane fuel cells, Beilstein Journal of Nanotechnology 6:8. 6 (2015) 68–83. https://doi.org/10.3762/BJNANO.6.8.

[64] G. Sobon, J. Sotor, J. Jagiello, R. Kozinski, M. Zdrojek, M. Holdynski, P. Paletko, J. Boguslawski, L. Lipinska, K.M. Abramski, Graphene Oxide vs Reduced Graphene Oxide as saturable absorbers for Er-doped passively mode-locked fiber laser, Optics Express. 20 (2012) 19463. https://doi.org/10.1364/OE.20.019463.

[65] G. Eda, G. Fanchini, M. Chhowalla, Large-area ultrathin films of reduced graphene oxide as a transparent and flexible electronic material, Nature Nanotechnology 2008 3:5. 3 (2008) 270–274. https://doi.org/10.1038/nnano.2008.83.

[66] J.C. Meyer, A.K. Geim, M.I. Katsnelson, K.S. Novoselov, D. Obergfell, S. Roth, C. Girit, A. Zettl, On the roughness of single- and bi-layer graphene membranes, Solid

State Communications. 143 (2007) 101–109. https://doi.org/10.1016/J.SSC.2007.02.047.

[67] S.S. Shojaeenezhad, M. Farbod, I. Kazeminezhad, Effects of initial graphite particle size and shape on oxidation time in graphene oxide prepared by Hummers' method, Journal of Science: Advanced Materials and Devices. 2 (2017) 470–475. https://doi.org/10.1016/J.JSAMD.2017.09.003.

[68] M.D.P. Lavin-Lopez, A. Romero, J. Garrido, L. Sanchez-Silva, J.L. Valverde, Influence of different improved hummers method modifications on the characteristics of graphite oxide in order to make a more easily scalable method, Industrial and Engineering Chemistry Research. 55 (2016) 12836–12847. https://doi.org/10.1021/ACS.IECR.6B03533/SUPPL_FILE/IE6B03533_SI_001.PDF.

[69] X. Hu, Y. Yu, W. Hou, J. Zhou, L. Song, Effects of particle size and pH value on the hydrophilicity of graphene oxide, Applied Surface Science. 273 (2013) 118–121. https://doi.org/10.1016/J.APSUSC.2013.01.201.

[70] M.S. Dresselhaus, G. Dresselhaus, Intercalation compounds of graphite, Advances in Physics. 51 (2002) 1–186. https://doi.org/10.1080/00018730110113644.

[71] A.M. Dimiev, S.M. Bachilo, R. Saito, J.M. Tour, Reversible formation of ammonium persulfate/sulfuric acid graphite intercalation compounds and their peculiar Raman spectra, ACS Nano. 6 (2012) 7842–7849. https://doi.org/10.1021/NN3020147/SUPPL_FILE/NN3020147_SI_001.PDF.

[72] A.M. Dimiev, G. Ceriotti, N. Behabtu, D. Zakhidov, M. Pasquali, R. Saito, J.M. Tour, Direct real-time monitoring of stage transitions in graphite intercalation compounds, ACS Nano. 7 (2013) 2773–2780.

https://doi.org/10.1021/NN400207E/SUPPL_FILE/NN400207E_SI_003.AVI.

[73] M. Inagaki, N. Iwashita, E. Kouno, Potential change with intercalation of sulfuric acid into graphite by chemical oxidation, Carbon. 28 (1990) 49–55. https://doi.org/10.1016/0008-6223(90)90092-D.

[74] F. Wang, J. Yi, Y. Wang, C. Wang, J. Wang, Y. Xia, F. Wang, J. Yi, Y.G. Wang, C.X. Wang, Y.Y. Xia, J.Q. Wang, Graphite Intercalation Compounds (GICs): A New Type of Promising Anode Material for Lithium-Ion Batteries, Advanced Energy Materials. 4 (2014) 1300600. https://doi.org/10.1002/AENM.201300600.

[75] K. Zhang, Y. Zhang, S. Wang, Enhancing thermoelectric properties of organic composites through hierarchical nanostructures, Scientific Reports. 3 (2013). https://doi.org/10.1038/SREP03448.

[76] F. Beck, J. Jiang, H. Krohn, Potential oscillations during galvanostatic overoxidation of graphite in aqueous sulphuric acids, Journal of Electroanalytical Chemistry. 389 (1995) 161–165. https://doi.org/10.1016/0022-0728(95)03870-M.

[77] B. Gurzęda, T. Buchwald, M. Nocuń, A. Bąkowicz, P. Krawczyk, Graphene material preparation through thermal treatment of graphite oxide electrochemically synthesized in aqueous sulfuric acid, RSC Advances. 7 (2017) 19904–19911. https://doi.org/10.1039/C7RA01678F.

[78] S. Park, J. An, J.R. Potts, A. Velamakanni, S. Murali, R.S. Ruoff, Hydrazine-reduction of graphite- and graphene oxide, Carbon. 49 (2011) 3019–3023. https://doi.org/10.1016/J.CARBON.2011.02.071.

[79] J. Shen, Y. Hu, M. Shi, X. Lu, C. Qin, C. Li, M. Ye, Fast and facile preparation of graphene oxide and reduced graphene oxide nanoplatelets, Chemistry of Materials. 21

(2009) 3514–3520. https://doi.org/10.1021/CM901247T/SUPPL_FILE/CM901247T_SI_001.PDF.

[80] H. Cho, E. Hur, D. Henkensmeier, G. Jeong, E. Cho, H.J. Kim, J.H. Jang, K.Y. Lee, H.A. Hjuler, Q. Li, J.O. Jensen, L.N. Cleemann, meta-PBI/methylated PBI-OO blend membranes for acid doped HT PEMFC, European Polymer Journal. 58 (2014) 135–143. https://doi.org/10.1016/J.EURPOLYMJ.2014.06.019.

[81] N. Üregen, K. Pehlivanoğlu, Y. Özdemir, Y. Devrim, Development of polybenzimidazole/graphene oxide composite membranes for high temperature PEM fuel cells, International Journal of Hydrogen Energy. 42 (2017) 2636–2647. https://doi.org/10.1016/J.IJHYDENE.2016.07.009.

[82] S. Wasterlain, D. Candusso, F. Harel, D. Hissel, X. Franois, Development of new test instruments and protocols for the diagnostic of fuel cell stacks, Journal of Power Sources. 196 (2011) 5325–5333. https://doi.org/10.1016/J.JPOWSOUR.2010.08.029.

[83] V. Ramani, H.R. Kunz, J.M. Fenton, Investigation of Nafion®/HPA composite membranes for high temperature/low relative humidity PEMFC operation, Journal of Membrane Science. 232 (2004) 31–44. https://doi.org/10.1016/J.MEMSCI.2003.11.016.

[84] C.Y. Lee, Y.C. Chiang, F.B. Weng, S.C. Li, P.H. Wu, H.I. Yueh, Flexible micro temperature, voltage and current sensors for local real-time microscopic diagnosis inside high temperature proton exchange membrane fuel cell stack, Renewable Energy. 108 (2017) 126–131. https://doi.org/10.1016/J.RENENE.2017.02.015.

[85] J. Yang, H. Jiang, L. Gao, J. Wang, Y. Xu, R. He, Fabrication of crosslinked polybenzimidazole membranes by trifunctional crosslinkers for high temperature proton exchange membrane fuel cells, International Journal of Hydrogen Energy. 43 (2018)

3299–3307. https://doi.org/10.1016/J.IJHYDENE.2017.12.141.

[86] K. Seo, K.H. Nam, H. Han, Proton Transport in Aluminum-Substituted Mesoporous Silica Channel-Embedded High-Temperature Anhydrous Proton-Exchange Membrane Fuel Cells, Scientific Reports 2020 10:1. 10 (2020) 1–9. https://doi.org/10.1038/s41598-020-66935-5.

5.11 Supplementary Information

The appearance of raw materials for electrochemical exfoliation are shown in **Figure S5. 1**. Nature graphite flakes and vein graphite are natural graphite without treatment. Graphite foil is made by natural graphite flake with chemical, thermal and mechanical treatment.
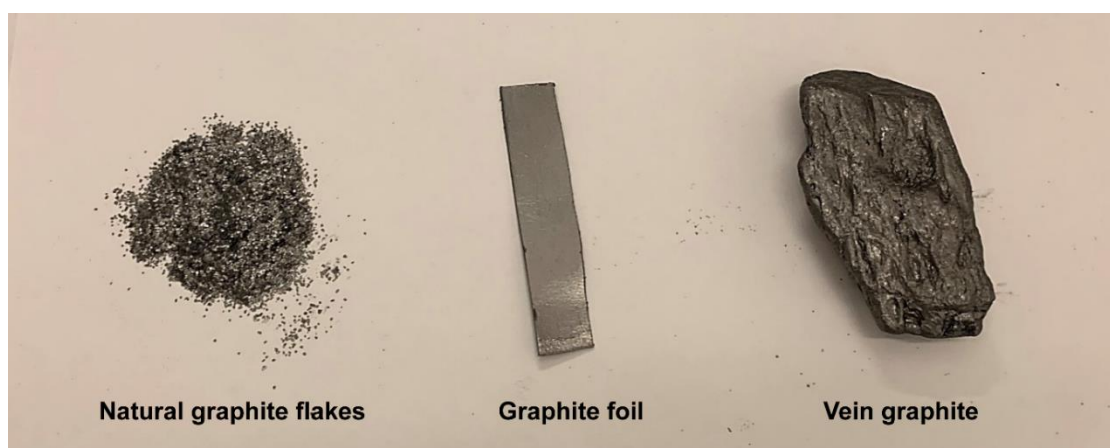
Figure S5. 1. The appearance of natural graphite flakes, graphite foil and vein graphite.

The engineering drawings of the exfoliation cell and parts are shown in **Figure S5. 2**. The shape of graphite after loading is generally inverted "T". The platinum rod was also bent at 90 degrees and then formed into a ring structure. As shown in **Figure S5. 2**a, the two 90-degree bends change the two electrodes from vertical parallel to horizontal parallel (as shown by the green line ① and blue line ②).

The base (shown in **Figure S5. 2**b) and the cover (shown in **Figure S5. 2**c) of the reactor of the reactor are connected by a tenon structure and can be easily removed by rotation. The role of the base is to raise the graphite to ensure that the copper sheet is not immersed in the solution while allowing enough solution for reaction in the beaker. The bottom of the cover is designed with an inclination of 10 ° to ensure that the graphite inside the reactor is fully squeezed in all directions. Although the holes on the cover are slightly larger than the size of natural graphite

266

flakes, due to the infiltration of the solution, the graphite as a whole is lumpy and fully squeezed inside, and the generate bubbles will seal the voids, so there is only a small amount of graphite leaked during reaction. The plug of the reactor (as shown in **Figure S5. 2**d) can seal the graphite from the top and apply pressure to the graphite by means of a spring. The slot on the side allows the copper sheet to attach to conduct current. The reason why the plug is not designed as a copper product is that it can be replaced at any time once the copper sheet is corroded, which greatly reduces the amount of metal.
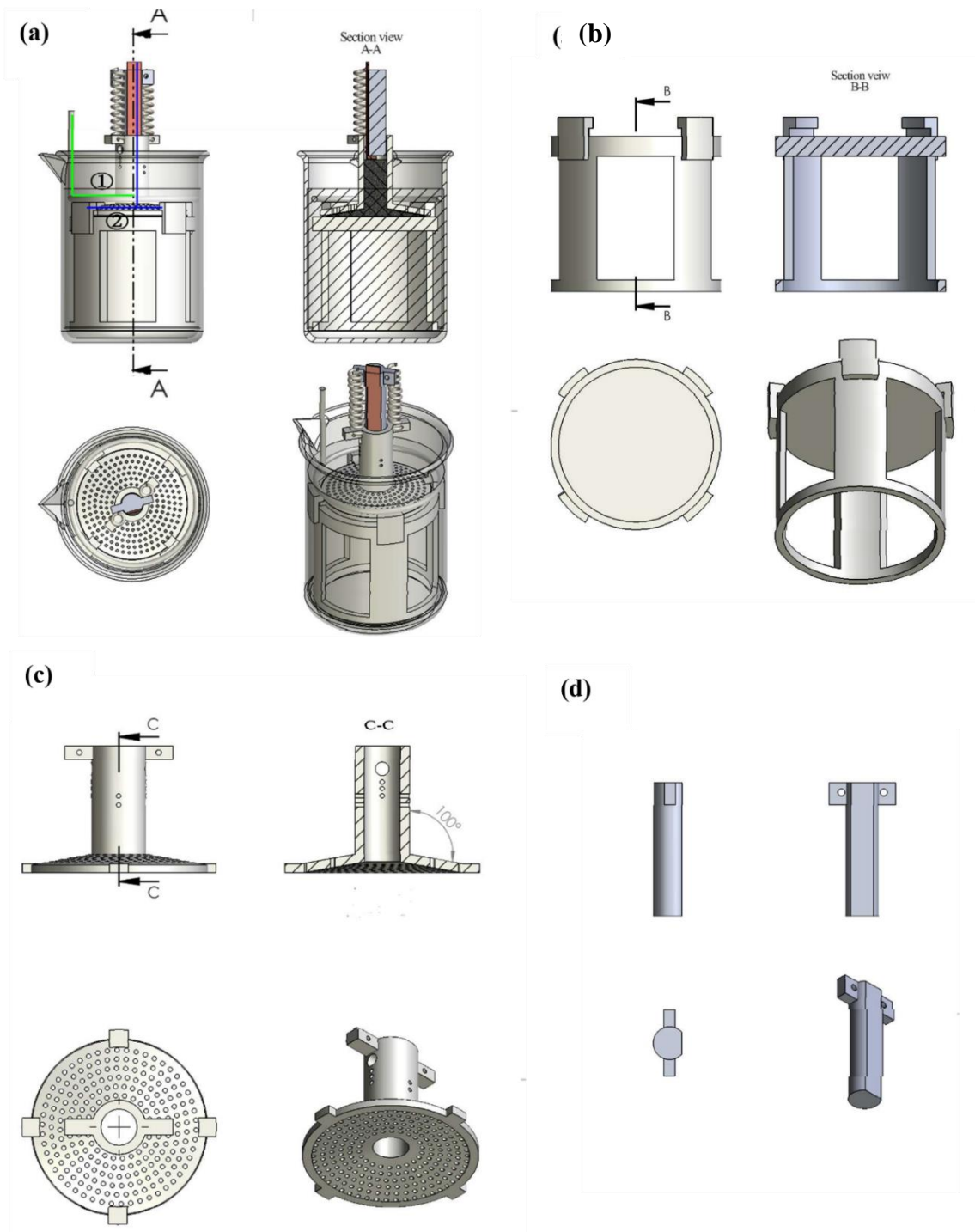
Figure S5. 2. Engineering drawing of (a) exfoliation cell, (b) Holder, (c) Cover, (d) Plug
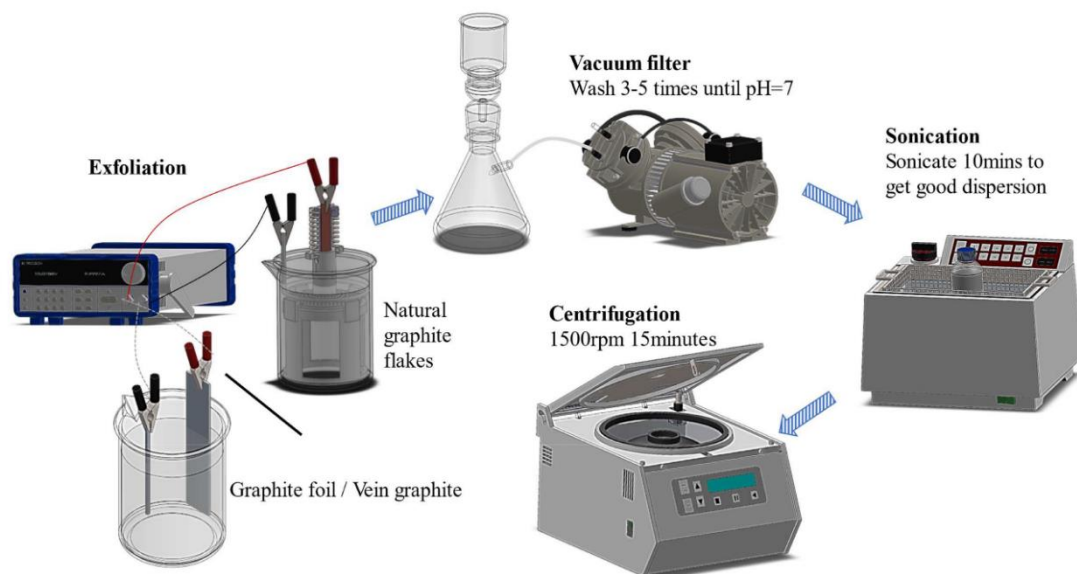
Figure S5. 3. Schematic diagram of electrochemical exfoliation of graphite process.

The Phosphoric acid doping level (ADL) is calculated according to **Equation S5- 1**. The content of phosphoric acid is obtained by drying the PA doped membrane at 80°C in vacuum oven for three hours to remove the moisture and subtract the initial weight of the membrane.

$ADL=(W_{PA}/M_{PA})/(W_{PBI}/M_{PBI})$

<div align="right">Equation S5- 1</div>

W_{PA}: phosphoric acid content

M_{PA}: molar mass of the phosphoric acid

W_{PBI}: PBI content

M_{PBI}: molar mass of the polymer repeat unit

The four-probe method used in this work to obtain conductivity is obtained by measuring the sheet resistance of graphene and then calculating it by **Equation S5- 2**.

$\sigma = 1/(R_s \cdot t)$

σ: Electrical conductivity

R_S : Sheet resistance

t: thickness

The oxidation reaction during exfoliation is shown in **Figure S5-4**.
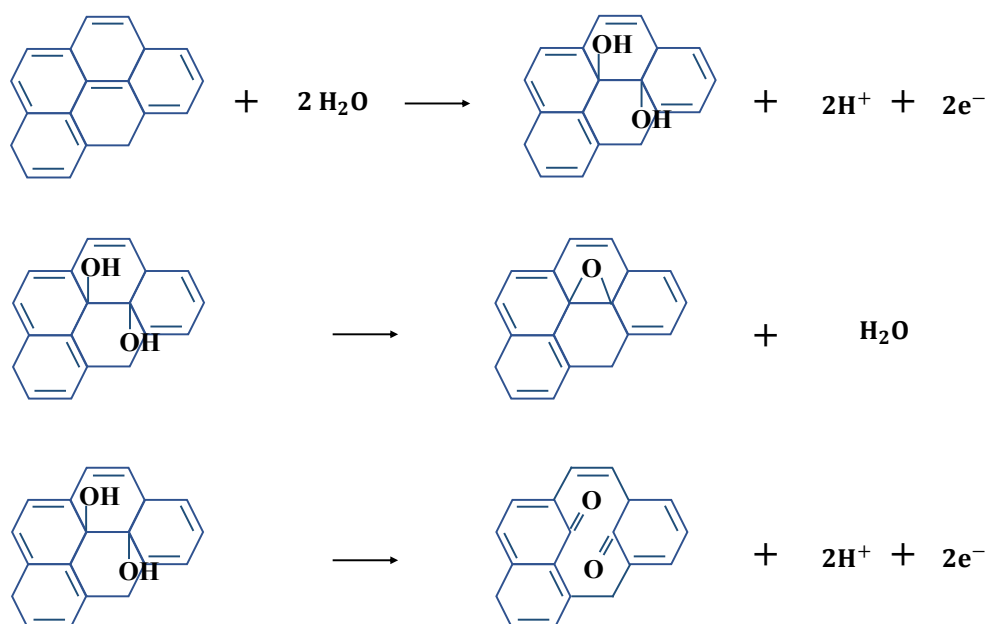
Figure S5. 4. The oxidation reaction during exfoliation
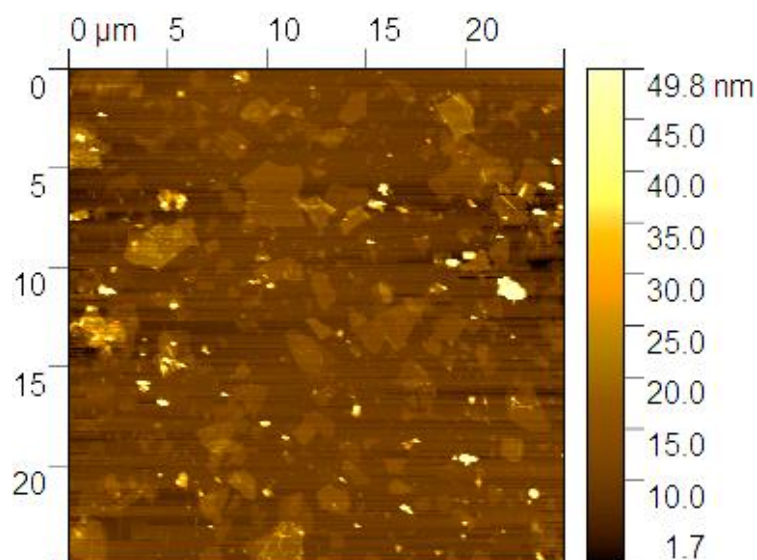
Figure S5. 5. AFM overview diagram of FL-0.1-1
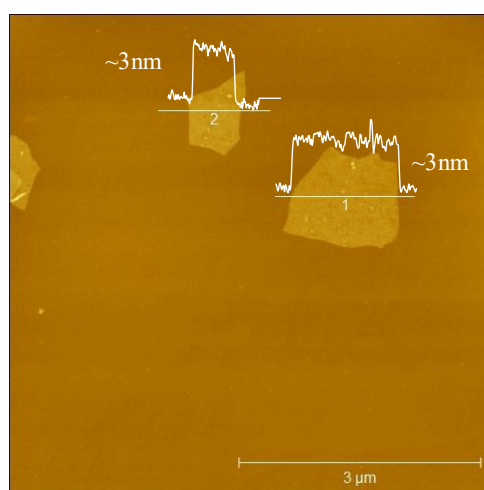
Figure S5. 6. Typical AFM image of FO-0.1-1

By observing the reaction, it is not difficult to find that the exfoliation process of graphite foil in the reactor is very slow. Compared to graphite flakes, which are smaller and thinner, graphite foil has a smaller specific surface area in contact with the solution, which slows down the exfoliation process. The SEM image of FOR-0.1-1 is shown in **Figure S5. 7**. Under SEM, the FOR-0.1-10 sample did not appear translucent and its color was dark, indicating that the

271

graphite sheet was not significantly exfoliated. Therefore, the reactor designed in this work is not suitable for electrochemical exfoliation of graphite foil. Combined with the aforementioned experimental phenomenon when using vein graphite as raw material, it is also difficult to use natural graphite for mass electrochemical exfoliation without the mechanical assistance of the reactor.
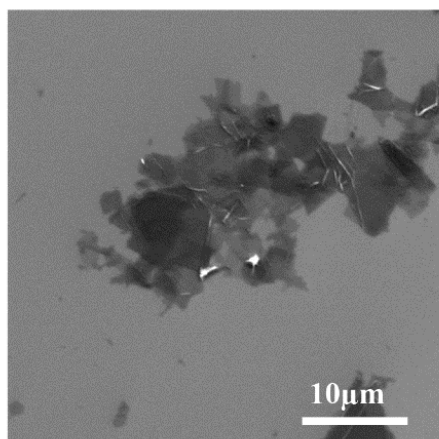
Figure S5. 7. SEM diagram of FOR-0.1-10

The Raman spectra and XPS survey spectra of FOR-0.1-10 are shown in **Figure S5. 8** a and b respectively. The Raman spectra of FOR-0.1-1 shows a high I_D/I_G being 2.15 which indicate a high disorder or high defect level. However, the XPS survey spectra show that their oxygen content is not that high, being 19.65% which is less than FL-0.1-1. Combining the high defect degree and lower oxidation degree of FOR-0.1-1 compared to FL-0.1-1, this product is more caused by non-oxidizing factors in the disorder and defect of the carbon structure. By comparing FOR-0.1-1 and FO-0.1-1, the use of the reactor can indeed improve the degree of oxidation of electrochemical exfoliation. However, the cause of FL-0.1-1 specific properties is most likely the combination of the structure of raw materials and the mechanical assistance of the reactor since simply using natural graphite or the reactor can not achieve the production of high-quality graphene oxide with a certain oxygen content.
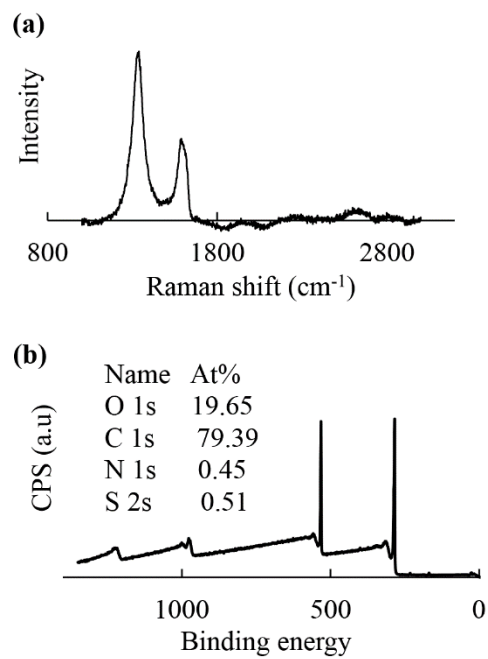
Figure S5. 8. Raman and XPS spectra: (a) Raman spectra of FOR-0.1-10; (b) XPS survey spectra of FOR-0.1-10
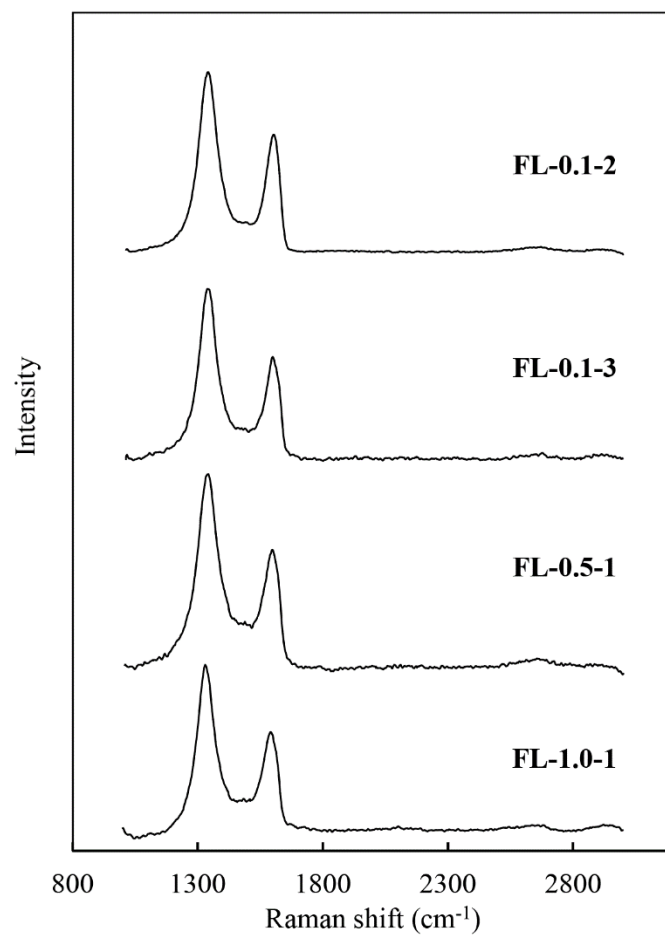
Figure S5. 9. Raman spectra of FL-0.1-2, FL-0.1-3, FL-0.5-1and FL-1.0-1
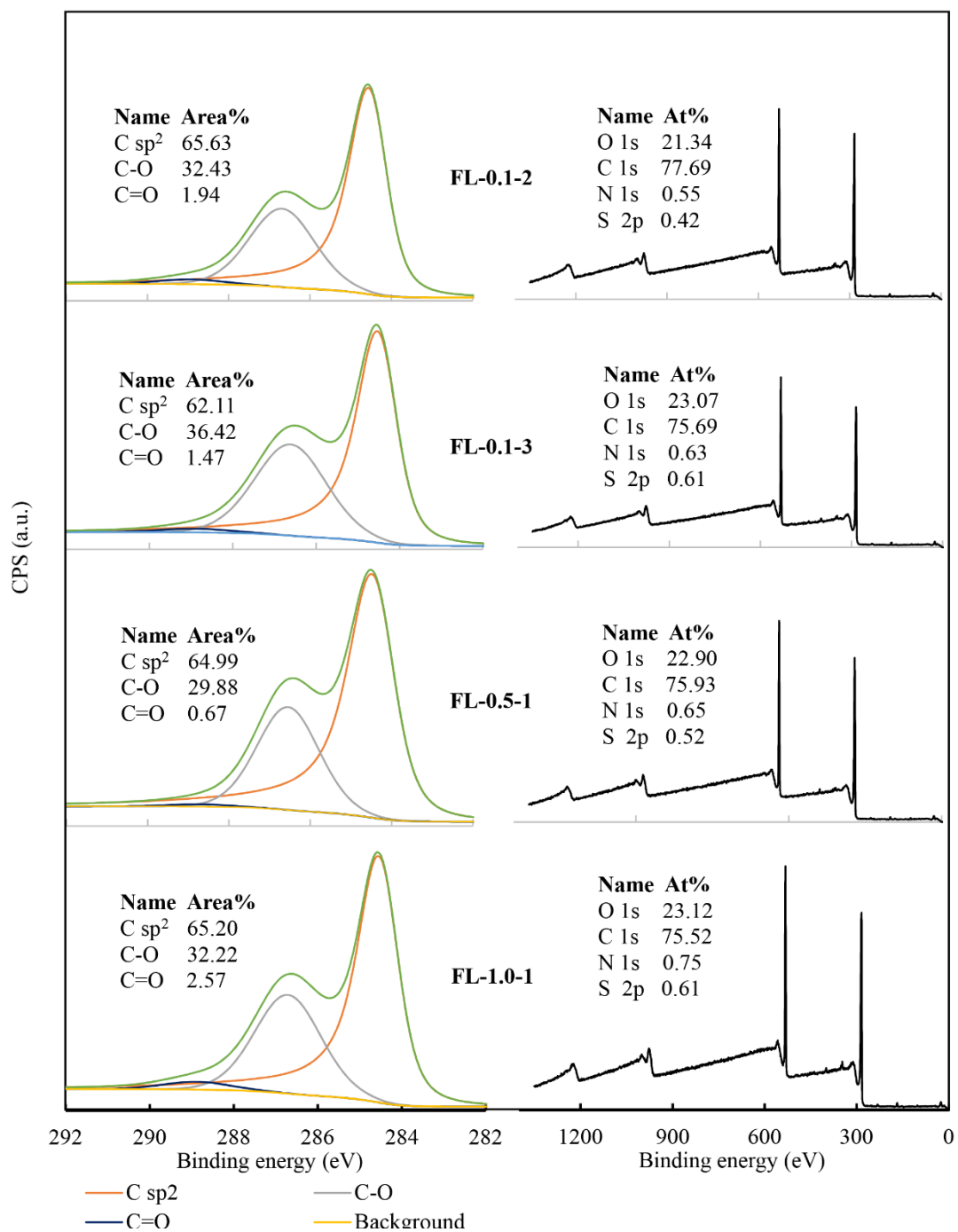
Figure S5. 10. XPS C1 s spectra and survey spectra of FL-0.1-2, FL-0.1-3, FL-0.5-1 and FL-1.0-1
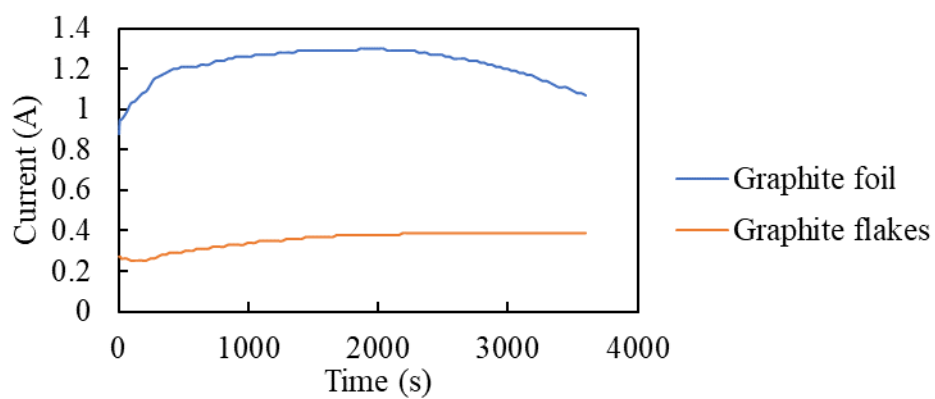
Figure S5. 11. The change of the current during the exfoliation process over time
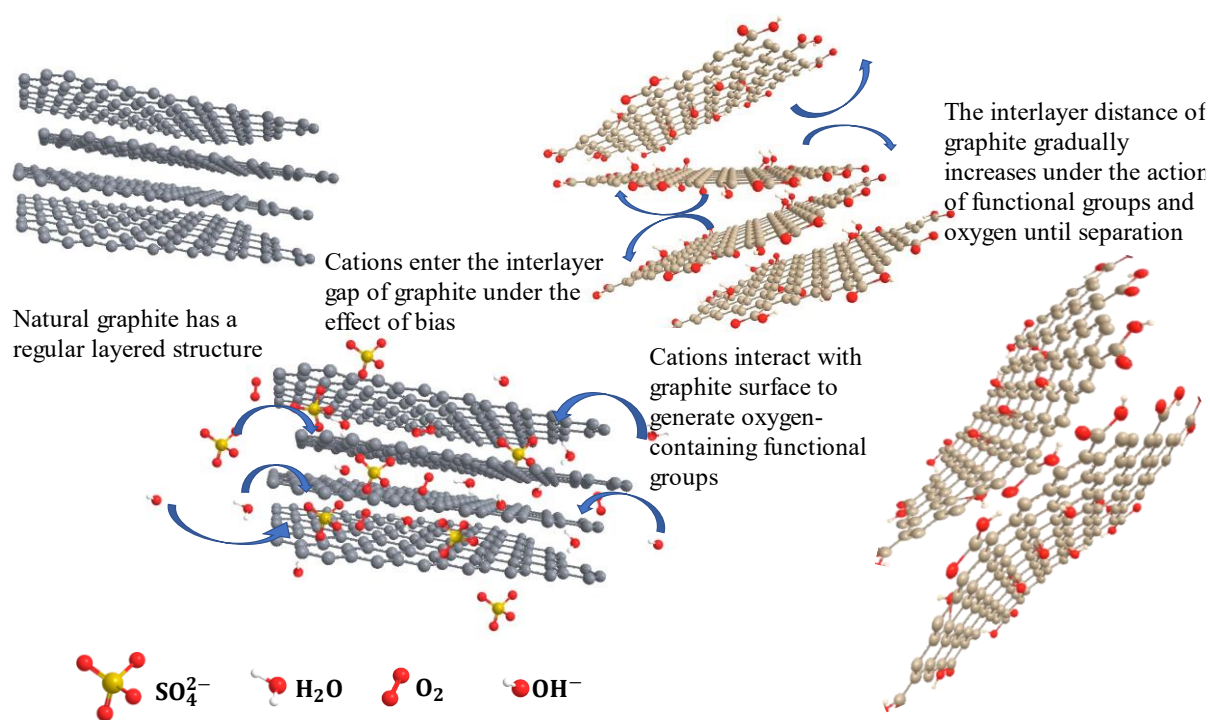
Figure S5. 12. Electrochemical exfoliation chemical mechanism.
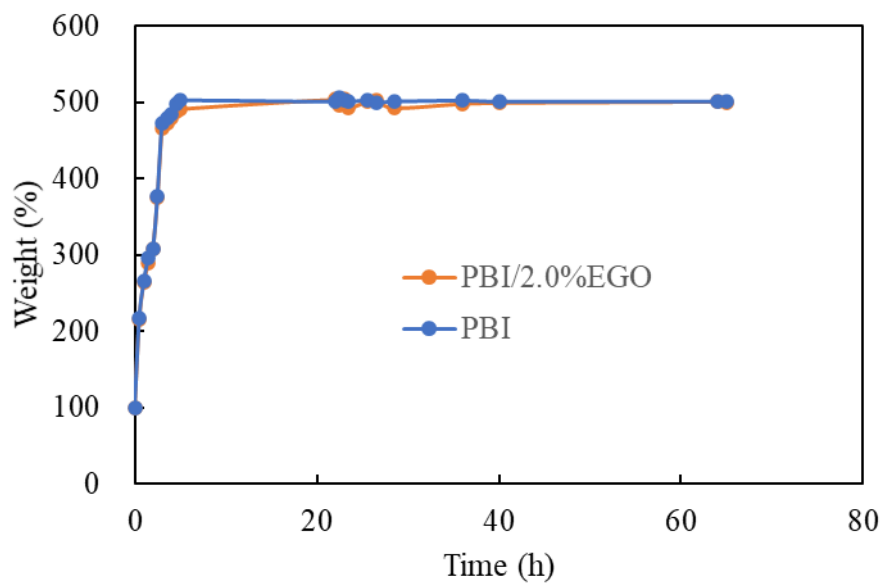
Figure S5. 13. Changes in weight of PBI membrane and PBI/2%EGO composite membrane with time during phosphoric acid doping
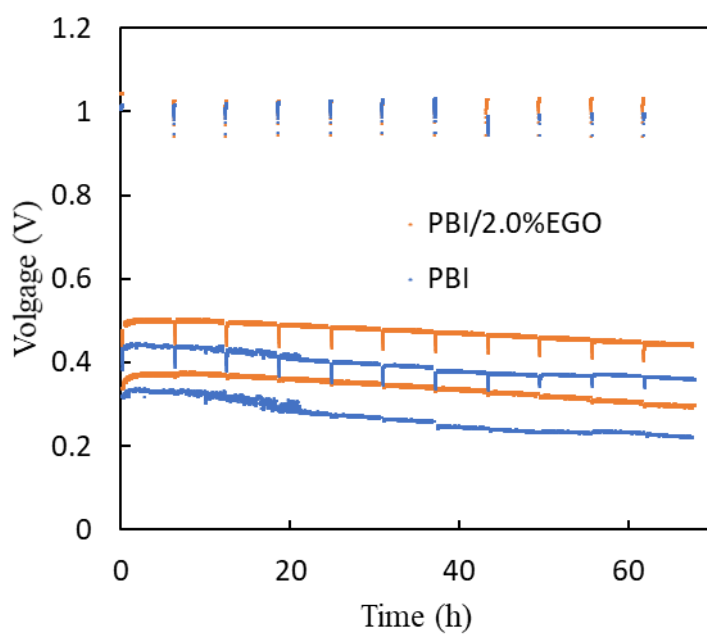
Figure S5. 14. AST of PBI and PBI/2%EGO based MEA

278

	Rs (Ω m^{-2})	thickness(μm)	σ (S m^{-1})
FO-0.1-1	10.9	10	9115
FL-0.1-1	382.0	10	261
FL-0.1-2	400.5	10	250
FL-0.1-3	410.7	10	243
FL-0.5-1	361.5	11	251
FL-1-1	414.8	10	241

The hydrogen crossover is calculated according to **Equation S5- 3**.

$$\dot{\eta} H_2 \ Crossover = \ j_{H_2 \ Cross} \times A/\ (n \times F)$$

$\dot{\eta} H_2 \ Crossover$: hydrogen crossover flux

$j_{H_2 \ Cross}$: limiting current density

A: fuel cell active area

n: the number of electrons taking part in the reaction (2e$^-$ per H$_2$ molecule)

F: Faraday's constant (96,485 C mol^{-1})

6. Synthesis of Phosphonated Graphene Oxide by Electrochemical Exfoliation to Enhance the Performance and Durability of High-temperature Proton Exchange Membrane Fuel cells

6.1 Manuscript Contribution

The results presented in Chapter 6 are prepared for publication

My contributions in this work are as follows:

Conceptualization: Propose the idea of preparing functionalized graphene oxide using a suitable electrolyte in the electrochemical exfoliation method

Methodology: Design and manufacture the 3D-printed reactor. Preparation of polybenzimidazole membranes. Prepare electrochemically exfoliated (phosphonated) graphene oxide. Characterize electrochemically exfoliated graphene (oxide) through Raman spectroscopy, scanning electron microscopy (with energy-dispersive X-ray spectroscopy), transmission electron microscopy, fourier-transform infrared spectroscopy, X-ray photoelectron spectroscopy and thermogravimetric analysis. Preparation, electrochemical performance testing, and durability testing of pristine membrane-electrode-assembly based on pure polybenzimidazole membrane and polybenzimidazole/ (phosphonated) graphene oxide composite membranes.

Formal analysis: Process and analyze the characterization results of electrochemically exfoliated (phosphonated) graphene oxide. Process and analyze electrochemical characterization results including polarization curves, Nyquist curves and chronopotentiometry scan curves.

Writing-original: Writing of the original draft of the manuscript.

Full author list: Jianuo Chen, Zunmin Guo, Maria Perez-Page, Yifeng Jia, Ziyu Zhao, Stuart

Authors contribution:

Zunmin Guo: Methodology (Energy-dispersive X-ray spectroscopy, tensile test)

Maria Perez-Page: Project administration, writing-review & editing

Yifeng Jia: Methodology (Electrochemical performance testing)

Ziyu Zhao: Methodology (Electrochemical exfoliation method)

Stuart M. Holmes: Supervision, project administration, funding acquisition, writing-review editing.

Synthesis of Phosphonated Graphene Oxide by Electrochemical Exfoliation to Enhance the Performance and Durability of High-temperature Proton Exchange Membrane Fuel cells

Jianuo Chen [a], Zunmin Guo [a], Maria Perez-Page [a], Yifeng Jia [b], Ziyu Zhao [a], Stuart Holmes [a] [*]

[a] Department of Chemical Engineering and Analytical Science, University of Manchester, Oxford Road, Manchester, M13 9PL, United Kingdom

[b] Chemistry Research Laboratory, Department of Chemistry, University of Oxford, 12 Mansfield Road, Oxford OX1 3TA, United Kingdom

Corresponding author: Stuart M. Holmes, stuart.holmes@manchester.ac.uk

6.2 Abstract

The doping of functionalized graphene oxide (GO) in the membranes becomes a promising method for improving the performance of high-temperature proton exchange membrane fuel cells (HT-PEMFC). Phosphonated graphene oxide (PGO) with a P/O ratio of 8.5% was quickly synthesised by one-step electrochemical exfoliation based on a 3D printed reactor and natural graphite flakes. Compared with the GO prepared by the two-step electrochemical exfoliation method, the PGO synthesized by the one-step electrochemical exfoliation can better improve the performance of the membrane-electrode-assembly (MEA) based on the Polybenzimidazole (PBI) membrane in the HT-PEMFC. The doping of 1.5 wt% GO or PGO synthesised by electrochemical exfoliation in PBI increased the peak power density of 17.4% or 35.4% compared to MEA based on pure PBI membrane at 150°C, respectively. In addition, the doping of PGO in PBI improves its durability under accelerated stress test (AST).

6.3 Keywords

6.4 Introduction

The importance of the application and development of the proton exchange membrane fuel cells (PMEC) as one of the most effective strategies of reducing resource deprivation and environmental pollution is being gradually recognised [1]. Different from low-temperature PEMFC based on humidified perfluorosulfonic acid (PFSA) membranes, phosphoric acid (PA) doped polymer-based high-temperature proton exchange membrane fuel cells (HT-PEMFC) can conduct protons through the hydrogen bond network between the polymer and PA to get rid of the excessively dependence on humidification and increasing the operating temperature [2][3][4]. The higher operating temperature is beneficial to the improvement of the catalyst activity and the promotion of the desorption of carbon monoxide on the surface of the catalyst, thereby reducing the HT-PEMFC's requirement for hydrogen purity. Besides, HT-PEMFC can effectively improve waste heat utilization [5]. Therefore, HT-PEMFC is promising for multiple fields such as automobile and aircraft manufacturing [6][7][8][9]. Polybenzimidazole (PBI) has become one of the most widely used polymers in HT-PEMFC due to its good physical and chemical properties [10]. However, the pure PBI membrane still faces the shortcomings such as insufficient proton conductivity, PA leaching, and weak mechanical properties under high acid doping levels (ADL) [11][12][13].

The doping of inorganic fillers or functionalized inorganic fillers such as clay [14], silica [15], titanium [16], and carbon-based substrates[16][17][18], is proposed as an effective way to improve the mechanical properties, conductivity and durability of PBI, or alleviate PA leaching. The abundant oxygen-containing functional groups contained in GO not only promote its dispersion and functionalization in water or organic solution but also facilitate its connection with the host polymer through (non-)covalent bonds [19][20]. Moreover, GO can facilitate the hopping of protons and provide additional channels for proton transfer to improve proton conductivity [12][21]. GO is thus considered to be one of the most promising additives for

polymers in PEMFC. Compared with pristine GO, the acid-functionalized GO such as carboxylic acid [22], sulfonic acid [23][24] and phosphonic acid [25][26][27], can provide higher proton conductivity, better promote dispersion, and have better compatibility with polymers which further affects the mechanical properties and chemical stability of composite membranes. Among the acid groups available for GO functionalization, the phosphonic acid group stands out in the application of HT-PEMFC with low humidity due to its relatively strong water retention capacity, strong hydrogen bonding and amphoteric characteristics.

The synthesis of acid-functionalized GO including phosphonated graphene oxide (PGO) usually involves a two-step or multi-step process, being the preparation of GO followed by the functionalization [22][23][24][25][26][27]. The preparation of graphene oxide mostly adopts the modified Hummers' method, which requires the long-term reaction of graphite in strong oxidants and strong acids [28][29]. Large-scale GO preparation based on this reaction process may not only cause environmental or safety issues but also be time-consuming and costly [30]. Moreover, the acid functionalization of GO also involves the use of strong acid [17], strong bases [31] or radiation [32]. Therefore, the use of low-cost and environmentally friendly methods to prepare acid-functionalized GO remains to be proposed. With its advantages of low pollution, low power consumption, high efficiency and high yield, electrochemical exfoliation has become a promising method to take place of traditional chemical methods to prepare GO [33][34][35]. The anodic electrochemical exfoliation makes the graphite inevitably partially oxidized during the reaction [36]. In order to further increase the content of oxygen-containing functional groups, a two-step electrochemical exfoliation method was proposed, that is, the first step is to obtain graphite intercalation compounds (GICs) in concentrated sulfuric acid, and the second step causes the graphene to be oxidized and peeled off [37]. However, this method still requires the use of strong acid and the raw materials needs to be graphite processing products used in most electrochemical exfoliation method [38][39][40] such as

graphite foil [37][40] instead of natural graphite. A method of using a mixed solution of $(NH_4)_2HPO_4$ and $(NH_4)_2SO_4$ as an electrolyte to prepare phosphor-doped GO has also been proposed [41]. However, the purpose of this method is to prevent further oxidation of the graphene surface through the combination of phosphorus groups and diols to generate graphene with low oxygen-containing functional group content.

In our previous work, natural graphite as raw material for electrochemical exfoliation without using strong acids and strong oxidants to synthesize GO with a certain oxygen-containing functional group content was achieved by designing a 3D printed reactor [21]. The relatively high oxygen content is due to the reactor binding the graphite inside to continually contact the current so that the nucleophilic ions can act on the graphene surface for a longer time. In addition to increase the content of oxygen-containing functional groups, a longer electrochemical action time may also allow the functionalization of GO to take advantage of opportunities.

This work is dedicated to the use of electrochemical exfoliation to prepare PGO for PBI composite membranes in HT-PEMFC. Different methods of one-step and two-step electrochemical exfoliation with graphite foil as raw material, and 3D printed reactor-based one-step electrochemical exfoliation with natural graphite flakes as raw material was utilized to compare the difference in types and contents of prepared GO's functional groups. The as-prepared GO/PGO was applied to the preparation of the PBI composite membranes of HT-PEMFC to explore their influence on the performance and durability of HT-PEMFC.

6.5 Experimental Section

6.5.1 The preparation of (P)GO

To explore the differences in the types and content of functional groups of electrochemical exfoliation products under different conditions, three electrochemical exfoliation methods were

adopted. Graphite foil (Alfa Aesar, 0.5 mm thick) and natural graphite flakes (Alfa Aesar, −10 mesh, 99.9%) were used as raw materials, alternatively. Concentrated sulfuric acid (>95% H_2SO_4) or 0.2 M ammonium dihydrogen phosphate ($NH_4H_2PO_4$, Fisher, UK) acted as the electrolyte in different electrochemical exfoliation methods. Pt wire (Goodfellow, UK) served as the counter electrode. As the schematic diagram of preparation methods shown in Figure 6.1, three electrochemical exfoliation methods are named 1-step method, 2-step method, and reactor method. The design of the reactor is explained in detail in our previous work [21]. In short, natural graphite flakes are assembled in a detachable porous cover and base assembly. The graphite is squeezed into the reactor by a plug with copper foil (Wruth electronics, UK) attached to the cover with springs. The reactor allows the gas and ions to enter and exit through the holes while confining the graphite in it.

- **1-step method**

The 45 mm × 15 mm × 0.5 mm graphite foil and Pt wire as the working electrode and the counter electrode were immersed in 100 mL of 0.2 M $NH_4H_2PO_4$ solution with 15 V voltage applied. After the graphene is completely peeled off from the graphite foil, the graphene dispersion is vacuum filtered 3-5 times with DI water until the dispersion becomes neutral to remove the $NH_4H_2PO_4$ residues. The washed graphene is dispersed in deionized (DI) water and sonicated for 10 min so that the graphene is further exfoliated and forms a uniform dispersion. The graphene dispersion was finally centrifuged at 1500 rpm for 15 minutes and the supernatant was taken to remove the graphite residue that was not fully exfoliated.

- **2-step method**

The working electrode and counter electrode of the 2-step method is exactly the same as the 1-step method but immersed in concentrated H_2SO_4 for the first step. The current was maintained at 100 mA and the voltage limit was 2.2 V in the first step. The first step ended 10 min after

287

the voltage reaches the limit voltage and the electrode is removed for the second step reaction. The second step of electrochemical exfoliation and subsequent processing steps are the same as the 1-step method mentioned above.

- **Reactor method**

The reactor assembly effect realizes that small-sized natural graphite flakes are used for electrochemical exfoliation to obtain large-scale products. Therefore, natural graphite flakes acted as working electrodes in this method. The copper foil extending along the wall of the plug can act as a medium for graphite to connect the external circuit. The reactor and the platinum wire serving as the counter electrode were placed in a beaker with an appropriate amount of 0.2 M $NH_4H_2PO_4$ solution. As shown in **Figure 6. 1**, the liquid level of the solution submerged the bottom of the cover of the reactor but was lower than the bottom of the copper foil to prevent the copper sheet from participating in the reaction and corroding. The subsequent reaction and treatment process is the same as the 1-step method.
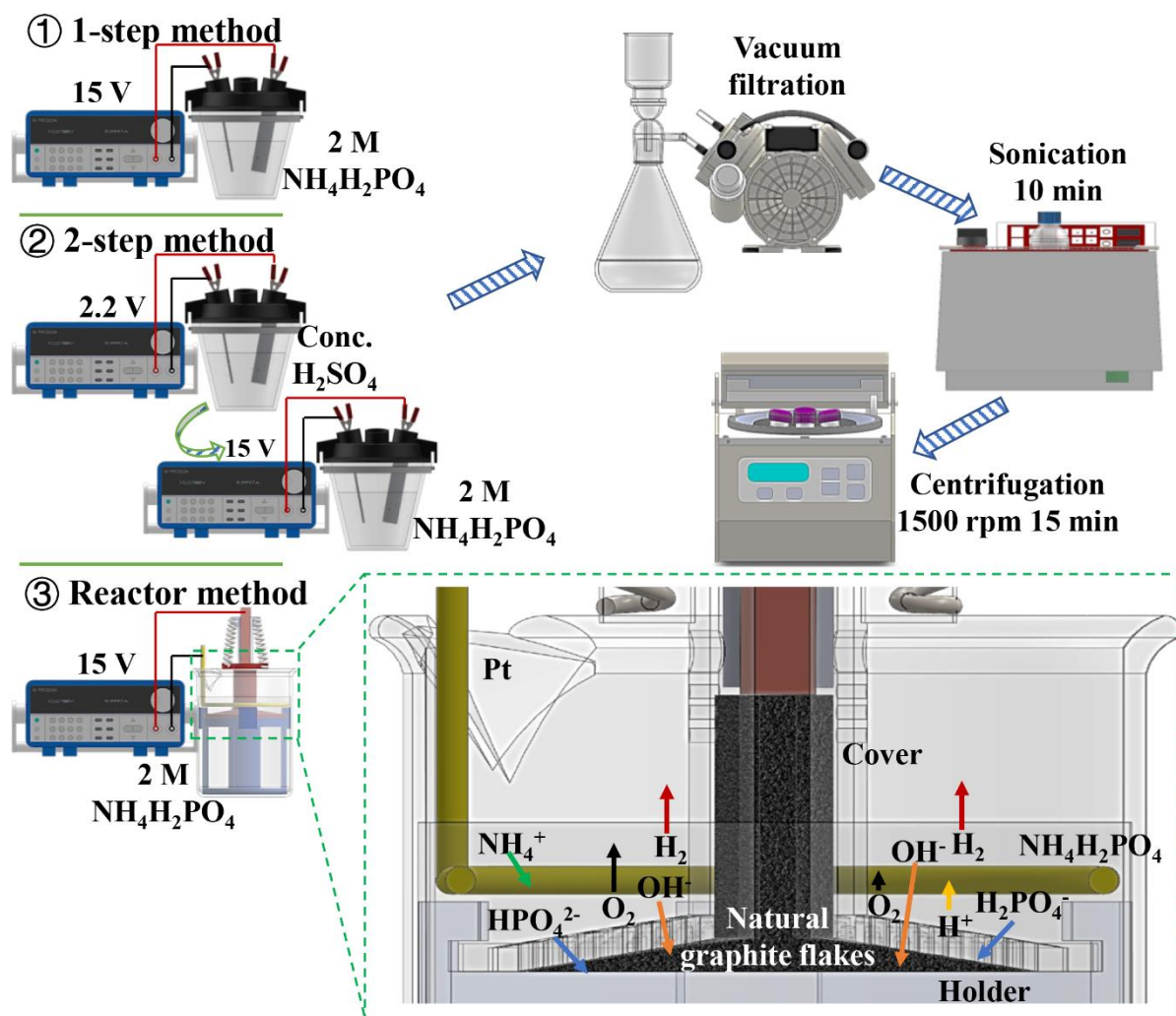
Figure 6. 1. Schematic diagram of (P)GO preparation methods

6.5.2 The Preparation of Membranes

The preparation of PBI membranes was carried out by the solution casting method. The 2 wt% PBI solution was prepared by stirring in an oil bath at 80 °C for 6 h to dissolve the PBI ionomer in dimethylacetamide (DMAc). 4 mL of as-prepared PBI solution was placed in the petri dish with a diameter of 50 mm and dried overnight at 80 °C followed by vacuum drying at 130 °C for 3h. The PBI membranes peeled off from Petri dishes were soaked in hot water at 60 °C for 1 h to remove the DMAc residue.

To prepare (P)GO/PBI composite membranes, the (P)GO dispersion prepared through different electrochemical exfoliation methods were vacuum filtered and dried at room temperature under

vacuum to form (P)GO films. The (P)GO films were dispersed into DMAc by ultrasonic, and then the amount of PBI ionomer that can form to (P)GO content ratio of 98.5 wt%: 1.5 wt% (PBI : (P)GO) was dissolved in (P)GO/DMAc dispersion in 80℃ oil bath to prepare 2 wt% (P)GO&PBI / DMAc solution. The subsequent preparation and processing methods are the same as the above-mentioned methods of pure PBI membranes.

6.5.3 The preparation of membrane-electrode-assembly (MEA)

The components of MEA are Toray carbon paper (TGPH 090, 280 μm), microporous layer (MPL), catalyst layer (CL), and membrane from outside to the inside. The structure and components loading of the anode and cathode are exactly the same. Both MPL and CL were loaded onto carbon paper by ink spraying. The preparation of MPL ink was carried out by mixing and dispersing Ketjen black (EC-300J, AkzoNobel) and polytetrafluoroethylene (PTFE, Sigma Aldrich) into iso-propanol (IPA) at a mass ratio of 9:1. The CL ink was prepared by dispersing Pt/Carbon catalyst (Fisher Scientific, 60% Pt loading) and PTFE in DI water and IPA, respectively, and finally mixing. The mass ratio of catalyst and PTFE is 80 wt%: 20 wt%. The spraying of MPL ink and CL ink is carried out by cross-spraying on carbon paper successively, companied by heating on a stove at 120℃ to remove the solvent until a load of Ketjen black and Pt reaches 1 mg cm^{-2}. The PBI membrane was doped with PA by soaking at room temperature for 3 days. PA doped PBI membrane was dried in an oven at 120℃ for 1 h to remove moisture and then weighed to calculate the acid doping level (ADL). The electrodes and membranes were cut into sizes of 1.5×1.5 cm^2 and 4×4 cm^2, respectively. The MEA was finally assembled by hot pressing at 80 psi and 140℃ for 4 min. 150 μm PTFE film was used as the gasket.

6.5.4 Characterization of PA Distribution and MEA Component Migration

To measure the thermal properties of prepared (P)GO, thermogravimetric analysis (TGA) was performed on TA Instruments TGA 550 by Alumina pan with 25 mL min^{-1} air supplying as carrier gas. The temperature raised from room temperature until 900°C with a heating rate of 10 °C min^{-1}. The TGA measurement of membranes was carried at the same condition as the measurement of (P)GO. Fourier-Transform Infrared Spectroscopy (FT-IR) was performed on Tensor 27 with the wavenumber range of 400-4000 cm^{-1} in transmission mode to study the chemical bonding of prepared (P)GO. (P)GO was loaded on a silicon wafer by drop-casting of the (P)GO/DI water dispersion for Raman spectroscopy measurement to study the defect or functionalization of (P)GO. Raman spectroscopy was performed on Horiba LabRAM Evolution equipped with 633 nm laser and the Raman shift ranges from 1000 cm^{-1} to 3000 cm^{-1}. Scanning Electron Microscope (SEM) was carried out on Tescan Mira3 SC with 5.0 kV beam energy at secondary electron mode to study the morphology of (P)GO. To explore the types and contents of elements or functional groups in (P)GO or membranes, X-ray photoelectron spectroscopy (XPS) and energy-dispersive X-ray spectroscopy (EDX) were carried out on Thermo NEXSA XPS and Tescan Mira3 SC equipped with EDX (Oxford Instruments). XPS was performed with a spherical sector analyser, 128 channel delay line detectors, 3 multichannel resistive plates, and a mono chromated Al kα X-ray source (1486.7 eV).

6.5.5 Performance Testing and Electrochemical Characterization of MEAs

MEAs were assembled in a homemade fuel cell set up with a 1.5 cm × 1.5 cm active area and tested at 150 °C feed with 100 mL min^{-1} dry hydrogen and 100 mL min^{-1} dry oxygen at anode and cathode, respectively. Potentiostat (Gamry Interface 5000) was used to take the measurement of polarization curves, electrochemical impedance spectroscopy (EIS) and accelerated stress test (AST). The activation of MEAs was accomplished by continuously discharging at 600 mA for approximately 3 days until the voltage stabilizes. Polarization curves

were acquired by discharging from OCV to 0.1 V with 0.1 A steps and 5 s dwell time. Nyquist curves were acquired by EIS at 0.5 A at the frequency range of 10,000-0.1 Hz. AST was operated through repeated chronopotentiometry by operating the fuel cell alternately at 0.6 A cm^{-2} for 4 min and 1 A cm^{-2} for 16 min. OCV was held for 10 min every 6 h during AST.

6.6   Results and Discussion

6.6.1 Characterization of (P)GO

Electrochemical exfoliation products synthesized by 1-step method, 2-step method and reactor method are named as 1-(P)GO, 2-(P)GO and R-(P)GO, respectively. The FT-IR spectroscopy characteristic peaks of different electrochemical products are referenced to determine the presence of phosphorus-doped functional groups and the types of oxygen-containing functional groups through the composition of chemical bonds. As shown in **Figure 6. 2**a, 1-(P)GO and R-(P)GO show almost the same identical characteristic peaks. Both spectra of 1-(P)GO and R-(P)GO show a characteristic peak of phosphonation between 941 cm^{-1} and 1126 cm^{-1}. P−OH, C$_{ring}$−P, P=O and P−O stretching peaks overlapped and displayed as a board peak centred at 1095 cm^{-1} in the spectrum of 1-(P)GO. P−OH at 941 cm^{-1}, P−O at 1023 cm^{-1} and overlapped board stretching peak of C−P, P=O and C$_{ring}$−P centered at 1126 cm^{-1} were detected in the spectrum of R-(P)GO [26][27][31]. However, the FT-IR spectrum of 2-(P)GO is relatively smooth in the wavenumber interval of the characteristic peak of phosphonation and may not contain phosphonated functional groups. 1-(P)GO, 2-(P)GO and R-(P)GO all show certain characteristics of graphene oxide according to characteristic peak at 3373 cm^{-1}-3517 cm^{-1} (O−H stretching), 1239 cm^{-1} / 1249 cm^{-1}(C−O stretching vibration of the hydroxyl group), 1720 cm^{-1} / 1722 cm^{-1} (C=O stretching vibration of a ketone, ester, aldehyde or carboxyl group), and 1620 cm^{-1} / 1625 cm^{-1} (C=C stretching vibration of sp^2 carbon) [21].

Raman micro-spectroscopy is an effective tool for exploring important properties such as the crystal structure, defect distribution and the number of layers in graphene-related materials [42]. This information is mainly reflected by the position, shape and intensity ratio of the three prominent peaks, which are a defect-related D peak (1328~1340 cm^{-1}), a G peak (1572~1599 cm^{-1}) corresponding to sp^2 carbon atoms, and a 2D peak (2648~2694 cm^{-1}), characteristic of few-layer graphene [43]. Raman spectrum of 1-(P)GO, 2-(P)GO and R-(P)GO are shown in **Figure 6. 2**b. The intensity ratio of D peak and G peak (I_D/I_G) indicates the degree of defects or disorders caused by functional groups or edge effects [44]. As shown in **Figure 6. 2**b, the calculated I_D/I_G of 1-(P)GO, 2-(P)GO and R-(P)GO are 1.49, 1.68 and 1.94, respectively. Compared with 1-(P)GO, 2-(P)GO does not show obvious phosphonation characteristics in the FT-IR spectrum, but the formation of GIC in the first step of electrochemical exfoliation promotes the oxidation of GO, which is most likely to cause the defect level of 2-(P)GO higher than that of 1-(P)GO [37][45]. As for the defect level of R-(P)GO higher than 1-(P)GO, it can be caused by the further phosphonation of R-(P)GO on the basis of graphene oxidation. However, the difference in I_D/I_G does not rule out that it is caused by the difference in the size of the graphite domain [46].

XPS is adopted to further confirm the exact composition of elements and functional groups on the basis of FT-IR. XPS survey spectra, C 1s spectra, O 1s spectra and P 2p spectra of different products are shown in **Figure 6. 2**c, d, e and f, respectively. From the XPS survey spectra in **Figure 6. 2**c, it can be seen that the certain oxygen content of different electrochemical exfoliation products reflects that graphene has certain oxygen-containing functional groups. Unlike the FT-IR spectrum, no obvious P 2s or P 2p peaks are detected in the XPS survey spectrum of 1-(P)GO which may be due to insufficient phosphorus content. Corresponding to the FT-IR spectrum, the peaks related to phosphorus are not detected at all in the XPS survey spectrum of 2-(P)GO, and the significant P 2s and P 2p peaks in the XPS survey spectrum of

R-(P)GO indicate that phosphorous was successfully incorporated to the graphene [31]. As shown in **Figure 6. 2**d and e, the C 1s and O 1s spectra peaks of different electrochemical exfoliation products can be deconvoluted into C—C at 384.8 eV, C—O at 285.9 eV or 532.8 eV, C=O at 287.1 eV or 531.3 eV, and C(O)OH at 288.0 eV or 534.3 eV. The presence of C—O, C=O and C(O)OH in C 1s and O 1s spectra indicates that 1-(P)GO, 2-(P)GO, and R-(P)GO have certain characteristics of graphene oxide. However, C—P, P—O and P=O may overlap with C-O and C=O, and the phosphonation characteristics need to be further confirmed by the P 2p spectra peaks. The P 2p spectrum peaks signal of 1-(P)GO and 2-(P)GO shown in **Figure 6. 2**f is noisy which indicates the insufficient P content. However, the spectrum of R-(P)GO presents a significant P 2p peak and can be deconvoluted into C-O-P 2p1/2 at 134.9 eV, C-O-P 2p3/2 at 134.1 eV, C-P 2p1/2 at 133.9 eV and C-P 2p3/2 at 133.0 eV. The content of C-P and C-O-P accounted for 83.9% and 16.1%, respectively. Compared with C-O-P, C-P has higher hydrolytic stability and is more stable under acidic conditions by virtue of its higher bond energy [31][47][48].
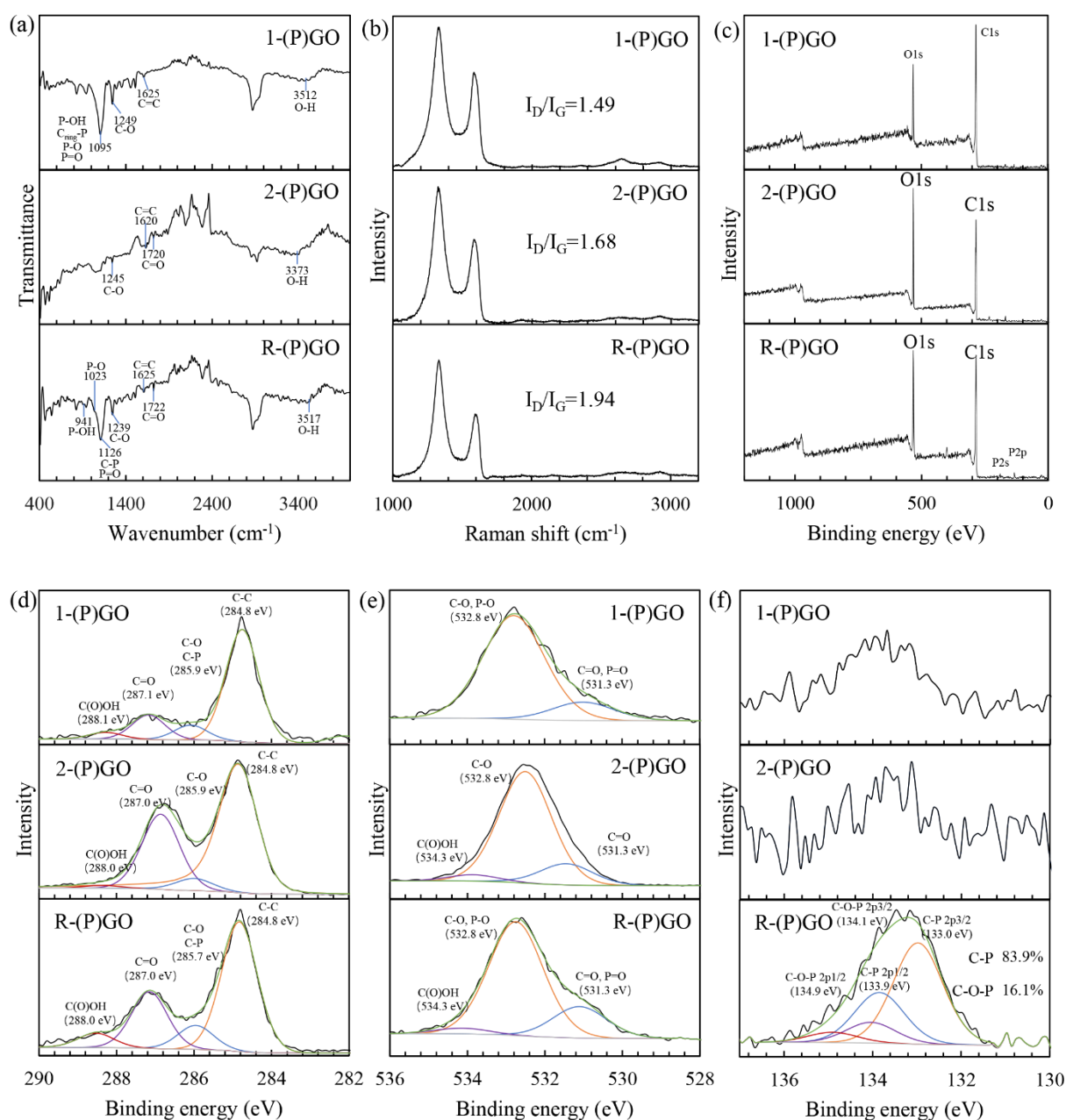
Figure 6. 2. Elements and chemical bonding characterization of 1-(P)GO, 2-(P)GO and R-(P)GO: (a) FT-IR spectra, (b) Raman spectra, (c) XPS survey spectra, (d) XPS C 1s spectra, (e) XPS O 1s spectra and (f) XPS P 2p spectra.

To explore the thermal stability of different electrochemical exfoliation products and to further infer the component content through the weight loss at different temperatures, TGA was carried out with a heating rate of 10°C/min under air. As the TGA thermograms are shown in **Figure 6. 3**, the thermal deterioration of as-prepared graphene oxide can be roughly divided into three steps. The first thermal deterioration occurs at around 100 °C associated with the removal of

moisture [21][41]. At this stage, the three products showed significant differences in thermal deterioration, with 2-(P)GO having the smallest weight loss and R-(P)GO having the largest weight loss. This phenomenon is due to the strong hydrophilicity of the phosphoric acid group, which causes the higher bound water content in R-(P)GO. The second stage of thermal deterioration occurs between 150°C and 330°C and is assigned to the removal of oxygen-containing functional groups [41]. At this stage, the weight loss of 2-(P)GO is the most, or because of its higher content of oxygen-containing functional groups dominated by hydroxyl, carbonyl, or carboxyl groups. The thermal deterioration in the last stage is the oxidation and degradation of the graphene material. At this stage, the weight of each product decreases slowly with the increase of temperature and remains relatively stable, and then decreases sharply. Compared with 2-(P)GO, 1-(P)GO and R-(P)GO have a higher stable temperature. Although 1-(P)GO and R-(P)GO have a smaller weight loss compared to 2-(P)GO at the second and the beginning of third stages, the weight loss cannot fully indicate the content of functional groups due to differences in the types and content of functional groups in different products. Phosphoric acid groups are dehydrated at high temperatures to form water vapour, and the derivatives such as phosphate esters, phosphate diesters. Besides, phosphoric anhydrides formed after dehydration will act as physical insulation to prevent heat transfer. Those reactions make the weight of phosphonated graphene oxide relatively stable [27].
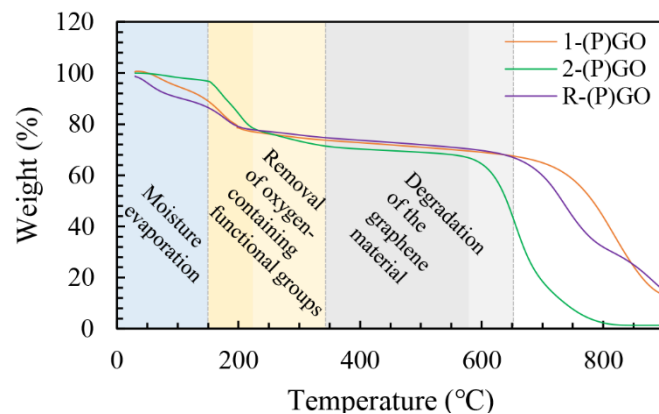
Figure 6. 3. TGA thermograms of 1-(P)GO, 2-(P)GO and R-(P)GO

The element content, oxidation level or phosphonation level of the as-prepared (phosphonated) graphene oxide was finally evaluated by SEM-EDX. The EDX spectra of 1-(P)GO, 2-(P)GO and R-(P)GO are shown in **Figure 6. 4**a, b and c, respectively. 1-(P)GO shows the lowest oxygen content indicating its lowest oxidation. In addition, 1-(P)GO exhibits extremely low P doping being 0.3 At% but exhibits highest nitrogen doping being 2.2 At%. The O/C ratio of 2-(P)GO can reach 0.42 indicating its highest oxidation. However, the P doping of 2-(P)GO is minimal. The O/C ratio of R-(P)GO can also reach 0.41. However, in consideration of R-(P)GO with the highest P doping of 2.4 At%, the partial oxygen content is contributed by the phosphate group. In summary, 1-(P)GO has the lowest degree of functionalization while 2-(P)GO has the highest degree of oxidation and only R-(P)GO succeeds to realize phosphonation with certain P doping. Therefore, the electrochemical exfoliation based on the reactor and the natural graphite flakes is more effective than the graphite foil-based one-step method and two-step method of electrochemical exfoliation to synthesize phosphonated graphene oxide. To further explore the distribution of elements in phosphonated graphene oxide, EDX mapping was performed. Stacked R-(P)GO SEM diagram of the area for EDX mapping, full element EDX mapping, C EDX element mapping, O EDX element mapping, P EDX element mapping, and N EDX element mapping of R-(P)GO are shown in **Figure 6. 4**d, e, f, g, h and i, respectively. All element mappings including P exhibit their respective homogeneous distributions. SEM diagram of R-(P)GO flakes and size statistics chart of it are shown in **Figure 6. 4**j and k, respectively. According to the SEM diagram of R-(P)GO flakes, it exhibits typical two-dimensional material lamellar characteristics. The layer size of R-(P)GO is mainly 4-6 µm, and a small amount exceeds 10 µm.
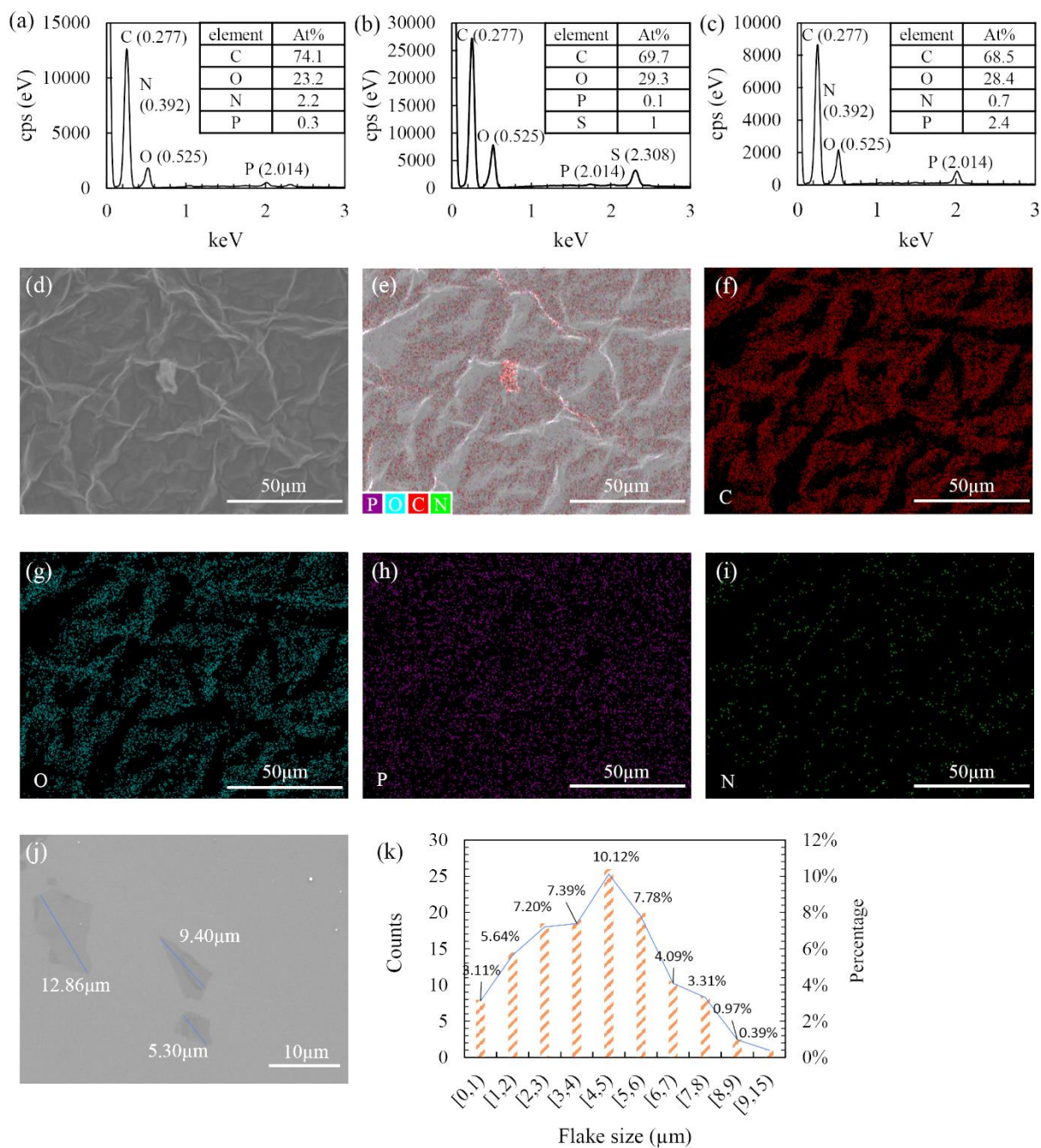
Figure 6. 4. EDX spectra of (a) 1-(P)GO, (b) 2-(P)GO and (c) R-(P)GO; (d) stacked R-(P)GO SEM diagram of the area for EDX mapping; EDX element mapping of R-(P)GO of (e) full element, (f) C, (g) O, (h) P and (i) N; (j) SEM diagram of R-(P)GO, and (k) flakes size distribution of R-(P)GO

6.6.2 Mechanism

According to the characterization of elements and components by FT-IR, XPS and EDX, as well as the mechanism of electrochemical exfoliation and phosphonation, the possible reactions in the electrochemical exfoliation process based on the reactor are proposed in **Figure 6. 5**. Firstly, under the action of the bias voltage, nucleophilic water molecules attack the graphene

layer so that it is oxidized to form a hydroxyl group, followed by the dehydration of the hydroxyl group to form an epoxy group [37][21]. The restraint effect of the reactor on the exfoliated graphene is conducive to continuous oxidation, which has been explained in detail in our previous work [21]. Secondly, the oxidized graphene sheet stays in the reactor to contact the current, and its epoxy group react with the phosphoric acid group from $NH_4H_2PO_4$ solution under the action of the bias voltage to generate P-C and P-O-C linkages to achieve phosphonation, which can be confirmed by XPS and FT-IR spectroscopy [26][27][31]. Although the one-step electrochemical exfoliation method based on graphite foil is carried out under the same voltage and electrolyte, it lacks the constraints of the reactor. The exfoliated graphene sheet quickly detaches and stops further reactions, which makes the number of functional groups insufficient.
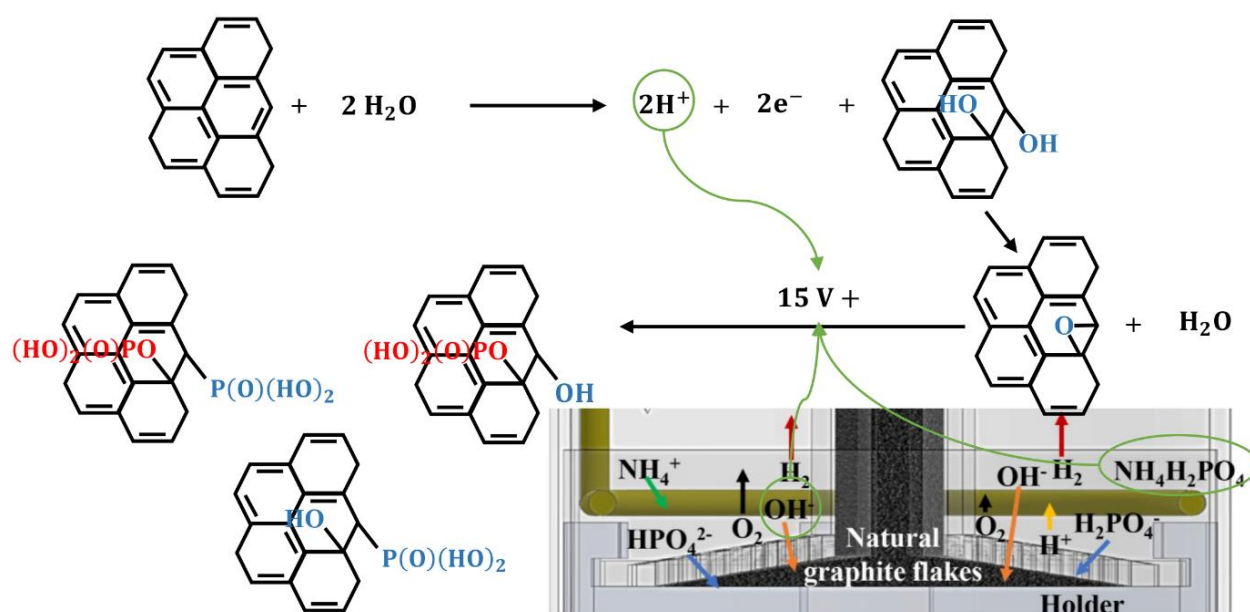
Figure 6. 5. Mechanism of reactor-based electrochemical exfoliation

6.6.3 Characterization of Membranes

Through the characterization of different electrochemical exfoliation products, 2-(P)GO and R-(P)GO have relatively abundant oxygen-containing functional groups or higher phosphonation levels, respectively. The doping of both in PBI is expected to improve the PBI

299

proton conductivity. Thus, pure PBI membrane, PBI/1.5wt%2-(P)GO composite membrane and PBI/1.5wt%R-(P)GO composite membranes were prepared to compare the properties and performance. The TGA thermograms of different membranes are shown in **Figure 6. 6**a. From TGA curves, the doping of 2-(P)GO and R-(P)GO did not significantly change the thermal properties of the PBI membrane. Although the thermogram of PBI/R-(P)GO composite membrane is slightly above PBI membrane and PBI/2-(P)GO composite membrane, this difference is mainly reflected before the temperature rises to 200°C. This could be caused by residual DMAc or water contained in different membranes. The thermograms of all membranes in the PBI decomposition stage from 200 ℃ to 700 ℃ remained basically the same and remained basically stable before 600 ℃. To explore the mechanical properties of different membranes and the reinforcing effect of (P)GO on PBI membranes, the tensile test was carried out. As stress-strain curves shown in **Figure 6. 6**b, the Young's modulus of all membranes is basically the same at 26.3 MPa. The maximum stress and strain of pure PBI membrane are 19.2 MPa and 24.5%, respectively. Although the maximum stress of PBI/2-(P)GO composite membrane of 18.7 MPa is slightly smaller than that of pure PBI membrane, the maximum strain of PBI/2-(P)GO composite membrane of 34.8% is much greater than that of PBI. PBI/R-(P)GO composite membrane has the greatest tensile strength and elongation at break. The maximum stress and strain of PBI/R-(P)GO composite membrane are 22.4 MPa and 41.1%, respectively.
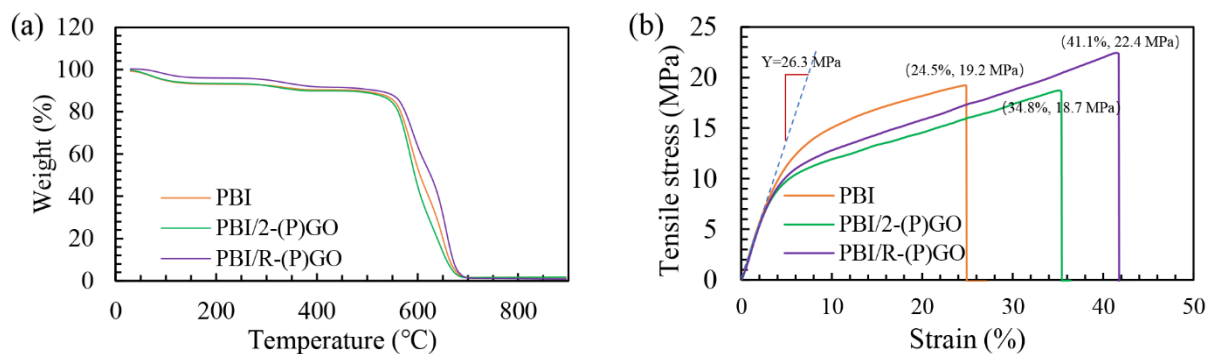
Figure 6. 6. Physical properties of membranes. (a) TGA thermograms, (b) stress–strain curves

To study the coupling effect of R-(P)GO and PBI membrane, the distribution of elements in the polymer was observed by EDX mapping. The SEM diagram of the cross-section of PBI/R-(P)GO composite membrane is shown in **Figure 6. 7**a, and the EDX element maps are shown in **Figure 6. 7**b-f. Each element shows a uniform distribution, of which C and N are mainly derived from the backbone of the polymer, while the homogeneous distribution of P and O reflects the uniform doping of PGO in the polymer.
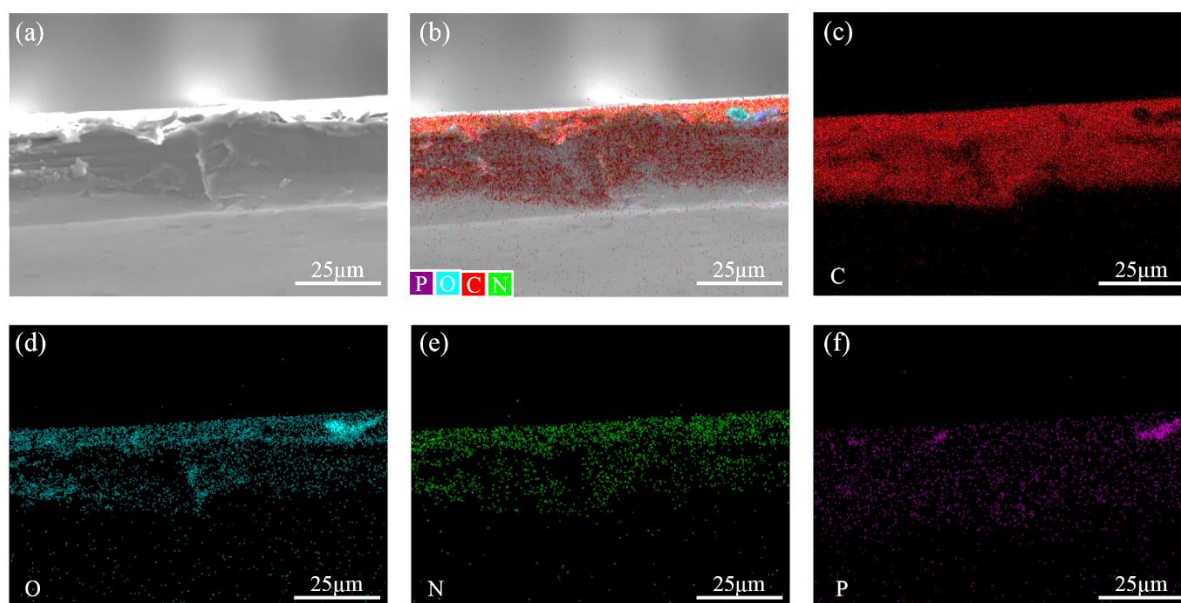
Figure 6. 7. SEM and EDX mapping of PBI/R-(P)GO cross-section: (a) SEM diagram; EDX element mapping of R-(P)GO of (b) full elements, (c) C, (d) O, (e) N and (f) P

6.6.4 Performance and Durability Study of Membranes

As mentioned above, 2-(P)GO and R-(P)GO can be recognized as graphene oxide with higher oxygen content and phosphonated graphene oxide, respectively. In order to explore the influence of the doping of graphene oxide and phosphonated graphene oxide in the PBI membrane on the performance and durability of HT-PEMFC, the polarization curves, EIS and AST of MEAs based on the pure membrane, PBI/2-(P)GO composite membrane and PBI/R-(P)GO composite membrane was tested. The polarization curves and power density curves of different MEAs after activation are shown in **Figure 6. 8**a. The polarization curves of different

MEAs did not show significant differences in the voltage loss dominated by activation polarization losses at low current densities. However, different polarization curves start to show significant differences under the medium current density mainly dominated by ohmic loss. The difference in ohmic loss largely depends on the proton conductivity of the membrane. It can be seen from **Figure 6. 8**a that in the current density phase dominated by ohmic loss, the voltage loss of MEA based on pure PBI membrane is the most rapid with the increase of current density, while the voltage loss of PBI/R-(P)GO is the slowest. The difference in polarization curves is further reflected in the power density curves. The peak power density of MEA based on pure PBI, PBI/2-(P)GO and PBI/R-(P)GO is 362 mW cm^{-2}, 425 mW cm^{-2} and 490 mW cm^{-2}, respectively. The difference in the performance of MEA based on different membranes can be visualized by the Nyquist curves obtained by EIS. As shown in **Figure 6. 8**b, the ohmic resistance (R$_\Omega$), which is mainly dominated by membrane resistance, of PBI, PBI/2-(P)GO and PBI/R-(P)GO is 258 mΩ cm^2, 216 mΩ cm^2 and 150 mΩ cm^2, respectively. The abundant functional groups on graphene oxide can help promote the hoping of hydrogen protons and build additional proton transport channels to improve the proton conductivity of the membrane [21]. The phosphonic acid groups have the ability to form stronger hydrogen bonds although its low acidity combined with its amphipathic characteristics can also increase the proton conductivity of the membrane [26].

The AST performance of MEAs based on different membranes is shown in **Figure 6. 8**c. As the data shown in **Figure 6. 8**c, the voltage of MEAs based on PBI/2-(P)GO and PBI/R-(P)GO composite membranes remained stable throughout the AST process under different currents densities. However, MEA based on pure PBI membrane showed a continuously slow drop in voltage. Its voltage at current densities of 0.6 A cm^{-2} and 1A cm^{-2} dropped by 23 mV and 27 mV, respectively. The polarization curves of different MEAs after AST are shown in **Figure 6. 8**d. The peak power density of MEAs based on PBI/2-(P)GO and PBI/R-(P)GO composite

membranes before and after AST remain basically unchanged, while the peak power density of MEA is based on PBI pure membrane dropped by 9 mW cm^{-2}. The impedance changes of MEA before and after AST can be utilized to explore the reasons that affect its durability. The Nyquist curves of MEAs after AST are shown in **Figure 6. 8**e. The ohmic resistance of PBI, PBI/2-(P)GO and PBI/R-(P)GO after AST are 236 mΩ cm^2, 202 mΩ cm^2 and 150 mΩ cm^2. Compared to before AST, the ohmic resistance of PBI and PBI/2-(P)GO dropped slightly, while the ohmic resistance of PBI/R-(P)GO remained unchanged after AST. This phenomenon could be caused by the relatively weak mechanical pressure resistance of PBI and PBI/2-(P)GO and the relatively weak retention of phosphoric acid, which causes the membrane to become thinner under long-term operation and extrusion [49]. The doping of PGO can improve the mechanical properties of PBI and increase the interaction between the polymer and PA so that the ohmic resistance of the composite membrane before and after AST can be maintained [26]. Although MEA based on pure PBI membrane has a slight decrease in ohmic resistance before and after AST, its charge transfer resistance (R_{change}) has increased significantly. Under the conditions of AST, the PA in the PBI membrane will be leached out continuously. Excessive PA leaching will cover the active sites of the catalyst, which will reduce the three-phase boundary in the catalyst and increase the charge transfer resistance [50]. This is most likely the cause of the gradual decline in the performance of MEA based on pure PBI membrane during AST. Both GO and PGO has the ability to prevent excessive leaching of PA [21][26] so that their performance remains stable during the AST process.
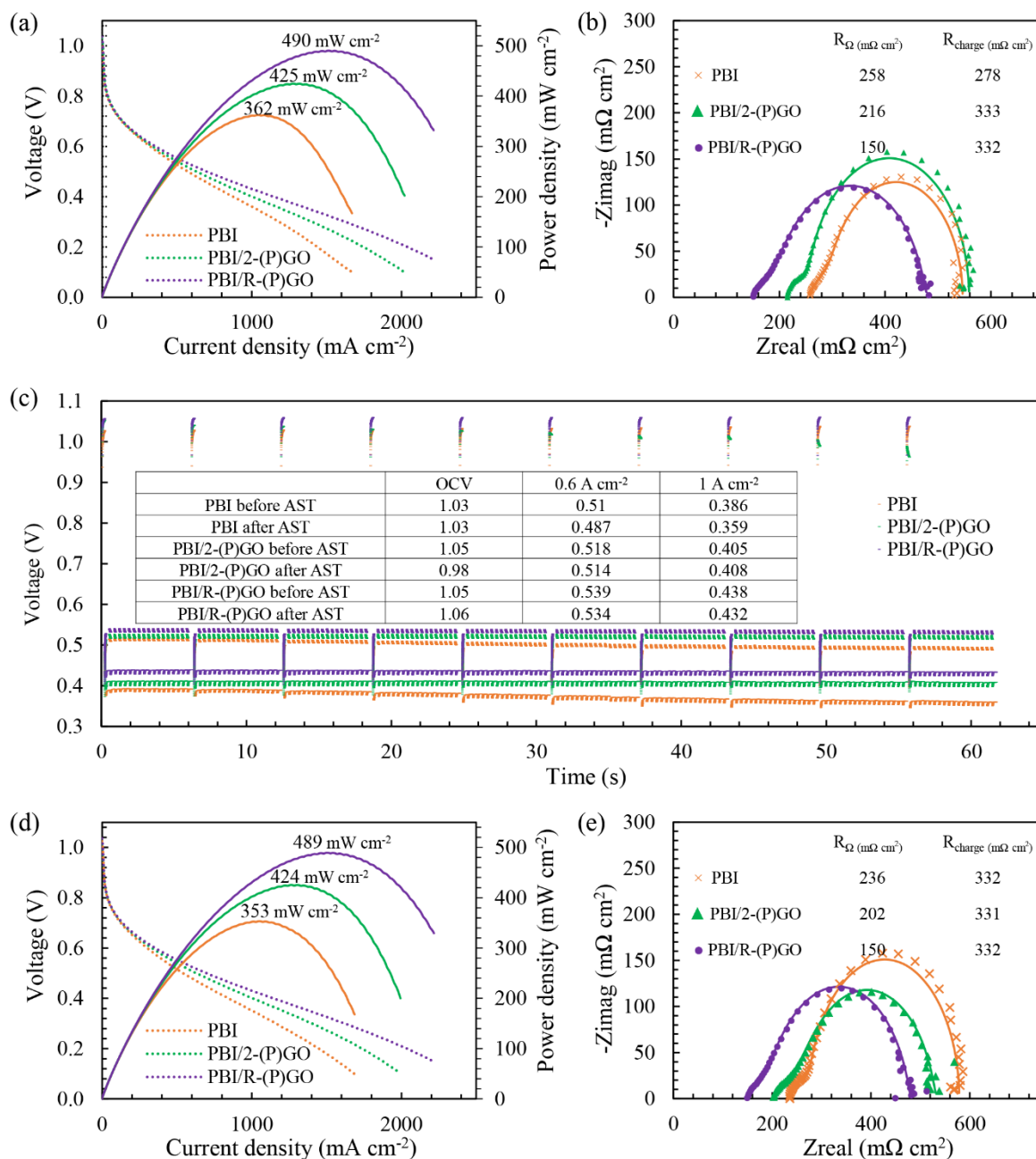
Figure 6. 8. Performance and durability of MEAs (a) polarization curves of MEAs before AST; (b) Nyquist curves of MEAs before AST; (c) AST process of MEAs; (d) polarization curves of MEAs after AST; (e) Nyquist curves of MEAs after AST.

6.7 Conclusions

With ammonium dihydrogen phosphate as the electrolyte, there are differences in the products of the one-step (1-(P)GO) and two-step (2-(P)GO) electrochemical exfoliation methods based on graphite foil and the reactor (R-(P)GO) electrochemical exfoliation method based on natural

graphite flakes. Through the characterization of FT-IR, Raman, XPS and EDX, the as-prepared 1-(P)GO, 2-(P)GO and R-(P)GO tend to be classified as graphene, GO and PGO, respectively. The 3D printed reactor realizes the preparation of PGO with a phosphorus content of 2.2 At% through one-step electrochemical exfoliation based on natural graphite flakes. The doping of R-(P)GO in the PBI membrane has good compatibility and very uniform distribution. Compared with 2-(P)GO, R-(P)GO can better improve the mechanical properties of PBI. In addition, the doping of 1.5wt% R-(P)GO in the PBI film can improve the performance of the PBI membrane better than 2-(P)GO. The peak power density and ohmic resistance of MEA based on PBI, PBI/2-(P)GO and PBI/R-(P)GO are 362 mW cm^{-2}, 425 mW cm^{-2}, 490 mW cm^{-2} and 258 mΩ cm^2, 216 mΩ cm^2, 150 mΩ cm^2, respectively. In addition, it can be shown by AST that PBI/2-(P)GO and PBI/R-(P)GO have better durability than pure PBI due to the retention of phosphoric acid in the membrane by GO or PGO.

6.8 Declaration of Competing Interest

The authors declare that they have no known competing financial interests or personal relationships that could have appeared to influence the work reported in this paper.

6.9 Acknowledgment

6.10 References:

[1]   Q. Li, J.O. Jensen, R.F. Savinell, N.J. Bjerrum, High temperature proton exchange membranes based on polybenzimidazoles for fuel cells, Progress in Polymer Science. 34 (2009) 449–477. https://doi.org/10.1016/J.PROGPOLYMSCI.2008.12.003.

[2]   H.A. Hjuler, D. Aili, J.O. Jensen, High temperature polymer electrolyte membrane fuel cells: Approaches, status, and perspectives, 2016. https://doi.org/10.1007/978-3-319-17082-4.

[3]   S. Yu, L. Xiao, B.C. Benicewicz, Durability Studies of PBI-based High Temperature PEMFCs ~, (2008) 165–174. https://doi.org/10.1002/fuce.200800024.

[4]   Jan-Patrick Melchior, Günter Majer, Klaus-Dieter Kreuer, Why do proton conducting polybenzimidazole phosphoric acid membranes perform well in high-temperature PEM fuel cells?, Physical Chemistry Chemical Physics. 19 (2016) 601–612. https://doi.org/10.1039/C6CP05331A.

[5]   H. Su, S. Pasupathi, B. Bladergroen, V. Linkov, B.G. Pollet, Optimization of gas diffusion electrode for polybenzimidazole-based high temperature proton exchange membrane fuel cell: Evaluation of polymer binders in catalyst layer, International Journal of Hydrogen Energy. 38 (2013) 11370–11378. https://doi.org/10.1016/J.IJHYDENE.2013.06.107.

[6]   A.S. Aricò, A. Stassi, I. Gatto, G. Monforte, E. Passalacqua, V. Antonucci, Surface Properties of Pt and PtCo Electrocatalysts and Their Influence on the Performance and Degradation of High-Temperature Polymer Electrolyte Fuel Cells, Journal of Physical Chemistry C. 114 (2010) 15823–15836. https://doi.org/10.1021/JP104528Q.

[7]   M.K. Debe, Electrocatalyst approaches and challenges for automotive fuel cells, Nature

2012 486:7401. 486 (2012) 43–51. https://doi.org/10.1038/nature11115.

[8]   Gwénaëlle Renouard-Vallet, Martin Saballus, Gerrit Schmithals, Johannes Schirmer, Josef Kallo, K. Andreas Friedrich, Improving the environmental impact of civil aircraft by fuel cell technology: concepts and technological progress, Energy & Environmental Science. 3 (2010) 1458–1468. https://doi.org/10.1039/B925930A.

[9]   J.W. Pratt, L.E. Klebanoff, K. Munoz-Ramos, A.A. Akhil, D.B. Curgus, B.L. Schenkman, Proton exchange membrane fuel cells for electrical power generation on-board commercial airplanes, Applied Energy. 101 (2013) 776–796. https://doi.org/10.1016/J.APENERGY.2012.08.003.

[10]   R. Savinell, E. Yeager, D. Tryk, U. Landau, J. Wainright, D. Weng, K. Lux, M. Litt, C. Rogers, A Polymer Electrolyte for Operation at Temperatures up to 200°C, Journal of The Electrochemical Society. 141 (1994) L46. https://doi.org/10.1149/1.2054875.

[11]   David Aili, Jin Zhang, M.T.D. Jakobsen, Haijin Zhu, Tianyu Yang, Jian Liu, Maria Forsyth, Chao Pan, J. Oluf Jensen, L. Nilausen Cleemann, S. Ping Jiang, Qingfeng Li, Exceptional durability enhancement of PA/PBI based polymer electrolyte membrane fuel cells for high temperature operation at 200 °C, Journal of Materials Chemistry A. 4 (2016) 4019–4024. https://doi.org/10.1039/C6TA01562J.

[12]   N. Üregen, K. Pehlivanoğlu, Y. Özdemir, Y. Devrim, Development of polybenzimidazole/graphene oxide composite membranes for high temperature PEM fuel cells, International Journal of Hydrogen Energy. 42 (2017) 2636–2647. https://doi.org/10.1016/j.ijhydene.2016.07.009.

[13]   N. Bevilacqua, M.G. George, S. Galbiati, A. Bazylak, R. Zeis, Phosphoric Acid Invasion in High Temperature PEM Fuel Cell Gas Diffusion Layers, Electrochimica Acta. 257

(2017) 89–98. https://doi.org/10.1016/J.ELECTACTA.2017.10.054.

[14]   D. Plackett, A. Siu, Q. Li, C. Pan, J.O. Jensen, S.F. Nielsen, A.A. Permyakova, N.J. Bjerrum, High-temperature proton exchange membranes based on polybenzimidazole and clay composites for fuel cells, Journal of Membrane Science. 383 (2011) 78–87. https://doi.org/10.1016/J.MEMSCI.2011.08.038.

[15]   H. Pu, L. Liu, Z. Chang, J. Yuan, Organic/inorganic composite membranes based on polybenzimidazole and nano-SiO2, Electrochimica Acta. 54 (2009) 7536–7541. https://doi.org/10.1016/J.ELECTACTA.2009.08.011.

[16]   F.J. Pinar, P. Cañizares, M.A. Rodrigo, D. Ubeda, J. Lobato, Titanium composite PBI-based membranes for high temperature polymer electrolyte membrane fuel cells. Effect on titanium dioxide amount, RSC Advances. 2 (2012) 1547–1556. https://doi.org/10.1039/C1RA01084K.

[17]   C. Xu, Y. Cao, R. Kumar, X. Wu, X. Wang, K. Scott, A polybenzimidazole/sulfonated graphite oxide composite membrane for high temperature polymer electrolyte membrane fuel cells, Journal of Materials Chemistry. 21 (2011) 11359–11364. https://doi.org/10.1039/c1jm11159k.

[18]   M.M. Hasani-Sadrabadi, E. Dashtimoghadam, F.S. Majedi, H. Moaddel, A. Bertsch, P. Renaud, Superacid-doped polybenzimidazole-decorated carbon nanotubes: a novel high-performance proton exchange nanocomposite membrane, Nanoscale. 5 (2013) 11710–11717. https://doi.org/10.1039/C3NR02886K.

[19]   Y. Qian, Y. Lan, J. Xu, F. Ye, S. Dai, Fabrication of polyimide-based nanocomposites containing functionalized graphene oxide nanosheets by in-situ polymerization and their properties, Applied Surface Science. 314 (2014) 991–999.

https://doi.org/10.1016/J.APSUSC.2014.06.130.

[20]   W. Gao, L.B. Alemany, L. Ci, P.M. Ajayan, New insights into the structure and reduction of graphite oxide, Nature Chemistry 2009 1:5. 1 (2009) 403–408. https://doi.org/10.1038/nchem.281.

[21]   J. Chen, M. Perez-Page, Z. Ji, Z. Zhang, Z. Guo, S. Holmes, One step electrochemical exfoliation of natural graphite flakes into graphene oxide for polybenzimidazole composite membranes giving enhanced performance in high temperature fuel cells, Journal   of   Power   Sources.   491   (2021)   229550. https://doi.org/10.1016/j.jpowsour.2021.229550.

[22]   J. Yang, C. Liu, L. Gao, J. Wang, Y. Xu, R. He, Novel composite membranes of triazole modified graphene oxide and polybenzimidazole for high temperature polymer electrolyte membrane fuel cell applications, RSC Advances. 5 (2015) 101049–101054. https://doi.org/10.1039/c5ra16554g.

[23]   C. Xu, Y. Cao, R. Kumar, X. Wu, X. Wang, K. Scott, A polybenzimidazole/sulfonated graphite oxide composite membrane for high temperature polymer electrolyte membrane fuel cells, Journal of Materials Chemistry. 21 (2011) 11359–11364. https://doi.org/10.1039/C1JM11159K.

[24]   Y. Cai, Z. Yue, S.X.-J. of A.P. Science, A novel polybenzimidazole composite modified by sulfonated graphene oxide for high temperature proton exchange membrane fuel cells in   anhydrous   atmosphere,   Wiley   Online   Library.   134   (2017)   44986. https://doi.org/10.1002/app.44986.

[25]   E. Abouzari-Lotf, H. Ghassemi, A. Shockravi, T. Zawodzinski, D. Schiraldi, Phosphonated poly(arylene ether)s as potential high temperature proton conducting

materials, Polymer. 52 (2011) 4709–4717. https://doi.org/10.1016/j.polymer.2011.08.020.

[26] E. Abouzari-Lotf, M. Zakeri, M.M. Nasef, M. Miyake, P. Mozarmnia, N.A. Bazilah, N.F. Emelin, A. Ahmad, Highly durable polybenzimidazole composite membranes with phosphonated graphene oxide for high temperature polymer electrolyte membrane fuel cells, Journal of Power Sources. 412 (2019) 238–245. https://doi.org/10.1016/j.jpowsour.2018.11.057.

[27] S. Some, I. Shackery, S.J. Kim, S.C. Jun, Phosphorus-Doped Graphene Oxide Layer as a Highly Efficient Flame Retardant, Chemistry - A European Journal. 21 (2015) 15480–15485. https://doi.org/10.1002/chem.201502170.

[28] L. Staudenmaier, Verfahren zur Darstellung der Graphitsäure, Berichte Der Deutschen Chemischen Gesellschaft. 31 (1898) 1481–1487. https://doi.org/10.1002/CBER.18980310237.

[29] N.I. Zaaba, K.L. Foo, U. Hashim, S.J. Tan, W.W. Liu, C.H. Voon, Synthesis of Graphene Oxide using Modified Hummers Method: Solvent Influence, Procedia Engineering. 184 (2017) 469–477. https://doi.org/10.1016/J.PROENG.2017.04.118.

[30] S. Eigler, M. Enzelberger-Heim, S. Grimm, P. Hofmann, W. Kroener, A. Geworski, C. Dotzer, M. Röckert, J. Xiao, C. Papp, O. Lytken, H.-P. Steinrück, P. Müller, A. Hirsch, Wet Chemical Synthesis of Graphene, Advanced Materials. 25 (2013) 3583–3587. https://doi.org/10.1002/ADMA.201300155.

[31] M. Etesami, E. Abouzari-Lotf, A. Ripin, M. Mahmoud Nasef, T.M. Ting, A. Saharkhiz, A. Ahmad, Phosphonated graphene oxide with high electrocatalytic performance for vanadium redox flow battery, International Journal of Hydrogen Energy. 43 (2018) 189–

197. https://doi.org/10.1016/j.ijhydene.2017.11.050.

[32] Y. Cai, Z. Yue, S. Xu, A novel polybenzimidazole composite modified by sulfonated graphene oxide for high temperature proton exchange membrane fuel cells in anhydrous atmosphere, Journal of Applied Polymer Science. 134 (2017) 1–8. https://doi.org/10.1002/app.44986.

[33] A.M. Abdelkader, I.A. Kinloch, R.A.W. Dryfe, High-yield electro-oxidative preparation of graphene oxide, Chemical Communications. 50 (2014) 8402–8404. https://doi.org/10.1039/C4CC03260H.

[34] B. Gurzęda, P. Florczak, M. Kempiński, B. Peplińska, P. Krawczyk, S. Jurga, Synthesis of graphite oxide by electrochemical oxidation in aqueous perchloric acid, Carbon. 100 (2016) 540–545. https://doi.org/10.1016/J.CARBON.2016.01.044.

[35] A. Ambrosi, M. Pumera, Electrochemically Exfoliated Graphene and Graphene Oxide for Energy Storage and Electrochemistry Applications, Chemistry – A European Journal. 22 (2016) 153–159. https://doi.org/10.1002/CHEM.201503110.

[36] F. Sharif, A.S. Zeraati, P. Ganjeh-Anzabi, N. Yasri, M. Perez-Page, S.M. Holmes, U. Sundararaj, M. Trifkovic, E.P.L. Roberts, Synthesis of a high-temperature stable electrochemically exfoliated graphene, Carbon. 157 (2020) 681–692. https://doi.org/10.1016/j.carbon.2019.10.042.

[37] J. Cao, P. He, M.A. Mohammed, X. Zhao, R.J. Young, B. Derby, I.A. Kinloch, R.A.W. Dryfe, Two-Step Electrochemical Intercalation and Oxidation of Graphite for the Mass Production of Graphene Oxide, Journal of the American Chemical Society. 139 (2017) 17446–17456. https://doi.org/10.1021/jacs.7b08515.

[38] C.-Y. Su, A.-Y. Lu, Y. Xu, F.-R. Chen, A.N. Khlobystov, L.-J. Li, High-Quality Thin

Graphene Films from Fast Electrochemical Exfoliation, ACS Nano. 5 (2011) 2332–2339. https://doi.org/10.1021/NN200025P.

[39]   J. Liu, C.K. Poh, D. Zhan, L. Lai, S.H. Lim, L. Wang, X. Liu, N. Gopal Sahoo, C. Li, Z. Shen, J. Lin, Improved synthesis of graphene flakes from the multiple electrochemical exfoliation of graphite rod, Nano Energy. 2 (2013) 377–386. https://doi.org/10.1016/J.NANOEN.2012.11.003.

[40]   Z. Tian, P. Yu, S.E. Lowe, A.G. Pandolfo, T.R. Gengenbach, K.M. Nairn, J. Song, X. Wang, Y.L. Zhong, D. Li, Facile electrochemical approach for the production of graphite oxide with tunable chemistry, Carbon. 112 (2017) 185–191. https://doi.org/10.1016/J.CARBON.2016.10.098.

[41]   F. Sharif, A.S. Zeraati, P. Ganjeh-Anzabi, N. Yasri, M. Perez-Page, S.M. Holmes, U. Sundararaj, M. Trifkovic, E.P.L. Roberts, Synthesis of a high-temperature stable electrochemically exfoliated graphene, Carbon. 157 (2020) 681–692. https://doi.org/10.1016/j.carbon.2019.10.042.

[42]   A.C. Ferrari, D.M. Basko, Raman spectroscopy as a versatile tool for studying the properties of graphene, Nature Nanotechnology 2013 8:4. 8 (2013) 235–246. https://doi.org/10.1038/nnano.2013.46.

[43]   A.C. Ferrari, Raman spectroscopy of graphene and graphite: Disorder, electron-phonon coupling, doping and nonadiabatic effects, Solid State Communications. 143 (2007) 47–57. https://doi.org/10.1016/j.ssc.2007.03.052.

[44]   L.M. Malard, M.A. Pimenta, G. Dresselhaus, M.S. Dresselhaus, Raman spectroscopy in graphene, Physics Reports. 473 (2009) 51–87. https://doi.org/10.1016/J.PHYSREP.2009.02.003.

[45] F. Wang, J. Yi, Y. Wang, C. Wang, J. Wang, Y. Xia, Graphite intercalation compounds (GICs): A new type of promising anode material for lithium-ion batteries, Advanced Energy Materials. 4 (2014) 1–6. https://doi.org/10.1002/aenm.201300600.

[46] C. Kiang Chua, M. Pumera, Renewal of sp^2 bonds in graphene oxides via dehydrobromination , (n.d.). https://doi.org/10.1039/c2jm34358d.

[47] E. Abouzari-Lotf, H. Ghassemi, S. Mehdipour-Ataei, A. Shockravi, Phosphonated polyimides: Enhancement of proton conductivity at high temperatures and low humidity, Journal of Membrane Science. 516 (2016) 74–82. https://doi.org/10.1016/J.MEMSCI.2016.06.009.

[48] B. Lafitte, P. Jannasch, Chapter Three On the Prospects for Phosphonated Polymers as Proton-Exchange Fuel Cell Membranes, Elsevier Ltd, 2007. https://doi.org/10.1016/S1752-301X(07)80008-1.

[49] Z. Guo, J. Chen, J.J. Byun, R. Cai, M. Perez-Page, M. Sahoo, Z. Ji, S.J. Haigh, S.M. Holmes, High-performance polymer electrolyte membranes incorporated with 2D silica nanosheets in high-temperature proton exchange membrane fuel cells, Journal of Energy Chemistry. 64 (2021) 323–334. https://doi.org/10.1016/j.jechem.2021.04.061.

[50] J.J. Bailey, J. Chen, J. Hack, M. Perez-Page, S.M. Holmes, D.J.L. Brett, P.R. Shearing, Lab-based X-ray micro-computed tomography coupled with machine-learning segmentation to investigate phosphoric acid leaching in high-temperature polymer electrolyte fuel cells, Journal of Power Sources. 509 (2021) 230347. https://doi.org/10.1016/J.JPOWSOUR.2021.230347.

7. Conclusions & Future Work

Based on the objectives proposed at the beginning of the thesis and the results obtained in Chapters 3-7, here is a summary of the results and conclusions made in the thesis.

1. The Application of Lab-based X-ray Micro-computed Tomography (CT) Coupled with Machine-learning Segmentation to Investigate Phosphoric Acid Leaching in High-temperature Polymer Electrolyte Fuel Cells (HT-PEMFC).

The third chapter describes the use of Lab-based X-ray CT combined with mechanical learning segmentation without the aid of synchrotron to explore the distribution and migration of each component of the membrane-electrode-assembly (MEA) of the HT-PEMFC and the change of porosity. Restricted by the detection speed and resolution, the Lab-based X-ray CT used in this work to detect MEA stays in the ex-suite stage. Laser milling and mechanical milling were compared to explore methods for obtaining reliable samples. Through multi-sample measurement of the dry membrane, phosphoric acid (PA) doped membrane, electrode and PA doped electrode can provide a base for MEA measurement. The mechanical learning applied can greatly assist segmentation to obtain high-quality, high-fidelity segmented volumes. This type of technical means can effectively detect the thickness distribution of the membrane, the catalyst distribution and content, the pore distribution and volume, and the ratio of the solid-liquid mixed phase. Restricted by laser energy and resolution and affected by the complex components in HT-PEMFC, it is difficult for Lab-based X-ray CT to accurately distinguish PA, microporous layer (MPL), gas diffusion layer (GDL) and binder inside MEA. Thus, chapter 3 focuses on exploring the influence of electrochemical factors on component migration and the correlation with component distribution by comparing the component changes before and after the constant current life test or accelerated stress testing (AST). Although Lab-based X-ray CT has limited differentiation of MEA components, this convenient method can still provide a lot

314

of information. As shown by continuous pore size distributions (cPSD) and tortuosity factor analysis, smaller pores are preferentially filled, and as the operation time increases, the difference in the connectivity of the pore network and the tortuosity factor between the two electrodes is greater. In addition, the degree of PA leaching can be inferred through the change of the contrast ratio and correlated with mass transfer. The establishment of this method enables low-cost and rapid exploration of the migration of phosphoric acid and catalyst layers without using synchrotron. Although the applied lab-based X-ray CT is difficult to accurately distinguish each component in HT-PEMFC, it can be utilized for rough diagnosis of the cause of performance degradation in the HT-PEMFC lifetime test. Furthermore, the application of this method can provide an effective tool for lab-based exploration of the effects of new materials on PA leaching and catalytst migration in HT-PEMFC.

2. Explore the Effect of Single-Layer Graphene (SLG) Load at Different Positions of HT-PEMFC on Its Performance, Durability, and PA Leaching.

Based on the method established in Chapter 3 and the effect of phosphoric acid leaching on the performance and durability of HT-PEMFC summarized in the life test of HT-PEMFC, Chapter 4 proposes the application of SLG in HT-PEMFC to improve its performance and durability and proposed the mechanism. Because the polybenzimidazole (PBI) membrane in HT-PEMFC is doped with PA, the technical feasibility of SLG loading on the PBI membrane is limited. SLG is loaded on the catalyst surface of the anode, the cathode or both. Because the wet chemical transfer method used will cause the SLG to lose coverage on the electrode due to damage when transferring the SLG prepared by chemical vapour deposition (CVD) method from the copper foil substrate to the electrode surface, the coverage of the SLG on the electrode surface is about 55%. It can be known by comparing the performance of MEA loaded with SLG at different positions before and after AST, the introduction of SLG may cause a delay in

the activation of HT-PEMFC in the initial stage and thus poor performance. However, with the progress of AST, MEA loaded with SLG gradually showed better performance than MEA based on pure PBI membrane. In other words, SLG can effectively improve the durability of HT-PEMFC. Through the characterization of electrochemical impedance spectroscopy (EIS), cyclic voltammetry (CV), X-ray CT and Raman spectroscopy mapping, the mechanism of SLG acting on HT-PEMFC can be proposed. When the catalyst activity and the proton conductivity of the membrane are constant, the performance of HT-PEMFC is largely determined by the area of the three-phase boundary composed of catalyst, electrolyte (PA), and fuel or oxidant. Due to the limited coverage of the SLG on the electrode, the PA quickly leaches in the uncovered areas and slowly leaches in the covered areas. This mechanism suppresses the overall excessive leaching of PA and improves durability. At the same time, the serrated PA leaching increases the three-phase boundary area and thus improves the performance of HT-PEMFC. In addition, SLG can effectively prevent the gradual increase of hydrogen crossover in the ultra-thin PBI film during the life test, so as to ensure that the ultra-thin PBI membrane has higher proton conductivity while preventing excessive hydrogen crossover. This work is the first to apply SLG to HT-PEMFC and propose a new method and mechanism to control the migration of PA in HT-PEMFC. It was demonstrated that SLG could prevent the migration of PA while maintaining high proton conductivity. This provides a new idea for controlling and maintaining the three-phase boundary area of HT-PEMFC in life tesing. This method of directly using physical barrier to influence PA leaching in HT-PEMFC provides a more reliable basis for the mechanistic explanation of the effect of PA leaching on the performance and durability of HT-PEMFC.

3. **Through the Design of Reactor Realized the Use of Natural Graphite Flakes as the raw materials for electrochemical exfoliation to quickly prepare graphene oxide (GO) with high-yield and high quality.**

316

The reactor based on 3D printing was designed and applied to electrochemical exfoliation to synthesize GO using natural graphite flakes as raw materials. The inverted funnel-shaped lid and the base are connected by a tenon structure to ensure that the natural graphite flakes can stay in the reactor. The porous structure on the lid ensures the ingress of ions and the exudation of gas. The plug with a copper foil extension is connected by a spring to ensure good contact between the graphite material and the external circuit.

Chapter 5 compares the difference between the products when graphite foil is used as the raw material without the assistance of the reactor and natural graphite flakes with the assistance of the reactor are used as the raw material. Under the same conditions (10V and 1 M Ammonium sulphate solution as electrolyte), the electrochemical exfoliation products of natural graphite flakes combined with reactor have better hydrophilicity, smaller size, and higher oxygen content. Through the X-ray diffraction (XRD) patterns of different reaction stages, it can be known that the reactor enables the natural graphite flakes to contact the current for a longer period, thereby being attacked by the nucleophile for a longer period of time and obtaining a higher oxidation level. The O/C ratio of electrochemical exfoliated GO (EGO) synthesized by natural graphite flakes with the assistance of the reactor can reach 0.247. The O/C ratio can be further improved by increasing the electrolyte concentration and reaction time. This design achieves one-step exfoliation using natural graphite flakes to obtain GO with tunable oxygen content without using strong oxidants or strong acids. Electrochemical exfoliation of natural graphite flakes directly as a raw material reduces raw material costs and shortens the manufacturing process. The production of graphene by means of electrochemical exfoliation realizes the production of materials for green energy generation equipment by using green energy. This makes the application of GO in HT-PEMFCs cheaper, more efficient and environmentally friendly.

4. **Synthesis of phosphonated (P)GO by electrochemical exfoliation through using appropriate electrolyte and reactor.**

Based on the method established in Chapter 5, Chapter 6 compared three methods based on ammonium dihydrogen phosphate as the electrolyte for electrochemical exfoliation, which are one step method based on graphite foil (1-step method), two-step method based on graphite foil (concentrated sulfuric acid is supplied as the electrolyte in the first step to synthesize graphite intercalation compounds (GIC), 2-step method) and one step method based on natural graphite flakes and reactor (reactor method). Through elemental and structural characterization, the products of the 1-step method, 2-step method and reactor method tend to be defined as pristine graphene with a small amount of oxygen-containing functional groups, GO rich in oxygen-containing functional groups and phosphonated GO with reasonable P content. Similar to the mechanism mentioned in Chapter 4, the realization of the synthesis of PGO by one-step electrochemical exfoliation may benefit from the restriction of the raw materials by the reactor so that it can have longer contact with current and the nucleophile that can be used for functionalization. This work is the first to realize the one-step preparation of PGO using electrochemical exfoliation without using any strong acid or strong oxidant, which is more cost-effective, efficient and safe. Further phosphonation of GO can enhance the performance and durability, of the HT-PEMFC.

5. **Apply electrochemical exfoliated (phosphonated, P) GO in HT-PEMFC to explore its effect on the performance and durability of HT-PEMFC.**

The EGO and PGO prepared by the methods mentioned based on natural graphite flakes and reactor were both doped in PBI membrane to explore its influence on the performance and durability of HT-PEMFC. Chapter 5 and Chapter 6 respectively report the application of as-prepared EGO and PGO in HT-PEMFC. Both EGO and PGO can effectively improve the

mechanical properties of PBI membranes and the performance and durability of HT-PEMFC. The 0.5%, 1% and 2% EGO loadings in the PBI membrane increased the peak power density by 13.8%, 24.4% and 29.2%, respectively. Due to the phosphonic acid group stands out in the relatively strong water retention capacity, strong hydrogen bonding and amphoteric characteristics of PGO, the doping of PGO in the PBI membrane performs better than GO with higher oxygen-containing functional group content prepared by the 2-step method. This demonstrates that electrochemically exfoliated GO and PGO can also be applied to the doping of PBI films to improve their performance and durability. Both EGO and PGO used for doping in the proton exchange membrane of HT-PEMFC were prepared in a clean electrochemical exfoliation method. In addition to improving the efficacy of HT-PEMFC as a clean energy source, this work also takes into account the greening of the production process of HT-PEMFC materials.

Future work

The methods used to detect the distribution and migration of PA in this thesis remain at the ex-situ level. Although the application of X-ray CT makes the distribution of PA at the 3D level, its resolution and discrimination still need to be improved, and tracking based on chemical elements is still lacking. The distribution and migration of PA may be affected by real-time electrochemical factors. Exploring fast and reliable in-situ methods to study the migration of phosphoric acid will be the next objective.

In the design of Chapter 6, PGO was obtained by replacing the electrolyte in Chapter 5. How to improve the functionalization level of electrochemically prepared PGO and replace different electrolytes to obtain different functionalized GO remains to be further explored. At the experiment level, the designed reactor shows the advantages of fast, efficient and green preparation of graphene oxide, and the use of small size graphite as raw material.

Industrialization based on this method and whether graphite from waster can be used as raw materials remains to be further explored to better serve sustainable energy.

Although SLG can effectively prevent excessive leaching of phosphoric acid, its coverage on the electrode is still uncontrollable. Exploring better methods for SLG transfer between different substrates needs to be developed such as roll to roll for commercialization.